Doctoral Dissertation
Doctoral Program in Physics (34th cycle)

High-precision measurement of the hypertriton lifetime and Λ-separation energy exploiting ML algorithms with ALICE at the LHC

Pietro Fecchio

* * * * *

Supervisor
Prof. S. Bufalino

Doctoral examination committee
Prof. L.L. Pappalardo, Referee, Università degli Studi di Ferrara
Prof. F. De Mori, Referee, Università degli Studi di Torino

Politecnico di Torino

I hereby declare that, the contents and organisation of this dissertation constitute my own original work and does not compromise in any way the rights of third parties, including those relating to the security of personal data.

. . . . . .

Pietro Fecchio
Torino, 13 Aprile, 2022

Summary

At the CERN Large Hadron Collider (LHC), the energies reached in heavy-ion collisions are such that a state of the matter called Quark-Gluon Plasma (QGP) can form. The production of the QGP is characterised by the large number of charged particles emerging from the collision ($\mathrm{d}N_{\mathrm{ch}}/\mathrm{d}\eta$ up to 2000 in Pb–Pb collisions at $\sqrt{s_{\mathrm{NN}}} = 5.02$ TeV), representing a major experimental challenge for the experiments operating in this high-multiplicity environment.

The A Large Ion Collider Experiment (ALICE) is designed precisely to operate in such conditions to study the properties of the QGP. Among the many particles produced in the collisions, (anti)hypernuclei are of particular interest. The lightest hypernucleus, the hypertriton, is a bound state of a neutron, a proton and a Λ baryon and is the subject of this thesis.

(Anti)hypernuclei provide the access door to study the hyperon-nucleon interaction, a crucial component of the nuclear force ruling the nuclear interactions. Therefore, the study of (anti)hypernuclei could provide significant clues for the comprehension of the nuclear force, with implications that go far beyond the High Energy Nuclear Physics. For example, determining the repulsive three-baryon interactions between nucleons and hyperons could explain the observation of two-solar-masses neutron stars.

New measurements of the (anti)hypertriton lifetime and Λ-separation energy (B_Λ), performed in recent years, have questioned the widespread belief – based on measurements from the late 60s and early 70s – that the (anti)hypertriton is a loosely bound object with a mean lifetime close to that of a free Λ baryon. The measurement of significantly higher B_Λ and lower lifetime suggested that the (anti)hypertriton is a much more bound and compact object than previously believed. However, the statistical and systematic uncertainties of the measurements did not allow for a conclusion on the (anti)hypertriton structure and lifetime.

The main goal of this thesis is to perform a new and more precise measurement of the (anti)hypertriton lifetime and B_Λ. Taking full advantage of the ALICE tracking and particle identification capabilities and a new dataset with an unprecedented number of detected collisions, the purpose was to obtain the most precise measurement ever achieved.

Thanks to state-of-the-art machine learning solutions for the signal/background discrimination and new approaches to the systematic uncertainty estimation designed

explicitly for this analysis, it was possible to outperform any other measurement obtained in modern experiments. This thesis's findings strongly support the loosely-bound nature of the hypertriton with a mean lifetime compatible with that of the Λ baryon.

Contents

List of Tables

List of Figures

Chapter 1

High Energy Nuclear Physics

The Universe, in its early stages, was extremely hot and dense according to modern cosmological theories [1–4]. Hadrons could not form due to the extremely high energy density, and the fundamental constituents of the matter were in a deconfined state. After the first microseconds, the energy density decreased enough to allow a phase transition, leading to the formation of ordinary matter.

High Energy Nuclear Physics (HENP) studies heavy-ion collisions at ultra-relativistic energies to investigate the properties of hot and dense nuclear matter and its transition to ordinary matter. Those studies are crucial to understanding the first moments of the Universe life and the behaviour of the matter under extreme conditions.

1.1 QCD: the Theory of the Strong Interaction

Quantum Chromodynamics (QCD) [5] describes the Strong Interaction in terms of the interaction between quarks and gluons. Quarks are the fundamental constituents of matter, while gluons are the gauge bosons that mediate the strong interaction between quarks. The formulation of this field theory poses its roots in the theory of Quantum Electrodynamics (QED) [5] which provided a framework for all field theories on which the Standard Model relies.

The QCD is a non-Abelian gauge field theory based on the SU(3) symmetry group. According to this theory, the charge responsible for the Strong Interaction carried by quarks and gluons comes in three different states. The charge is called *colour* and its three states are named: *red, blue* and *green*. The colour interaction is then mediated by eight massless gauge bosons – the gluons – arising from from the invariance of the theory under local SU(3) transformations in the colour space [6]. The QCD Lagrangian can be written as follow:

$$\mathcal{L}_{\text{QCD}} = \bar{\psi_i}(i\gamma^\mu(D_\mu)_{ij} - m\delta_{ij})\psi_j - \frac{1}{4}G^a_{\mu\nu}G^{\mu\nu}_a. \tag{1.1}$$

The first term of Equation (1.1) describes the quark field $\psi_i(x)$ with indices i and

j running from 1 to 3 and γ^μ are the Dirac matrices. The symbol $(D_\mu)_{ij}$ denotes the gauge covariant derivative that describes the coupling of the quark field $\psi_i(x)$ with the gluon field $\mathcal{A}^a_\mu(x)$:

$$(D_\mu)_{ij} = \partial_\mu \delta_{ij} - ig_s(T_a)_{ij}\mathcal{A}^a_\mu. \tag{1.2}$$

In Equation (1.2) g_s is the coupling constant of the Strong Interaction and T_a are the infinitesimal generators of SU(3) in the fundamental representation. The Gell-Mann matrices λ_a $(a = 1, \dots, 8)$ can be used to provide and explicit representation of the generators: $T_a = \lambda_a/2$. In the second term of Equation (1.1) $G^a_{\mu\nu}$ is the gauge invariant gluon field strength tensor:

$$G^a_{\mu\nu} = \partial_\mu \mathcal{A}^a_\nu - \partial_\nu \mathcal{A}^a_\mu + g_s f^{abc}\mathcal{A}^b_\mu \mathcal{A}^c_\nu. \tag{1.3}$$

Here, $\mathcal{A}^a_\mu(x)$ (a, b and $c = 1, \dots, 8$) is the aforementioned gluon field and f^{abc} are the SU(3) group structure constants.

The gluon–quark interaction described by the first term of the QCD Lagrangian describes a QED-like vertex, represented by the diagram shown in Figure 1.1. The second term of the QCD Lagrangian contains the non-Abelian part of the theory – $g_s f^{abc}\mathcal{A}^b_\mu \mathcal{A}^c_\nu$ – and allows for three gluons and four gluons vertices at the tree level. These vertices, shown in Figure 1.2, lead to the gluons self-interaction that characterises the QCD theory.

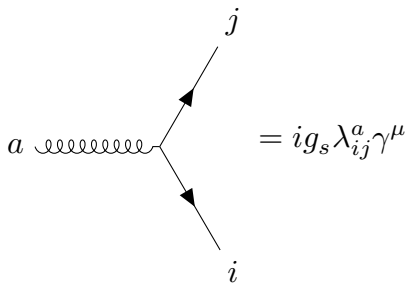

Figure 1.1: The gluon-quark interaction vertex.

The presence of the gauge bosons' self-interactions term in the QCD Lagrangian has essential implications for the renormalisation of the theory. In the computation of the gluon propagator, the gluon loops corrections and the quark loops corrections contribute to the sum with opposite signs. The quark loop is responsible for a colour charge *screening effect* – analogous to the electric charge screening characteristic of the QED theory [7] – while gluon loops give rise to a colour charge *anti-screening* effect

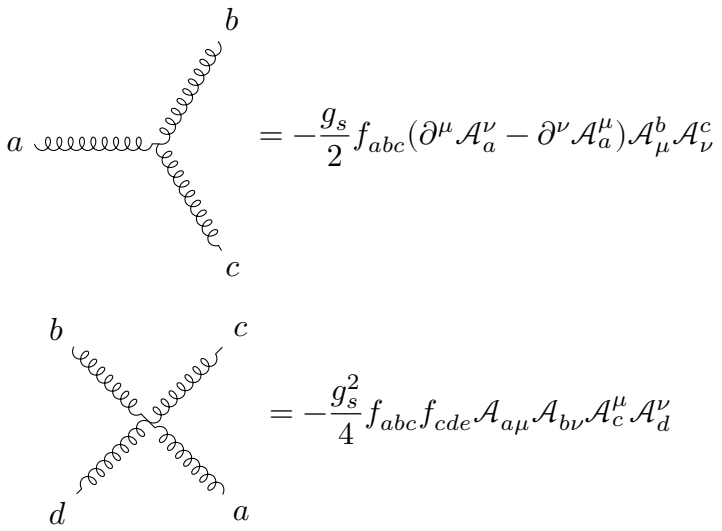

Figure 1.2: Feynman diagrams for three and four gluons self interaction vertices at the tree level.

characteristic of non-Abelian theories. As a result, the QCD coupling constant depends on the transferred four-momentum of the considered process, as derived by Politzer [8] and Gross [9] and confirmed by the experiments over the years – see Figure 1.3.

By defining $\alpha_s = g_s^2/4\pi$, the strong coupling constant can be written as [4]:

$$\alpha_s(Q^2) = \frac{\alpha_s(\mu^2)}{1 + \alpha_s(\mu^2)(33 - 2n_f)\ln(Q^2/\mu^2)} \tag{1.4}$$

where n_f is the number of quark flavours and μ is the renormalization scale of the theory. From Equation (1.4) two different features of the QCD theory emerge, depending on the energy scale Q of the process.

For high Q^2 processes – i.e. for small distances – the strong coupling constant α_s goes to zero, and the QCD becomes a free theory. This condition where the screening effect entirely suppresses the colour charge is called *asymptotic freedom*. On the other hand, for low Q^2 processes – i.e. for large distances – the strong coupling is extraordinarily high, and the quarks are forced to form bound states. Even if there is no analytic proof for this effect called *confinement*, it is very well established from the experimental evidence that free quarks are not observable. By fixing the energy scale, the Equation (1.4) can be rewritten as:

$$\alpha_s(Q^2) = \frac{12\pi}{(33 - 2n_f)\ln(Q^2/\Lambda_{QCD})} \tag{1.5}$$

where Λ_{QCD} is the renormalization scale of the QCD theory, typically $\Lambda_{\text{QCD}} \approx 200\,\text{MeV}$.

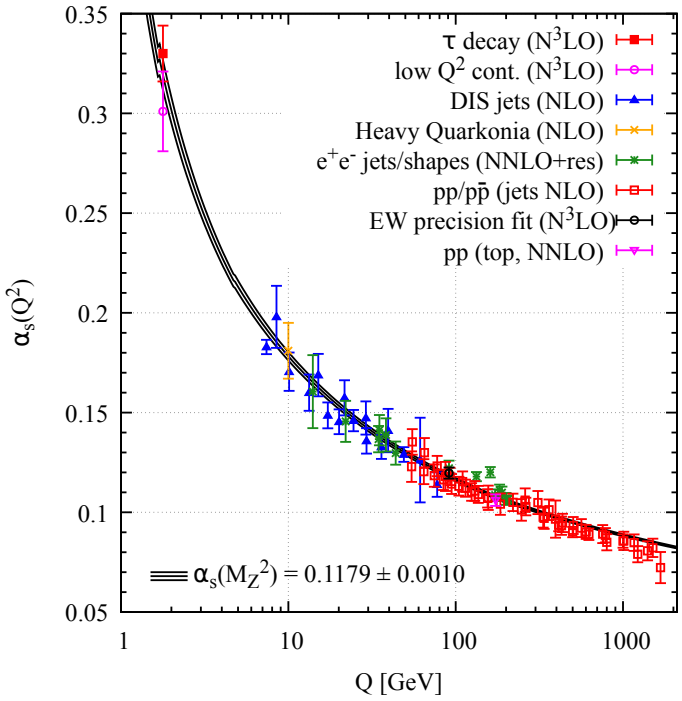

Figure 1.3: Summary of the α_s measurements as a function of the energy scale Q [4].

Because of the Q^2 dependence of α_s, it is possible to calculate the elements of the S-matrix with a perturbative approach (pQCD) only for high Q^2 processes – $Q^2 \gg \mu^2$ –, for which $\alpha_s \ll 1$. In low transferred momentum processes, α_s is of the order of unity, and it is impossible to compute the elements of the S-matrix in terms of a power series expansion of the strong coupling constant. In 1974 Wilson [10] proposed a new method to solve gauge theories calculations, suited for diverging coupling constant theories as to the QCD. The idea is to evaluate Green's functions of the QCD Lagrangian on a space-time lattice with space a and extrapolate the results to the continuum limit $a \to 0$, making it possible to compare the calculations with the experiments. This method – called lattice regularised QCD or LQCD – reached a remarkable success in determining the proton mass with a precision of 2 % [11].

1.2 States of the Hadronic Matter

Describing the interactions between quarks and gluons, QCD predicts the possibility of having different states of the hadronic matter. It is a fascinating consequence of the running coupling constant of the strong interaction. In a system of interacting quarks and gluons, the mean transferred energy of the interactions – that define the mean value of α_s – determines the state of the system. For low mean transferred momentum systems, the high α_s value forces the system to be in the confinement regime and

quarks and gluons are precisely confined in bound states: the hadrons. Otherwise, for systems characterised by a high mean transferred momentum, the asymptotic freedom regime allows the formation of a plasma where quarks and gluons are essentially free. This plasma, formed by free quarks and gluons, is called Quark-Gluon Plasma (QGP) [12]. The study and characterisation of the QGP and the phase transitions between the different states of the hadronic matter are among the HENP's primary goals.

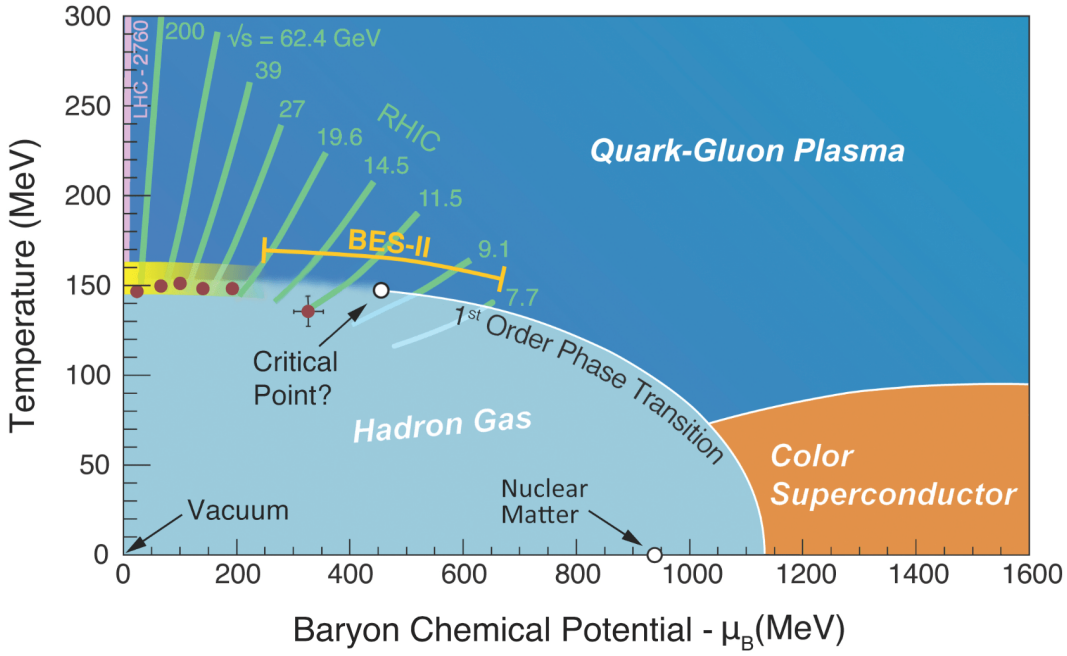

Figure 1.4: An experimental and theoretical exploration of the QCD phase diagram. (Illustration: Swagato Mukherjee, Brookhaven National Laboratory.)

In a thermodynamical picture, it is possible to describe a system composed of hadronic matter with finite dimensions using global variables like the temperature T and the baryon chemical potential μ_B. In such a framework, μ_B represents the energy required to create a baryon state. The T, μ_B diagram in Figure 1.4 shows the different phases of the QCD derived from both experimental observations and theoretical predictions. The origin – $T = \mu_B = 0$ GeV – corresponds to the QCD vacuum. Along the μ_B axis the ordinary nuclear matter – composed by protons and neutrons – sits just below $\mu_B = 1$ GeV that is, in fact, approximately the energy of a nucleon at $T = 0$. At higher μ_B values, a phase transition between the ordinary matter and the colour-flavour locked (CFL) phase – a state of the matter in which the flavour and the colour of the quarks are correlated in a one-to-one correspondence – is expected [13]. The QCD coupling is weak at these high densities; therefore, quarks of all three colours form a condensate of Cooper pairs, showing both superconductivity and superfluidity [14]. The conditions needed to reach this phase could occur in nature only in particular neutron stars where a stable superconducting quark matter core can form [15]. Moving along the T axis –

where $\mu_B = 0$ – a phase transition takes place when $T \gg \Lambda_{QCD}$. At this temperature, the *asymptotic freedom* is reached due to the high average momentum exchanged between partons; hence they are no longer confined in colour singlets states. They form the QGP mentioned above, a plasma of free quarks and gluons, similar to the primordial Universe. At lower temperatures, the hadronic matter is in a hadron gas state.

The order of a phase transition describes how fast the system's free energy varies in a neighbourhood of the transition temperature. In particular, it determines whether the time derivative of the system free energy is continuous or not. If the time derivative is discontinuous, a *first order* transition takes place, and this implies that latent heat is involved in the process. A *second order* transition, instead, takes place when the first derivative with respect to the time is continuous while higher-order derivatives are not. The particular transition that occurs when both the free energy of the system and its derivatives with respect to the time are continuous is called *crossover* transition.

The QCD phase diagram shows a *crossover* transition between the QGP and the hadronic matter phase for temperatures around $150\,\text{MeV}$ for μ_B close to 0, while in the region of higher μ_B the transition is of a *first order* type. The precise determination of the critical point of the QCD phase diagram, which separates the *crossover* region from the *first order* transition line, is still an open question in the HENP field.

1.3 Heavy-Ion Collisions

An active sector of the nuclear theory community tries to derive the equation of state (EoS) of the nuclear matter and its phase diagram from theories and models. Unfortunately, with the current technology, predictions are difficult to test. The extremely high density or high temperature – or both at the same time – necessary to explore the whole phase diagram are impossible to be produced in the laboratory.

The astronomic observation of massive neutron stars provides access to the high μ_B region at $T \approx 0\,\text{GeV}$ since these conditions should be present in their inner core. Recently it has also been shown that a phase transition of the nuclear matter in the inner core of neutron stars can be linked to the observation of particular oscillation modes in gravitational waves [16], opening new frontiers for the exploration of the QCD phase diagram.

In the laboratory, it is possible to explore the high T and low μ_B region by colliding ultra-relativistic heavy ions. If it is provided with enough energy, this type of collision can create a *fireball* where the temperature is such that the phase transition to the QGP takes place. The first experiments with heavy-ions collisions (HIC) occurred in the '70s at the Lawrence Berkeley National Laboratory (LBNL), giving way to High Energy Nuclear Physics. Over the years, incredible progress has been made in this field, passing from the barely relativistic conditions at LBNL – collisions at $\approx 2\,\text{GeV/nucleon}$ – to the extreme energies available nowadays at the CERN Large Hadron Collider (LHC) –

where the centre-of-mass energy of the collisions is more than 5 TeV for colliding nucleon pair. Besides the LHC, there is another hadron collider that carries on a HENP program with HIC and dedicated experiments: the Relativistic Heavy Ion Collider (RHIC) at the Brookhaven National Laboratory (BNL) [17].

1.3.1 Glauber Model of Nucleus–Nucleus Collisions

The nuclei are systems with finite dimensions composed of nucleons, and it can be very complex to describe their collision, especially at ultra-relativistic energies. The Glauber model [18] addresses this problem by describing a nucleus–nucleus interaction in terms of incoherent overlap of nucleon–nucleon (NN) interactions in a semi-classical picture. The goal of the Glauber model is to connect distributions of experimental observable to the distributions of geometric quantities of the collision.

The model requires some experimental data as inputs to calculate all the geometric parameters of the collision. The most important ones are the inelastic nucleon–nucleon cross-section as a function of the energy and the nuclear charge densities.

A Fermi distribution with three parameters – commonly known as Woods-Saxon – is usually used to model the functional form of the nuclear density:

$$\rho(r) = \rho_0 \frac{1 + w(r/R)^2}{1 + \exp(\frac{r-R}{a})}, \tag{1.6}$$

where ρ_0 is the nucleon density in the centre of the nucleus, R is the radius of the nucleus, a corresponds to the skin depth, and w is needed to describe non-spherical nuclei.

The input nucleon–nucleon cross-section σ_{inel}^{NN} is measured since it is impossible to calculate it using perturbative QCD since the process involves low momentum interactions.

Historically, two approaches have been developed to calculate geometry-related quantities: the Optical Limit approximation and the Monte Carlo Glauber approach.

Optical Glauber Model

If the energy of the collision is sufficiently high – and this is, of course, the case at modern hadron colliders like LHC and RHIC – it is possible to assume the *optical limit* approximation. This implies that nucleons are not deflected in the collision since they carry enough momentum; they travel in a straight line. It is also possible to consider the independent motion of the nucleons inside the nucleus since the range of the nucleon–nucleon force is minimal compared to the nucleus radius.

Figure 1.5 shows the geometry of two colliding nuclei at relativistic velocities. The nuclei are Lorentz contracted in the motion direction – side view (a) – due to the relativistic momentum, so they are squeezed in that direction. Instead, their transverse

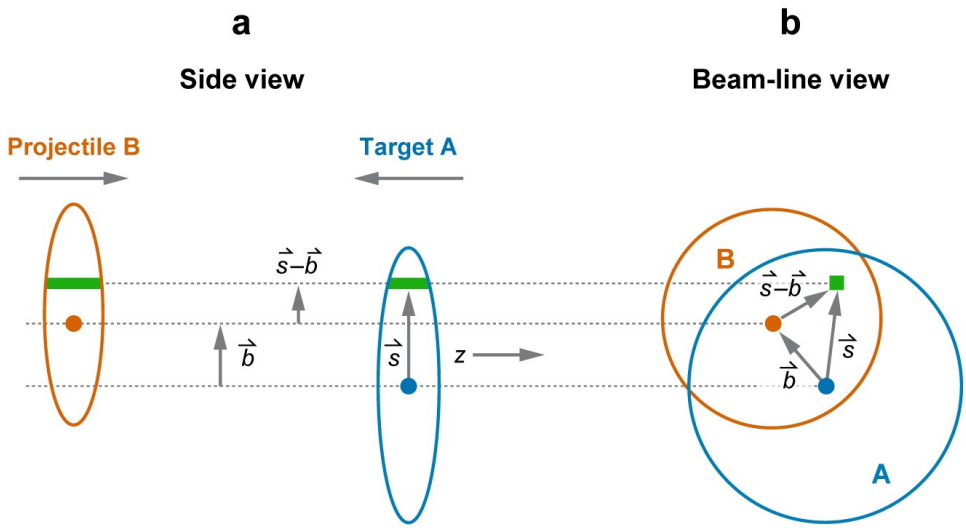

Figure 1.5: Optical Glauber model geometry for the collision of a projectile nucleus B with a target nucleus A – the distinction between the target and projectile nuclei is a matter of convenience for colliding beam experiments – as described in [18]. The vector, in the beam-line view, joining the centre of A and the centre of B is defined as the impact parameter $\vec{b}$.

section is visible in the beam-line view (b). Following the notation introduced in the figure, it is possible to define the *thickness functions* for nuclei A and B:

$$T_A(\vec{s}) = \int \rho(\vec{s}, z_A) dz_A \tag{1.7}$$

and

$$T_B(\vec{s}, \vec{b}) = \int \rho(\vec{s} - \vec{b}, z_B) dz_B. \tag{1.8}$$

Since $\rho(\vec{s}, z)$ represents the probability of finding a nucleon in the unit of volume located at $\vec{s}$, $T_A(\vec{s})$ and $T_B(\vec{s}, \vec{b})$ represent the probability per unit of transverse area. Thus, Equation (1.9) defines the *nuclear overlap function* for two colliding nuclei.

$$T_{AB}(\vec{b}) = \int T_A(\vec{s}) T_B(\vec{s} - \vec{b}) d^2 s \tag{1.9}$$

In the *optical limit* approximation, elastic interactions between nucleons are not considered since they have negligible effects. Furthermore, only binary interactions between nucleons are considered and each nucleon can participate in more than one binary collision. Given that nucleus A have A nucleons and nucleus B have B nucleons and σ_{inel}^{NN}

is the measured nucleon–nucleon inelastic cross-section, the probability of having n binary nucleon–nucleon interactions is then given by Equation (1.10).

$$P(n,\vec{b}) = \frac{AB!}{n!(AB-n)!}\left[T_{AB}(\vec{b})\sigma_{inel}\right]^{n}\left[1-T_{AB}(\vec{b})\sigma_{inel}^{NN}\right]^{AB-n}. \tag{1.10}$$

The total inelastic cross-section as a function of the impact parameter is hence obtained integrating the double differential cross-section for two colliding nuclei:

$$\frac{d^2\sigma_{inel}^{AB}(\vec{b})}{db^2} = \sum_{n=1}^{AB} P(n,\vec{b}) = 1-\left[1-T_{AB}(\vec{b})\sigma_{inel}^{NN}\right]^{AB} \tag{1.11}$$

$$\sigma_{inel}^{AB}(\vec{b}) = \int_0^{\infty}\left(1-\left[1-T_{AB}(\vec{b})\sigma_{inel}^{NN}\right]^{AB}\right)2\pi b db. \tag{1.12}$$

The number of nucleon–nucleon collisions $N_{coll}(b)$ is then:

$$N_{coll}(b) = \sum_{n=1}^{AB} nP(n,b) = AB\,T_{AB}\,\sigma_{inel}^{NN}. \tag{1.13}$$

The impact parameter vector $\vec{b}$ can be replaced by a scalar distance b if the nuclei are not polarised since, in this case, the colliding system has a cylindrical symmetry. The number of *participants* nucleons – also known as the number of *wounded nucleons* – at impact parameter b, $N_{part}(b)$ is given by:

$$\begin{aligned} N_{part}(b) = \int d^2s \Big[& AT_A(\vec{s})\Big[1-\left(1-T_B(\vec{b}-\vec{s})\sigma_{inel}\right)^{B}\Big] \\ & +BT_B(\vec{b}-\vec{s})\Big[1-\left(1-T_A(\vec{s})\sigma_{inel}\right)^{A}\Big]\Big]. \end{aligned} \tag{1.14}$$

So the optical limit approximation allows to express N_{part} and N_{coll} as a function of the impact parameter $\vec{b}$. The main limitation of this approach is that the model considers continuous nucleon density distributions, while nucleons are discrete objects, and their spatial position inside the nucleus can differ event by event.

Both N_{part} and N_{coll}, then, should be considered as average values over a high number of collisions.

Monte Carlo Glauber Model

In the optical limit approximation, the colliding nuclei are described through a continuous nuclear density distribution. In the Monte Carlo Glauber model, instead, nuclei are modelled, generating a three-dimensional discrete distribution of A nucleons for the nucleus A and B nucleons for the nucleus B, according to their nuclear density

function. Then the $A + B$ collision with impact parameter b is simulated with b drawn from the distribution $d\sigma/db = 2\pi b$.

The nucleus–nucleus collision is treated as the sum of N_{coll} independent binary nucleon collisions with a nucleon–nucleon inelastic cross-section σ_{inel}^{NN} assumed independent from the number of collisions in which a nucleon participated. In addition, the nucleons are considered to travel in a straight line, and elastic nucleon interactions are neglected, just as in the case of the optical limit approximation. It is possible to use different methods to determine if a nucleon–nucleon interaction occurs. The simplest way is to consider the distance between the nucleons in the transverse plane with respect to the beam axis d. In this case the collision takes place if:

$$d \leq \sqrt{\sigma_{inel}^{NN}/\pi}. \tag{1.15}$$

Then a large number $A + B$ collisions are simulated and the experimental observable

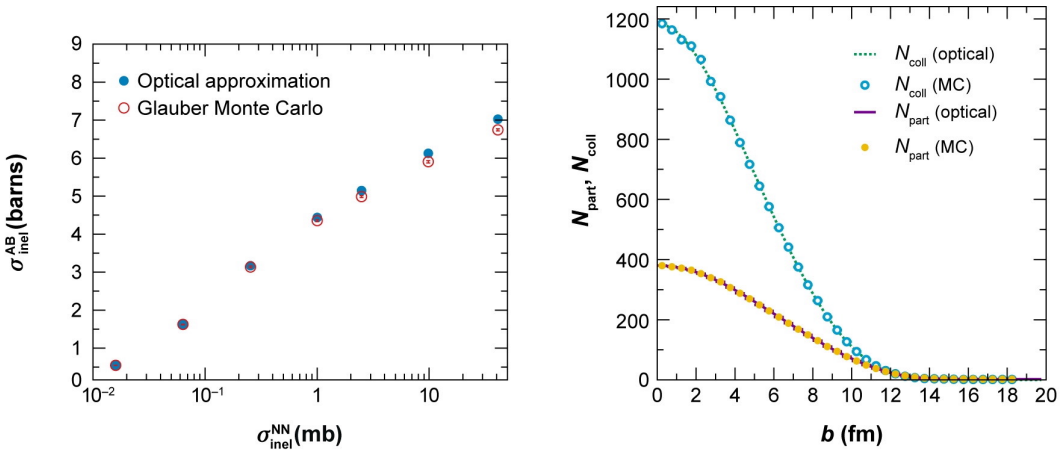

Figure 1.6: (*Left*) The total cross-section, calculated in the optical approximation and with a Glauber Monte Carlo (MC) – both with identical nuclear parameters – as a function of the inelastic nucleon–nucleon cross-section σ_{inel}^{NN}. (*Right*) N_{coll} and N_{part} as a function of the impact parameter, calculated in the optical approximation (*lines*) and with a Glauber Monte Carlo (*symbols*).

– e.g. $\langle N_{coll} \rangle$ and $\langle N_{part} \rangle$ – are computed as the average of the number of collisions.

The two approaches to the Glauber model give comparable results in the calculation of the geometrical quantities as shown in Figure 1.6. The computed nucleus–nucleus cross-sections converge to the same value (*left plot*) for small σ_{inel}^{NN} cross-section. Minor deviations are, instead, present for high σ_{inel}^{NN} and this is, however, expected since, in that case, the point-like approximation for the nucleons is not precise enough.

1.3.2 Space-time Evolution of the Collision

The collision of two ultra-relativistic atomic nuclei creates a strongly interacting system in the impact region, where it reaches extremely high hadron and energy densities. This system, while evolving, passes through some crucial stages and may also occur the phase transition to the QGP and ordinary matter again. Figure 1.7 summarises the current view of the space-time evolution of this strongly interacting system. The different stages – represented with different colours – are characterised by the time range in which they occur:

1. $t < 0\,\mathrm{fm}/c$: the two nuclei are travelling in the beamline at ultra-relativistic energies. Because of their velocity, close to the speed of light, they are Lorentz contracted in the motion direction – by a factor $\sim$2700 at the LHC.

2. $t = 0\,\mathrm{fm}/c$: collision time. The Glauber model is usually used to describe the geometry of the collision.

3. $0 < t \lesssim \tau_0$: the high transferred momentum interactions between colliding partons characterises the early stages of the collision; it is called *pre-equilibrium* phase. In the hard processes occurring in this phase, all the particles with high mass or/and high momentum are produced. The partons, forming the colliding nuclei, tend to escape from the collision region at forward rapidity ($|y| \gg 0$) while losing their energy at mid-rapidity ($y \approx 0$). If the collision energy is large enough, the escaping partons bring the baryonic potential at forward rapidity, leaving a null baryon chemical potential at mid-rapidity. The resulting system at mid-rapidity is extremely hot and dense. The transition phase to the QGP is expected if the energy density reached in this stage is large enough. In the event for which the transition phase occurs, droplets of QGP are formed, and after a parton rescattering phase, they reach the thermal equilibrium at a proper time τ_0 – in the collisions at the LHC energies $\tau_0 \sim 0.2\,\mathrm{fm}/c$.

4. $\tau_0 \lesssim t \lesssim 10\,\mathrm{fm}/c$: the QGP droplets reached the thermal equilibrium at τ_0. They are now subject to thermal pressure gradients at the system boundaries, so they collectively expand because of these pressures. The expansion of the QCD matter is rapid and influences the system's final state, which is what one can experimentally observe. It is then crucial to describe the dynamic of this expansion to interpret the experimental data, which is typically done through relativistic hydrodynamics models [19]. During the expansion, the system cools down, and the energy density decreases until it meets the conditions for the transition phase from the QGP to the ordinary hadronic matter. The system then returns to the hadronic matter state with a crossover transition.

5. $10 \lesssim t \lesssim 15\,\mathrm{fm}/c$: the system is now at the critical temperature between the QGP and the hadronic matter phase. In this time range, the hadronisation process starts, and the system turns into an interacting hadron resonance gas while

it continues to expand and cool down. Meanwhile, the hadrons interact with each other both elastically and inelastically. The inelastic interactions led to a continuous mixing of the particle species until the energy density decreases so much that the system stops to interact inelastically. The relative abundances of the particle species are fixed, and the temperature which characterises this instant is called *chemical freeze-out temperature* T_{ch}. Only elastic interactions are allowed at this point of the system's evolution, varying the particles' momentum spectra. The particles ' momentum distribution is fixed when even the elastic interactions can no longer occur due to the system expansion. The temperature at which the particles produced in the collision are completely decoupled is called *kinetic freeze-out temperature* T_{Kin}.

6. $t \gtrsim 15\,\mathrm{fm}/c$: hadrons are free to escape from the interaction region. This stage is also called *free hadron stream.*

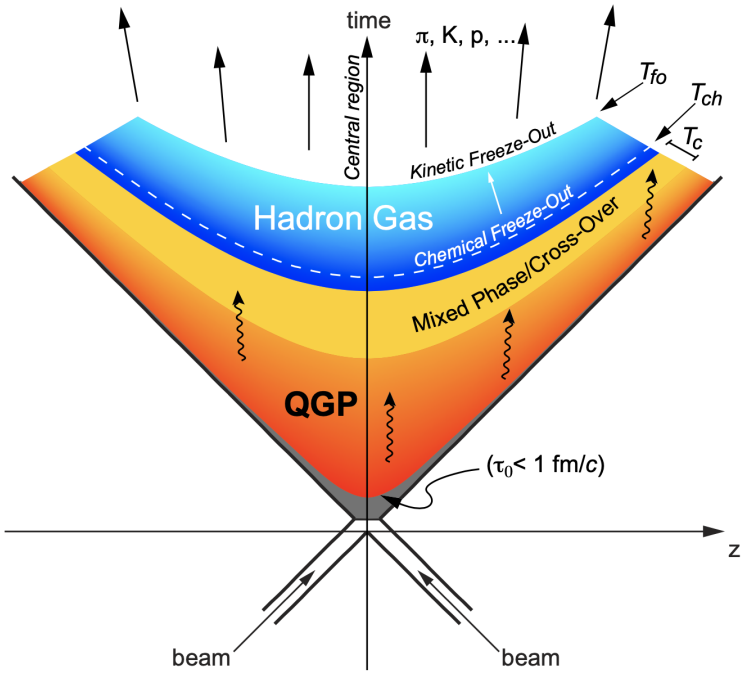

Figure 1.7: Sketch of the space-time evolution of the strongly interacting system created in the mid-rapidity region of a central HIC.

After escaping from the interaction region, the particles produced in the collision can be detected by the detectors installed in the collider experiments. The experimental apparatus used to study the HIC surround the collider interaction point, covering a specific rapidity region. They can detect the particles emerging from the collisions and

measure the particle production spectra and their correlations; it is possible to infer crucial information about the system produced in the collisions and the medium they travelled.

1.4 Probing Quark-Gluon Plasma

> The combined data coming from the seven experiments on CERN's Heavy Ion programme have given a clear picture of a new state of matter. This result verifies an important prediction of the present theory of fundamental forces between quarks. It is also an important step forward in the understanding of the early evolution of the Universe. We now have evidence of a new state of matter where quarks and gluons are not confined.

At that time, Professor Luciano Maiani, CERN Director General, announced the observation of a new state of the matter at the Super Proton Synchrotron (SPS) in a seminar held on February 10, 2000. This announcement followed the publication of a review [20] of the results achieved by the CERN's Heavy Ion programme from 1994 to 2000. This publication confirmed the existence of the QGP by multiple indirect experimental evidence since a single, direct and incontrovertible proof is not available. It was a "proof by circumstantial evidence".

Even today, a single, direct and incontrovertible proof of the existence of the new state of the matter is not available. However, multiple experimental measurements corroborating the existence of the QGP through indirect evidence have been performed since the '90s. So there are no doubts about its existence anymore.

The following sections present the most significant experimental results that show the evidence of the QGP and shed light on its features and properties.

1.4.1 Soft Probes

Hadrons Momentum Spectra

The low momentum hadrons represent the majority of the hadrons produced in a HIC ($\approx$99 %). Important insights about the status of the emitting source can be inferred by studying the momentum spectra of these particles, often referred to as *soft hadrons*. Since the elastic interactions between the particles emerging from the collision stopped at the kinetic freeze-out, the momentum spectra of the identified particles provide an indirect snapshot of the system.

The particle spectra for the i species can be described by:

$$\frac{1}{m_{\mathrm{T}}}\frac{\mathrm{d}^2 N_i}{\mathrm{d}m_{\mathrm{T}}\,\mathrm{d}y} \propto e^{-\beta m_{\mathrm{T}}}, \tag{1.16}$$

where the m_{T} is transverse mass defined as $m_{\mathrm{T}} = \sqrt{m^2 + p_{\mathrm{T}}^2}$ and p_{T} is the transverse momentum. This relation relies on the assumption that the Boltzmann-Gibbs distribution describes the system at the kinetic freeze-out, and in this picture, all the particle species are emitted at a common emission temperature $T = 1/\beta$. Thus, particle spectra are expected to be the same for all the species – this behaviour is called m_{T} *scaling* – as observed in pp collisions at a low centre of mass energy of the collision ($\sqrt{s}$).

In HIC, however, the m_{T} scaling breaks down, and each particle species shows a different slope – i.e. different temperature – in the measured spectra; in particular, the slope of the particle spectra decreases with the mass of the specific species. The spectra shift towards higher p_{T} for higher mass particles, translating into a lower temperature T. This effect can be interpreted as the superimposition of a collective hydrodynamical expansion of all the particles along the transverse plane – called *radial flow* – with the thermal agitation of the system at the moment of the kinetic freeze-out. The temperature parameter for the i-th species, therefore, can be written as:

$$T_i = T_{\mathrm{Kin}} + \frac{1}{2} m_i \langle v_\perp \rangle^2. \tag{1.17}$$

The parameter T_{Kin} is the temperature of the kinetic freeze-out while the other term takes into account the hydrodynamical expansion which takes place with an average transverse velocity $\langle v_\perp \rangle$. The result is a modification in the production spectra that are pushed to higher values of the transverse momentum the higher is the particle mass. This phenomenon is clearly visible in the pion, kaon and proton spectra in Figures 1.8a and 1.8b where the pions spectrum exhibits a steeper slope (*soft spectrum*) while the slope of the protons spectrum is reduced (*hard spectrum*). The slope of the measured spectra depends also on the energy available in the collision as shown in Figure 1.8b. At lower collision energy the measured p_{T} spectra [22, 23] exhibit a softer profile with respect to the ones measured at the LHC [24], where the $\sqrt{s_{\mathrm{NN}}}$ is almost 14 times larger. This phenomenon is interpreted in the hydrodynamical picture as the consequence of stronger pressure gradients in the expanding medium, causing stronger radial flow, in the collisions energy at the LHC.

The hydrodynamical models can reproduce the dynamics of the matter produced in HIC and describe the slope modification of the production spectra. However, to obtain an accurate description of the measured spectra over a wide momentum range, they implement some corrections to take into account the bulk viscosity at the chemical freeze-out – as done in the Krakow model [25] –, or a hybrid approach with a direct description of the hadronic phase followed by a hydrodynamic expansion – as done in the HKM model [26]. The agreement between hydrodynamical calculations and data shown in Figures 1.8a and 1.8b is a good indication that the radial flow interpretation captures some fundamental features of the medium generated in the collision.

The temperature of the kinetic freeze-out T_{Kin} is usually extracted from a simultaneous fit of the measured spectra of pions, kaons and protons with a Blast Wave model

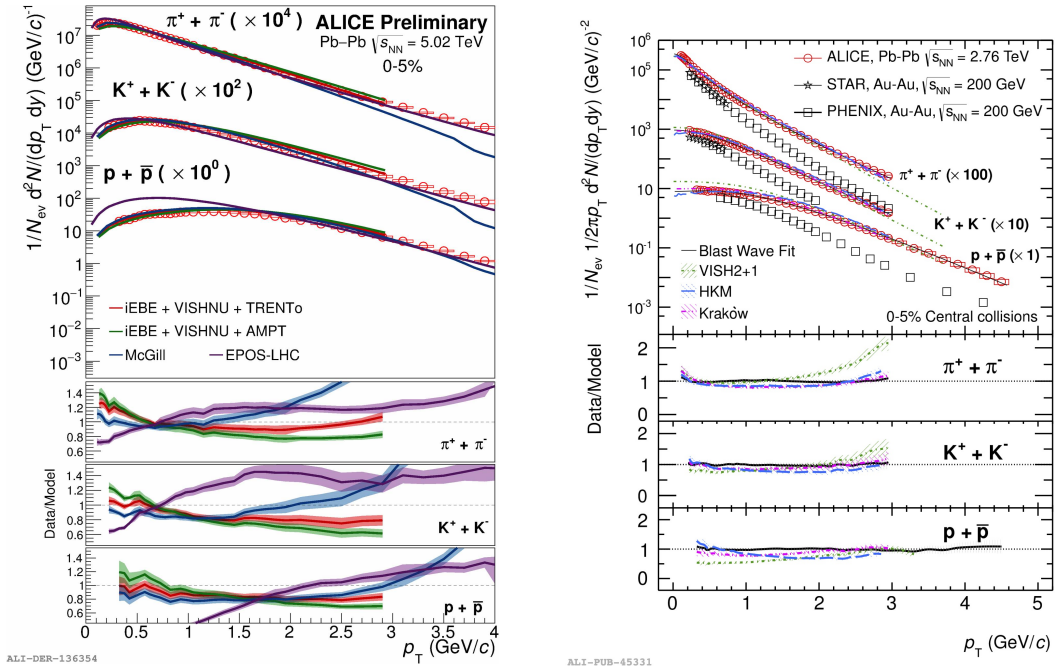

(a) **(b)**

Figure 1.8: Pion, kaon and proton transverse momentum spectra in central (0–5 % centrality class) Pb–Pb collisions at $\sqrt{s_{\mathrm{NN}}} = 5.02\,\mathrm{TeV}$ [21] (a), in central (0–5 % centrality class) Au–Au collisions at $\sqrt{s_{\mathrm{NN}}} = 200\,\mathrm{GeV}$ at the RHIC [22, 23] and in central (0–5 % centrality class) Pb–Pb collisions at $\sqrt{s_{\mathrm{NN}}} = 2.76\,\mathrm{TeV}$ at the LHC [24] (b).

[27]. Although it provides a simplified description of the hydrodynamics of the expansion, this model provides an important tool to derive the T_{Kin} parameter together with the mean radial velocity $\langle\beta_\perp\rangle$ of the particles at the kinetic freeze-out. The comparison of the results of these fits [24] highlights how both the kinetic freeze-out temperature T_{Kin} and the radial flow velocity $\langle\beta_\perp\rangle$ are larger at LHC energies compared to those obtained at the RHIC.

Anisotropic Flow

When two heavy ions collide, they usually overlap only partially; the collision with impact parameter close to zero, are just a small fraction of all the possible events. The overlap region takes the typical elliptic form as shown in Figure 1.9, causing geometrical anisotropies in the nuclear matter generated in the collision. These anisotropies are transferred to the momentum space by the pressure gradients, leading to azimuthal anisotropies in the particle production spectra that can be measured with the following

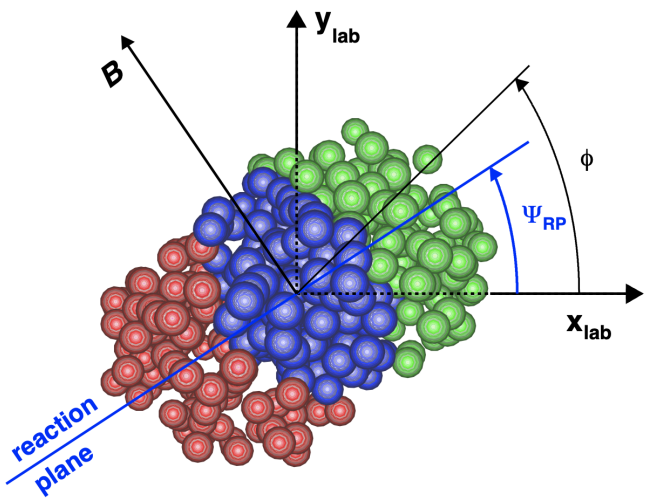

Figure 1.9: Schematic depiction of the transverse plane of a HI collision from [28]. The left nucleus (red nucleons) is emerging from the page and the right nucleus (green nucleons) is going into the page, while in blue are represented the nucleons in the overlap region.

Fourier expansion:

$$\frac{\mathrm{d}N}{\mathrm{d}\Phi} \propto 1 + 2\sum_{n=1}^{\infty} v_n \cos[n(\Phi - \Psi_n)]. \tag{1.18}$$

This effect provides another signature of the collective motions of the particles produced in HI collision. In Equation (1.18) the coefficients v_n quantifies the magnitude of the anisotropy with respect to the symmetry plane Ψ_n. In collisions with a significant impact parameter, with an accentuated elliptic-shaped fireball, the pressure gradient is parallel to the reaction plane defined by the impact parameter and the beam axis. However, the reaction plane direction cannot be determined directly; therefore, the v_1 coefficient of Equation (1.18) is not measured. Higher-order event planes contribute to the calculation of the Fourier expansion in Equation (1.18), and each coefficient represents different components of the particle flow anisotropies. The v_2 coefficient describes the ellipticity of the particle flow – reflection of the almond-shaped overlap region and the pressure gradients in the reaction plane – and is usually called *elliptic flow*. Instead, the higher-order Fourier coefficients describe more complex inhomogeneities in the medium generated in the collision. However, the ability of the system to efficiently propagate the initial conditions – and its inhomogeneities – through the evolution of the fireball, manifesting final state effects translated in the v_n coefficients, strongly depends on the medium properties. The bulk viscosity over the medium entropy ζ/s,

its lifetime, and the shear viscosity over the medium entropy η/s, affect the propagation efficiency. Therefore, it is crucial to compare the measured v_n coefficients with the available model predictions to understand the features of the medium. Although it provides a simplified description of the hydrodynamic of the expansion, this model provides an important tool to derive the T_{Kin} parameter together with the mean radial velocity $\langle\beta_\perp\rangle$ of the particles at the kinetic freeze-out. The comparison of the results of these fits [24] highlights how both the temperature of kinetic freeze-out T_{Kin} and the radial flow velocity $\langle\beta_\perp\rangle$ are larger at LHC energies with respect to those obtained at the RHIC. The ALICE experiment measured the v_n coefficients up to the fourth-order

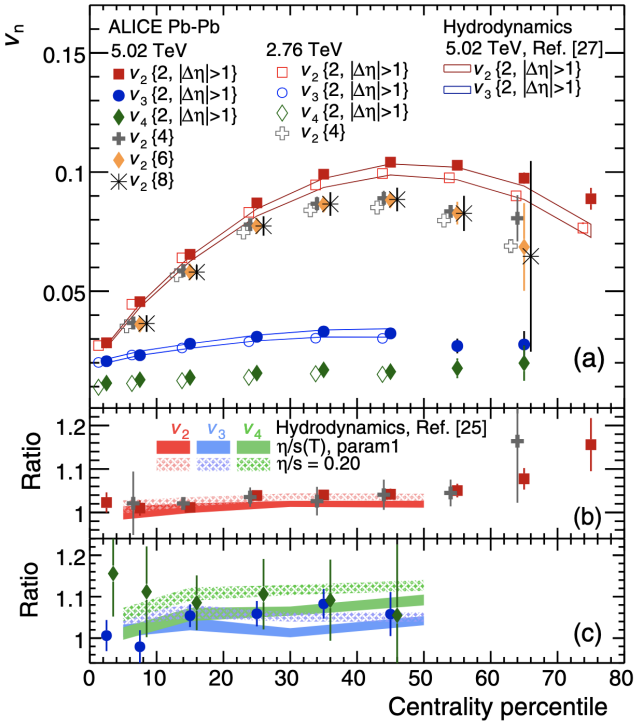

Figure 1.10: (a): Fourier coefficients v_n up to the fourth order measured by the ALICE experiment in Pb–Pb collisions at different energies [29], for low transverse momentum particles ($0.2 < p_{\mathrm{T}} < 5.0\,\mathrm{GeV}/c$) as a function of the event centrality. (b) and (c): ratios of v_2 (red and grey points), v_3 (blue points) and v_4 (green point) measured in Pb–Pb collisions at $\sqrt{s_{\mathrm{NN}}} = 5.02\,\mathrm{TeV}$ and $\sqrt{s_{\mathrm{NN}}} = 2.76\,\mathrm{TeV}$. The coloured areas represent the ratios between the experimental data and the hydrodynamic model (see the references in [29]), showing good agreement with calculations using a small η/s value.

in Pb–Pb collisions at different energies [29] and compared the results with a hydrodynamical model that takes into account initial geometric anisotropies and the medium response (Figure 1.10). This detailed study constitutes a positive test for the hydrodynamic picture ad allows stating that the medium created in HIC has a small shear viscosity, according to the v_n measurements.

1.4.2 Hard Probes

High Momentum Particles and Heavy Flavours

The processes at high transferred momentum take place only in the early moments of the collision, during the pre-equilibrium phase; therefore, high momentum quarks and charm and beauty quarks (*heavy flavour* quarks) can be created only in this stage. After their creation, they travel through the whole evolution of the system before being detected – if they emerge from the fireball and hit the experimental apparatus – bringing information about the medium in which they propagated and interacted. The study of heavy-flavour hadrons and high momentum hadrons – usually referred as *hard particles* – is then crucial to investigate the mechanisms underlying the parton propagation and energy loss in the QGP.

These types of processes – also called *hard processes* – are characterised by high transferred momentum and can therefore be treated with the perturbative QCD (pQCD). In addition, if the collision between two nuclei is considered as the superimposition of independent nucleon–nucleon collisions, the production cross-section of hard particles should be, in principle, equal to the pp cross-section multiplied for a scaling factor N_{coll} i.e. the number of nucleon–nucleon interactions. It is therefore expected that the *nuclear modification factor*, defined as

$$R_{\text{AA}} = \frac{1}{\langle N_{\text{coll}} \rangle} \frac{\mathrm{d}^2 N_{\text{AA}} / \mathrm{d}p_{\text{T}} \, \mathrm{d}y}{\mathrm{d}^2 N / \mathrm{d}p_{\text{T}} \, \mathrm{d}y} \tag{1.19}$$

is equal to unity for hard particles, since a HI collision is just the incoherent sum of N_{coll} nucleon–nucleon collisions. Some phenomena, for instance the *nuclear shadowing* [30] and the Cronin enhancement [31], can explain deviations of the R_{AA} from unity without considering the presence of the QGP. It is still possible to study p–Pb collisions to isolate these *cold matter effects* obtaining the information about the QGP by comparing the results with the Pb–Pb measurement. The CMS experiment, for instance, has measured the nuclear modification factor in both p–Pb and Pb–Pb collisions at $\sqrt{s_{\text{NN}}} = 5.02\,\text{TeV}$ as reported in Figure 1.11. As expected the R_{pA} is close to unity for the hard particles ($p_{\text{T}} \geq 3\,\text{GeV}/c$) and it is even larger than one at very high p_{T}. The R_{AA}, conversely, shows that the production of hard particles is suppressed, suggesting the presence of an hot and dense medium in which they propagated loosing energy. At the highest values of the transverse momentum ($p_{\text{T}} \geq 100\,\text{GeV}/c$) the R_{AA} rises up until it reaches unity. This behaviour, as interpreted by the models described in [32], is due to the ability of the highest momentum partons to escape from the collision before the formation of the medium because of their extremely high velocity.

Besides the study of generic high momentum particles, a significant interest in the hard probes sector is prompted by the study of heavy-flavour production. The measurement of the heavy-flavour hadrons allows us to tag the specific quark – either charm or bottom – underlying the production of the hadron itself. Furthermore, it is possible to investigate the energy loss of the heavy quarks in detail. The observed hadron,

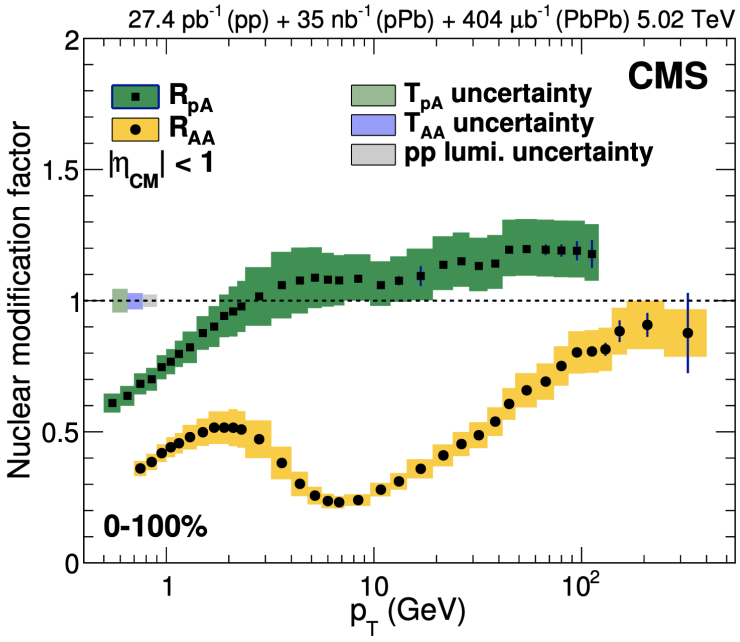

Figure 1.11: Nuclear modification factors of charged particles measured by the CMS Collaboration [32] in p–Pb and Pb–Pb collisions at $\sqrt{s_{\mathrm{NN}}} = 5.02\,\mathrm{TeV}$. The statistical uncertainties are represented by the vertical bars, while the coloured boxes refer to the systematic uncertainties of the measurement.

in fact, inherits most of the momentum carried by the quark due to the fragmentation functions. The energy loss of heavy-flavour quarks derives from two contributions: the *collisional energy loss* – caused by the elastic scatterings with other partons – and the *radiative energy loss* – resulting from inelastic scatterings. The ALICE experiment measured the R_{AA} for the D mesons [33] finding out that models including both collisional and radiative effects better describes the observed data (Figure 1.12).

Another subject of particular interest in the context of the hard processes in HIC is the *jet quenching*. This is, once again, related to the modification of well-known phenomena in the presence of a hot and dense medium, and it provides indirect proof of the QGP formation in HIC. A *jet* is a cone-structure in the spatial distribution of the particles – mainly hadrons – produced by the hadronisation of a quark or gluon generated in a scattering process. In pp collisions, hence in the vacuum and without energy loss, the *dijets* is a physical phenomenon consisting of two jets of equal transverse momentum produced back-to-back. In a HI collision, a dijet can originate from the hard scattering of two partons. However, in this case, the jets travel through the medium losing energy and eventually changing their direction, resulting in a modification of the dijet structure. The larger the distance travelled inside the medium, the larger the energy loss and the probability of having a significant jet direction deviation. Thus,

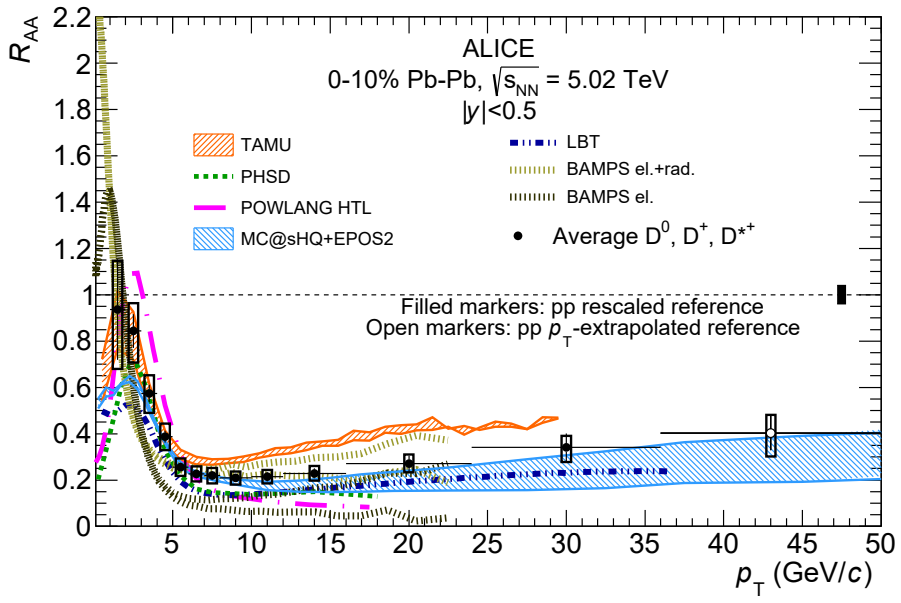

Figure 1.12: Nuclear modification factors for the D mesons as a function of transverse momentum in Pb–Pb collisions at $\sqrt{s_{\mathrm{NN}}} = 5.02\,\mathrm{TeV}$ measured in small impact parameter collisions by the ALICE Collaboration [33]. The vertical bars represent the statistical uncertainties, while the boxes refer to the systematic uncertainties. The predictions from different models are reported with coloured lines.

when the jets emerging from the collision are detected, it can be observed that one jet carries more energy – *leading jet* – than the other one – *subleading jet*. This is due to the difference in the path length that each parton covers in the medium. Moreover, due to the interactions with the dense medium, the two jets can show significant deviations from the back-to-back configuration observed in pp collisions.

The CMS experiment measured [34] the *jet shapes*[1] for back-to-back dijets in Pb–Pb and pp collisions at $\sqrt{s_{\mathrm{NN}}} = 5.02\,\mathrm{TeV}$, showing that the particle relative distance and the momentum distributions around the jet axis are modified in Pb–Pb concerning pp collisions. They also compared leading jet and subleading jet shapes as a function of the dijet momentum imbalance – i.e. the ratio between the momentum carried by the subleading jet and the one carried by the leading jet – showing that in highly imbalanced events, the modifications are much more pronounced. These results confirm that the presence of the QGP modifies the dijet structure, and the extent of the modifications is related to path length followed by the hard partons inside the medium.

[1] the *jet shape* is the distribution of charged transverse momentum of the charged particles as a function of the distance from the jet axis Δr.

Quarkonia

One of the most fundamental features of the QGP is that the elementary constituents of matter – i.e. quarks – are *deconfined*, that is, the strong interaction no longer forces them to form bound states. This phenomenon can be seen as a modification of the two quarks' interaction potential in the presence of the pressure and temperature conditions required to have the deconfined state. The two quarks interaction potential in the vacuum can be parametrised as a Cornell potential

$$V(r) = -\frac{\alpha(r)}{r} + kr, \tag{1.20}$$

where $\alpha(r)$ is the strong interaction coupling constant and k is a parameter related to the $q\bar{q}$ string tension due to the gluon self interaction. Inside the deconfined medium, instead, the presence of free colour charges screens the quark–quark interaction modifying the interaction potential, which then can be parametrised as a Yukawa potential:

$$V(r) = -\frac{\alpha(r)}{r} e^{-r/r_D}. \tag{1.21}$$

The potential in the medium is attenuated by the exponential with a characteristic length r_D called *Debye radius* that is closely linked to the temperature of the medium T and the strong interaction coupling constant g_s[2]: $r_D \sim 1/(g_s T)$. This implies that as a result of the colour charge screening in the deconfined medium, a $q\bar{q}$ pair cannot bind together to form a hadron in the QGP if the hadron radius is larger than r_D. Furthermore, the value of r_D depends on the temperature of the medium. For this reason, a suppression of heavy flavour quarkonia states – $c\bar{c}$ and $b\bar{b}$ states – is expected in HIC, and the study of these states provides access to the temperature of the QGP created in the collisions. Specifically, it is possible to measure the relative suppression of a particular $q\bar{q}$ state in HIC concerning pp collisions. This measurement indicates that the temperature of the QGP is such that the Debye radius for the strong interaction is smaller than the radius of the investigated $q\bar{q}$ state.

The most interesting and studied quarkonia states are charmonia and bottomonia, $c\bar{c}$ and $b\bar{b}$ states, respectively. Since they are heavy, they are rarely produced; therefore, the probability of the recombination with another charm/bottom quark for a dissociated charmonium/bottomonium state is very low. The ALICE Collaboration measured the J/Ψ nuclear modification factor in Pb–Pb collisions at $\sqrt{s_{\mathrm{NN}}} = 5.02\,\mathrm{TeV}$ [35]. A suppression of the J/Ψ production in the high p_{T} region was observed while for $p_{\mathrm{T}} < 3\,\mathrm{GeV}/c$ the R_{AA} is compatible with unity. These results are qualitatively descried by different models as shown in Figure 1.13. In these models [36, 37] the dominant contribution of generated and regenerated J/Ψ explains the increasing R_{AA} value

[2] g_s is closely connected to α_s by the relation $\alpha_s = \frac{g_s^2}{4\pi}$ as already discussed in Section 1.1.

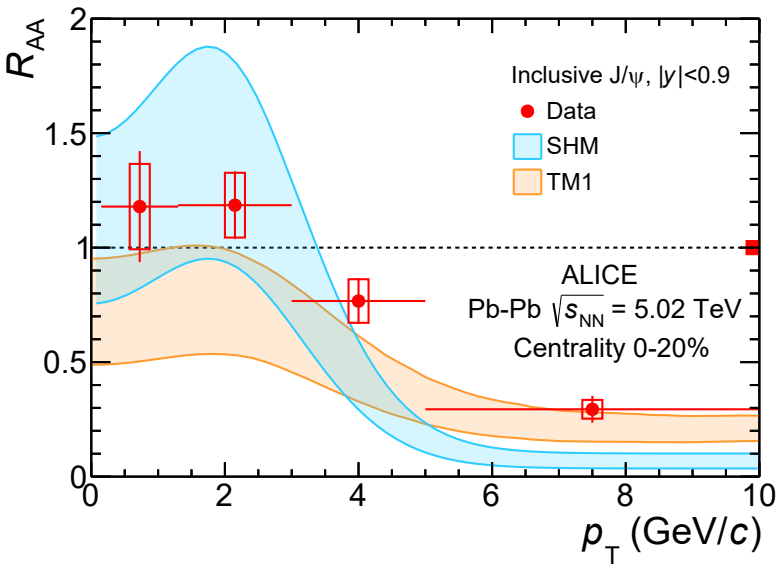

Figure 1.13: Inclusive measurement of the J/Ψ nuclear modification factor at midrapidity in Pb–Pb collisions at $\sqrt{s_{\mathrm{NN}}} = 5.02\,\mathrm{TeV}$ as a function of p_{T} compared with model calculations [36, 37] in the centrality class 0–20 %.

towards low p_{T}, while at higher p_{T} the contribution from recombination drops leading to the J/Ψ suppression. As pointed out in [35], this measurement indicates that low p_{T} charmonium is produced mainly via generation and regeneration in the late stages of the collision. The high p_{T} J/Ψ come from primordial production and feed-down contribution from beauty decays thus explaining why they are widely suppressed.

The CMS Collaboration measured the nuclear modification factor also for bottomonium states $\Upsilon(1S)$, $\Upsilon(2S)$ and $\Upsilon(3S)$ in Pb–Pb collisions at $\sqrt{s_{\mathrm{NN}}} = 5.02\,\mathrm{TeV}$ [38]. The significant suppression of all the three states is already visible from the invariant mass spectra in Figure 1.14a where the pp and Pb–Pb measurements are compared. Figure 1.14b also shows a sequential ordering of the suppression $R_{\mathrm{AA}}(\Upsilon(1S)) > R_{\mathrm{AA}}(\Upsilon(2S)) > R_{\mathrm{AA}}(\Upsilon(3S))$ and the $R_{\mathrm{AA}}(\Upsilon(3S))$ compatible with the non observation of the $\Upsilon(3S)$ state. This sequential melting is what one would expect from the *Debye screening*: the less bound states are the ones more suppressed. These results are a clear indication of the heavy quark interaction with the medium and play a crucial role in characterising the QGP state.

1.4.3 Electroweak Probes

The electroweak probes provide an essential tool to cross-check whether the strongly interacting medium that originates from a HIC is a droplet of QGP. In the Standard Model, leptons, Z and $\mathrm{W}^{\pm}$ bosons are not coupled, at the tree level, with the strong interaction. They do not interact with the QGP and bring information about the very

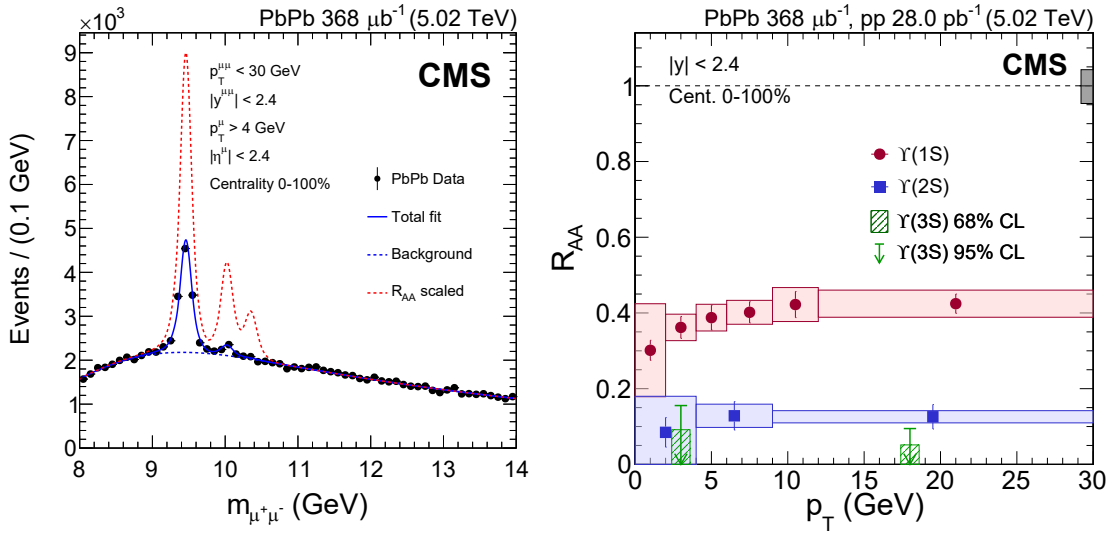

(a) **(b)**

Figure 1.14: (a) Invariant mass distribution of the muon pairs in Pb–Pb collisions. The red dashed line represents the amplitude of the three Υ peaks found in the fit procedure and scaled by the inverse R_{AA} for the corresponding Υ state. (b) Nuclear modification factors for Υ(1S), Υ(2S) and Υ(3S) states measured as a function of the transverse momentum. The statistical uncertainties are represented by the error bars while the boxes represent the systematic uncertainties. The measurements are performed by the CMS experiment as reported in [38].

first stages of the collision without any alterations. Excluding the effects caused by the modification of the parton distribution inside the nucleon and the N_{coll} scaling, no changes in the production spectra are expected for these particles.

The CMS Collaboration measured the Z boson yields and azimuthal anisotropy [39] to test this prediction. According to Glauber model predictions, the Z boson yield scales with the centrality, except for peripheral collisions for which deviations are found. This suggests the existence of an effect due to the initial collision geometry, and the measured v_2 coefficient[3] is found to be compatible with zero (Figure 1.15). These results confirm that the Z bosons are insensitive to the presence of the medium produced in the collision and do not undergo significant final state interactions.

The photons are not coupled with the interacting medium at the tree level. They pass through the QGP leaving the fireball undisturbed, carrying information about the system's condition at the moment of its creation. *Direct photons* – for simplicity in this work, all the photons not produced by hadron decay are considered direct photons – are created at every stage of the collision; thus, their spectrum represents the

[3] definition of the v_2 coefficient in Section 1.4.1.

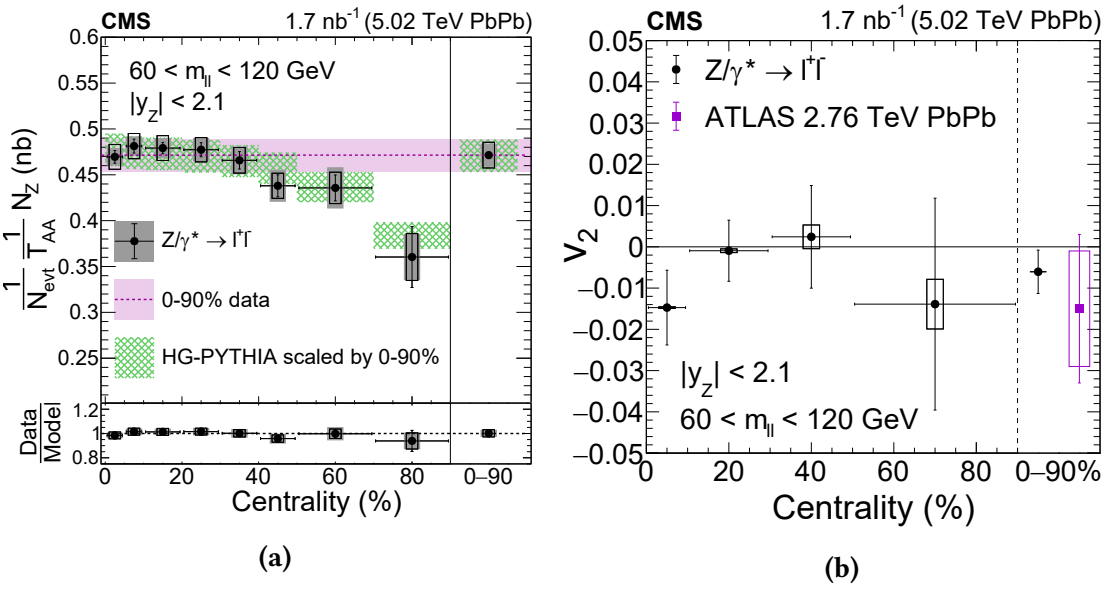

Figure 1.15: (a) The T_{AA}-normalised yields of Z bosons as a function of centrality, compared with Glauber model calculations implemented in HG-PYTHIA [40]. (b) The v_2 coefficient of Z bosons measured for various centrality bins. In both figures, the error bars represent the statistical uncertainties and the error boxes represent the systematic uncertainties.

whole evolution of the system. The high transverse momentum region of the spectrum ($p_{\mathrm{T}} > 5\,\mathrm{GeV}/c$) is dominated by the hard parton scattering occurring in the initial stage of the collision, carrying information about the parton distribution functions and the dynamics of parton collisions. The low transverse momentum region ($p_{\mathrm{T}} \lesssim 5\,\mathrm{GeV}/c$) instead, is dominated by the thermal photons produced by the medium. They provide precious information on the temperature and space-time evolution of the thermalised QGP.

The ALICE experiment measured the direct photons yields in Pb–Pb collisions at $\sqrt{s_{\mathrm{NN}}} = 5.02\,\mathrm{TeV}$ [41], showing (Figure 1.16) a clear direct photon signal whose spectrum at low p_{T} follows the the calculations performed including QGP formation effects. The high p_{T} region instead is in good agreement with expectations from pQCD calculations for the pp system and scaled by N_{coll}, confirming that this region of the spectra is dominated by photons produced in hard scatterings.

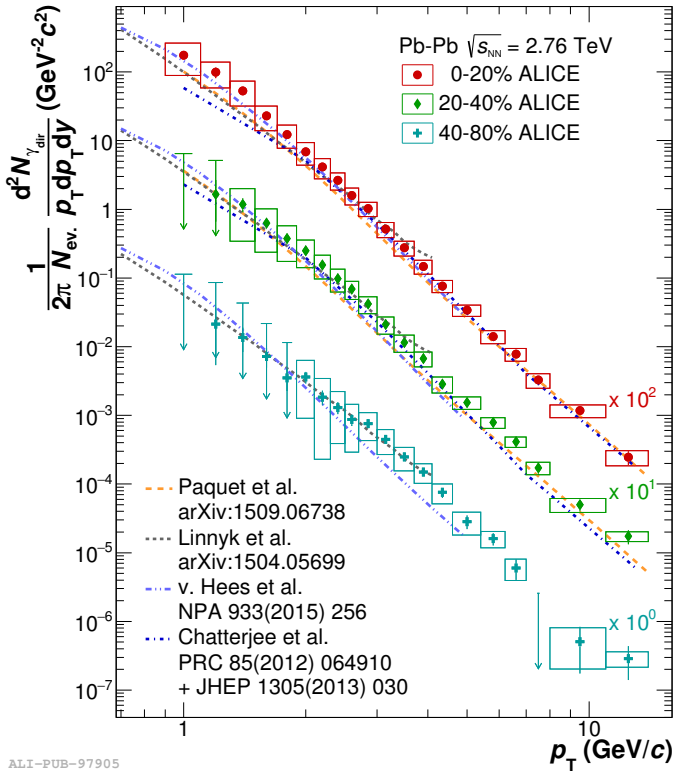

Figure 1.16: Direct photon spectra measured by ALICE in Pb–Pb collisions at $\sqrt{s_{\mathrm{NN}}} = 2.76\,\mathrm{TeV}$ compared to NLO pQCD calculations for the direct photon yield in pp collisions at the same energy and scaled by N_{coll}. (see references in [41]).

Chapter 2

The ALICE Experiment

The largest and most powerful particle collider in the world, reaching collision energies of the TeV scale, is the CERN Large Hadron Collider (LHC), located beneath the France-Switzerland border near Geneva. With its 27 km ring of superconducting magnets and accelerating structures, it is the final stage of the CERN's accelerator complex and provides the most energetic nucleus–nucleus collisions – tipically p–Pb and Pb–Pb, but also Xe–Xe – ever reached in laboratory.

In such energetic nucleus–nucleus collisions, the formation of the QGP is expected, so a significant part of the LHC physics programme is dedicated to the study of the QGP and, more in general, to heavy-ion physics. Since the beginning of the LHC operations in 2008, four major collaborations have been running experiments at the LHC. Among them, the ALICE Collaboration – where ALICE stands for A Large Ion Collider Experiment – is the one more focused on the investigation of the QGP physics and the soft QCD observables.

2.1 The Large Hadron Collider

The LHC is the spearhead of the CERN's accelerator complex, a succession of machines that accelerate protons and nuclei to increasingly higher energies through the application of electric and magnetic fields as shown in Figure 2.1. Each machine accelerates a beam of particles, whether protons or nuclei, by boosting its energy before injecting the beam into the next machine. The last element of this chain is the Large Hadron Collider where the particle beams reached the record energy of 6.5 TeV per beam.

The protons, taken from an ionised hydrogen tank, start their journey in the accelerator complex in the linear accelerator LINAC2, where they are accelerated up to 50 MeV. Into the Proton Synchrotron Booster (PSB), protons are boosted to 1.4 GeV. Then they are injected into the Proton Synchrotron (PS), where they reach the energy of 25 GeV, here they are structured in bunches. After this stages, the proton bunches are sent to the Super Proton Synchrotron (SPS), where they are accelerated to 450 GeV.

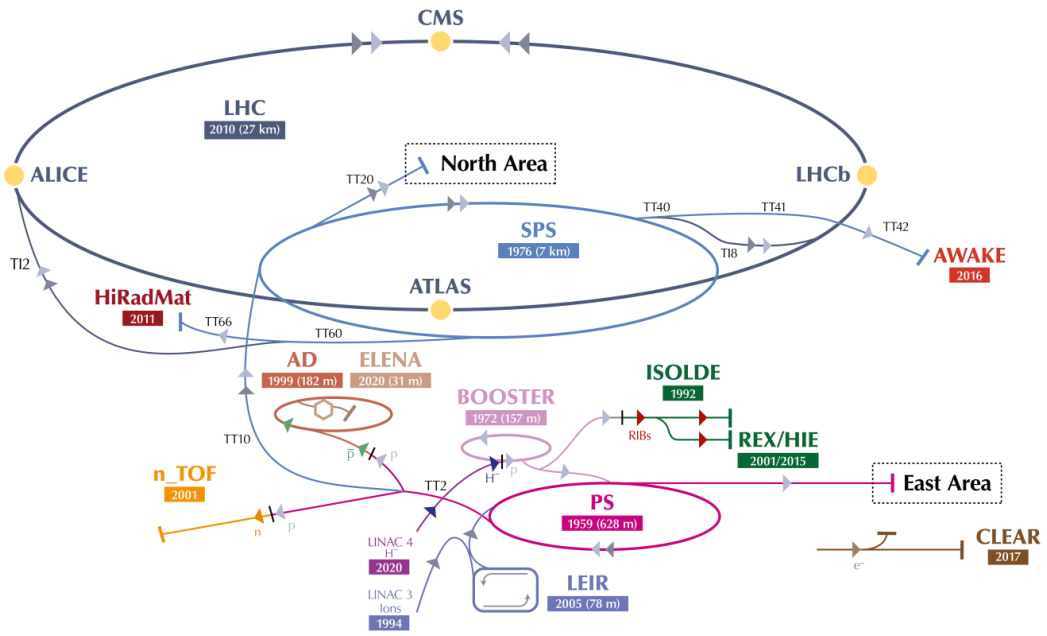

Figure 2.1: Schematic view of the CERN accelerator complex and experiments [42].

Finally, they are injected into the LHC.

The lead ions are taken from an ionised lead vapour obtained by heating a sample of highly isotopically pure ^{208}Pb to 800 °C. The lead vapour contains many charge states with a maximum around Pb^{29+}. These ions are selected using an electric field and accelerated up to an energy per nucleon of 4.2 MeV/u, then a carbon foil strips other electrons from the nuclei obtaining Pb^{59+} charge state. The Pb^{59+} ions are accumulated, forming an ion beam. The beam is sent to the Low Energy Ion Ring (LEIR), where it is accelerated to 72 MeV/u, then it is transferred to the PS. Here the beam is further accelerated to 5.9 GeV/u and fully stripped to Pb^{82+} by passing into a second carbon foil. The beam at this point is injected into the SPS and boosted to 177 GeV/u before being injected into the LHC, where it reaches the record energy of 5.02 GeV/u.

Inside the LHC ring, the two counter-rotating beams – whether they are proton or ion beams – are guided and focused by 1232 dipole magnets and 392 quadrupole magnets in separate vacuum-filled pipes. When the beams are stable, they are made to collide in the four interaction points (IP) along the ring inside the major LHC experiments: ATLAS, ALICE, CMS and LHCb. The top centre of mass energy reached at the LHC, which are worldwide records, is 13 TeV for pp collisions and 5.02 TeV per nucleon pair for Pb–Pb collisions.

For the LHC experiments, besides the maximum collision energy, another crucial parameter is the *luminosity* ($\mathcal{L}$) delivered to the experiments. The luminosity relates

the reaction rate R for a given process with the cross-section of the process $\sigma_{process}$ through the relation:

$$R = \mathcal{L}\,\sigma_{process}. \tag{2.1}$$

The LHC has been designed to search for extremely rare processes; therefore the luminosity needs to be adequate.

The instantaneous luminosity is defined as:

$$\mathcal{L} = \frac{N_b N^2 f_{rev}\gamma}{4\pi\epsilon_n\beta^*}F, \tag{2.2}$$

where N_b is the number of bunches running in the collider, N is the number of charges in each bunch, f_{rev} is the frequency of revolution of the beam, γ is the Lorentz factor, ϵ_n is the normalised emittance[1], β^* is the amplitude function[2] evaluated in the interaction point – where the luminosity is actually estimated – and F is a geometrical factor. Usually, the luminosity delivered by the collider is measured through a dedicated experimental procedure called *van der Meer scan* [43].

The two beams are not entirely parallel when they intersect each other in the IP in order to avoid – or at least to reduce as much as possible – the long-range electromagnetic interactions. The angle between the two beams is called *crossing angle* θ_c and it is relatively small at the LHC, about 300 µrad. However, the non-zero crossing angle also limits the instantaneous luminosity of the collider since it reduces the volume region in which the beams cross each other, which is taken into account by the geometrical factor. By defining the root mean square (RMS) of the transverse and longitudinal size of the beam, namely σ_{T} and σ_z respectively, the geometrical factor is expressed as:

$$F = \left[\sqrt{1 + \left(\frac{\sigma_z}{2\sigma_{\mathrm{T}}}\theta_c\right)^2}\right]^{-1}. \tag{2.3}$$

Each proton bunch at the LHC can contains up to $N{\sim}10^{11}$ protons so with a 25 ns spacing the ring can store up to 2808 bunches [44, 45]. At the end of the acceleration, when the beams are stable and ready for the collisions, the normalised emittance is 3.75 µm · rad while β^* depends on the interaction point.

The peak luminosity in pp collisions required by the ATLAS and CMS experiments to carry on their physics programme is $\mathcal{L} = 10^{34}\,\mathrm{cm}^{-2}\,\mathrm{s}^{-1}$ while for the LHCb experiment is $\mathcal{L} = 4 \times 10^{32}\,\mathrm{cm}^{-2}\,\mathrm{s}^{-1}$. The target for ALICE is, instead, a peak luminosity of $\mathcal{L} = 10^{27}\,\mathrm{cm}^{-2}\,\mathrm{s}^{-1}$ in Pb–Pb collisions. Figure 2.2a shows the luminosity for pp collisions delivered by the LHC during different years, Figure 2.2b shows instead the integrated luminosity collected by ALICE during the LHC Run 2 – from 2015 to 2018.

[1] The emittance ϵ is defined as the spread in the position-momentum phase space of the beam particles. The normalised emittance then is defined as $\epsilon_n = \beta\gamma\epsilon$, where $\beta = v/c$ and γ it the usual Lorentz factor.

[2] The amplitude function $\beta(s)$ represent the amplitude of the particle trajectories in the beam. It is used together with the emittance to define the transverse size of the beam: $\sigma_{\mathrm{T}}(s) = \sqrt{\epsilon\beta(s)}$.

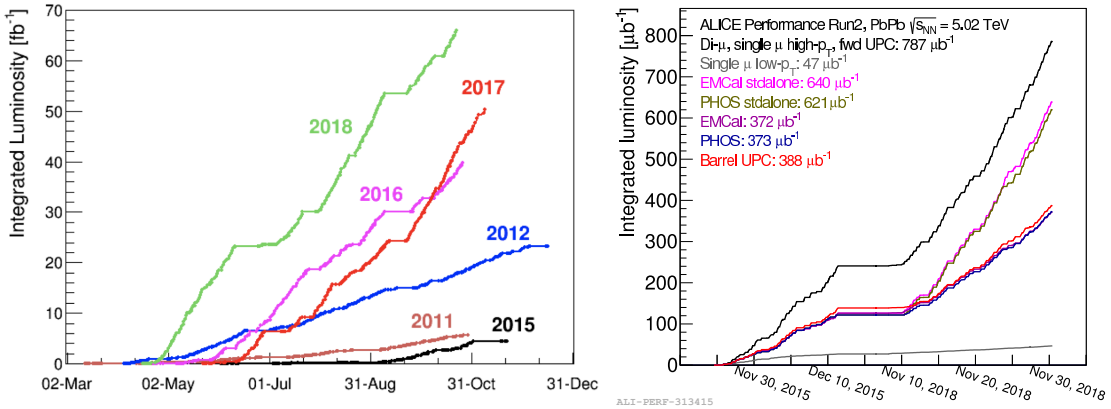

(a) **(b)**

Figure 2.2: (a) Overview of the LHC integrated luminosity. (b) Integrated luminosity collected by ALICE for various triggers in Pb–Pb collisions during the LHC Run 2 data taking period from 2015 to 2018.

Another critical parameter for the experiments operating at the LHC is the *primary vertex* position, which is the position where the collision between the two beams takes place. The nominal position of the primary vertex is represented by the origin of the coordinate reference frame of the experiment. The position of the primary vertex fluctuates around the nominal position due to the finite size of the beam. It is possible to show that, assuming a gaussian shape in the three dimensions for the bunches, the RMS of the vertex dispersion is:

$$\sigma_{x,y,z}^{vertex} = \frac{\sigma_{x,y,z}^{bunch}}{\sqrt{2}}. \tag{2.4}$$

$\sigma_{x,y,z}^{bunch}$ is the RMS of the size of the bunch and it is related to the beam emittance ϵ and the amplitude function at IP β^* by:

$$\sigma_{x,y,z}^{bunch} = \sqrt{\frac{\epsilon_{x,y,z}\,\beta^*}{\sqrt{\pi}}}. \tag{2.5}$$

In pp collisions the typical values at the IP2 – the interaction point where ALICE is located – are $\sigma_{x,y}^{vertex} \sim 50\,\mu\text{m}$ and $\sigma_{z}^{vertex} \sim 5\,\text{cm}$.

2.2 ALICE Design

The whole experimental apparatus of ALICE has been designed and optimised to carry on a general-purpose experimental programme [46, 47]. The main goal of the ALICE Collaboration is the *extensive* study of the nuclear matter created in ultra-relativistic

HIC. In order to reach this goal, the experiment must have a large acceptance and must be able to track and identify all the charged particles emerging from the collisions, even at very low momentum. Furthermore, the detector must operate in an environment where the number of charged particles produced in each collision is extremely high. At the time of the ALICE detectors design, the expected number of charged particles in Pb–Pb collisions at the LHC energies ranged between 2000 and 8000 per pseudorapidity unit [48]. The granularity of the detectors, while maintaining a low material budget, was the reason for the adoption of relatively slow detectors such as the Silicon Drift Detector and the Time Projection Chamber [46, 47].

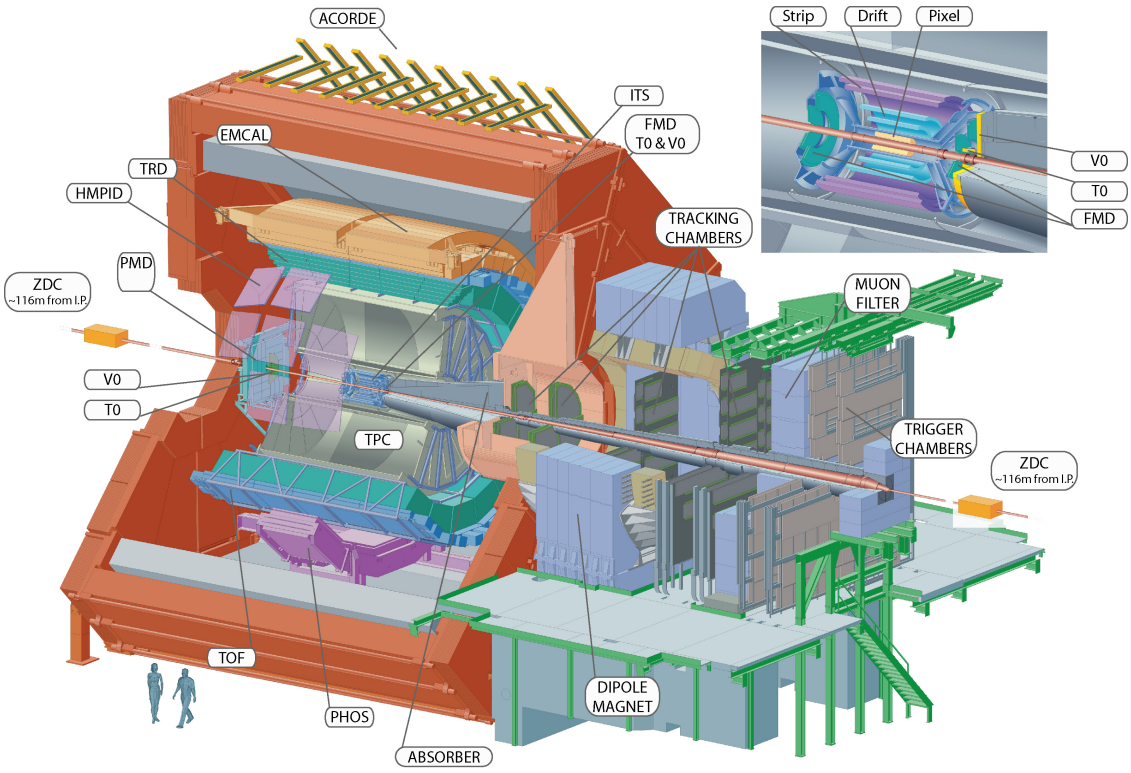

Figure 2.3: The ALICE experimental setup. The big red structure is the L3 solenoid magnet while in the top right inset a zoom view shows the details of the V0, T0, FMD and the ITS detectors.

Figure 2.3 shows the layout of the ALICE experiment during the Run 2 data taking period, started in 2015 and ended in 2018. The data used for this thesis have been recorded in this period. The experiment is now in a commissioning phase after major infrastructures and detectors upgrades to improve the performance in preparation for LHC Run 3. Table 2.1 lists the sub-detectors with the details of the position and the purpose of each one.

The ALICE coordinate system is, by convention, a right-handed orthogonal Cartesian system, and the origin is the nominal interaction point. The x and y axes lie in

a plane orthogonal to the beam direction. The x axis points to the centre of the LHC, and the y axis points upward. The beam determines the direction of the z axes, and the chirality of the coordinate system defines its positive direction. A cylindrical coordinate system is also defined since it usually provides a more helpful description of the ALICE apparatus and the physical quantities. The z axis is the same as described above, and the observer stands at positive z and looks in the direction of the Compact Muon Solenoid (CMS) experiment. The *azimuthal angle* φ then starts from the x axis ($\varphi = 0$) and increases counter-clockwise. The *polar angle* ϑ finally increases from z ($\vartheta = 0$) to $-z$ ($\vartheta = \pi$).

In this thesis and more in general in the ALICE papers, two other variables are extensively used for a particle with four-momentum $p = (E, \vec{p})$: the *rapidity*

$$y = \frac{1}{2} \ln \left(\frac{E + p_z}{E - p_z} \right) \tag{2.6}$$

and the *pseudorapidity*

$$\eta = \frac{1}{2} \ln \left(\frac{|p| + p_z}{|p| - p_z} \right) = - \ln \left[\tan \left(\frac{\theta}{2} \right) \right] . \tag{2.7}$$

In the case of ultra-relativistic objects, η numerically converges to y.

The ALICE apparatus can be ideally divided into three main parts: the *central barrel*, the *muon arm* and the *forward detectors*.

Central Barrel

The central barrel consists of all the detectors covering the pseudorapidity region $|\eta| < 0.9$. These detectors are immersed in a low solenoidal magnetic field – with respect to the other LHC experiments – of $0.5\,\mathrm{T}$ generated by a warm resistive magnet that was previously used for the L3 experiment at LEP [50]. This soft magnetic field has been adopted to extend the transverse momentum reach of the tracking detectors down to $80\,\mathrm{MeV}/c$ [49].

The detectors of the central barrel used for the reconstruction of the tracks of the charged particles – i.e. *tracking* – are the Inner Tracking System (ITS), the Time Projection Chamber (TPC) and the Transition Radiation Detector (TRD): they cover the whole azimuthal angle in order to maximise the acceptance. These detectors also provide information for particle identification (PID), together with the Time Of Flight (TOF) detector and the High-Momentum Particle Identification (HMPID). The TOF and the HMPID, in particular, are specifically designed to identify high momentum particles. Inside the L3 magnet, the Electromagnetic Calorimeter (EMCal) and a Photon Spectrometer (PHOS) are installed to study high p_T photons and jets physics. The ACORDE detector, composed of 60 large scintillators used to study the high-energy cosmic air showers, is finally located on top of the ALICE solenoid.

	Acceptance			
Detector	***Polar***	***Azimuthal***	**Position**	**Main purpose**
SPD† *layer 1*	$\|\eta\|$ < 2.0	full	r = 3.9 cm	tracking, vertex
SPD† *layer 2*	$\|\eta\|$ < 1.4	full	r = 7.6 cm	tracking, vertex
SDD *layer 3*	$\|\eta\|$ < 0.9	full	r = 15 cm	tracking, PID
SDD *layer 4*	$\|\eta\|$ < 0.9	full	r = 23.9 cm	tracking, PID
SSD *layer 5*	$\|\eta\|$ < 1.0	full	r = 38 cm	tracking, PID
SSD *layer 6*	$\|\eta\|$ < 1.0	full	r = 43 cm	tracking, PID
TPC	$\|\eta\|$ < 0.9	full	85 < r/cm < 247	tracking, PID
TRD†	$\|\eta\|$ < 0.8	full	290 < r/cm < 368	tracking, $e^{\pm}$ id
TOF†	$\|\eta\|$ < 0.9	full	370 < r/cm < 399	PID
PHOS†	$\|\eta\|$ < 0.1	220°<ϕ<320°	460 < r/cm < 478	photons
EMCal†	$\|\eta\|$ < 0.7	80°<ϕ<187°	460 < r/cm < 478	photons, jets
HMPID	$\|\eta\|$ < 0.6	1°<ϕ<59°	r = 490 cm	PID
ACORDE†	$\|\eta\|$ < 1.3	30°<ϕ<150°	r = 850 cm	cosmics
PMD	2.3 < η < 3.9	full	z = 367 cm	photons
FMD	3.6 < η < 5.0	full	z = 320 cm	ch. particles
	1.7 < η < 3.7	full	z = 80 cm	ch. particles
	-3.4 < η < -1.7	full	z = -70 cm	ch. particles
V0 A†	2.8 < η < 5.1	full	z = 329 cm	ch. particles
V0 C†	-3.7 < η < -1.7	full	z = -88 cm	ch. particles
T0 A†	4.6 < η < 4.9	full	z = 370 cm	time, vertex
T0 C†	-3.3 < η < -3.0	full	z = -70 cm	time, vertex
ZDC†	$\|\eta\|$ > 8.8	full	z = ±113 cm	fwd neutrons
	6.5 < η < 7.5	$\|\phi\|$<10°	z = ±113 cm	fwd protons
	4.8 < η < 5.7	$\|2\phi\|$<32°	z = ±113 cm	photons
MCH	-4.0 < η < -2.5	full	-14.2 < z/m < -5.4	muon tracking
MTR†	-4.0 < η < -2.5	full	-17.1 < z/m < -16.1	muon trigger

Table 2.1: Geometrical details and main purposes of the ALICE sub-detectors. The ALICE apparatus and its performances are described in details in [49], this table is taken and adapted from there. The transverse (r) and longitudinal (z) coordinates as well as the acceptance (*polar* and *azimuthal*) are measured with respect to the ALICE coordinate reference frame, described in the text. The azimuthal coverage for the detector is 2π when it is not specified. When the detector is composed by two or more parts more than one position value is specified reporting the minimum and maximum distances from the interaction point. A dagger (†) marks the detectors used also for triggering.

Muon Spectrometer

The muon spectrometer covers the pseudorapidity region $-4 < \eta < -2.5$, and it is designed to measure the spectrum of vector-mesons resonances originating from heavy quarks. It is composed of the front absorber, the tracking system, the trigger system and a dipole magnet.

The front absorber is made of a wall with small atomic number Z – carbon and concrete mainly – and it suppresses the hadronic background coming from the interaction vertex and limiting at the same time the multiple scattering and the energy loss of the muons. For the background coming from small angles, the protection is given by the inner beam shield made of tungsten, lead and stainless steel.

The tracking system is made of 5 stations of pad/strips chambers, 2 for each station. The chambers are made of composite materials in order to have the low material budget needed to reach the spatial resolution of $100\,\mathrm{mm}$.

The target of the muon spectrometer is the heavy quark resonance decay. The trigger system is designed to operate a selection on the transverse momentum of two individual muons coming from the same collision. It is made of 4 planes Resistive Plate Chambers (RPCs) disposed into two stations, and they are employed to measure the p_{T} of each muon. A dedicated front-end electronics allows to obtain a time resolution better than 2 ns, that is needed to discriminate different bunch crossings, while the spatial resolution is around 1 cm.

The dipole magnet is one of the biggest warm dipoles in the world, and it is located about 7 m from the interaction point. It provides a magnetic field of 0.7 T, and the mass resolution requirement drives this value.

Forward Detectors

Contrary to what the name suggests, the forward detectors are located in both forward and backward pseudorapidity regions. They include the Forward Multiplicity Detector (FMD), the Photon Multiplicity Detector (PMD) and the Zero Degree Calorimeters (ZDC). In addition, there is also the V0 detector made of scintillators and the T0 detector made of Cherenkov counters, which are used for triggering.

2.3 The ALICE Detectors

The following sections provide a more detailed discussion on the detector used to measure the hypertriton lifetime and Λ-separation energy.

2.3.1 Inner Tracking System

The Inner Tracking System (ITS) is the closest detector to the interaction point, and its purpose is to determine the position of the primary and the secondary vertices with

high spatial resolution. As already mentioned, it also plays a crucial role in the track reconstruction, particularly for low momentum particles. It consists of six layers of silicon detectors with a cylindrical shape and with variable length and radius, surrounding the beam pipe – a Beryllium pipe 800 µm thick – and the interaction point.

The ITS consists of three sub-detector, each composed of two layers, according to the different technologies used for the realisation of the sensors (Figure 2.4). The innermost detector is the Silicon Pixel Detector (SPD) which is surrounded by the Silicon Drift Detector (SDD), which is in turn surrounded by the Silicon Strip Detector (SSD).

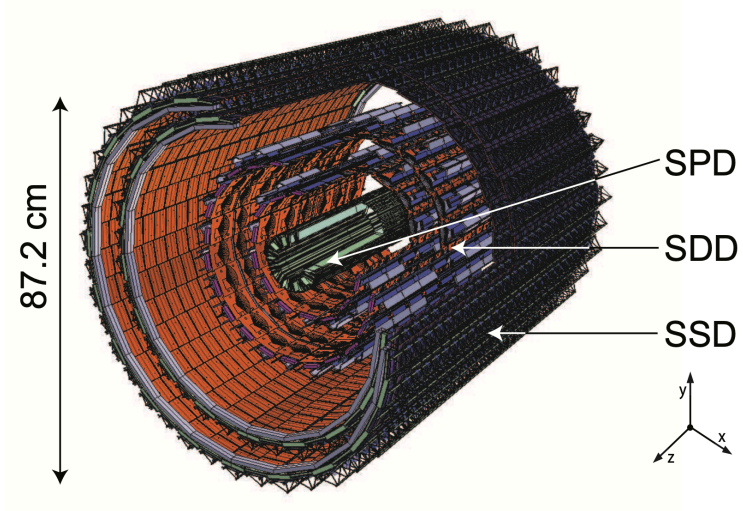

Figure 2.4: Layout of the Inner Tracking System and its sub-detectors.

The ITS is able to determine the position of the vertices with a resolution better than 100 µm. At the same time, it allows extending the tracking capabilities of the whole apparatus down to $p_{\mathrm{T}} = 80\,\mathrm{MeV}/c$. These outstanding performances are made possible by three factors: the ITS position very close to the interaction point, each detector layer's low material budget, and the high spatial resolution achieved by each sub-detector. However, the global material budget of the ITS is greater than the sum of its parts. In fact, due to detector operation constraints, the sub-detectors are separated by thermal shields that inevitably increase the material budget. Taking into account the detector layers, the support structures and the thermal shields, the total material budget of the ITS corresponds to $7.18\,\% \; X/X_0$ for particles in the rapidity region $y \approx 0$ – including also the air the X/X_0 ratio goes to $7.26\,\%$.

Table 2.2 provides details about the material budget and the spatial resolution of the ITS sub-detectors.

The SDD and the SSD detectors, besides the spatial position of the track, can also measure the amplitude of the electric charge cluster generated in their sensitive volume by the passage of the charged particle. This information is related to the specific energy

Parameter	SPD	SDD	SSD
Total number of modules	240	260	1770
Number of readout channels per module	240	2×256	2×768
Radius (cm)	3.9 - 7.6	15.0 - 32.9	38.0 - 43.0
Material budget per layer ($\%X_0$)	1.14 - 1.14	1.13 - 1.26	0.83 - 0.86
Spatial resolution $r\phi$ (μm)	12	35	20
Spatial resolution z (μm)	100	25	830
Two track resolution $r\phi$ (μm)	100	200	300
Two track resolution z (μm)	850	600	2400
Active cell size (μm^2)	$50\times$ 425	202×294	95×40000
Number of readout channels (k)	9835	133	2603

Table 2.2: Details about the material budget (for each layer) and the spatial resolution of the ITS sub-detectors [48].

loss of the particle in the detector material, and it is exploited to identify low momentum particles in the transverse momentum region below $200\,\mathrm{MeV}/c$.

The SPD is crucial in the primary vertex reconstruction since it is the closest detector to the interaction region. In particular, it provides a local *Fast–OR* information that is used in the Level 0 trigger as shown in Section 2.4.

2.3.2 Time Projection Chamber

The main ALICE tracking detector is the Time Projection Chamber (TPC). The TPC also measures the specific energy loss of the tracked particles that pass through its volume. Therefore, it is also one of the main detectors for particle identification.

The layout of the TPC is presented in Figure 2.5. The detector has a cylindrical shape with an active volume of $88\,\mathrm{m}^3$ filled with gas: the inner radius of the cylinder is $85\,\mathrm{cm}$, the outer radius is $247\,\mathrm{cm}$, and total length is $500\,\mathrm{cm}$ along the beam direction. It is divided into two drift regions by the central cathode – located at its axial centre, dividing the detector into two halves – and it is closed off at each end by the end-plates. The gas used for the LHC Run 2 (2015–2018) is a mixture of Ar and CO_2 while a mixture of Ne and CO_2 was used during the Run 1.

The central cathode together with the end-plates generate in each half an highly uniform electric field of $400\,\mathrm{V/m}$. The passage of charged particles in the detector's sensitive volume causes the localised ionisation of the detector's gas in the form of electron clouds. The electric field drives the electron clouds towards the readout chambers located in the end-plates. The end-plates host the readout detectors and are divided into 18 azimuthal sectors. Each sector, in turn, is partitioned into pads organised in

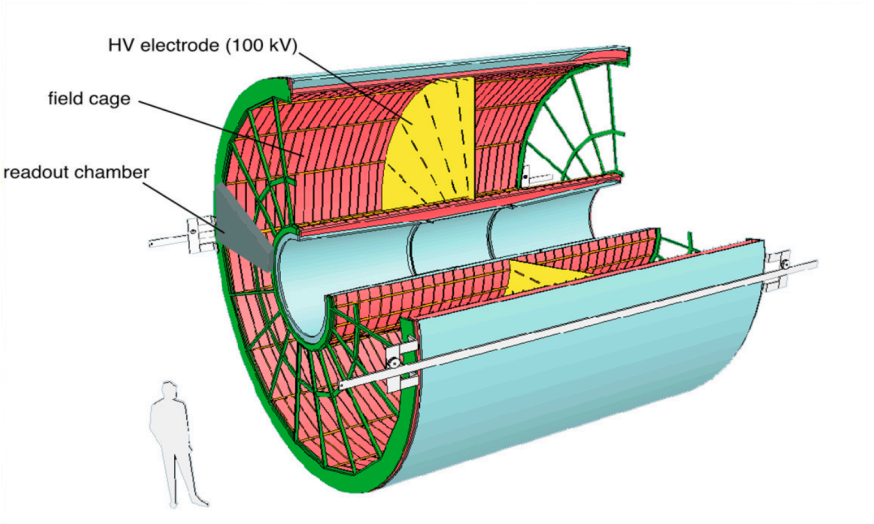

Figure 2.5: Schematic representation of the Time Projection Chamber.

rows orthogonal to the radial direction. The readout chambers consist of multi-wire proportional chambers (MWPC), and the readout is located in the cathode pad. Smaller pads ($4 \times 7.5\,\mathrm{mm}^2$) are used for the inner readout chambers (IROC) and larger pads ($6 \times 15\,\mathrm{mm}^2$) for the outer readout chambers (OROC). This segmentation schema has been designed to improve the tracking performance in the high multiplicity environment expected for the ALICE operations.

The readout chambers provide the 3-dimensional space position of the charged particle generating the electric cloud using the information from the activated pads (x and y coordinates) and the drift time of the cloud (z coordinates). The determination of the charged particle track relies on these spatial position measurements (up to 159 for each particle). The energy loss of the track is also measured. It provides crucial information for the PID, as discussed in Section 2.6.1.

The tracking and PID performances of the TPC are excellent, but these performances are achieved at the expense of the data acquisition rate (1 kHz) that is limited by the drift time ($88\,\mu\mathrm{s}$).

The pseudorapidity range spanned by the TPC is $|\eta| < 0.9$. The azimuthal angle is fully covered except for the edges between the different sectors that are inactive, which represent dead zones for the acceptance of the detector. Nevertheless, they are small with respect to the active regions.

2.3.3 VZERO

The V0 detector is composed by two sub-detectors (V0A[3] and V0C[4]) each of which consists in 64 scintillator counters segmented in 8 concentric rings. The two sub-detectors

are located in line with the beam axis on the opposite sides of the interaction point covering the high pseudorapidity region (Table 2.1).

Together with the SPD detector, the V0 defines the minimum bias trigger selection for ALICE, the logical *or* between the signals of V0A, V0C and SPD. The V0 also measure the time difference between the V0A and the V0C signal, helping to reject the beam-gas interactions. It also plays a role in the definition of the centrality of the collision in Pb–Pb and p–Pb events (See Section 2.7).

2.3.4 TZERO

The detector is composed by two arrays (T0A[3] and T0C[4]) of Cherenkov counters (geometrical informations in Table 2.1). The primary purpose of the T0 is the measurement of the event time with a resolution below 50 ps.

The event time is determined independently from the vertex position determination and the track reconstruction that involves other detectors. The T0 can also provide an independent measurement of the z coordinate of the vertex position with a precision of 1.5 cm and gives the first level trigger (L0) when this position falls within the expected range.

2.3.5 Zero Degree Calorimeter

The Zero-Degree Calorimeter (ZDC) measures the energy of the spectator nucleons emerging from the interaction point to determine the collision's geometrical properties. It consists of six calorimeters: two electromagnetic calorimeters, two proton calorimeters and two neutron calorimeters (see Table 2.1 for the position and the geometrical details).

The electromagnetic modules (ZEM) are located relatively close to the interaction point ($\sim$7 m on both sides), and they measure the energy deposited by photons and neutral pions produced at forward rapidity. This measure allows distinguishing between peripheral and central collisions.

The proton modules (ZP) and the neutron modules (ZN) instead are located far from the interaction point ($\sim$115 m on both sides). The measurement of the energy carried by the spectator nucleons is crucial for the determination of the centrality of the collision (see Section 2.7) related to the impact parameter and the event plane orientation. The ZDC also provides a veto on the parasitic beam–beam background interactions.

[3] A = ATLAS: it is located on the side of the beam line towards the ATLAS experiment.

[4] C = CMS: it is located on the side of the beam line towards the CMS experiment.

2.4 Data Acquisition and Trigger

The complexity of the ALICE apparatus requires a system able to handle the different readout times and latencies of the many detectors installed in ALICE. The adopted system relies on three trigger levels managed by the Central Trigger Processor (CTP). The role of the CTP is to grab the trigger signals coming from the various detectors and check if some of the trigger conditions are satisfied, also keeping into account the information on the LHC filling scheme.

The Level 0 (L0) trigger decision is based on the individual triggers provided by the fast detectors: SPD, V0, T0, the Muon Trigger, and the electromagnetic calorimeters. It is the first and most basic trigger selection in ALICE, and the CPT takes $\sim 0.9\,\mu s$ from the bunch crossing to elaborate this decision. After $\sim 6.5\ \mu s$ the CPT provides the Level 1 (L1) trigger. The Level 2 (L2) trigger is instead slower – $\sim 100\,\mu s$ – since it uses the information of the TPC; it is necessary to wait for the drift of the electron clouds in the detector gas.

Only the events that pass the L2 selection are forwarded to the Data Acquisition (DAQ) system [51], and to the High-Level Trigger (HLT) [52] to be further processed.

Once the L2 trigger signal is given, the raw data are sent from the detectors to the Local Data Concentrators (LDCs) through the Detector Data Links (DDLs) optical connections. Each detector is connected to one or more LDCs depending on the workload involved in reconstructing its raw data. The LDCs are computer nodes that check and process the raw data and, for each sub-detector, reconstruct a fragment of the entire event called sub-event.

The HLT, at the same time, perform a fast reconstruction of the data and apply further selections on the reconstructed data that was not doable at the hardware level. If the HLT selection is passed, the TPC data are compressed – the data coming from the TPC represent the $90\,\%$ of the total size of the event – and passed to the Global Data Collectors (GDCs).

The GDCs collect and aggregate the sub-events produced by the LDCs and the data arriving from the HLT – managing a data rate up to $20\,GB/s$ – to build the full event. The reconstructed events are then stored in a local disk pool that serves as a buffer for the data waiting to be moved to the CERN computing centre, where they are finally registered on tape.

2.5 ALICE Offline Framework

In this section, the ALICE experiment's simulation framework and analysis operations will be briefly introduced. Usually, these operations are referred to as *offline* since they do not involve the acquisition data flow and are done independently.

2.5.1 Monte Carlo Simulations

Modern High Energy Physics experiments make extensive use of Monte Carlo simulations. Monte Carlo simulations are used for different purposes: from the detector design to the data analysis optimisation for the search for new Physics, from the simulation of particle interactions with the detector's material to the development of very complex algorithms for signal extraction. In ALICE, all these aspects are handled by a simulation framework that aggregates the two crucial parts of the simulations: the *event generation* and the *transport code*.

In the event generation step, the interactions involved in the LHC collisions are simulated, obtaining a set of particles – accompained by their kinematic parameters – generated in the collisions. These interaction simulations can be based on first principles or on parametrisations of the collision physics depending on the particular event generator used. Strong decays is also handled at this stage since they happen in the same spatial region.

At this point, the transport code comes into play. It propagates the kinematic parameters of all the particles emerging from the event – produced either in the collision itself or in the strong decays – through a detailed geometrical and physical representation of the ALICE apparatus integrated into the simulation framework. The transport code provides information about the particles-detector interaction and the energy loss in the detector sensitive volume, including also the secondary particles generation. The secondary particles may originate from the interaction with the detector's material and the decay of unstable particles. The transport code describes both phenomena. In the ALICE simulation framework three different transport codes are available: GEANT3 [53], GEANT4[54–56] and FLUKA[57–59].

The simulation of the impact points with the related energy deposited in the detectors is stored in objects called *hits*. The electronic response of each detector to the hits is then simulated, obtaining the corresponding signals. These signals are then processed and stored in the same raw-data format used during the data taking and can be analysed using the same software.

2.5.2 Event Reconstruction

The raw data, regardless of the fact that they are generated via Monte Carlo simulations or are collected during the experiment run, are reconstructed with the same procedure, following the reconstruction flow shown in Figure 2.6.

The reconstruction starts from the conversion of the raw data into *recpoints* or *clusters*: objects containing the information of the spacetime coordinates of the interaction between the particles and the detectors' active volume. This task is undertaken by algorithms that reconstruct the raw data for each detector separately. For the detectors used for the PID, other information is attached to the clusters, like the time of flight, the Cherenkov angle, or the energy lost in the detectors' active volume. This additional

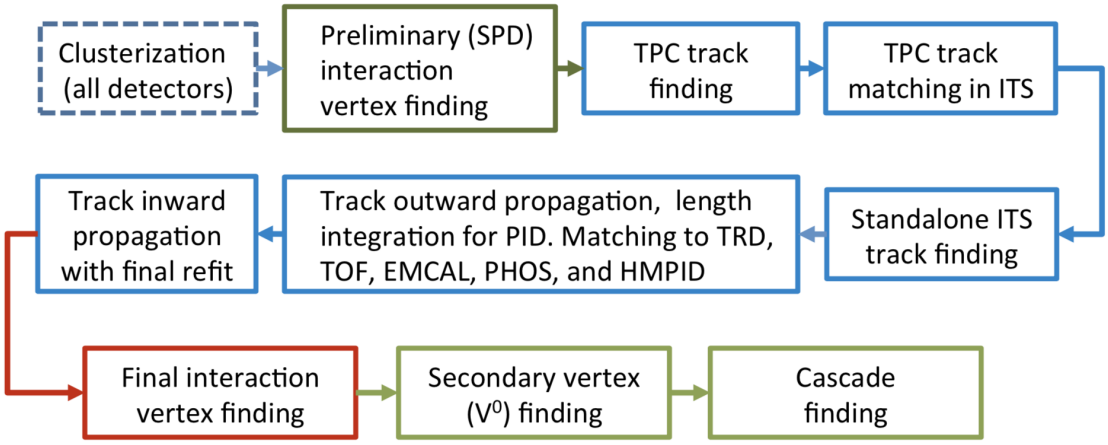

Figure 2.6: Event reconstruction flow in ALICE. Reprinted from [49].

information is crucial for the identification of the particles.

The second step is the preliminary estimation of the primary vertex of the collision. The best estimation of the primary vertex – in terms of resolution, precision and accuracy of the measurement – is obtained by using all the reconstructed tracks, maximising the information used in the estimate. However, the track reconstruction is extremely time-consuming and can be sped up by using the primary vertex position – it helps to discriminate roughly between valid track candidates and the noise. Then a preliminary and extremely fast estimate of the primary vertex position is obtained using the two innermost layers of the ITS, the SPD.

The algorithm that carries on this task starts connecting the cluster on the SPD Layer 0 with those on the SPD Layer 1, falling within a defined azimuthal acceptance window. Thus a set of proto-tracks called *tracklets* is obtained. The preliminary primary vertex – also called SPD vertex – is estimated by a routine that looks for the space point which minimises the distance between all the tracklets and excludes the outliers. This method operates with at least two tracklets. However, in pp collisions, it is not uncommon to have just one tracklet. In this situation, the algorithm uses the beamline position in the transverse plane to compute the z position of the primary vertex.

At this point, the track reconstruction can start and benefit from the primary vertex estimate, resulting in a much faster process. The complete tracking procedure used in ALICE during the Run 2 is extensively illustrated in [49], and it is summarised in the following.

First, the algorithm builds the *track seeds* that are pairs of clusters in the outer part of the TPC with the additional constraint that they must point to the SPD vertex – they

are track hypotheses. Then each track is extended inward, looking for compatible clusters in subsequent steps, building a helicoidal parametrisation of the track. Whenever the algorithm finds a compatible cluster at some step of the track propagation, a Kalman Filter [60] updates the track parameters. This procedure is applied to each track seed. It is relatively frequent, using this procedure, that one or more track candidates have some common clusters. A dedicated routine prune the track candidates that share a substantial fraction of clusters – the threshold on the fraction of shared clusters is between $25\,\%$ and $50\,\%$ – leaving just the track candidate with the best track parameters quality. Two further checks help to reject low-quality tracks. One rejects the track candidates built with less than 20 clusters – on up to 159. The other rejects the tracks with a ratio of the number of clusters over the crossed rows smaller than 0.5. Figure 2.7 shows the track reconstruction efficiency at this stage, using only the TPC information. The drop in the efficiency observed for low p_{T} tracks is due to the energy loss in the detector. The interactions with the material cause a deviation from the helicoidal trajectory, and this effect is much more pronounced for low momentum tracks. At higher p_{T}, the efficiency trend is due to the dead zone of the detector involving the loss of some clusters.

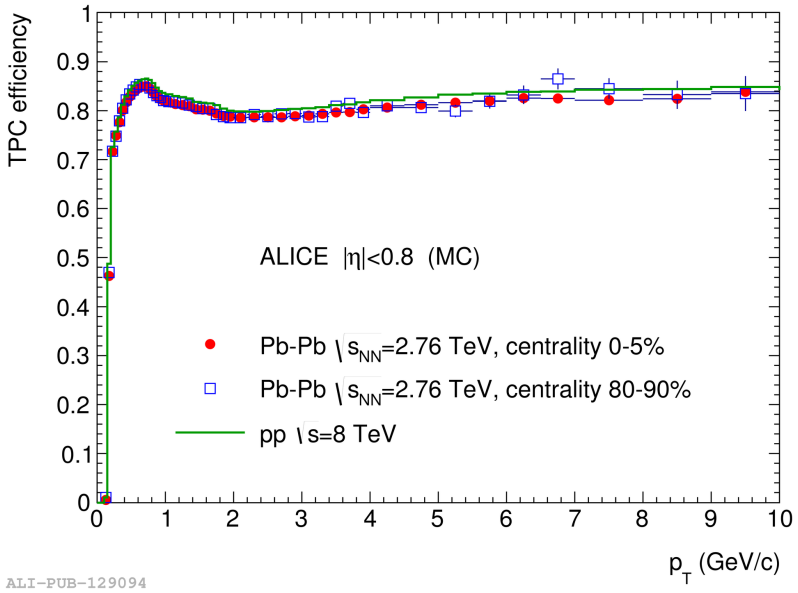

Figure 2.7: TPC single track reconstruction efficiency in pp collisions at $\sqrt{s} = 8\,\mathrm{TeV}$ (green line) and for central (red dots) and peripheral (blue open square) Pb–Pb collisions at $\sqrt{s_{\mathrm{NN}}} = 2.76\,\mathrm{TeV}$ respectively [48]. It is can be noted that the track reconstruction efficiency does not depend on the detector occupancy.

Once the algorithm completes the track reconstruction in the TPC, it is possible to associate the first hypothesis about the particle specie to each track candidate based on the energy loss and the momentum measurement. This is important to consider the particle's energy loss when the track candidate is propagated toward the ITS.

The track reconstruction goes on then, including the ITS clusters. The process is the same as in TPC: the track candidate is prolonged toward the next ITS layer, and if one or more *compatible* clusters are found, the track candidate parameters are updated with the Kalman Filter, including the information of the new clusters. A cluster is considered compatible if it lies in the proximity[5] of the expected intersection between the track prolongation and the considered ITS layer. In the event for which no compatible clusters are found on a layer, the track candidate is penalised by adding a penalty factor to its χ^2 parameter. This process produces a set of ITS track hypotheses for each TPC track candidate. The ITS track with the best quality parameters is associated with the TPC track candidate, thus forming an ITS+TPC track stored in the reconstructed event. The other track hypotheses are discarded.

If the track of a particle is not long enough for the main reconstruction algorithm, it is treated differently. This is the case of very low momentum particles ($p_{\mathrm{T}} < 200\,\mathrm{MeV}/c$). An ITS standalone algorithm was developed for these particles, analogous to that dedicated to the TPC. The ITS standalone reconstruction starts building the track seeds from the clusters – at least two – in the three innermost ITS layers. The track seeds are constrained to the SPD vertex. Then the track seeds are propagated outward using the Kalman Filter to update the track's parameters when compatible clusters are found in the other layers. This procedure is repeated a few times with different tolerances of the proximity criterion for the cluster compatibility to improve the efficiency at the lowest p_{T}. Finally, only ITS tracks satisfying specific quality criteria are stored in the reconstructed event.

In parallel to the ITS standalone reconstruction, the ITS+TPC tracks are refitted using the Kalman Filter, this time starting from the inner wall of the TPC and proceeding outward to the outer radius of the TPC. In this phase, the tracks are processed to obtain additional information crucial for particle identification with the Time Of Flight (TOF) detector. The expected time of flight for the different particle species is computed together with the integrated length. These pieces of information are also attached to the track.

The track is further propagated to the Transition Radiation Detector (TRD) when the refit is complete. Here the TRD tracklets, based on the clusters, are built independently. The reconstruction algorithm tries to match the track propagated from the TPC with the TRD tracklets. The algorithm updates the track parameters with the TRD tracklet information when the matching succeeds. The track is then extrapolated to the TOF regardless if matches or not in the TRD. Once again, the algorithm looks for possible matches with the TOF clusters. The track parameters are updated by including the TOF information for those events having a compatible cluster.

The track is then extrapolated up to the external detectors (HMPID, EMCAL and

[5] the criterion of the spatial proximity selection depends on many factors, and it is optimised in order to maximise the track reconstruction efficiency, still keeping into account the computing time of the task.

PHOS), looking for some match with the detectors' hits. All the tracks are finally refitted for the third time with the Kalman Filter. The final refit starts from the external detectors and goes toward the innermost ITS layers, including the information of all the clusters attached to the tracks.

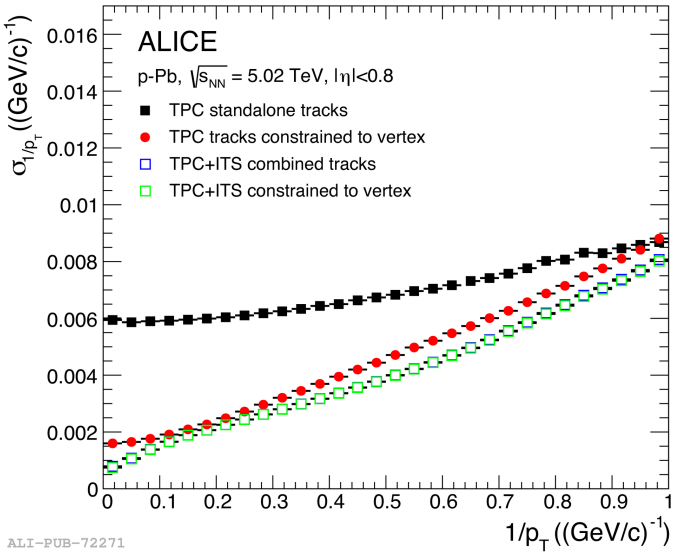

Figure 2.8: Resolution on $1/p_{\mathrm{T}}$ in p-Pb collisions for TPC tracks with (red dots) and without (black squares) vertex constraint and for ITS+TPC tracks with (green square) and without (blue square) vertex constraint. It is quoted for $1/p_{\mathrm{T}}$ because this can be extracted directly from the covariance matrix of the Kalman Filter fit.

Figure 2.8 shows the track resolution on $1/p_{\mathrm{T}}$ which is connected to the p_{T} resolution by the relation:

$$\frac{\sigma_{p_{\mathrm{T}}}}{p_{\mathrm{T}}} = \frac{\sigma_{1/p_{\mathrm{T}}}}{1/p_{\mathrm{T}}}. \tag{2.8}$$

The figure shows that the momentum resolution for tracks with momentum in the range 0.1–$100\,\mathrm{GeV}/c$ is within 1 and $10\,\%$. Nonetheless, it should be noted that these performances are obtained considering mainly *primary tracks* – i.e. tracks originating from the primary vertex, as distinct from *secondary tracks* that are not originating from the primary vertex. A dedicated algorithm performs a tracking procedure for the secondary tracks without the constraint on the primary vertex position in the track seeds building.

Once all the primary tracks are reconstructed, it is finally possible to proceed with the primary vertex estimation using the complete information of the tracks. By propagating all the tracks to the nominal beamline position, it is possible to reject the outlier tracks – tracks with distance with respect to the beamline exceeding $\mathcal{O}(100\,\mu\mathrm{m})$ – that are not used for the computation. The starting point for *vertexing* is set to the point of closest approach to the set of reconstructed tracks. Figure 2.9 shows, as an example of the ALICE vertexing performances, the resolution on the primary vertex position

for both full tracks vertex and SPD vertex as a function of the charged particle multiplicity; these results are obtained in pp collisions at $\sqrt{s} = 7\,\text{TeV}$. Then the precise determination of the primary vertex is done through a fit procedure described in [61].

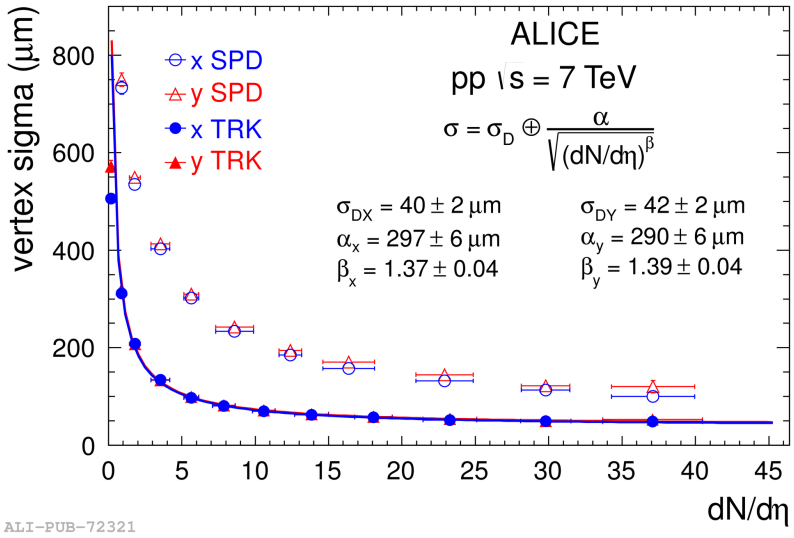

Figure 2.9: Primary vertex resolution on the x and y direction (transverse plane) using the SPD and the track algorithms as a function of the charged particle multiplicity of the event in pp collisions at $\sqrt{s} = 7\,\text{TeV}$ [48].

The case of pile-up events is treated with dedicated strategies and solutions. Reference [49] provides more details on this point.

The final steps of the event reconstruction are dedicated to the reconstruction of the *secondary vertex* and *cascades* structures. These parts of the event reconstruction involve searching topological features of sets of tracks that characterise the decay of some particle species produced in the collision using dedicated algorithms. Since it plays a crucial role in the analyses presented in this work, the secondary vertex reconstruction must be looked in more depth.

The reconstruction of the secondary vertices is used to reconstruct the decay of a neutral particle – called mother particle or mother track – into two charged particles – called daughter particles or daughter tracks – forming the V-shaped topology. The algorithm dedicated to this task is often referred to as the V^0*-finder*. In the ALICE offline framework two V^0-finder algorithms are available: the *on-the-fly* V^0 and the *offline* V^0. Both the algorithms are based on the search of all the track pairs whose tracks are close enough in space to suppose that they come from a common mother particle – displaced from the primary vertex. So all the possible track pairs with opposite charges are considered, and then the distance of closest approach is computed. If the track pair fulfils a defined set of selection criteria based on the topological structure of the decay and the quality of the tracks, the track pair is stored as a V^0-candidate, and the momentum of the mother particle is computed.

The on-the-fly V^0-finder operates during the track fitting and reconstructs the V^0 topology using the full cluster information. First, the V^0-finder looks for tracks matching the primary vertex whose χ^2 is above e certain threshold. If the condition occurs, the track is assumed to be produced in a secondary vertex. All the secondary tracks satisfying the selection criteria and close in space are stored together in a list. Then all the possible track pairs passing the selections are refitted, assuming that they originate from the secondary vertex. Further quality cuts are applied before they are stored as V^0-candidates.

The principle of the offline V^0-finder is similar to the on-the-fly algorithm, but it is based on the reconstructed tracks and does not take into account the cluster information. Furthermore, it is part of the ALICE offline framework that the analysers can execute when they run offline the analysis tasks. It is typically used to apply different selection criteria to the V^0 topology since it can be re-run offline multiple times.

The advantage of the on-the-fly is the usage of the cluster information which allows having the local description of the helix representation of the track. This means that, in the refit, an accurate correction of the momentum of the daughter tracks is possible, taking correctly into account the material budget and the dead zones of the detector. The on-the-fly V^0-finder ensures a better resolution of the mother particle momentum.

A complete description of the algorithms and the selection criteria is provided in [49]. However, it is important to provide more details about the selections applied by the V^0-finder since they will be widely discussed in this work. The main selections are:

- the *Distance of Closest Approach (DCA)* of the single track to the primary vertex;
- the distance between the tracks at the secondary vertex;
- the *Cosine of the Pointing Angle* ($\cos\theta_{pointing}$).

A representation of a V^0 decay is given in Figure 2.10 highlighting the topological features used for the selections.

It is also possible to apply the so-called *causality cut* to reduce the combinatorial background. This selection requires not having clusters for the daughter tracks when prolonged before the secondary vertex position. The on-the-fly algorithm applies this cut as a default. The offline algorithm, instead, executes a modified version of the cut.

These two algorithms have been developed to reconstruct the V^0 topology that strictly describes a neutral particle's decay into two charged particles. The V^0-finder algorithms can also look for charged particles decays; this requires minor modification in the procedure and the selection criteria, as in the case of the hypertriton.

2.5.3 ALICE Analysis Framework

High Energy Physics experiments produce a massive amount of data – in the order of tens of petabytes every year of data taking – that requires a dedicated infrastructure to

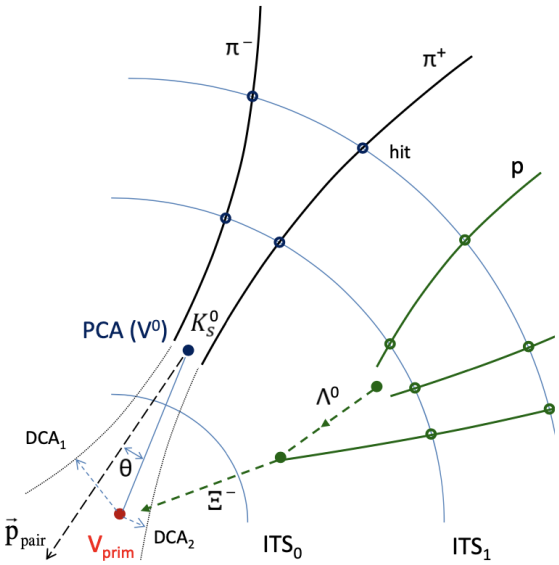

Figure 2.10: Example of the reconstruction of the secondary vertex for the K_S^0 (in black) and the Ξ^- (in green) using the V^0 topology. The daughter tracks are represented with solid lines indicating that they are actually reconstructed, while the mother tracks are represented with dashed lines indicating that they are *extrapolated* to the primary vertex (red dot).

be stored and analysed. This infrastructure is the *analysis framework* and provides a complete set of tools intended to store, process and analyse the reconstructed events.

The advent of the LHC required the realisation of the Worldwide LHC Computing Grid (WLCG), a collaboration of computing centres whose purpose is to provide computing resources to manage the LHC experiments data flow. The WLCG was designed as four layers – or *tiers* – structure, and each tier provides a specific set of services to distribute and analyse ∼50–70 PB of data per year of operations. Tier 0 is the CERN computing centre; it hosts a copy of the raw data and takes care of the first reconstruction of the raw data, which is then distributed to the Tiers 1 centres. Tiers 1 are thirteen large computer centres storing a second replica of the data, distributed with a proportional share of raw and reconstructed data. It also takes care of large-scale reprocessing and distributing the data to Tier 2. Finally, Tier 2 are the centres dedicated to running Monte Carlo simulations and analysis processing. Individual users (scientists) access these infrastructures through the initialisation of a local resource – namely the Tier 3, that do not have any formal engagement with the WLCG – that can be an individual laptop or a local cluster, to deploy the analysis task to the WLCG.

The ALICE data, both raw and reconstructed, are stored using the ROOT [62] framework data format. ROOT is also the core of the ALICE software: AliRoot and AliPhysics,

a collection of libraries and routines that enclose almost all the software used in the ALICE Collaboration. The raw data are represented in the form of Event Summary Data (ESD), a low-level object mainly used for the calibration and performance study of the detector. The analysis code run by the users mainly involves the Analysis Object Data (AOD), which is a more basic version of the ESD. In the AODs, the low-level information – that usually are not used in the final analysis – is dropped, leaving the relevant significant information at the analysis level – i.e. the track parameters and some connected physical quantities.

The support for the analysis task developed by the users is provided by the ALICE Environment (`Alien`) grid middleware. `Alien` links the request of the users with the WLCG infrastructures allowing them to access the globally distributed data and Monte Carlo simulations and to run the analysis task on this data. ALICE also developed a tool to organise different analysis tasks that work on the same data. This tool defines a default data flow that uses an access pattern called *analysis train* to optimise the run of different tasks from different users in the same job.

2.6 Particle Identification

The Particle Identification in ALICE uses the ITS, TPC, TOF and HMPID detectors with different techniques. The PID, in TPC and ITS, relies on the energy loss measurement attached to the clusters. The TOF, instead, employs the measurement of the particle time of flight, while the HMPID uses the Cherenkov angle.

This information, combined with the momentum measurement, allows us to identify the particle species over a wide momentum range. In this thesis, the PID is performed with the TPC detector. Therefore the following section provides detailed insight into the techniques used to identify the charged particles with the TPC in this thesis.

2.6.1 TPC Particle Identification

The charged particles traversing the active volume of the TPC release part of their energy in the detector gas, generating electron clouds that drift toward the readout pads. The pads measure the amplitude of the signal generated by the electron clouds, and this signal is related to the specific energy loss of the charged particle in the detector gas. Since the relation between the energy loss and the momentum characterises a defined particle specie, it is possible to identify a particle using the energy loss and momentum measurements through the relation

$$f(\beta\gamma) = \frac{P_1}{\beta^{P_4}} \left[P_2 - \beta^{P_4} - \ln\left(P_3 + \frac{1}{(\beta\gamma)^{P_5}} \right) \right]. \tag{2.9}$$

Equation (2.9) – where β and γ are the usual Loerntz factors and P_{1-5} denote five free parameters – is a Bethe–Bloch parametrization of the energy loss of the light hadrons

as a function of the particle momentum derived by the ALEPH collaboration [63]. It can be used to describe the energy loss/momentum relation for any given particle specie, by fitting this function to the data. In ALICE, a data-driven spline parametrisation provides the energy loss/momentum relation. These splines are integrated into the central analysis framework. Figure 2.11 shows the $\mathrm{d}E/\mathrm{d}x$ measured by ALICE in the Pb–Pb collisions collected during 2018 for a large sample of particles with the related splines overlaid.

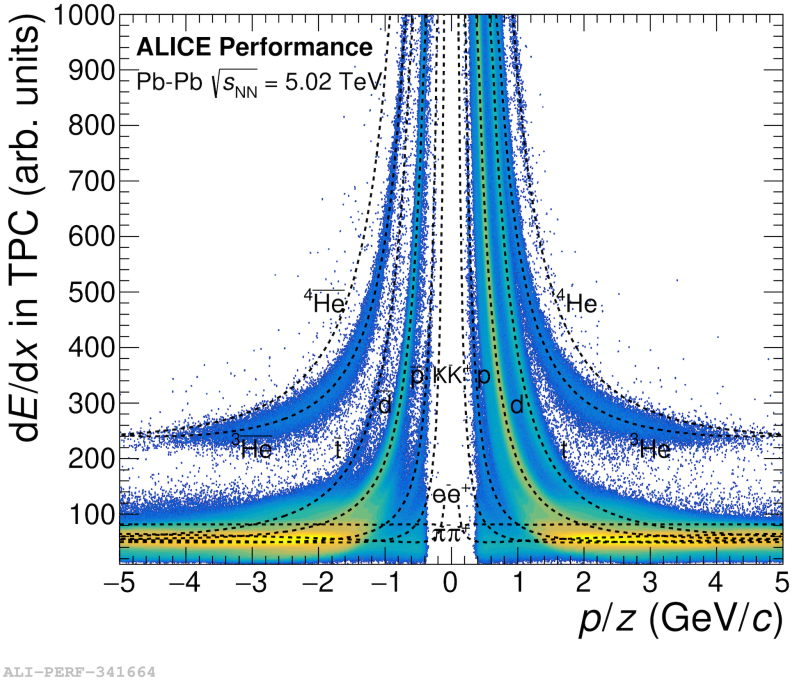

Figure 2.11: Specific energy loss of particles traversing the TPC volume as a function of the particle rigidity p/z in Pb–Pb collisions at $\sqrt{s_{\mathrm{NN}}} = 5.02\,\mathrm{TeV}$. The dashed lines represent the splines used in ALICE to parametrise the expected energy loss for the considered species.

In the low momentum region ($p < 1\,\mathrm{GeV}/c$) the $\mathrm{d}E/\mathrm{d}x$ depends mainly on the $1/\beta^2$ factor. This allows selecting the particle belonging to the species under consideration track-by-track by picking the tracks whose energy loss lies in a fiducial range around the expected value. Usually, the number of σ – where σ is the TPC resolution on the $\mathrm{d}E/\mathrm{d}x$ for the considered track – defines the extension of the fiducial region. The expected relative resolution on the $\mathrm{d}E/\mathrm{d}x$ for the TPC is $5.2\,\%$ in pp collisions and $6\,\%$ in Pb–Pb collisions. A clear separation of the different species is not possible for higher momentum particles using the TPC standalone. However, it is still possible to derive the relative weight of the different particle species via the statistical unfolding of the $\mathrm{d}E/\mathrm{d}x$ distributions. Nevertheless, by integrating the information provided by other detectors – mainly the TOF, if available for the considered track – it is possible to

extend the momentum region where a clear identification of particles is possible.

A separate discussion should be done for the particles with electric charge $z > 1$. For these particles, the distribution of the expected $\mathrm{d}E/\,\mathrm{d}x$ is entirely separate from the distributions of the $z = 1$ particles, as clearly visible in Figure 2.11 in the case of the (anti)helium and the (anti)helium-3. The TPC standalone particle identification allows clear identification of these species over a wide momentum range.

2.7 Centrality Determination in Pb–Pb Collisions

In High Energy Nuclear Physics, it is customary to classify the nucleus–nucleus collisions based on the degree of overlap of the colliding nuclei since many physical quantities correlate in a meaningful way to this parameter. The degree of overlap represents the scalar impact parameter b; however, this quantity can not be directly derived using the Glauber model as discussed in Section 1.3.1.

Other experimental strategies are used to derive the impact parameter, exploiting the correlations between the impact parameter of the collision and other physical quantities that are measured directly by the detectors, such as the energy deposited in the ZDCs or the number of charged particles produced in the collision – usually called *charged particle multiplicity*.

In the literature, the collisions are categorised in *centrality classes* matching the percentiles of the total hadronic cross-section of the colliding nuclei:

$$c(b) = \frac{1}{\sigma_{AA}} \int_0^b \frac{\mathrm{d}\sigma}{\mathrm{d}b'}\,\mathrm{d}b' \qquad \text{where} \qquad \sigma_{AA} = \int_0^\infty \frac{\mathrm{d}\sigma}{\mathrm{d}b'}\,\mathrm{d}b'.$$

Assuming a monotonic dependence of the energy deposited at zero degrees and the charged particle multiplicity on the impact parameter, the centrality can be written as:

$$c \approx \frac{1}{\sigma_{AA}} \int_{N_{ch}}^\infty \frac{\mathrm{d}\sigma}{\mathrm{d}N'_{ch}}\,\mathrm{d}N'_{ch} \approx \frac{1}{\sigma_{AA}} \int_0^{E_{ZDC}} \frac{\mathrm{d}\sigma}{\mathrm{d}E'_{ZDC}}\,\mathrm{d}E'_{ZDC}.$$

The total hadronic interaction cross-section of the colliding nuclei σ_{AA} can be replaced by the number of considered collisions – or events – corrected for the background and the trigger efficiency:

$$c \approx \frac{1}{N_{ev}} \int_{N_{ch}}^\infty \frac{\mathrm{d}\sigma}{\mathrm{d}N'_{ch}}\,\mathrm{d}N'_{ch} \approx \frac{1}{N_{ev}} \int_0^{E_{ZDC}} \frac{\mathrm{d}\sigma}{\mathrm{d}E'_{ZDC}}\,\mathrm{d}E'_{ZDC}.$$

In peripheral collisions – i.e. for $c > 50\,\%$ – some nuclear fragments can be deflected outside the ZDC acceptance by the LHC magnets reducing the energy deposit in the detector. This effect can mimic the energy deposition of the most central collisions,

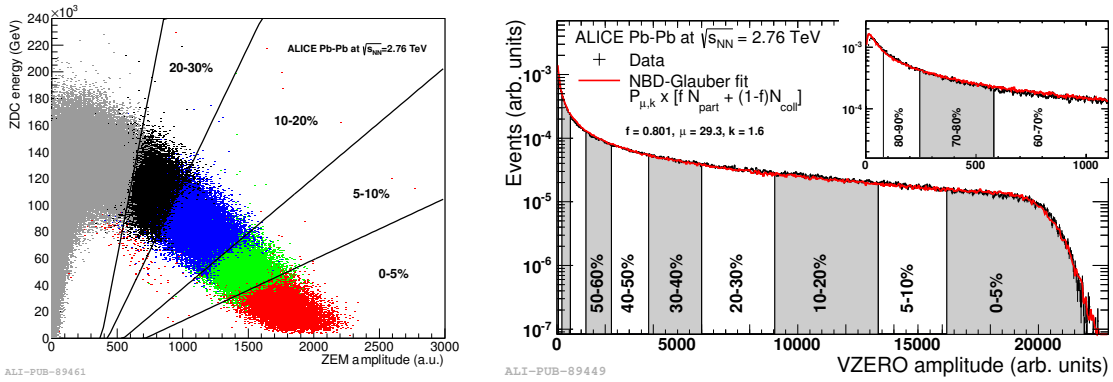

(a) **(b)**

Figure 2.12: ZDC energy deposit as a function of the ZEM energy deposit (a). The solid lines represent the cut-off lines for the different centrality classes determined with the ZDC while the different colours represent the centrality classes obtained with the V0. (b) The distribution of the sum of the V0 amplitudes used to determine the centrality classes with the V0 amplitude percentiles method and the fit of the NBD-Glauber model (red line) is shown.

breaking the monotonic decrease of the energy deposit as a function of the event centrality. The ambiguous events can be discriminated by exploiting the correlation with the energy deposit in the ZEM as shown in Figure 2.12a.

In Figure 2.12b the distribution of the sum of the signals measured by the V0 detector – i.e. the sum of the two individual distributions related to the V0A and the V0C detectors – is reported. It is used to determine the centrality in Pb–Pb collisions as described in the following. This distribution is fitted with a parametric function based on the Negative Binomial Distribution and the Glauber Monte Carlo model (NBD–Glauber fit), connecting the measured V0 amplitude with the impact parameter of the collision. In particular, the number of participant nucleons N_{part} and the number of binary collisions N_{coll} are generated using the Monte Carlo Glauber model. The multiplicity of particles produced per nucleon–nucleon collision is then described with the NBD distribution

$$P_{\mu,k}(n) = \frac{\Gamma(n+k)}{\Gamma(n+1)\,\Gamma(k)} \cdot \frac{(\mu/k)^n}{(\mu/k+1)^{n+k}}$$

with parameters μ and k.

The distribution of the number of tracks in the TPC and the number of clusters in the SPD Layer 2 are two other distributions that can be fitted with the NBD–Glauber function to obtain the impact parameter of the collision. However, it has been shown that the centrality resolution depends on the width of the pseudo-rapidity region covered by the detector used for the NBD–Glauber fit. The best choice falls on the sum of the V0 distributions under the 4.3 pseudo-rapidity units covered by V0A and V0C

combined. The resolution on the centrality estimated with the V0 ranges from $0.5\,\%$ for the most central collisions up to $2\,\%$ for the most peripheral.

The collision centrality can also be estimated by exploiting the following relation between the energy deposited in the ZDC detector (E_{ZDC}) and N_{part}:

$$N_{part} = 2A - E_{ZDC}/E_A,$$

where $2A$ is the sum of the atomic numbers of the colliding nuclei and E_A is the energy they brought in the collision. The N_{part} and E_{ZDC} relation is not monotonic due to the nuclear fragments escaping the ZDC acceptance in peripheral collisions, as mentioned above. The centrality classes then can be defined by selecting with straight lines regions of the ZEM amplitude versus ZDC energy deposit plane, as shown in Figure 2.12a. In Figure 2.12b instead the centrality classes obtained with the percentiles of the V0 amplitude method – reliable for $c < 30\,\%$ – are shown.

Chapter 3

(Anti)(Hyper)Nuclei in Heavy-Ion Collisions

This chapter focuses on the hypernuclei, particularly on the hypertriton ($^{3}_{\Lambda}$H), the main character of this thesis. Special attention is given to highlighting the importance of measuring the hypertriton lifetime and its Λ-separation energy (B_{Λ}). These measurements provide crucial information for understanding the hypertriton structure with significant implications in many fields ranging from the knowledge of the nuclei production mechanism in HIC to the hyperon–nucleon interaction and the study of the nuclear matter equation of state in the neutron stars core.

3.1 (Anti)Hypernuclei

An ordinary nucleus is a bound state of nucleons that are protons and neutrons. A hypernucleus, instead, is a nucleus in which hyperons replace one or more nucleons, where the hyperons (Y[1]) are baryons containing at least one strange quark but no charm, bottom or top quarks (Section 3.1).

The first hypernucleus was observed by Danysz and Pniewski in 1953 [64] exposing photographic emulsions to cosmic radiation at an altitude of about 26 km. Starting from their discovery, the hypernuclei have been extensively studied in cosmic rays experiments first and in accelerators experiments later. These studies provided observations on the production yields, structure and decay rates of about 40 single-Y and double-Y hypernuclei [65].

The hypernuclei play a crucial role in understanding the nuclear force that rules the nuclear matter and holds nuclei together. For this reason, they stimulate a lively debate in the nuclear physics community.

[1]The letter Y usually refers to a generic hyperon, a baryon that carries strangeness, without specifying the particle specie.

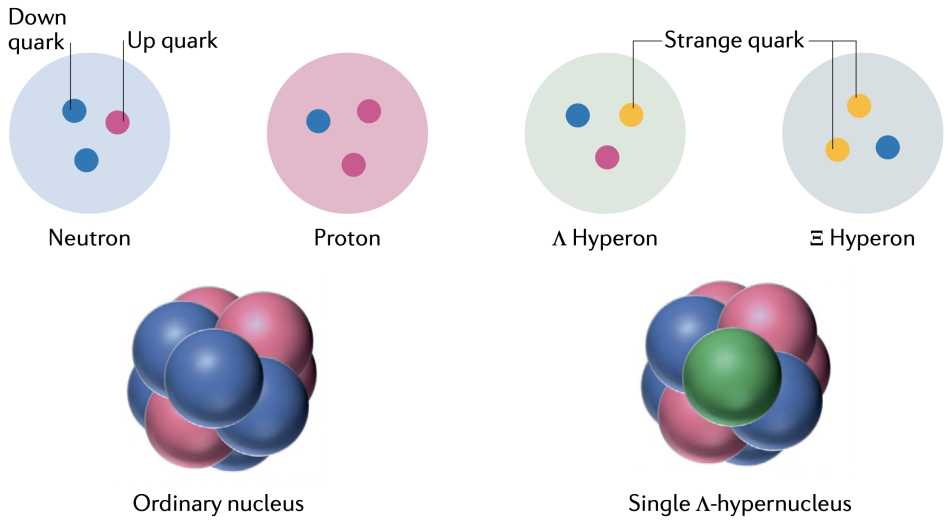

Figure 3.1: Schematic representation of an ordinary nucleus and an hypernucleus with their constituents (Figure from [66]).

The nuclear force results from the fundamental interactions among nucleons as a first approximation. Two-body and three-body interactions between nucleons – NN and NNN interactions – have been studied in detail through many different nuclear reactions obtained with nuclear beams in particle accelerators. These studies allowed us to understand the fundamental nature of the nuclear force, especially at medium and long distances.

However, a more profound comprehension of the nuclear force is necessary to understand the nuclear matter behaviour in extreme conditions such as in the inner core of neutron stars and the strongly interacting medium generated in an ultra-relativistic heavy-ion collision. In this respect, it is crucial to increase the degrees of freedom of the nuclear system by adding one or more strange quarks and investigating the hyperonic component of the nuclear force.

Two-body and three-body interactions between hyperons and nucleons and between hyperons themselves – YN, YNN, YY, YYN and YYY interactions – are pivotal for the nuclear force. A prime example is the cold nuclear matter equation of state used to describe the neutron star interiors, where the presence of strange quarks seems inevitable. It is thought that hyperons, together with neutrons [67, 68], are major ingredients of the neutron stars' inner core. However, the equation of state of the nuclear matter with neutron–hyperon mixing is unable to reproduce the mass of the observed two-solar-masses neutron star [69–71].

One of the possible solutions to conciliate the neutron star masses with the presence of hyperonic matter in their interiors is to consider a repulsive three-baryon interaction that works universally for the YNN, YYN, YYY and NNN components [72]. However,

the behaviour of the three-baryon component of the nuclear interaction in a neutron-rich environment involving hyperons still needs to be investigated. The properties of these interactions could be studied in very neutron-rich hypernuclei, which, unfortunately, are extremely hard to produce. Moreover, the interactions involving multiple hyperons are not yet clear since the experimental identification of double-Y hypernuclei is limited to just a few observations [73–76].

Observing extremely massive neutron stars has renewed interest in the hypernuclear physics sector from both the theoretical and the experimental side. A theoretical effort to describe the hyperonic component of the nuclear interaction is ongoing, but more inputs from the experiments are necessary. The hypernuclei represent a micro-laboratory for investigating the nuclear interaction between hyperons and nucleons. Therefore, several experimental programmes are ongoing, and others are planned to be carried on in many accelerator facilities, aiming to understand the nature of the hypernuclei in more detail [66].

3.1.1 Weak Decay of Hypernuclei

A single-Λ hypernucleus in the ground state decays to non-strange nuclear matter through two weak processes: the non-mesonic weak decay (NMWD) and the mesonic weak decay (MWD).

The NMWD converts the Λ inside in the hypernucleus into a nucleon through a $\Lambda \rightarrow \pi$N process involving a virtual π. The nuclear medium absorbs the virtual pion; hence it is not emitted in the final state, resulting in a non-mesonic decay. Examples of these types of processes are the *one-nucleon induced decays*:

$$\Lambda \mathrm{n} \rightarrow \mathrm{nn}, \ \Lambda \mathrm{p} \rightarrow \mathrm{np}$$

and the *two-nucleon induced decays*:

$$\Lambda \mathrm{NN} \rightarrow \mathrm{nNN}.$$

The MWD follows the mesonic decay modes of a free Λ baryon:

$$\Lambda \rightarrow \mathrm{p} + \pi^{-}, \tag{3.1}$$

$$\Lambda \rightarrow \mathrm{n} + \pi^{0}, \tag{3.2}$$

converting the Λ inside the nucleus into a nucleon without involving the other constituents of the nucleus. Light-A and medium-A are thus converted into non-hyperonic nuclei through the reactions:

$${}^{A}_{\Lambda}Z \rightarrow^{A} (Z+1) + \pi^{-} \tag{3.3}$$

$${}^{A}_{\Lambda}Z \rightarrow^{A} Z + \pi^{0}. \tag{3.4}$$

where the final states are not necessarily stable.

The total decay amplitude of a Λ-hypernucleus $\Gamma(^{A}_{\Lambda}Z)$ is the sum of the amplitudes of the mesonic and the non-mesonic decay channels:

$$\Gamma = \Gamma_{\text{NMWD}} + \Gamma_{\text{MWD}} \,.$$

The first term Γ_{NMWD} is the sum of all the one-nucleon and two-nucleon induced decay amplitudes, while the second term Γ_{MWD} represents the contribution of the processes described in Equations (3.3) and (3.4).

The lifetime of the hypernuclei is related to the total decay amplitude by the relation:

$$\tau(^{A}_{\Lambda}Z) = \hbar/\Gamma(^{A}_{\Lambda}Z)$$

where $\hbar$ is the reduced Plank constant whose value is $1.054\,571\,817 \times 10^{-34}$ J s.

The weak decay of a Λ via non-mesonic channels – i.e. ΛN → NN – would provide direct access to the study of the hyperon-nucleon interaction. However, a free Λ decays only through the mesonic processes described in Equations (3.1) and (3.2). In the hypernuclei, the Λ is embedded into the nuclear medium, making the emission of virtual pion possible, leading to a non-mesonic decay. This is the reason why the decay of the hypernuclei is so interesting.

The experimental investigation of the lifetime of the hypernuclei and its mass dependence have been investigated in many experiments carried out with different experimental techniques and analysis methods [77]. The lifetime of light hypernuclei is generally expected to be close to that of the free Λ, while it is believed that it shortens quickly when the mass of the hypernucleus increases. This is due to the increasing weight of the non-mesonic channel in the total decay amplitude. The lifetime instead is expected to settle to a saturated value with increasing masses of the hypernuclei due to the short-range nature of the ΛN interactions. Two recent theoretical works [78, 79] calculated the expected lifetime for the whole mass range of the hypernuclei up to $A = 209$, predicting a saturation value around 200 ps.

3.2 Hypertriton: the Lightest Known Hypernucleus

The first observations of hypernuclei – already mentioned in Section 3.1 – were performed by using glass-backed emulsion plates, and dates back to 1953. The thickness of the plates, which was only 400–600 µm, did not allow to completely record the event preventing the determination of the identity of the hypernucleus.

The following year Bonetti et al. reported the detection of a complete event thanks to the innovative use of a stack of stripped emulsion pellicles [80]. It was the first observation of the ".. ejection of a meson-active triton from a nuclear disintegration" [80, p. 208], confirming that the nucleus was bound to a Λ baryon. That was actually the first observation of the hypertriton and Figure 3.2 shows the portion of the emulsion with which Bonetti et al. made their discovery.

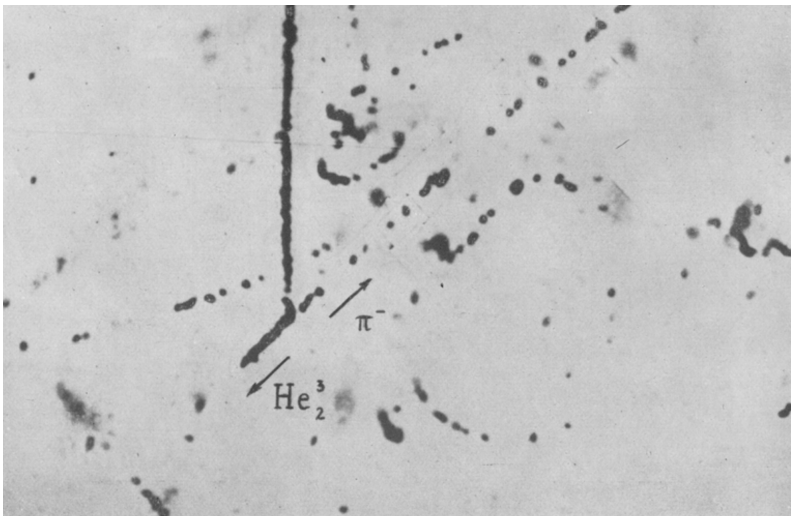

Figure 3.2: The first observation of the decay of a hypertriton.

After the first observations in cosmic ray reactions, the experimental study of hypernuclei moved to particle accelerators in the late fifties. Thanks to the availability of K^- beams, the accelerators allowed an abundant production of hypernuclei and, in particular, of hypertritons. In the following years, the production and the detection techniques continually improved to the present days, allowing the first observation of an antimatter hypertriton ($^3_\Lambda\overline{\mathrm{H}}$) in 2010 by the STAR Collaboration at RHIC [81].

The hypertriton is the lightest known Λ-hypernucleus, and it is a bound state of a proton, a neutron and a Λ hyperon. It can be interpreted as a $\mathrm{d}-\Lambda$ halo system, with a deuteron core loosely bound to a Λ. In fact, the most accepted value of the Λ-separation energy – that is the binding energy of the Λ to the nucleons core[2] – is just:

$$B_\Lambda = 0.13 \pm 0.05\ (\text{stat.}) \pm 0.04\ (\text{syst.})\ \text{MeV} \tag{3.5}$$

as reported by [82]. Due to the low B_Λ, the Λ wave function is expected to be only slightly modified by the interaction with the nucleons. The hypertriton lifetime then is expected to be extremely close or slightly below the free Λ lifetime whose value – reported by the PDG [4] – is:

$$\tau(\Lambda) = 263.2 \pm 2.0\,\text{ps}. \tag{3.6}$$

[2]In nuclear physics, the term *separation energy* refers to the energy needed to remove a nucleon – or another specified constituent particle – from a nucleus [83]. The term *nuclear binding energy*, instead, refers to the energy needed to disassemble the whole nucleus in its constituent particles [83]. Usually, the term *binding energy* is more general, and it can mean separation energy or nuclear binding energy – or other meanings – depending on the context. In this thesis, the binding energy is always intended as separation energy without ambiguity since nuclear binding energy is not addressed.

The ${}^{3}_{\Lambda}\mathrm{H}$ decays weakly, essentially into the mesonic channels (MWD). Table 3.1 reports the partial and total mesonic and non-mesonic decay amplitudes as calculated by Kamada et al. in the most comprehensive work on the ${}^{3}_{\Lambda}\mathrm{H}$ decay [84]. The value of the amplitudes led to a branching ratio (BR) of 25 % for the two-body charged decay (${}^{3}_{\Lambda}\mathrm{H} \rightarrow {}^{3}\mathrm{He} + \pi^{-}$) and 40 % for the three-body charged decay (${}^{3}_{\Lambda}\mathrm{H} \rightarrow \mathrm{d} + \mathrm{p} + \pi^{-}$).

Channel	Γ (s^{-1})
Mesonic	
${}^{3}\mathrm{He} + \pi^{-}$ ${}^{3}\mathrm{H} + \pi^{0}$	0.146×10^{10}
$\mathrm{d} + \mathrm{p} + \pi^{-}$ $\mathrm{d} + \mathrm{n} + \pi^{0}$	0.235×10^{10}
$\mathrm{p} + \mathrm{p} + \mathrm{n} + \pi^{-}$ $\mathrm{p} + \mathrm{n} + \mathrm{n} + \pi^{0}$	0.368×10^{10}
Non mesonic	
$\mathrm{d} + \mathrm{n}$	0.67×10^{7}
$\mathrm{p} + \mathrm{n} + \mathrm{n}$	0.57×10^{8}
All channels	0.391×10^{10}

Table 3.1: Total and partial mesonic and non mesonic decay rates of the ${}^{3}_{\Lambda}\mathrm{H}$.

3.2.1 The Hypertriton Puzzle

The hypertriton and its properties were extensively investigated until the 1970s using bubble chambers, and nuclear emulsions [65]. As already mentioned in the previous section (Section 3.2), those experiments determined the Λ-separation energy with high precision $B_{\Lambda} = 0.13 \pm 0.05\ (\mathrm{stat.})$ MeV [82, 85]. The interpretation of the hypertriton as a deuteron core very weakly bound to a Λ hyperon arose from those results, and the value of the B_{Λ} became a benchmark for any theoretical calculations concerning hypernuclei.

There have also been attempts to measure the hypertriton lifetime [86–94] with visualising techniques in He bubble chambers and nuclear emulsions experiments. In these experiments, the number of detected hypertriton was very small, leading to significant statistical uncertainties. Back then, the technologies employed in these experiments induced significant systematic uncertainties. Therefore, it was impossible to obtain a solid and agreed result due to measurement inaccuracy.

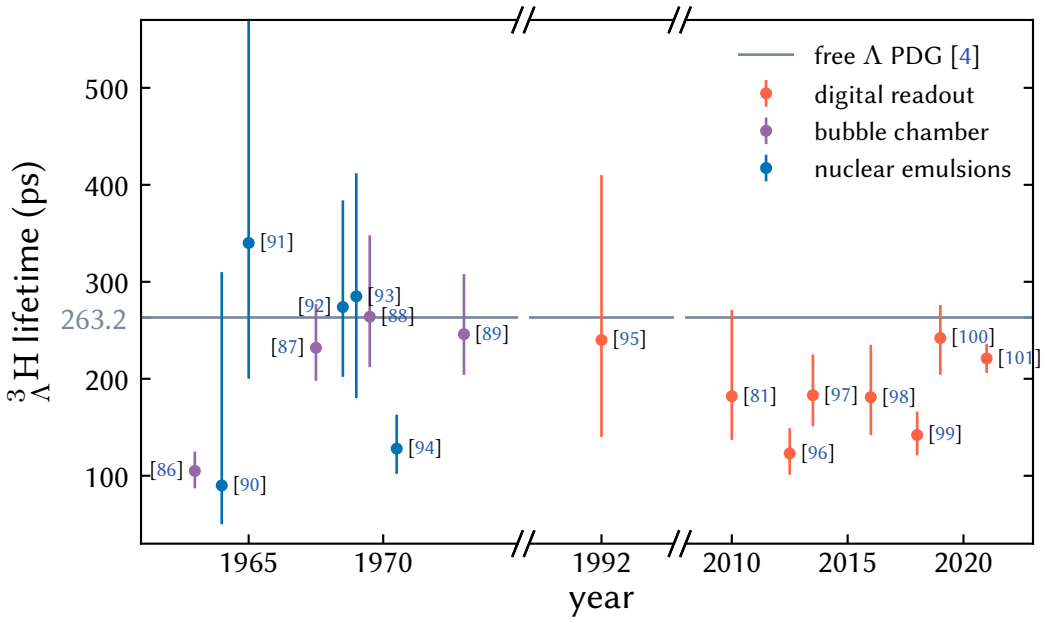

Figure 3.3: Chronological synopsis of the experimental values obtained for the $^3_\Lambda$H lifetime. Purple points are results from He bubble chambers, blue points from photographic emulsions and red points from digital readout experiments which include the STAR and the ALICE experiments. The free Λ baryon lifetime is also reported as a reference.

The hypertriton lifetime was thus assumed very close to the lifetime of a free Λ hyperon (Equation (3.6)), relying on its very small binding energy. This assumption comes from a simple argument. Because of the very small binding energy, the binding with the deuteron core has little influence on the Λ wave function. It follows that the Λ decay is not significantly affected by the interactions with the deuteron core.

However, new experiments in recent years have found surprising and conflicting results measuring significantly shorter lifetime than the assumed value. The HypHI experiment at GSI in 2013 derived a lifetime of 183^{+42}_{-32} (stat.) $\pm$ 37 (syst.) ps [97] using ^{6}Li + ^{12}C reactions at 2AGeV. Since the 2010s, ultra-relativistic heavy-ion collision have also proven to be a powerful tool to investigate the hypertriton properties. The STAR collaboration at RHIC measured the production of $^3_\Lambda$H and – for the first time ever – $^3_\Lambda\overline{\text{H}}$ in Au+Au collisions at $\sqrt{s_{\text{NN}}} = 200$ GeV. By combining the observations of the $^3_\Lambda$H and the $^3_\Lambda\overline{\text{H}}$ they measured a lifetime of 182^{+89}_{-45} (stat.) $\pm$ 27 (syst.) ps [81]. This value is compatible with the free Λ lifetime within 1σ having large uncertainties. Later, in 2018, STAR measured the hypertriton lifetime in both the 2-body ($^3_\Lambda\text{H} \rightarrow {}^3\text{He} + \pi^-$) and the 3-body ($^3_\Lambda\text{H} \rightarrow \text{d} + \text{p} + \pi^-$) decay channels and found a significantly smaller value of 142^{+24}_{-21} (stat.) $\pm$ 29 (syst.) ps [99]. The lifetime of the hypertriton has been

measured also at the LHC by the ALICE Collaboration in 2016 in Pb–Pb collisions at $\sqrt{s_{\rm NN}} = 2.76$ TeV finding a value of 181^{+54}_{-38} (stat.) $\pm$ 33 (syst.) ps [98]. In 2019 ALICE updated the measurement using a larger sample of data collected in Pb–Pb collisions at $\sqrt{s_{\rm NN}} = 5.02$ TeV finding a larger value, 242^{+34}_{-38} (stat.) $\pm$ 17 (syst.) ps [100].

Excluding the latest measurement of ALICE, all the measurements after 2010 are significantly below the free Λ value in contrast to what was expected. These short lifetimes can be hardly reproduced by theoretical calculations assuming the very small binding energy of 0.13 ± 0.05 MeV. Table 3.2 reports the chronology of the experimental data existing for the ${}^{3}_{\Lambda}$H lifetime, while Figure 3.3 shows the time series of the measurements compared with the PDG value of the free Λ lifetime.

The hypertriton Λ-separation energy, as previously mentioned, is expected to be strongly correlated to its lifetime, and this is also of great interest. The most accepted value of B_Λ (Equation (3.5)) relies on measurements dating back to the late 1960s and early 1970s, performed with nuclear emulsions [82, 85]; therefore, it needs to be revisited. Further experimental investigations of the hypertriton binding energy have not been performed until 2020 when the STAR Collaboration published a new measurement. They combined ${}^{3}_{\Lambda}$H and ${}^{3}_{\Lambda}\overline{\rm H}$ data under the assumption of the CPT symmetry invariance and found B_Λ to be 0.41 ± 0.12 (stat.) ± 0.11 (syst.) MeV. This value is significantly larger then the previously reported B_Λ value of 0.13 ± 0.05 MeV. However, a firm conclusion can not be reached due to the significant uncertainty of the STAR's value.

Stimulated by the recent experimental outcomes, new theoretical works have been published to reproduce these experimental results. The lifetime and the B_Λ have been calculated using a chiral effective field theory (χEFT), finding a strong correlation between the lifetime and the binding energy [102]. A strong relation between lifetime and binding energy has also been found by determining the lifetime and the partial decay width ratio R in an effective field theory approach [103]. The expected value of the decay amplitude computed for B_Λ = 0.13 ± 0.05 MeV is $\Gamma_{{}^{3}_{\Lambda}\rm H} = (0.975 \pm 0.150)\Gamma_\Lambda$ which implies a ${}^{3}_{\Lambda}$H lifetime very close to the free Λ. Considering the higher value of the binding energy measured by STAR, the lifetime is expected to be slightly reduced but the value reported by STAR of $\sim$142 ps is significantly lower than the predicted lifetime. STAR also measured the partial decay width ratio R reporting the value of R^{STAR} = 0.32 ± 0.05 (stat.) ± 0.08 (syst.) which results significantly lower than the calculations.

Thanks to the aforementioned theoretical effort, some progress has been made in understanding the hypertriton nature. New experimental data with enhanced precision on both the lifetime and the binding energy are necessary to improve the theoretical calculations, aiming to come to a conclusion. Furthermore, it has been pointed out that the solution of the so-called hypertriton puzzle may impact the understanding of the hyperonic component of the nuclear interaction [66] with implications that stretch far beyond the hypernuclear physics sector.

Year	Laboratory	Beam	Exp. method	Lifetime (ps)	Ref.
1963	LBL Bevatron	stopped K^-	He bubble chamber	105^{+20}_{-18}	[86]
1964	BNL AGS	K^- 2.3–2.5 GeV/c	nucl. emulsions	90^{+220}_{-40}	[90]
1965	BNL AGS and LBL Bevatron	K^- 2.3 GeV/c K^- 790 MeV/c	nucl. emulsions	340^{+820}_{-140}	[91]
1968	ANL ZGS	stopped K^-	He bubble chamber	232^{+45}_{-34}	[87]
1968	LBL Bevatron	K^- 1.1 GeV/c	nucl. emulsions	274^{+110}_{-72}	[92]
1969	BNL AGS	K^- 1.1 GeV/c	nucl. emulsions	285^{+127}_{-105}	[93]
1970	CERN PS	stopped K^-	nucl. emulsions	128^{+35}_{-36}	[94]
1970	ANL ZGS	stopped K^-	He bubble chamber	264^{+84}_{-52}	[88]
1973	ANL ZGS	stopped K^-	He bubble chamber	246^{+62}_{-41}	[89]
1992	Dubna	He, Li ions 2.2–5 GeV/c	digital readout	240^{+170}_{-100}	[95]
2010	BNL RHIC	Au+Au HIC 200 GeV	digital readout	182^{+89}_{-45}	[81]
2013	BNL RHIC	Au+Au HIC 7.7–200 GeV	digital readout	123^{+26}_{-22}	[96]
2013	GSI SIS	Li ions 2 GeV	digital readout	183^{+42}_{-32}	[97]
2016	CERN LHC	Pb–Pb HIC 2.76 TeV	digital readout	181^{+54}_{-38}	[98]
2018	STAR RHIC	Au+Au HIC 7.7–200 GeV	digital readout	142^{+24}_{-21}	[99]
2019	CERN LHC	Pb–Pb HIC 5.02 TeV	digital readout	242^{+34}_{-38}	[100]
2021	STAR RICH	Au+Au HIC 3.0 and 7.2 GeV	digital readout	221^{+15}_{-15}	[101]

Table 3.2: Chronology of ${}^{3}_{\Lambda}$H lifetime measurements: year, laboratory, beam, experimental method, measured lifetime and publication Reference are given. HIC stands for heavy-ions collisions and the related energy value refers to the center-of-mass energy per nucleon pair.

Chapter 4

Principles of Machine Learning

Machine learning (ML) is a branch of artificial intelligence dedicated to studying computer algorithms that can automatically solve given tasks. The algorithms are programmed to *learn* the solution through experience and by the use of data, progressively improving their performance. ML is handy in situations where the analytical solution of the problem is unknown; however, we have data with which we can build an empirical solution. This view covers many domains, and indeed ML is one of the most widely used approaches in the industry and in science nowadays.

The first part of this chapter provides the basics of Machine Learning, giving particular attention to the binary classification problem – the task addressed in this thesis. The second part presents and analyses the Boosted Decision Trees (BDTs) model employed in this thesis and the adopted training methods.

4.1 The Learning Problem

The learning problem, in general, can be seen as the task of finding the hidden relation between input data and output data.

The main components of the learning problem, are the following. The unknown target function $f : X \longmapsto Y$, where X represents the input space, and Y is the output space. The input space X is the set of all the possible input data $\vec{x}$, and the output space Y is the set of all the possible output data y. The data set D is the set of examples of the input-output relation $(\vec{x_1}, y_1), \cdots, (\vec{x_N}, y_N)$, where $y_i = f(x_i)$ for $i = 1, \dots, N$. The examples belonging to D are usually referred to as data points. Finally, the learning algorithm $\mathcal{A}$ that finds the function $g : X \longmapsto Y$ that approximates f by using the examples in D. The learning algorithm is equipped with a set of candidate functions H. The process by which the algorithm $\mathcal{A}$ selects g in H is called *training*, and H is called the hypothesis set. A hypothesis set with the associated learning algorithm is called *learning model.*

For instance, D could be a set of time-position measurements of a projectile in motion under the action of gravity only. H would be the set of all the second-degree polynomials, and A an algorithm to find the parabola that best fits the data points.

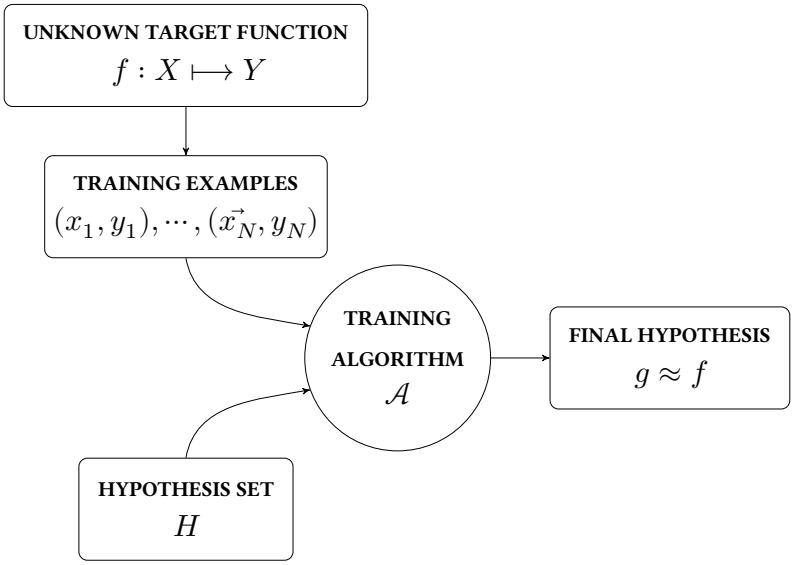

Figure 4.1: Basic layout of the learning problem.

Figure 4.1 conveys the basic layout of the learning problem and it is a simplified illustration of a vastly more complex topic. Some refinements and adaptations to this simple setup should be considered to have a complete panorama of the learning problem. However, the core of the problem will remain identical.

It would be too restrictive to think about ML just as a valid tool to describe mappings between data. The profound nature of machine learning is *predictive*, not descriptive, with very few exceptions. The learning models are designed to *generalise* the patterns learned from the training examples to unseen data. Moreover, the generalisation power is exactly what makes ML models so attractive and valuable in countless applications. The term learning itself is used precisely for this reason. The ability to accomplish tasks by generalising the patterns learned through experience to new scenarios and, eventually, the possibility to improve the performances on the tasks are conceptually analogous to what humans and other animals do.

4.2 Types of Machine Learning

The illustration of the learning problem provided in the previous section is very broad: an algorithm operates on a set of observations to unveil an underlying process. Multiple ML paradigms have emerged to address various problems and different situations. All

the paradigms share the basic concept of programming a machine to learn from data, but each has different premises and peculiarities. In this section, the main ML paradigms are introduced.

4.2.1 Supervised Learning

When the learning task provides explicit input-output examples, it consists of Supervised Learning (SL). In SL each data point is a $(\vec{x}, y)$ pair where the value of the target y_i is known for each input object $\vec{x}_i$. The training algorithm processes the labelled training data to infer the mapping between the input and the output.

In SL, the idea behind the training process is pretty straightforward. The hypothesis set H is a collection of functions h with parameters $\mathbf{w} = \{w_j \text{ for } j = 0, \dots, M\}$. Each set of possible parameters $\mathbf{w}$ defines a particular model hypothesis $h(\mathbf{w}, \vec{x})$. Therefore, for each data point, it is possible to compute the model prediction $h(\mathbf{w}, \vec{x}_i) = \hat{y}_i$. Since the pairs $(\vec{x}_i, y_i)$ are known for the training dataset D, it is feasible to assess how well $\hat{y}_i$ approximate y_i. The evaluation of the approximation quality enables tuning the parameters $\mathbf{w}$ to minimise the difference between the target value and the predicted one. Once the approximation is satisfactory, the parameters $\mathbf{w}'$ are determined, and the final hypothesis is $g(\vec{x}) = h(\mathbf{w}', \vec{x})$. The learning process can be highly complex, and the number of model parameters can be huge; however, it follows this basic concept.

From the above arise the importance of evaluating the goodness of the approximation. To assess how well g approximates f, we ought to define an error measure[1] that quantifies the distance between the model and the target function. The error measure

$$\text{Error} = E(h, f)$$

assign to each hypothesis h a value derived from the comparison with the target f. E relies on the whole h and f functions; however, f is unknown except in D. Therefore, an estimator $\widehat{E}$ - at least computable on D - is used as a proxy for E. A typical example of error estimator is the mean pointwise error. The pointwise error $e(h(\vec{x}_i), f(\vec{x}_i))$ is computed for each data points, and the estimator is the average value on D. In the light of the essential function of the error measure in the context of SL, the learning problem setup shown in Figure 4.1 is updated for the supervised learning scenario in Figure 4.2.

It is worth saying a few more words about the error measure since it plays a critical role in SL. It is of utter importance to stress that $\widehat{E}$ is used to estimate two different errors: the in-sample error E_{in} and the out-of-sample error E_{out}. E_{in} represents the estimate of the model error on the training data, while E_{out} is the estimate of the error on unseen data and can be seen as an estimate of the generalisation error. $\widehat{E}(D)$ that is $\widehat{E}$ computed on D is a reliable estimate of E_{in}; however, it could be a too optimistic

[1] The error measure is also referred to as the error *function* in the literature. Other terms are used, such as *cost*, *objective* or *loss*.

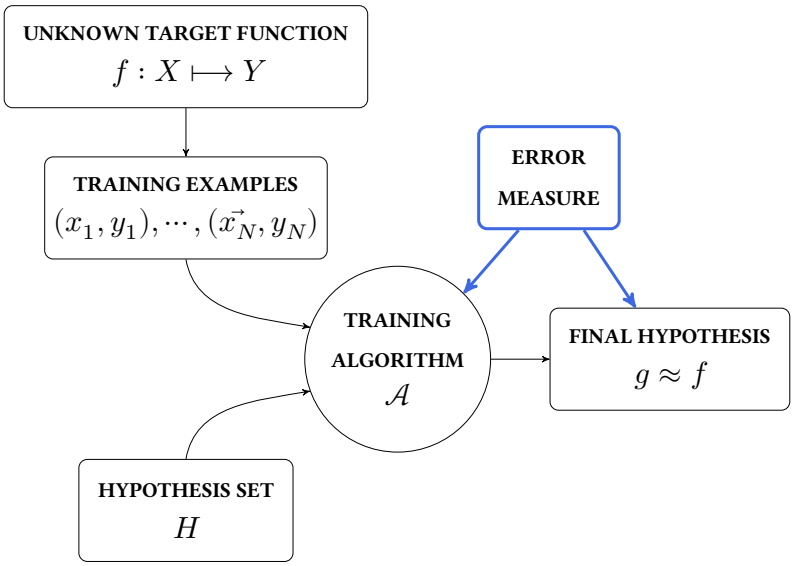

Figure 4.2: Basic layout of the supervised learning problem.

estimate of E_{out}. The training relies on the minimisation of $\hat{E}(D)$, bringing an ad hoc minimisation of E_{in}. For this reason it is reasonable to expect a larger value for E_{out}.

The key to overcoming this problem is to split D into two sub-samples: a training set (D_{train}) and a test set (D_{test}). The training set continues to feed the learning algorithm with the information needed to learn the input-output relation. Instead, the test set provides an independent sample to estimate E_{out} with the estimator: $\hat{E}(D_{\text{test}})$. It is crucial not to include any information coming from D_{test} in the training process; otherwise, the estimate of the generalisation error would be biased. $\hat{E}(D_{\text{test}})$ is only used to evaluate the expected model performance out-of-sample and can not be employed in the training.

The definition of the test set clarifies how to assess the model performance when dealing with out-of-sample data. The test set requirement is not to include any of its elements in the training process. It must be used for the estimation of $\hat{E}(D_{\text{test}})$ only. It remains unclear how it is possible to optimise the model to achieve a small E_{out}.

In fact, the minimisation of $\hat{E}(D_{\text{train}})$ does not ensure the contextual minimisation of E_{out}. The extreme consequence of this behaviour is that a model could perfectly describe the training data without any ability to make predictions on new data. If a model has enough parameters could even get $\hat{E}(D) = 0$, having at the same time a huge E_{out}. The situation where a model has too good in-sample performance at the cost of lacking generalisation power is called *overfitting*.

The clue to avoiding overfitting is twofold. On the one hand, there is regularisation, a set of techniques designed specifically for this purpose. The regularisation idea is to reduce the number of degrees of freedom of the model to limit its ability to describe

the data leading to better generalisation performances. The regularisation relies on a solid theoretical framework, the Vapnik-Chervonenkis theory [104, 105]. However, the regularisation techniques – as well as many others ML tools – are developed empirically. On the other hand, there is the possibility to reserve a portion of D_{train} to estimate the generalisation error. This sample belonging to the training set is usually called the validation set (D_{val}). The model is then optimised to minimise $\hat{E}(D_{\text{val}})$ during the different training phases. $\hat{E}(D_{\text{val}})$ provides a biased estimate of the generalisation error but allows the model optimisation. Once the model is optimised, the test set – that remains entirely independent – is available for the unbiased estimate of the error out-of-sample.

Many different techniques have been developed to optimise an ML model using a validation set. However, they follow the same simple concept. A portion of the available data is reserved for estimating the generalisation error to assess the model performances out-of-sample. This portion of the data is not included in any phases of the optimisation and training of the model. Instead, the other data are dedicated to the model training and optimisation. Usually, the optimisation relies on the minimisation of a proxy for the out-of-sample error that is computed on a sub-sample of D_{train} called validation set. This proxy is a biased estimate of E_{out}; nevertheless, it enables the model optimisation.

4.2.2 Unsupervised Learning

In the unsupervised learning (UL) domain, the output associated with the data points – i.e. the value of y – is unknown. UL can be regarded as the task of spontaneously uncovering structures and patterns in the data. The model aims to construct a representation of the data and obtain valuable information from the representation. UL models are successfully operated in many applications, among the main are:

- clustering;
- anomaly detection;
- latent variable models.

4.2.3 Reinforcement Learning

Reinforcement learning (RL) is a ML area regarding learning tasks where the explicit relation between input and output is unknown, just like unsupervised learning. However, RL concerns the implementation of intelligent agents (IA) – i.e. any object that senses the environment and acts autonomously to reach a goal – able to act in a defined environment to maximise the reinforcement signal, also called *reward*. RL mimic the behaviour of biological systems in learning comportments by receiving positive or negative feedback from the environment – such as pain or pleasure – in response to actions.

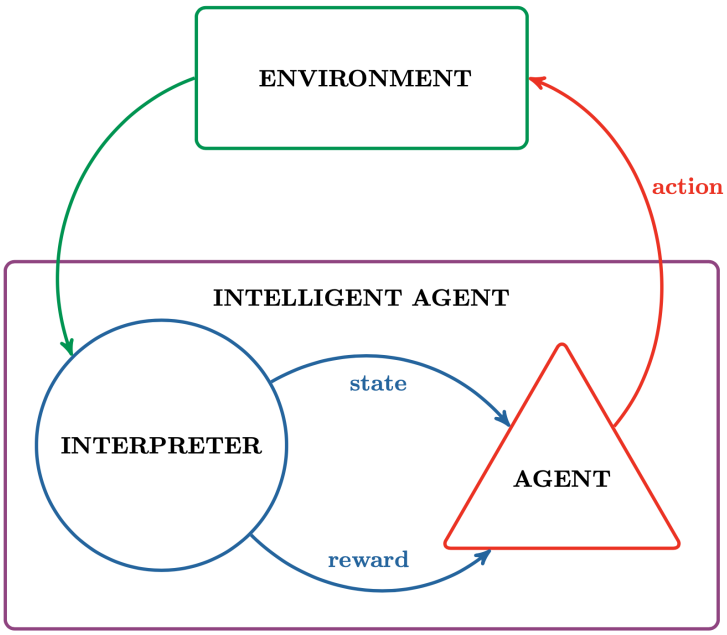

Figure 4.3: Typical layout of the reinforcement learning scenario.

A typical scenario in reinforcement learning is presented in Figure 4.3. The IA perceives the environment and interprets it in the form of states and rewards. The state is nothing but the system configuration, while the rewards measure the goodness of the state, given the IA goal. Based on the system state, the agent act on the environment, trying to maximise the future reward. The agent does not take into account the present reward only. IA considers a cumulative reward for promoting a series of rewarding moves instead of single advantageous actions. A *policy* is the set of the agent actions, based on the environment states, intended to maximise the future reward. Once the IA has gained enough experience in the environment, it has developed an optimal – or nearly optimal – policy.

RL demonstrated outstanding performances in tackling problems where exploring all the possible configurations of the systems is unfeasible from a computational point of view. Autonomous driving[108] and playing games[109] are among the fields where RL is widely applied. The most famous RL application is AlphaGo Zero[110], a software developed by DeepMind that learned to play Go[2], *tabula rasa*, achieving superhuman proficiency.

[2]Go is a Chinese strategy board game for two players. The goal of the players is to surround the opponent's territory. It is incredibly complex, despite being based on simple rules. The game board is estimated to have $\sim 2.1 \times 10^{170}$ allowed configurations [106]. Go is way more complex than the chess game – which has a number of legal configurations between 10^{40} and 10^{50}[107].

4.3 Binary Classification Problem

Classification is the recognition and grouping of a population into predefined sub-groups called *categories* or *classes*. The grouping is based on given attributes – also called *features* – of the population elements. The task is called clustering when the sub-populations are unknown a priori – i.e. in an unsupervised learning context. Another and more abstract way of thinking about classification is that it is involved when the output space Y consists of categorical variables.

In supervised learning, classification is a prevalent task. Exploiting pre-classified data, the model detects patterns and structures in the input, learning the correct classification. The goal – as always in ML – is not just to learn patterns; instead, it consists in extrapolating what is learned from the training to new and unseen data. There is a broad spectrum of ML models to classify data ranging from simple decision trees to extremely complex convolutional neural networks with billions of parameters. In addition, the scope of the application of these models is very broad, ranging from email spam filters to super-human proficiency image classification.

The most straightforward classification problem is binary classification when the target categories are just two. This thesis aims to apply a ML model to the task of selecting hypertritons from the background. It is, therefore, a binary classification problem.

4.3.1 Assessing Performances in Binary Classification Tasks

The confusion matrix (CM) is the starting point for assessing the model performances in every binary classification task. The CM is a table layout that returns a representation of a classifier performance. The matrix rows denote the instances of the true values, while the columns denote the predicted values. The value C_{ij} - element on the i-th row and j-th column - is the number of data points belonging to the i class to which the model assigned the j class. Figure 4.4 reports an example of the confusion matrix. It is worth mentioning that the CM is usually expressed in terms of two classes: Positive and Negative. This nomenclature derives from the medical diagnostic, a field that extensively uses CM.

From the definition of the CM elements, follow that:

- TP is the number of True Positive that are the Positive data classified as Positive by the model;
- FP is the number of False Positive that are the Negative data classified as Positive by the model – therefore, a misclassification error;
- FN is the number of False Negative that are the Positive data classified as Negative by the model – therefore, a misclassification error;
- TN is the number of True Negative that are the Negative data classified as Negative by the model.

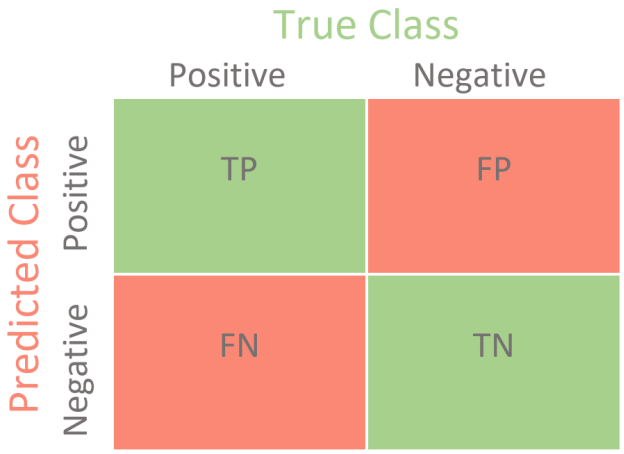

Figure 4.4: Layout of the confusion matrix.

This matrix is so important because starting from the matrix elements it is possible to define many metrics used to assess the performance of a classifier. Different behaviours characterise every metric in different conditions, and the choice of the specific metric is task-dependent. It is worth mentioning some metrics which, either directly or indirectly, are employed in this thesis:

- True Positive Rate or *sensitivity*: being P the number of Positive in the given sample $\mathrm{TPR} = \mathrm{TP}/\mathrm{P}$;
- True Negative Rate or *specificity*: being N the number of Negative in the given sample $\mathrm{TNR} = \mathrm{TN}/\mathrm{N}$;
- False Positive Rate or *fall-out*: $\mathrm{FPR} = \mathrm{FP}/\mathrm{N} = 1 - \mathrm{TNR}$.

Another widely used metric is the Receiver Operating Characteristic (ROC) curve and the value of its Area Under Curve (AUC): the ROC AUC. Since it is the metric employed in this thesis to assess the classification performance of the models, it is worth spending a few words on the ROC AUC.

To explain the ROC AUC and how it is computed, it should be anticipated that many classifiers do not assign the class directly to a data point. They assign a number – called *score* in this thesis – to each data point that is proportional to the probability to belong to the target class, assigned to the specific input. After that, the final classification relies on an external decision of the classification threshold: the data points with a score above the threshold are considered Positive, the others negative. The choice of the classification threshold is not trivial and can be done with different approaches. However, it must be said that usually, it is not done by the model itself but it is in charge of the user.

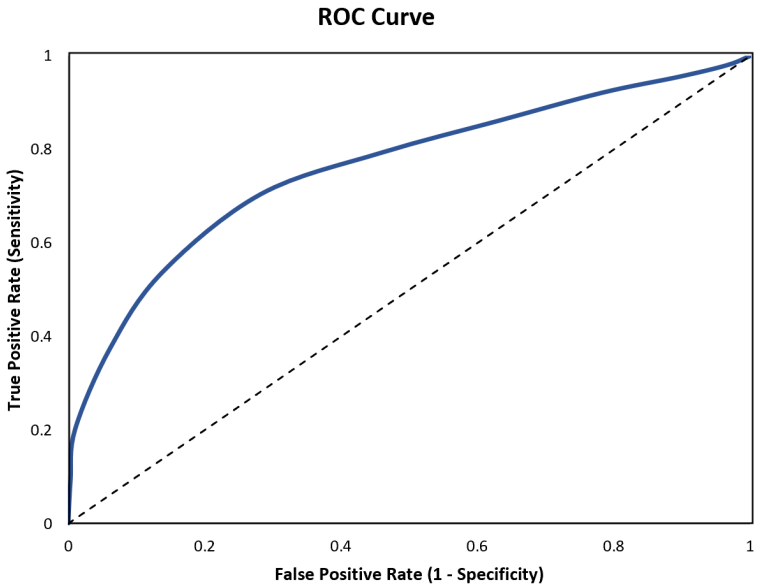

Figure 4.5: Example of a ROC curve.

The ROC curve is built by plotting the points with coordinates (TPR, FPR) as a function of the classification threshold in a plane where FPR is the x-axis and TPR is the y-axis. Figure 4.5 shows a basic example of a ROC curve. The AUC is the value of the area between the curve and the x-axis. It ranges from 0.5, corresponding to a random classifier, to 1 in the case of a perfect classifier. The advantages of using the ROC AUC are basically two. It is not dependent on the specific threshold used for the final classification, instead gives a global estimation of the performance. It does not depend on the relative abundances of the classes in the data sample. It is for these reasons that the ROC AUC is employed in the analysis described in this thesis.

4.4 BDTs for Classification

The ML model used in this thesis is the Boosted Decision Trees (BDTs). This section briefly presents the BDTs, also giving some insight into its learning algorithm and the optimisation of this class of models.

4.4.1 The BDTs and its learning algorithm

The BDTs [111] is a class of ML models widely employed for regression and classification tasks. The BDTs is an ensemble model based on simple Decision Trees (DT). A Decision Tree is a flowchart-like system of nodes, each defining a test on a single attribute of the data points. In each test, the attribute is compared with a threshold value

– or against a set of possible values if the attribute is categorical. After a series of tests, each tree branch ends with a terminal node – usually called a leaf – that represents a class label. From the root to the leaf, the paths followed by the data represent the classification rules. Figure 4.6 shows a basic example of a DT, where the green leaves represent the Positive class and the red leaves the Negative class.

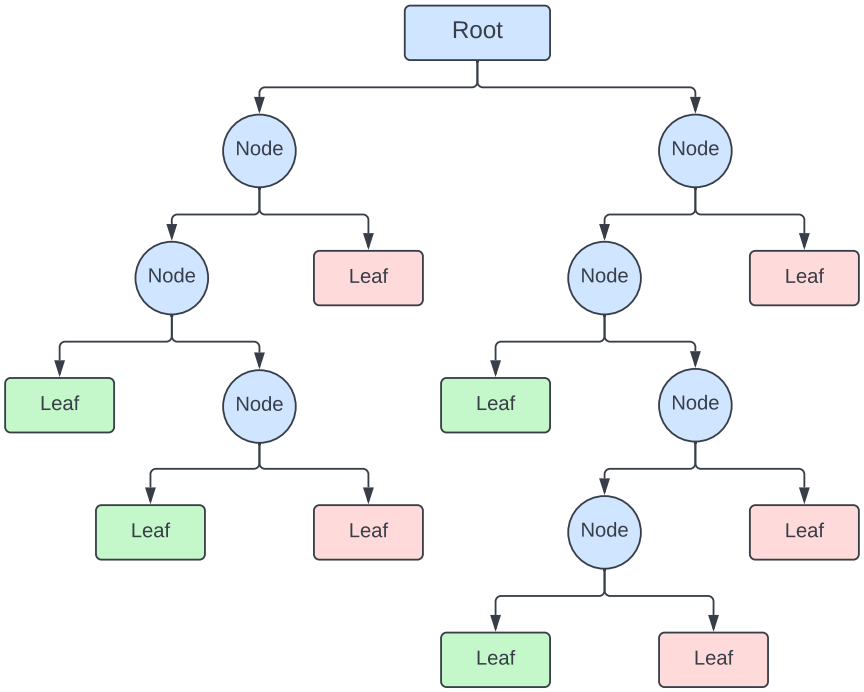

Figure 4.6: Example of Decision Tree. Each node corresponds to a test on a single attribute of the data points. After the node, the data are split according to the test outcome. The green leaves are related to the Positive class, and the red leaves to the Negative class.

The training algorithm of a DT is described in the following. The tree is built by selecting recursively the attribute of the data that maximises the class separation after the node split. The data are partitioned again and again by building new nodes until a user-defined condition is reached.

A tree with enough nodes can always classify a training set correctly. However, such a tree would have poor generalisation performances. Therefore a DT is considered a weak learner.

The *boosting* technique [112] has been applied to the DTs to overcome this weakness, obtaining a much more reliable and robust ML model: the Boosted Decision Trees. The boosting sequentially builds a series of trees in which each one is built to take care of the data points misclassified by the previous one. This is done by weighting the data

points and giving a higher weight to the misclassified data. The trees are built until the algorithm fulfils a user-defined condition. The final model is the ensemble of the single trees, and the output of the model is a weighted mean of the single tree outputs, where the weights are connected to the classification performances of each tree. The ensemble model outperforms the single tree in generalisation power thanks to the boosting.

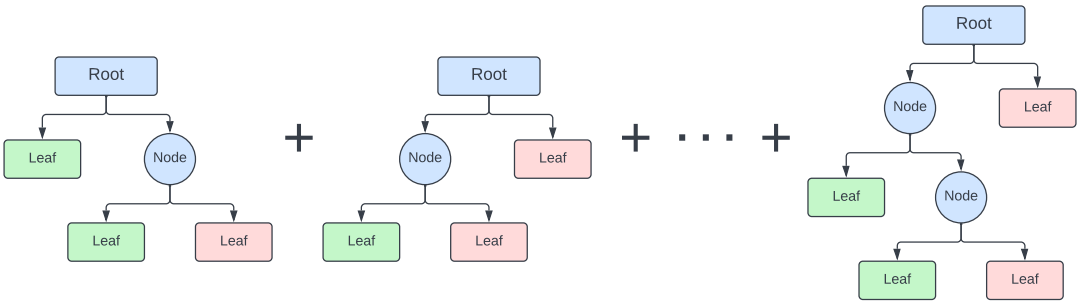

Figure 4.7: Example of a Boosted Decision Trees model. The single DTs are built recursively to compensate for the previous tree classification error. The final model is a succession of very simple DTs, each providing an output for each data point. The output of the ensemble model is a weighted mean of the single outputs, and the weights are connected to the classification performance of each tree.

The BDTs, like every ML model, have a set of parameters that are not tuned during the training process called hyperparameters. These parameters steer the training process and the regularisation of the model. They determine the maximum depth and number of the DTs and many other aspects of their structure. Furthermore, they are involved in regulating the random process used to diversify the single trees and its related to the regularisation of the model.

It is crucial to tune the hyperparameters properly to take full advantage of the BDTs' performances since the optimal set of hyperparameters is task-dependent.

4.4.2 Cross-Validation for hyperparameters tuning

There are many ways to perform the hyperparameter optimisation of a ML model. However, all of them share the same basic process. The idea is to define a metric - also called objective function - to assess the model out-of-sample performance and to study how the metric variates as a function of the hyperparameters.

This process involves two crucial factors. The first is the definition of the objective function; the second is the implementation of a strategy to explore the hyperparameter space. The objective function is function $o : S_P \longmapsto \mathbb{R}$ which returns a real value for each set P of hyperparameters belonging to the hyperparameter space S_P. In this Section the cross-validation method to compute the metric and evaluate the model performance employed in this analysis will be described. Instead, the following Section

presents the Bayesian Optimisation, a state-of-the-art technique to efficiently explore the hyperparameter space.

In Section 4.2.1, the performance assessment problem has already been introduced, highlighting the necessity to use a validation set. The validation set allows estimating the model performance and using this estimate to drive the model optimisation. The test set is not involved in this process. It remains independent and is used after the optimisation to evaluate the final model.

Cross-validation (CV) [113] is a class of model validation techniques for the generalisation performance assessment. CV uses different, randomly-defined complementary data portions to train and validate the model in various iterations. First, the training set is split into k subsets or folds. Then in k iterations, the model is trained on $k-1$ subsamples and validated on the remaining one; the left-off sample is different at each iteration. The validation produces an error/loss for the model in each iteration on a different data set. Finally, the CV error/loss is the k-average of the single errors/losses.

The CV allows validating the model against all the available data, obtaining a reliable estimate of the generalisation performance. In fact, the multiple rounds of training and validation using different data samples reduce the error/loss estimate variability. Figure 4.8 shows an example of a 7-fold data partitioning for CV. The orange rectangles represent the validation set left off the training in each iteration, while the blue rectangles represent the training data in each iteration.

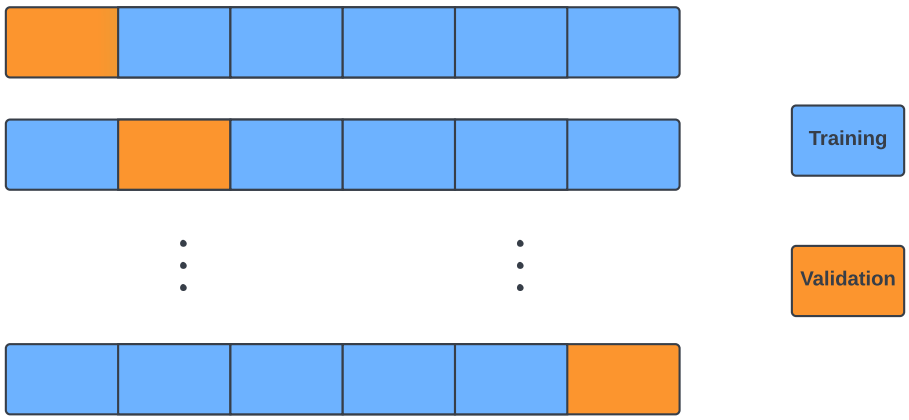

Figure 4.8: Example of the train/validation data split in 7-fold cross-validation. Blue rectangles represent the training data in each iteration, while the orange rectangle is the validation set.

4.4.3 Bayesian Optimisation of the Hyperparameters

In this analysis, the hyperparameter optimisation strategy - i.e. the policy for the hyperparameter space exploration - is done using a *Bayesian Optimization* (BayesOpt)

algorithm [114].

In general, BayesOp allows to explore the domain D of an unknown *target function* $f(\vec{x})$ – that is, however, possible to evaluate on any given value $\vec{x} \in D$ – looking for the maximum of f in as few iterations as possible. The Bayesian strategy is to treat f as a random function since it is unknown and assign a *prior probability* to it. The prior encodes the beliefs about the function behaviour. The target function is evaluated on a defined number (N_{init}) of random points, obtaining a set of observations of f. These observations are treated as data points to build the posterior distribution of functions that best describes f. The posterior distribution is used, in turn, to construct an *acquisition function* that estimates the most probable position of the maximum ($\vec{x}_{\text{guess}}$) based on the available observations of the objective function. Then f is evaluated on $\vec{x}_{\text{guess}}$ and the posterior is updated with the new observation of f. The posterior improves with the increase of the number of iterations, and the acquisition function becomes more confident about which regions in D are worth exploring to find the maximum. This process is repeated for a defined number of iterations (N_{iter}) or until it reaches a user-defined condition.

There are many possible methods to define and build the prior/posterior distributions, the most common is the Gaussian Process [115], which is employed in this thesis. Bayesian optimisation is a general method for function optimisation and can be easily adapted to the hyperparameter optimisation task by identifying the target function of the optimisation with the error/loss function of the ML model.

BayesOpt proved to be more efficient than other optimisation tools based on a random sampling of the hyperparameter space. In fact, BayesOpt improves the description of the target function in each step and uses this knowledge to improve the research of the best hyperparameters. Therefore, in a defined number of iterations N_{iter}, it ensures having a better chance to find an optimal or near-optimal set of hyperparameters than a random search in the same number of iterations.

Chapter 5

(Anti)Hypertriton Identification in ALICE Reconstructing the 2-body Decay

The previous chapter discussed the importance of a new and more precise measurement of the hypertriton lifetime and Λ-separation energy. This thesis aims to perform the most precise measurement of the hypertriton lifetime and revisit the B_Λ value by analysing the data collected with the ALICE experiment.

The starting point for these measurements is reconstructing the 2-body decay of the (anti)hypertriton. First, the decay products are identified, and all the possible (anti)hypertriton candidates[1] are built by pairing the possible combinations of the decay products. Then, a set of BDTs Section 4.4 is trained on dedicated data to discriminate between signal (real hypertritons) and background (combinatorial background). Finally, the BDTs are used to select the candidates, obtaining a high purity sample of the identified (anti)hypertritons.

ML-based classifiers are intended to boost the classification performances with respect to standard kinematic and topological selections on the hypertriton candidates. The goal is to obtain a high signal selection efficiency – that is the true positive rate (TPR) or *sensitivity* – having a high background rejection efficiency – that is the true negative rate (TNR) or *specificity*.

This chapter discusses the analysis methods used in these steps and the study of the performances of the analysis method itself, using dedicated Monte Carlo data samples.

[1] In this thesis the term *hypertriton candidate* or ${}^{3}_{\Lambda}H$ *candidate* refers to each pair of ${}^{3}\mathrm{He} + \pi^-$ and ${}^{3}\overline{\mathrm{He}} + \pi^+$ tracks, with the associated hypothetical decay vertex and mother particle.

Note: naming convention

The CPT theorem [116] states that the physical laws are symmetric under the simultaneous operations of charge conjugation (C), parity transformation (P) and time-reversal (T). This implies that particles and antiparticles have the same mass and lifetime but opposite charge and magnetic moment. The CPT symmetry of the hypertriton has been tested recently by the STAR Collaboration [117], so it is fair to assume it as the working hypothesis of this thesis. Therefore, in this analysis, hypertriton and antihypertriton are generically referred to as hypertriton or ${}^{3}_{\Lambda}\mathrm{H}$ for simplicity. By the same principle, the hypertriton decay products are referred to as ${}^{3}\mathrm{He}$ and π. Explicit reference is made only when necessary to avoid ambiguity and explain particular differences. The same applies to the other particle species mentioned in this chapter and the following ones. Unless necessary, both particles and antiparticles are referred to by the particle name and symbol for simplicity.

5.1 Data and Monte Carlo Samples

The work presented in this thesis is based on the data collected by the ALICE experiment in the winter of 2018 during the LHC runs dedicated to the heavy-ion programme. In this data taking period the LHC delivered Pb–Pb collisions at $\sqrt{s_{\mathrm{NN}}} = 5.02\,\mathrm{TeV}$ and with a high interaction rate of 1–8 kHz for a total of 248 LHC runs [118].

The data were collected with a combination of a minimum bias (MB) trigger and an online selection to enhance the recording of the most central (0–10 %) and semi-central (30–50 %) collisions. The MB trigger is given by the coincident signals of the V0A and V0C detectors, while the online selection is based on the sum of the signal amplitudes of the V0 detectors.

An additional offline selection is applied to reduce possible biases from particular data taking conditions and it is discussed in more details in the next section (Section 5.2). After the offline selection the data sample consist of about 2.79×10^{8} MB events. Figure 5.1 shows the centrality distribution of the events used in this analysis, with the 0–10 % and 30–50 % centrality classes enhanced by the online event selection.

The Monte Carlo simulations[2] play a crucial role in this thesis. The machine learning models deployed to select the hypertritons are trained and tested on a data and MC simulation combination. Furthermore, the analysis performances and systematic uncertainties study employ the MC data. The simulations are based on a complete and detailed description of the geometry of the whole ALICE apparatus and the response of the detectors. They are tuned to reproduce the experimental conditions of the different

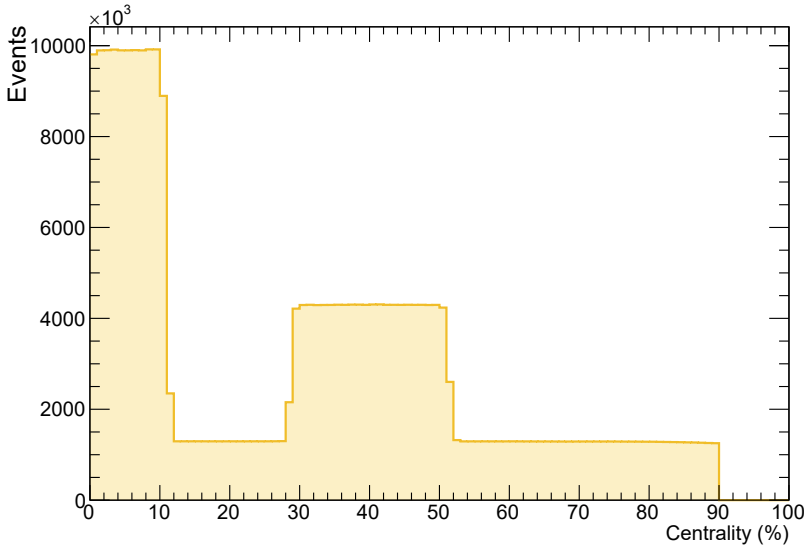

Figure 5.1: Centrality distribution Pb–Pb collisions at $\sqrt{s_{\mathrm{NN}}} = 5.02\,\mathrm{TeV}$ used in this thesis.

detectors along the data taking period.

The Monte Carlo data are obtained by simulating a number of ${}^{3}_{\Lambda}\mathrm{H}$ decays on top of Pb–Pb collisions that are simulated independently. The hijing generator [119] is used for the underlying Pb–Pb event, while an *ad-hoc* generator is used for the injection of the ${}^{3}_{\Lambda}\mathrm{H}$ decay in the event. In order to reproduce the centrality distribution of the data (Figure 5.1), the MC sample has been split into three sub-sample according to the centrality and each sub-sample has a flat centrality distribution. The three sub-sample reproduce the 0–10 %, 10–30 % and 30–50 % centrality classes of the real data and are composed by 1.2×10^5, 4×10^5 and 4×10^5 MC events, respectively.

Since little is known about the production spectra of the hypernuclei in HIC, their kinematics is arbitrarily determined. The transverse momentum p_{T} is extracted from a uniform distribution in the 0 to $10\,\mathrm{GeV}/c$ interval. Also the azimuthal angle φ and the rapidity y are extracted from an uniform distribution, in the 0 to 2π and -1 to 1 intervals, respectively. In each simulated Pb–Pb collision 20 ${}^{3}_{\Lambda}\mathrm{H}$ and 20 ${}^{3}_{\Lambda}\overline{\mathrm{H}}$ decaying into the 2-body channel are injected.

Once the kinematics of the particles is simulated they are propagated through the ALICE apparatus using the GEANT3 transport code [53]. This includes both particles

[2] In this thesis the terms *Monte Carlo data* or *MC data* refer to Monte Carlo simulations used to mimic real data.

produced in the decay of the (anti)hypertritons and particles belonging to the underlying event. The GEANT4 toolkit [54–56] is used to cross-check the performances of the simulations and for the study of some components of the systematic uncertainties as will be described later.

5.2 Offline Event Selection

Identifying the hypertriton decay in a heavy-ion collision is particularly challenging due to the large combinatorial background. In order to reduce the background and avoid the analysis of low-quality data, further selections on the recorded events are applied offline. The set of offline event selections used in this analysis and described in the following is the standard set used to analyse the Pb–Pb collisions in ALICE. Thus it is tested and validated by many analyses, ensuring a high-quality sample of events.

The background events caused by the machine-induced beam-gas interactions are discarded using the timing information provided by the ZDC (Section 2.3.5) and V0 (Section 2.3.3) detectors. After the primary vertex reconstruction – described in Section 2.5.2 – the events with a reconstructed primary vertex outside a ± 10 cm region around the nominal position, along the beam direction, of the interaction point are rejected ($|V_z| < 10$ cm). This ensures symmetric geometrical acceptance of the detectors, allows each ITS layer to have a $|\eta| < 0.8$ pseudorapidity coverage, and helps to discard satellite collisions.

Because of the high interaction rate delivered by the LHC during the 2018 data taking, a significant part of the events, named as *pile-up events*, contains more than one primary vertex. The pile-up events are rejected by applying a selection based on the tracklets used to build the SPD vertex. After finding the first vertex, the algorithm tries to build a new vertex using the SPD tracklets not pointing to the primary vertex. If a second vertex is found, the selection is applied to the number n of tracklets contributing to the secondary vertex. If n is larger than an event-dependent threshold, the event is tagged as a pile-up event and rejected. Since previous analyses have shown a multiplicity dependence of the false-positive rate of pile-up events, the threshold on n depends on the total number of tracklets in the event. It is set to 3 for the events with less than 20 tracklets, to 4 for the events with tracklets number ranging from 20 to 50 and for all the remaining events it is set to 5. This criterion removes the pile-up due to multiple vertices in the same bunch crossing[3] and out-of-bunch pile-up within the SPD readout time of 300 ns. However, this method based on the SPD vertex finding is not able to identify pile-up vertices closer than 8 mm along the beam direction due to the finite spatial resolution of the SPD detector.

[3]The bunch crossing is defined as the time at which two particle bunches – whether they are protons or ions – coming from the LHC beams cross each other at the ALICE interaction point.

Other selections based on the correlations between centrality estimators help reduce the effect of the pile-up and reject events with multiple vertices that were not rejected by applying the SPD cut. The number of clusters in the innermost layer of the SPD (CL0) correlates to the V0M centrality estimator. The outliers of the CL0-V0M correlation are interpreted as residual pile-up events and discarded. Another selection is applied to the correlation between the V0M amplitude and the number of SPD tracklets; this final selection cleans up the correlation between the two centrality estimators. The outliers are suppressed with a request of a $5\ \sigma$ selection on the correlations mentioned above (Figure 5.2).

One apparent effect of the multiple vertices pile-up is the presence of spikes in the distribution of the z coordinate for the reconstructed vertices as visible in Figure 5.3a. When the pile-up rejection based on the SPD vertex fails to resolve two vertices, the vertex finding algorithm based on the full tracks information is not able to determine the correct primary vertex position[4]. This effect is suppressed by a selection of the difference along the z between the SPD vertex and the tracks vertex ($|\Delta V_z|$). For multiple vertices events, $|\Delta V_z|$ is large due to the incorrect vertex position determined by the tracks algorithm. Therefore a selection based on the resolution of the two vertex finder algorithm can reject multiple vertices events. In particular $|\Delta V_z| < 10\ \sigma_{SPD}$ for the SPD vertex and $|\Delta V_z| < 20\ \sigma_{tracks}$ for the tracks vertex where σ_{SPD} and σ_{tracks} are the resolutions of the SPD vertex and the track based vertex, respectively. Moreover, $|\Delta V_z| < 0.2\,\text{cm}$ is required to improve the quality of the selected data sample.

Variable	Selection
$\lvert V_z\rvert$	$\leq 10\,\text{cm}$
|V0M–CL0|	$\leq 5\ \sigma$
|V0M–$n_{tracklets}$|	$\leq 5\ \sigma$
$\lvert\Delta V_z\rvert$	$\leq 20\ \sigma_{track}$
$\lvert\Delta V_z\rvert$	$\leq 10\ \sigma_{SPD}$
$\lvert\Delta V_z\rvert$	$\leq 0.2\,\text{cm}$

Table 5.1: Summary of the event selection applied for the pile-up rejection and to increase the quality of the data sample.

Figure 5.2 shows the correlations between the centrality estimators V0M and CL0 and between the number of SPD tracklets and V0M before (Figure 5.2a and Figure 5.2c respectively) and after (Figure 5.2b and Figure 5.2d respectively) the event selection. Figure 5.3, similarly, shows the V_z and ΔV_z distributions before (Figure 5.3a and Figure 5.3c

[4]This behaviour could be explained by the failure of the analytical minimisation procedure used to find the global minimum in the vertex finding process.

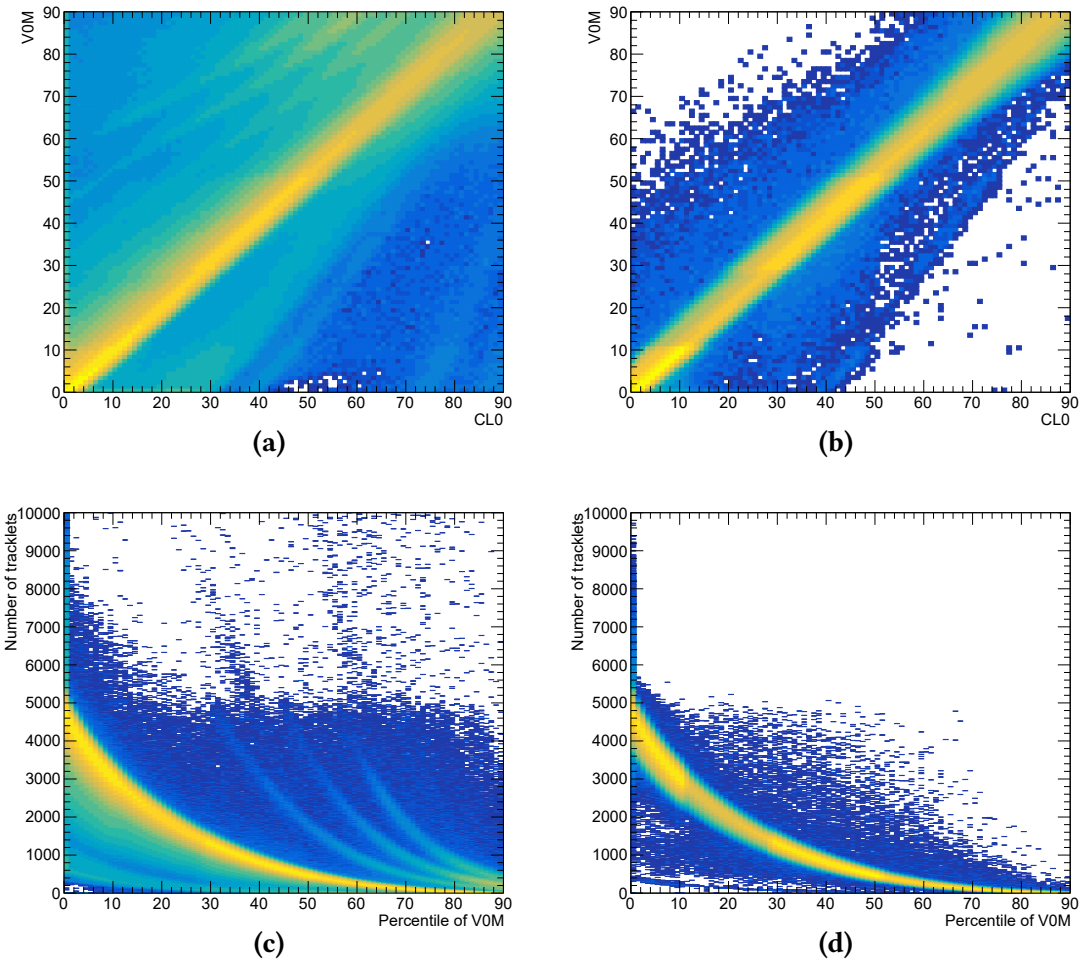

Figure 5.2: Correlation plots between different centrality estimators. (top row) Correlation between the CL0 centrality estimator – proxy for the number of clusters in the SPD innermost layer – and the V0M centrality estimator; (bottom row) correlation between the number of tracklets reconstructed in the SPD and the V0M estimator. The left column (a and c) shows the correlations before the event selection, while the right column (b and d) shows the correlations after the event selection, highlighting the cleaning effect of the event selection.

respectively) and after (Figure 5.3b and Figure 5.3d respectively) the event selections. Table 5.1 summarises the set of event selections used in this analysis.

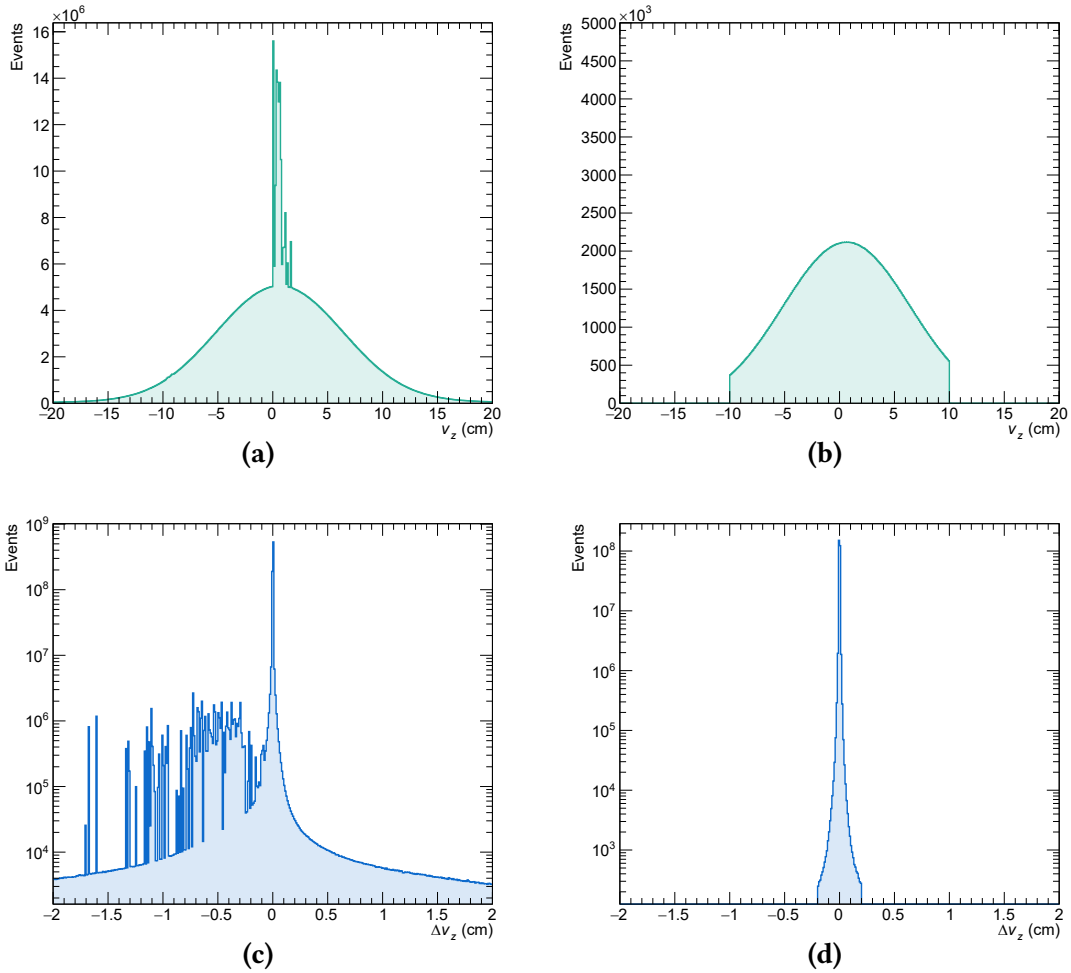

Figure 5.3: Distribution of the vertex position along the z axis (top row) and the difference between the z vertex reconstructed with the track based and the SPD only vertex finding algorithms (bottom row). The left column (a and c) shows the distributions before the event selection, where the spikes indicate pile-up events; while the right column (b and d) shows the distributions after the event selection, highlighting the cleaning effect of the event selection.

5.3 Track Selection

This section presents the set of selections applied for each track used in the analysis. The precise tracking of the ${}^{3}_{\Lambda}\mathrm{H}$ decay products and their identification is of utter importance in this analysis. Therefore, these selections aim at rejecting low-quality tracks in terms of momentum and $\mathrm{d}E/\,\mathrm{d}x$ resolution and reliability of the track fitting procedure.

The tracks outside the pseudorapidity region $|\eta| < 0.8$ are rejected to ensure using only the geometrical region in which the ALICE detectors can perform the full tracking

and provide the highest quality PID information. In addition, it is required to each track to have at least 50 clusters in the TPC to guarantee a momentum resolution of 2 % and a ∼6 % resolution on the $\mathrm{d}E/\,\mathrm{d}x$ used for the PID. A successful TPC refit is also required for the selected tracks, and the χ^2 per TPC cluster, computed during the track fitting procedure, is required to be ≤ 4. Finally, tracks coming from weak decays involving neutral particles in the final state are rejected by a routine that looks for rapid changes in the track momentum (kink topologies). Table 5.2 summarises the set of track selections used in this analysis.

Track selections
$\lvert\eta\rvert < 0.8$
$n_{\text{TPCcluster}} \geq 50$
$\chi^2/n_{\text{TPCcluster}} \leq 4$
Kink topology rejected

Table 5.2: Summary of the selections applied to the analysed tracks.

5.4 Reconstruction of the (Anti)Hypertriton Candidates

Once the events and the tracks are selected, the next step in the analysis is to reconstruct the ${}^{3}_{\Lambda}\mathrm{H}$ candidates. This is done in two phases, event-by-event.

First, the possible decay products belonging to the same event – that are the ${}^{3}\overline{\mathrm{He}}$, ${}^{3}\mathrm{He}$, π^+ and π^- – are identified exploiting the PID capabilities of the TPC detector. Additional selections, based on the study of the Monte Carlo data, are applied to the tracks depending on the particle species. Then, the ${}^{3}\mathrm{He} + \pi^-$ and ${}^{3}\overline{\mathrm{He}} + \pi^+$ pairs are matched combining – within the same event – each ${}^{3}\mathrm{He}$ track with every π^- track and each ${}^{3}\overline{\mathrm{He}}$ track with every π^+ track. Finally, for each pair the hypothetical decay vertex[5] and the hypothetical mother particle are reconstructed. Further selections are then applied to reject unlikely decay vertices.

The purpose of this part of the analysis is to define the set of ${}^{3}_{\Lambda}\mathrm{H}$ candidates to be used in the data analysis. The actual selection of the ${}^{3}_{\Lambda}\mathrm{H}$ is done in a further step with the use of BDTs models. Therefore, the selection criteria applied at this level of the analysis are quite loose, since it is crucial to have the highest number of real ${}^{3}_{\Lambda}\mathrm{H}$ – i.e.

[5]The *decay vertex* is usually referred as *secondary vertex*, as already mentioned in Section 2.5.2. Therefore, in the context of this thesis *decay vertex* and *secondary vertex* are to be considered synonyms.

high TPR – even at the cost of including a sizeable percentage of background –i.e. high *false positive rate* (FPR). In fact, the background is widely rejected at the BDTs level.

In the following sections (Section 5.4.1 and Section 5.4.2) a detailed description of the methods used to identify the decay products and to reconstruct the decay vertices and the mother particles is given.

5.4.1 Identification of the Decay Products

The identification of the daughter particles[6] is performed track-by-track, using the TPC measurement of the specific energy loss ($\mathrm{d}E/\,\mathrm{d}x|_{TPC}$) in the detector gas (Section 2.6.1).

The $n\sigma_{TPC}$ variable is defined for each track as the deviation of the $\mathrm{d}E/\,\mathrm{d}x$ measured in the TPC ($S_{measured}$) from the expected value for the species i ($S^i_{expected}$), in terms of the detector resolution ($\sigma^i_{expected}$):

$$n\sigma_{TPC} = \frac{S_{measured} - S^i_{expected}}{\sigma^i_{expected}} \tag{5.1}$$

and it is used to select the sample of particles identified as belonging to the i species. The expected values of the TPC response as a function of p_{T} for the different particle species are parametrised as splines. The splines are stored in the ALICE Offline framework and are shared among the different analyses.

The TPC is the primary detector used for the identification of low-to-mid momentum particles in ALICE, and usually, a $|n\sigma_{TPC}| \leq 3$ selection is applied to select a defined species. This selection also leads to considerable sample contamination in the case of case of multiple minimum ionising particles (MIP) in the considered momentum range – e.g. π^+,π^- and K^+,K^- for $p > 1\,\mathrm{GeV}/c$. The information provided by other detectors is usually integrated to enhance the PID performance and suppress this contamination. However, it is not crucial to avoid sample contamination in this phase of the analysis since the discrimination between true hypertritons and fake candidates is subsequently done at the BDTs level. Therefore a $|n\sigma_{TPC}| \leq 5$ selection is applied to both the species we are interested in, ^{3}He and π.

The problem of the sample contamination concerns mainly the pions. The expected $\mathrm{d}E/\,\mathrm{d}x|_{TPC}$ for the ^{3}He, is very well separated from those of the other particle species for $p > 1\,\mathrm{GeV}/c$, thanks to its electric charge $z = \pm 2$. The Bethe–Bloch formula [4, Chapter 34.2] for the specific energy loss shows that the $\mathrm{d}E/\,\mathrm{d}x$ depends on z^2. Contamination from the ^{4}He is expected but is negligible because of its low production yield. ALICE preliminary results [120] show that it is about 2 orders of magnitude lower with respect to the ^{3}He yield. In the low rigidity region, the specific energy loss

[6] The term *daughter particles* refers to *decay products* and the two terms are considered synonyms

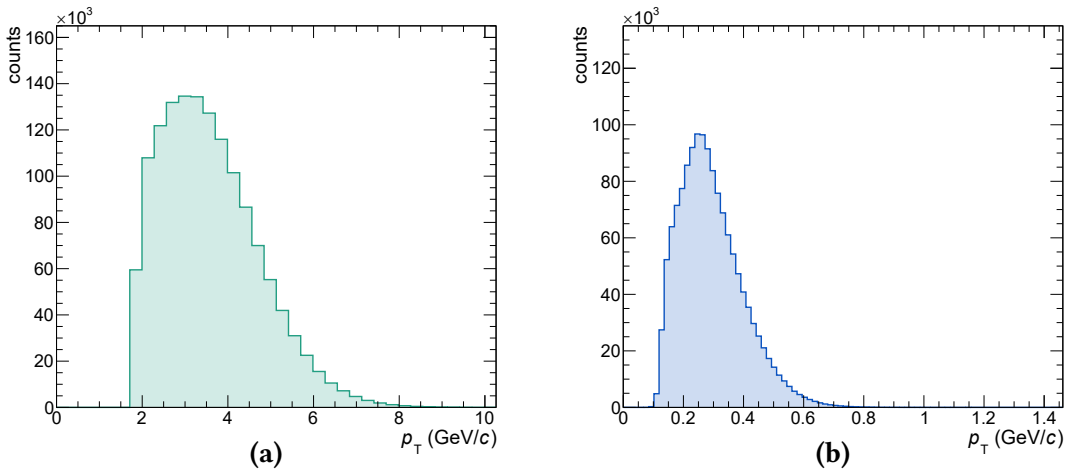

Figure 5.4: Transverse momentum distribution of the decay products – ^{3}He in the left panel (a) and π in the right panel (b) – of the reconstructed (anti)hypertritons in the Monte Carlo data.

of the ^{3}H becomes similar to that of the ^{3}He, thus leading to contamination in the low momentum region.

Monte Carlo data shows that the p_T spectrum of the ^{3}He produced by the $^3_\Lambda$H decay (Figure 5.4a) is bounded below by $\sim$ 1.7 GeV/c. Thus, $p_T \geq 1.7$ GeV/c is required for the ^{3}He tracks. The p_T spectrum of the daughter $(\pi^+)\pi^-$ (Figure 5.4b), similarly, is bounded below at $\sim$ 0.1 GeV/c and $p_T \geq 0.1$ GeV/c is required for the $(\pi^+)\pi^-$ tracks. The DCA to primary vertex (DCA_{pv}) distributions, instead, are bounded above as shown in Figure 5.8. Thus, $DCA_{pv} < 8$ cm is required for the ^{3}He tracks and $DCA_{pv} < 50$ cm for the $(\pi^+)\pi^-$ tracks. Table 5.3 summarises the selections used for the identification of the decay products.

5.4.2 Building the Hypertriton Candidates

Once all the possible daughter particles are identified within the same event, the $^3_\Lambda$H candidates are built by associating a decay vertex and a mother particle hypothesis to each daughter particles pair. A dedicated algorithm[7] – based on the offline V^0-finder already mentioned in Section 2.5.2 and optimised for the hypertriton decay – reconstructs the decay vertices.

First, the distance of closest approach between the daughter tracks (DCA_{daug}) is

[7] In the context of this thesis, the algorithm dedicated to the hypertriton decay vertex reconstruction is called V^0-finder. The name comes after the fact that the algorithm derives from the default ALICE offline V^0-finder.

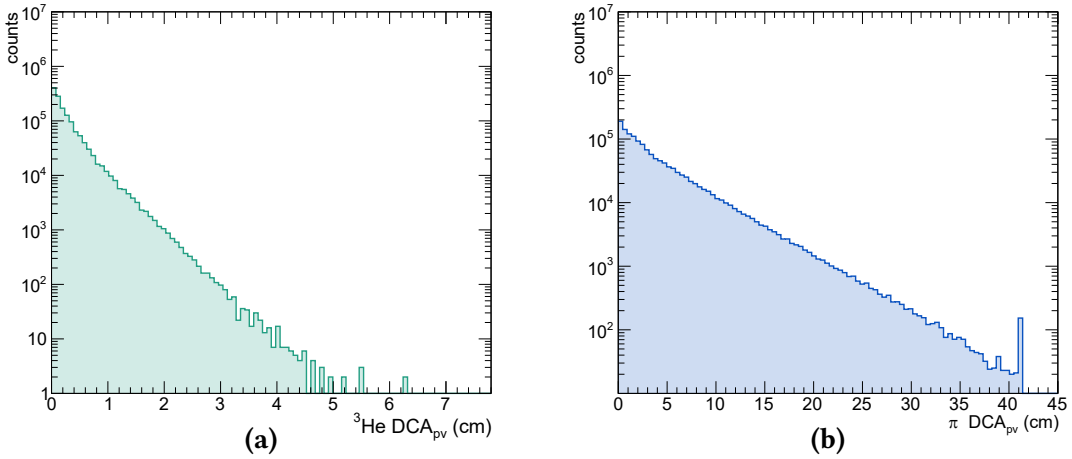

Figure 5.5: Distribution of the distance of closest approach of the decay products to the primary vertex: ^{3}He in the left panel (a) and π^+,π^- in the right panel (b). Data refers to the reconstructed Monte Carlo (anti)hypertritons.

Decay products identification	
^{3}He	$\lvert n\sigma_{TPC}\rvert \leq 5$
	$p_{\mathrm{T}} > 1.7\,\mathrm{GeV}/c$
	$\mathrm{DCA}_{\mathrm{pv}} < 8\,\mathrm{cm}$
$(\pi^+)\pi^-$	$\lvert n\sigma_{TPC}\rvert \leq 5$
	$p_{\mathrm{T}} > 0.1\,\mathrm{GeV}/c$
	$\mathrm{DCA}_{\mathrm{pv}} < 50\,\mathrm{cm}$

Table 5.3: Summary of the selections used for the identification of the decay products.

analytically computed. The pairs of tracks with $\mathrm{DCA}_{\mathrm{daug}} > 2\,\mathrm{cm}$ are discarded since the MC data show that the fraction of real hypertritons having a $\mathrm{DCA}_{\mathrm{daug}}$ above this threshold is negligible. Then, the initial decay vertex position is roughly estimated as the midpoint of the minimum segment connecting the two tracks. In those events for which the distance between the decay vertex and the primary vertex – the so-called *decay radius* (R) – is greater than 200 cm, the pairs of tracks are rejected. In order to have a better momentum estimate, the daughter tracks are propagated to the point of minimum distance to the preliminary vertex. Finally, the offline V^0-finder – provided by the ALICE offline framework – is used to compute the decay vertex position and to reconstruct the four-momentum of the mother particle.

At this point, further selections are required. The distance between the secondary and the primary vertex is required to be less than 200 cm – using the best estimate of the secondary vertex position instead of the preliminary estimate. The invariant mass of the mother particle ($m_{^3\mathrm{He}\pi}$) is required to be in the hypertriton mass region $2.9\,\mathrm{GeV}/c^2 \leq m_{^3\mathrm{He}\pi} \leq 3.1\,\mathrm{GeV}/c^2$.

The pointing angle (θ_{pa}) is defined as the angle between the momentum of the mother particle and the straight line connecting the primary and the secondary vertex. If the hypothetical mother particle is generated in the primary vertex and decayed in the secondary vertex, the momentum vector should point to the primary vertex and θ_{pa} is expected to be ~ 0. Therefore, the $\cos(\theta_{\mathrm{pa}})$ is computed, and the candidates with $\cos(\theta_{\mathrm{pa}}) < 0.99$ are rejected. Figure 5.6 represents a sketch of the ${}^3_\Lambda\mathrm{H}$ 2-body decay where the topological variables used to select the candidates are highlighted.

Secondary vertex selections
$\mathrm{DCA}_{\mathrm{daug}} < 2\,\mathrm{cm}$
$R_{\mathrm{prel.}} < 200\,\mathrm{cm}$
$R < 200\,\mathrm{cm}$
$\cos(\theta_{\mathrm{pa}}) > 0.99$
$2.9\,\mathrm{GeV}/c^2 \leq m_{^3\mathrm{He}\pi} \leq 3.1\,\mathrm{GeV}/c^2$

Table 5.4: Summary of the selections applied during the reconstruction of the secondary vertex.

The ${}^3\mathrm{He} + \pi^-$ pairs with the corresponding decay vertex and mother particle hypothesis, passing all the selections described before – and summarised in Table 5.4 – form the set of hypertritons candidates.

5.4.3 Pre-selection Efficiency

In this thesis, the set of selections used to determine the hypertriton candidates are referred to as *pre-selections*. This specification is helpful to distinguish them from the discrimination of the hypertriton candidates carried out by the BDTs and referred to as *ML-selections*. The pre-selections include the track selection (Section 5.3), the PID cuts (Section 5.4.1) and the selections concerning the reconstruction of the decay vertex (Section 5.4.2).

The performance of the pre-selections is evaluated in the Monte Carlo data by calculating the *pre-selection efficiency* ($\mathrm{Eff}_{\mathrm{p.s.}}$) that is the ratio between the number of the MC ${}^3_\Lambda\mathrm{H}$ which has passed all the pre-selections ($N_{\mathrm{rec.}}$) and the total number of the ${}^3_\Lambda\mathrm{H}$

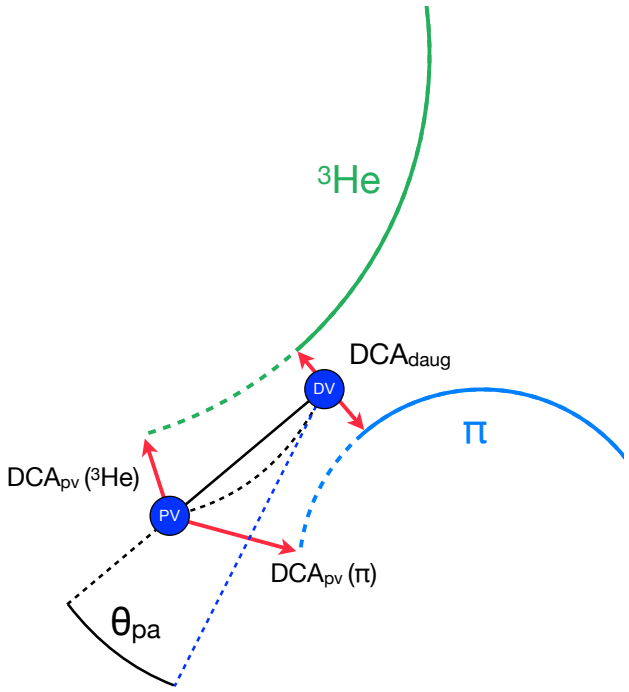

Figure 5.6: Sketch of the ${}^{3}_{\Lambda}\mathrm{H}$ 2-body decay. The topological variables used to select the candidates are highlighted.

generated in the MC ($N_{\text{gen.}}$). The $\mathrm{Eff}_{\text{p.s.}}$, as it is defined, do not only takes into account the efficiency of the whole process of the decay reconstruction (Efficiency), but also the geometrical acceptance of the ALICE detectors as well as their possible inefficiencies (named as Acceptance). The *pre-selection efficiency* ($\mathrm{Eff}_{\text{p.s.}}$) is defined as:

$$\mathrm{Eff}_{\text{p.s.}} = \mathrm{Efficiency}(ct) \times \mathrm{Acceptance}(ct) = \frac{N_{\text{rec.}}(ct)}{N_{\text{gen.}}(ct)}. \tag{5.2}$$

$\mathrm{Eff}_{\text{p.s.}}$ is evaluated as a function of the particle proper time (ct) – that is closely linked to the decay length L by the relation $L/\beta\gamma = ct$ – in order to take into account the dependence on the ct and it is shown in figure Figure 5.7.

The $\mathrm{Eff}_{\text{p.s.}}$ assesses the performances of the reconstruction process, but it also plays a key role in the lifetime measurement since it is necessary to estimate the absolute number of (anti)hypertriton decays from the number of observed ones.

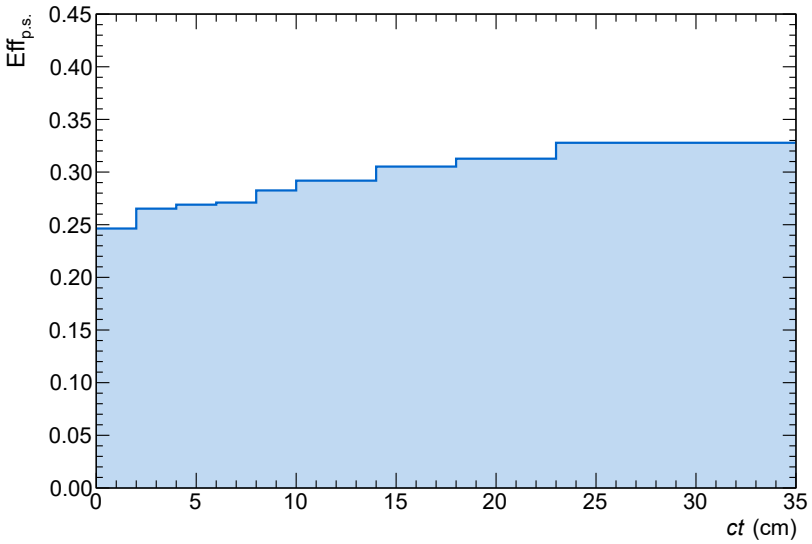

Figure 5.7: Pre-selection efficiency as a function of the hypertriton proper time ct.

5.5 Training and Test Set Preparation

This section presents and discusses the data used to train and test the BDTs models employed to identify the real hypertritons among all the candidates.

The task of discriminating the real ${}^{3}_{\Lambda}\mathrm{H}$ from the combinatorial background is a binary classification problem (Section 4.3). The ${}^{3}_{\Lambda}\mathrm{H}$ represents the signal class, while the combinatorial background – the only known background source for this channel – represents the background class.

In principle, the data used to train and test a supervised ML model and the data on which the model is applied should be homogeneous. However, a pure (anti)hypertritons sample is not available for obvious reasons. Similarly, a sample of pure ${}^{3}\mathrm{He} + \pi^{-}$ pairs not originating in a ${}^{3}_{\Lambda}\mathrm{H}$ decay vertex is unavailable. It is necessary to use proxy data capable of mimicking the properties of the signal and the background as faithfully as possible.

For the signal, Monte Carlo data specially tuned for this purpose are used, while for the background, like-sign pairs are employed. In the following sections these proxy data are discussed in more details (Section 5.5.1 and Section 5.5.2) as well as the Training and Test Set (TTS) (Section 5.5.3).

5.5.1 The Signal Proxy: Monte Carlo Data

The Monte Carlo data used as a proxy for the signal are the simulated ${}^{3}_{\Lambda}\mathrm{H}$ already described in Section 5.1 with appropriate modifications.

As already mentioned, the momentum distribution of the simulated (anti)hypertritons is uniform from 0 to 10 GeV/c since it is handy for performance studies but do not describe the actual distribution. The transverse momentum distribution of the hadrons produced in HIC is usually described with a Blast-Wave (BW) model [27]. A precise determination of the (anti)hypertritons momentum distribution, on the other hand, is not available because of the lack of data needed for the BW fit. Therefore, the BW fit to the ^{3}He spectrum measured by ALICE [121] it is used as a surrogate.

The (anti)hypertriton spectrum is reshaped implementing a *sampling method* [122] – also called *accept-reject method* – that uses the ^{3}He BW as target function. Figure 5.8a shows the flat p_{T} distribution of the simulated $^3_\Lambda$H, while Figure 5.8b shows the shape of the distribution after the reshaping.

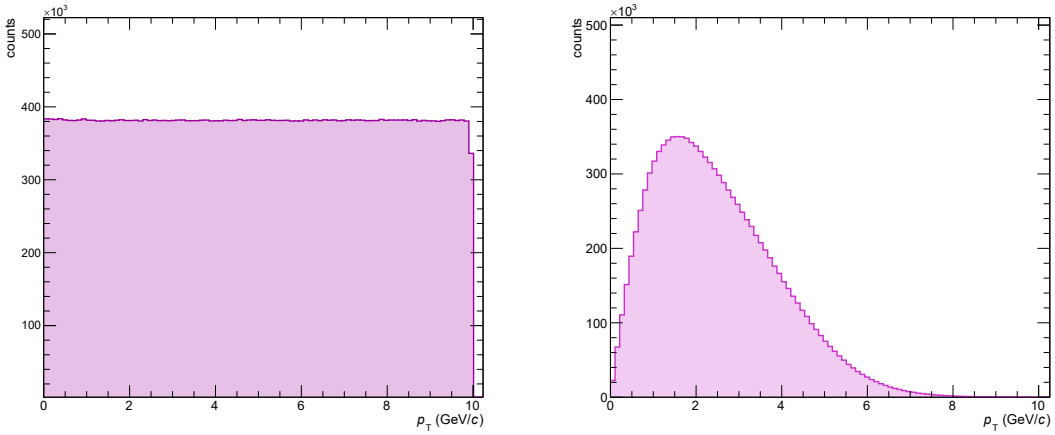

Figure 5.8: Transverse momentum distribution of the simulated $^3_\Lambda$H before (a) and after (b) the reshaping performed by using a sampling method with the ^{3}He BW fit as the target function.

After the p_{T} reshaping, the MC $^3_\Lambda$H pass through the same reconstruction process used to reconstruct the real data and the pre-selections are then applied, ensuring homogeneity with respect to the real data. The number of MC (anti)hypertritons passing the pre-selections and thus available for the TTS is $9.515\,22 \times 10^5$.

5.5.2 The Background Proxy: Like-Sign Pairs

For the background component of the training and test set, the choice fell on the *like-sign pairs*, which are $^3\mathrm{He} + \pi^+$ and $^3\overline{\mathrm{He}} + \pi^-$ pairs taken in the data. The electric charge of the like-sign pairs ensures not to include any actual signal.

The like-sign method is commonly used for the background subtraction in dipion [123] and dilepton [124–126] analyses at high energy. It can be shown that it is an exact method in certain cases, while in general, it is an approximation of the combinatorial

background. The like-sign method brings two main advantages to this analysis. First, it ensures a sample size comparable to that of the data. Second, it provides a reliable description of the data, especially the p_{T} distribution. The p_{T} distribution of the mother particle – whether it is built from a like-sign or an unlike-sign pair – is dominated by the ^{3}He transverse momentum. So, building the background from the real ^{3}He ensures a reliable momentum distribution for the background.

Other methods, commonly used for combinatorial background subtraction, were considered: the *sidebands background* and the *event-mixing* method.

The sidebands background consists in using the real $^3\mathrm{He} + \pi^-$ and $^3\overline{\mathrm{He}} + \pi^+$ pairs, excluding those with the invariant mass in the $^3_\Lambda$H mass region. It is necessary to exclude a wide region around the expected $^3_\Lambda$H peak, at least 3σ, to rule out any possible signal pairs. The sidebands background is not a surrogate of the background, while the like-sign and the event-mixing methods are. It is a portion of the real combinatorial background, which is the great advantage of this method. On the other hand, excluding the $^3_\Lambda$H invariant mass region prevents a representation of the background in the signal region where the background reproduction is critical. The performances of the BDTs may suffer from the lack of information about decay kinematics and topology in the region of interest. Furthermore, excluding the $^3_\Lambda$H invariant mass region significantly reduces the sample size. For both these reasons, the sidebands background has not been used.

The event-mixing method consists in building the uncorrelated $^3\mathrm{He} + \pi^-$ pairs taking one particle species from one event – e.g. all the ^{3}He identified in a specific event – and the other particle species from a different event – e.g. all the π^+ identified in another event. This ensures having totally uncorrelated pairs. The main advantage of this method is that it can provide an – almost – arbitrarily large background sample, just increasing the number of events combinations. However, the event-mixing method has two main disadvantages. First of all, it is costly in computing resources since it requires keeping in memory many events for the mixing, while the usual workflow provides to process the events one at a time. In addition, it requires to be appropriately tuned to ensure a fair description of the background. Drijard et al., in an extensive review on this method [127], pointed out that the kinematic cuts induced by the event and track selections can lead to biases in the representation of the combinatorial background. To avoid this problem, it is necessary to mix *similar* events only, but the definition of similar events is not unique. In HIC, it is usual to mix only events belonging to the same centrality class and with similar V_z, but, again, the definition of similar centrality and V_z is not unique. Therefore, it is necessary to deeply examine the parameters of the mixing procedure with a trial and error approach to ensure a fine description of the background.

Hence, the choice of the like-sign pairs as combinatorial background proxy relies on the simplicity, reliability, and sample size assured by this method compared to the others. Like-sign pairs are processed with the same method used for the hypertriton

candidates, and the same pre-selections are applied, ensuring homogeneity of the data. The number of like-sign pairs passing the pre-selections and thus available for the TTS is 5.055×10^7.

5.5.3 Features Variables Studies

Once the training and test set elements are defined, each element is processed to extract the features used to train the BDTs. The features are also extracted for the real data the BDTs will select – the application sample.

After the features extraction, the TTS and the application sample are stored in ROOT files for a total size of $\sim$ 3 GB. Thanks to the event selection and the pre-selections, the data size at this point of the analysis is dramatically reduced with respect to the whole data sample and do not require the WLCG and the ALICE central resources to be processed. Therefore the selected data and the TTS are moved on a dedicated local machine that provides computing resources for training, testing and applying the BDTs. Furthermore, the use of local resources provided an agile and flexible solution for developing the software employed for the ML part of this analysis.

The choice of the features takes place in several steps. The complete list of the physical quantities measured for each data point was considered at first. Then, the unnecessary features – for the classification performances of the BDTs – were excluded, obtaining the list of features reported in Table 5.5. Some of them are related to the PID of the daughter particles – the first four in Table 5.5 – while the others are related to the decay topology. The distribution of the features in the signal and the background sample is different, as shown in Figure 5.9, and it is possible to exploit these differences to select the signal and reject the background. During the training, the BDTs learn how to take full advantage of these differences to maximize the signal/background discrimination.

Figure Figure 5.10 shows the correlations between the features, with the addition of the invariant mass ($m_{^3\mathrm{He}\pi}$) and the proper time (ct) of the mother particle. In particular Figure 5.10a reports the correlations for the signal component and Figure 5.10b for the background component and a comparison between the two figures clearly shows differences in the correlations. The BDTs can also exploit these deviations in the correlations to optimize the classification.

The correlations between $m_{^3\mathrm{He}\pi}$ and the other features are pretty small, basically irrelevant. It is essential because a feature strongly correlated with $m_{^3\mathrm{He}\pi}$ could lead to an artefact peak in the invariant mass distribution of the hypertriton candidates. We call this effect *mass shaping* and cross-checks are performed in this analysis to avoid it. However, the absence of strongly $m_{^3\mathrm{He}\pi}$-correlated features suggests that no mass shaping is expected. Furthermore, the ct of the mother particle is not included in the training features since it is recommended not to include both the ct and the p_{T} in training to avoid mass shaping.

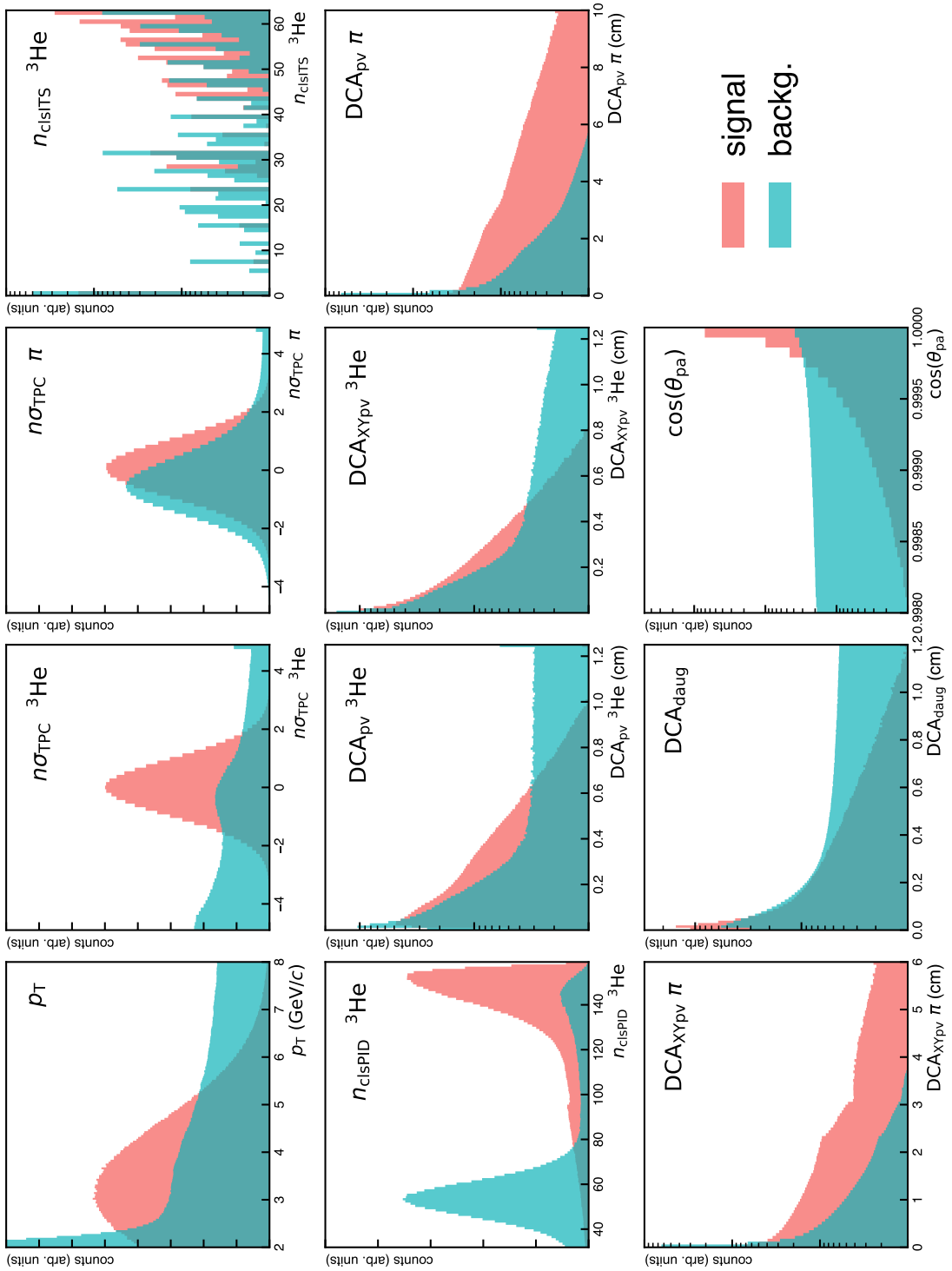

Figure 5.9: Comparison, for all the features, between the signal component (red) and the background component (green water) of the training and test set.

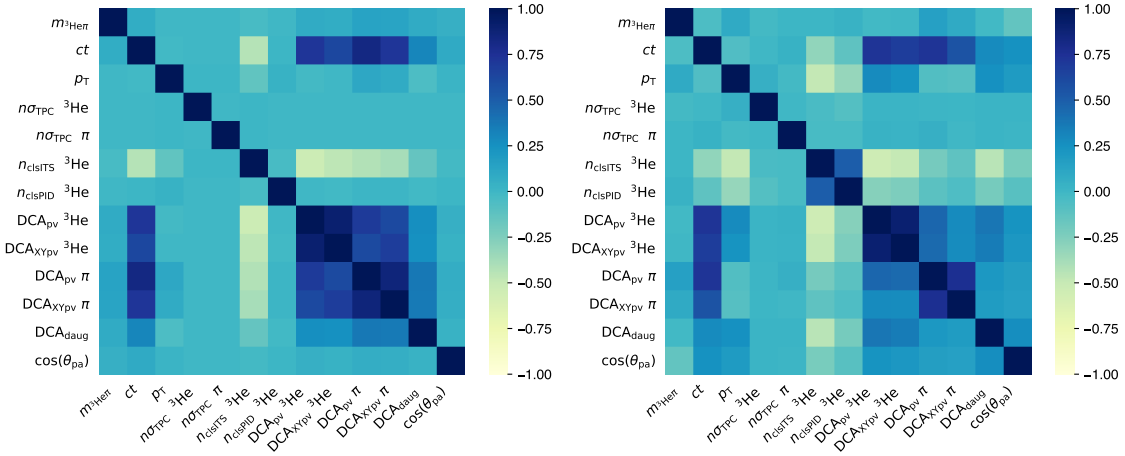

(a) **(b)**

Figure 5.10: Correlation matrix of the features of the signal (a) and the background (b) components of the training and test set. The invariant mass and the proper time of the mother particle are also reported.

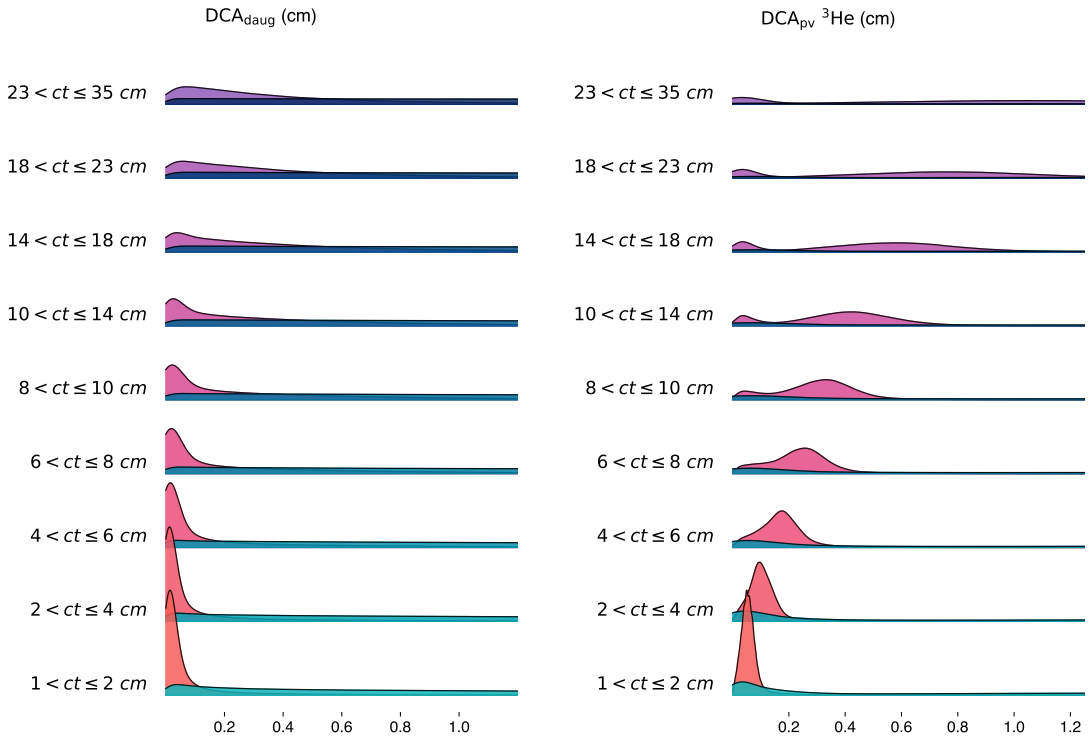

Figure 5.11: Evolution of the probability density functions of the signal (scale of reds) and the background (scale of blues) component of the TTS, in the 9 ct-bins, for the DCA_{daug} (a) and the ^{3}He DCA_{pv} (b) features. The p.d.f.s are derived with a KDE.

Features variables	Category
$n\sigma_{\text{TPC}}$ ^{3}He	particle id.
$n\sigma_{\text{TPC}}$ π	
n_{clsITS} ^{3}He	
n_{clsPID} ^{3}He	
DCA_{pv} ^{3}He	decay topology
DCA_{XYpv} ^{3}He	
DCA_{pv} π	
DCA_{XYpv} π	
DCA_{daug}	
p_{T} (mother)	
$\cos(\theta_{\text{pa}})$	

Table 5.5: List of the features with which the BDTs are fed.

The training and test set is finally split into 9 sub-samples – or ct-bins – as summarized in Table 5.6. In the table, the number of signal ($\text{N}_\text{s}$ig.) and background ($\text{N}_\text{b}$kg.) examples available for each ct-bin is also reported. Then, for each subsample, a different BDTs model is trained. The variation of some features distribution as a function of the ct supports this choice. On the other hand, the ct is not included in the training; therefore, the ML models could miss this dependence. Splitting the training helps the BDTs catch and exploit the distributions' peculiarities in the different ct bins.

For example, in Figure 5.11 the evolution of the DCA_{daug} (Figure 5.11a) and the DCA_{pv} for the ^{3}He track (Figure 5.11b) in the different ct bins are presented. In particular, the figures show a data-driven estimate[8] of the *probability density function* (p.d.f.) of the features for both the signal and the background, highlighting the variations in the p.d.f. of the signal sample. It is reasonable to suppose that a dedicated model for each ct bin would better exploit the features. This approach actually ensures a total number of extracted hypertritons larger than by training a single model for the full ct range. Finally, for each ct-bin, the training and test set is split into two subsamples. One half is to train the model; the other one is dedicated to testing the performances. The split is done after a random shuffling of the data sets, avoiding any bias induced by the data ordering.

[8]The p.d.f. are obtained from the TTS with a *Kernel Density Estimation* (KDE).

Bin number	ct **interval** (cm)	$N_{sig.}$	$N_{bkg.}$
1	$1 < ct \leq 2$	240 000	233 000
2	$2 < ct \leq 4$	409 000	217 000
3	$4 < ct \leq 6$	301 000	122 000
4	$6 < ct \leq 8$	224 000	80 000
5	$8 < ct \leq 10$	171 000	65 000
6	$10 < ct \leq 14$	222 000	110 000
7	$14 < ct \leq 18$	123 000	105 000
8	$18 < ct \leq 23$	78 000	134 000
9	$23 < ct \leq 35$	58 000	500 000

Table 5.6: List of the ct bins in which the training and test set is split. A dedicated ML model is trained for each bin. The number of signal and background available examples ($N_{sig.}$ and $N_{bkg.}$ respectively) is also reported.

5.6 Training and Testing the BDTs

According to Section 5.5.3, the TTS is split into 9 ct-bins, and for each one, a different BDTs model is trained. The procedure for the training is the same for each model and takes place in two stages: First, a series of iterative training is done with training and validation sets of reduced size to optimise the hyperparameters of the BDTs. Then a final training on the whole training set is done using the optimal set of hyperparameters. After the training, the models are evaluated by estimating their out-of-sample performances on the test set.

The training, optimisation and testing phases of this analysis have been carried out with the help of the `hipe4ml` library. `hipe4ml` is a minimal environment to simplify some common aspects of the machine learning analysis in heavy-ion physics. In particular, it provides a unique interface to load and manage `ROOT` files in `Python` and to train, optimise, test and deploy different ML models on heavy-ion data. It is distributed under the free copyleft licence GNU General Public License v3 [GPL] and it is freely available on `PyPi` [128]. `hipe4ml` born from the idea to share and reuse the code developed independently by different ALICE members, including myself, for their analyses. The skeleton of the project was indeed the code developed for this analysis. Now it is maintained and developed by a team of 7 people, including myself, and it is used by 15+ analysers for their work. In particular, I took care of the package's tests.

5.6.1 Models Training and Hyperparameter Optimisation

As already mentioned in the previous sections, the machine learning model used in this analysis is the Boosted Decision Trees, and in particular, the XGBoost [129] implementation of such model. The website of the XGBoost project declares: "XGBoost is an optimised distributed gradient boosting library designed to be highly efficient, flexible and portable". It implements a parallel tree boosting model under the Gradient Boosting framework. XGBoost is widely used in the data science field to solve many problems in a fast and accurate way. In fact, it has been chosen by many teams of machine learning competitions in their winning solutions [130].

The XGBoost model has a set of hyperparameters that rules the learning process and helps to avoid the *overfitting*, the situation in which the models learn how to reproduce the data in the training set *too well* at the cost of poor performances on the test set. A sub-set of the hyperparameters for the optimisation and an optimisation domain for each were defined. The choice relies on the documentation provided by XGBoost on its operation and heuristic considerations. For the remaining hyperparameters, the default value was used. Table 5.7 reports the list of the optimised hyperparameters, together with their optimisation domain and the optimal value found with the optimisation process. It also provides a brief description of the hyperparameters to explain their function in the training algorithm. A detailed description is available in the official XGBoost documentation.

The output function is set to `binary:logistic` that is the standard configuration for binary classification problems. In this configuration, the BDTs return for each data point an output value proportional to the probability to belong to a defined class, the signal class in this analysis. Furthermore, the `hist` method is used as the tree-building algorithm. This algorithm discretises the continuous variables in histograms. The node splits are then performed on the histograms rather than on the variable. This method speeds up the training and does not compromise the model performances for variables that are physical measurements with a finite resolution.

The hyperparameter optimisation is done using the *Byesian Optimisation* described in Section 4.4.3 and implemented in the BayesianOptimization library [131]. The target function f optimises the ROC AUC score computed with a 5-fold cross-validation (Section 4.4.2) as a function of the hyperparameters. The optimisation has been done independently for each model – i.e. for each ct-bin –, however the set of optimal values H_{opt} found by the algorithm are the same for all the models and are reported in Table 5.7. The models are then re-trained on the whole training set with the hyperparameters P_{opt} and the ROC AUC score is computed on the test set. The ROC AUC score obtained for each model is reported in Table 5.8.

Name	Description	Opt. domain	H_{opt} value
`max_depth`	maximum number of nodes from the root to the deepest leaf of the tree	$[5, 20]$	13
`learning_rate`	makes the model more robust by shrinking the weights on each step	$[0.01, 0.3]$	0.0982
`n_estimators`	number of trees composing the model	$[50, 500]$	181
`gamma`	minimum reduction of the loss function required to make a further split on a leaf node	$[0.3, 1.1]$	0.4467
`min_child_weight`	minimum number of instances required to create a new node in the tree	$[1, 12]$	5.75
`subsample`	fraction of randomly sampled training data used to growing the trees to prevent overfitting	$[0.5, 0.9]$	0.74
`colsample_bytree`	subsample ratio of columns when constructing each tree to prevent overfitting	$[0.5, 0.9]$	0.57

Table 5.7: List of the `XGBoost` model hyperparameters included in the optimisation. In addition, a brief description of their role in the model's training is provided with the optimisation domain and the optimised value.

5.6.2 Models Performances

Once the models are trained, they return a *BDTs score* for each given data point. As already mentioned, the BDTs score is connected to the probability the model assign to the data point to belong to the signal class. Therefore, the higher the BDTs score, the higher the probability of being a true hypertriton according to the BDTs. Figure 5.12a shows the distribution of the BDTs score obtained in the training set (markers) and the test set (filled area) for both the signal (red) and the background (blue). The figure refers to the model trained for the third ct-bin ($4 < ct \leq 6$ cm), while the figures referred to all

Bin number	ROC AUC score
1	0.996 199
2	0.997 432
3	0.997 857
4	0.997 736
5	0.997 850
6	0.998 115
7	0.998 104
8	0.998 478
9	0.999 066

Table 5.8: ROC AUC score for each optimised model, computed on the test set.

the analysed ct-bins can be found in Appendix A and they exhibit a similar behaviour. This figure highlights two significant aspects of the model performances.

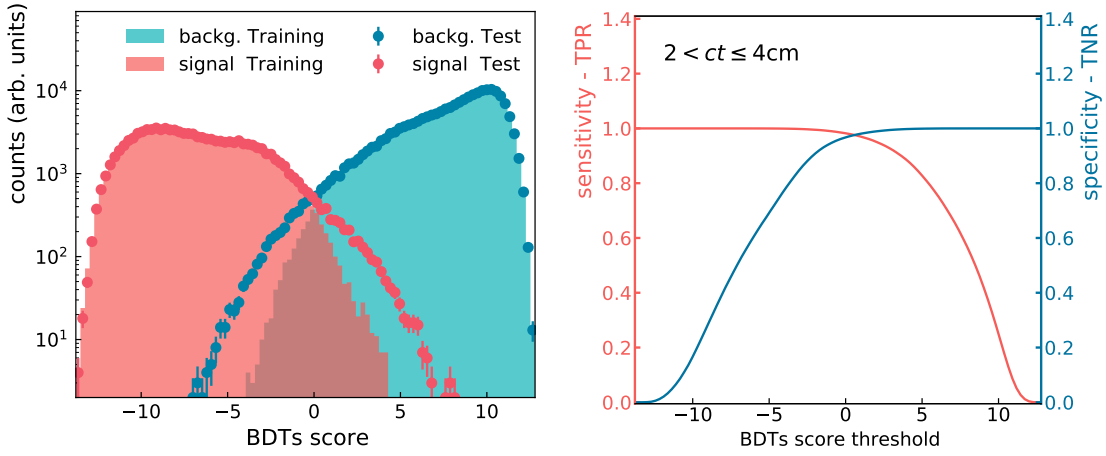

(a) **(b)**

Figure 5.12: (a) distribution of the BDTs score in the training set (markers) and the test set (filled area) for both the signal (red) and the background (green water). (b) sensitivity (red) and specificity (blue) of the model selection as a function of the threshold on the BDTs score. The sensitivity and the specificity are estimated on the Test Set. Both the plots are referred to the $2 < ct \leq 4$ cm ct-bin.

First, the distributions in the training set are well reproduced in the test set, except for minor discrepancies in the tails – note the log-linear scale of the figure. This means that the models can – generalise – well, in the sense that they can reproduce the classification pattern learned in the training set also on new data, the test set. There is no overfitting a part for the minor discrepancies in the tails. It was tried to limit the model complexity by reducing the number of trees by hand, a sort of early stop regularisation [132]. It reduced the discrepancies in the tails and the ROC AUC score simultaneously; basically, the regularisation penalised out-of-sample performances. Therefore this level of overfitting is not *pathological* since it does not affect the performances on the test set. In addition, the overestimate of the models' capabilities observed in the training set is not taken into account in any aspect of the analysis. Therefore the conclusion is that the models are well trained, and the slight discrepancies between the performance on the train set and the test set are under control.

Second but not least, the distribution of the signal examples is well separated from that of the background examples. It is the *crux* of this analysis since it means that the BDTs have an excellent classification power. More specifically, when the hypertriton candidates are processed by BDT, they are assigned a score. Putting a threshold (Th) on the BDTs score and rejecting all the candidates with scores under the threshold makes it possible to reject most of the background without losing too much signal. The choice of the optimal threshold ($\mathrm{Th}_{\mathrm{best}}$) is, thus, crucial for the hypertriton selection.

Figure 5.12b shows the BDTs signal selection efficiency ($\mathrm{Eff}_{\mathrm{BDTs}}$) and the background rejection efficiency as a function of the threshold on the BDTs score of one of the models – in particular, the model of the ct-bin 4, the figures related to the other models can be found in Appendix A. From this picture, it is clear that the choice of the $\mathrm{Th}_{\mathrm{best}}$ is not trivial. It is a matter of balancing the signal's preservation and maximising the background rejection. However, in the region around 5, it is possible to achieve a good trade-off between the two. The following section (Section 5.6.3) presents the algorithm responsible for the choice of the BDTs score threshold. It implements a data-driven optimisation and provides a reliable method to determine the BDTs score threshold for each model.

5.6.3 BDTs Selection Optimisation

The BDTs selection optimisation method relies on the estimation of the expected *statistical significance* S for the hypertriton signal as a function of the threshold on the BDTs score. Since the number of expected hypertritons is different for each ct-bin, the selection threshold of each model is optimised independently. The statistical significance is computed as:

$$S = \sqrt{\frac{N_{\mathrm{S}}}{N_{\mathrm{S}} + N_{\mathrm{B}}}} \tag{5.3}$$

where N_{S} and N_{B} are the signal and background counts respectively.

The significance S is estimated for 1000 values of Th corresponding to as many $\mathsf{Eff}_{\mathrm{BDTs}}$ values, from 0.0 to 1.0 in steps of 0.001. For each Th, the number of expected ${}^{3}_{\Lambda}\mathrm{H}$ is computed starting from the ALICE measurement of the hypertriton production in Pb–Pb collisions [98]. Then, correction factors are applied to consider the different collision energy, the number of analysed events, and the considered p_{T} and ct intervals under analysis. The expected signal N_{S} derives from the number of expected ${}^{3}_{\Lambda}\mathrm{H}$ corrected for the $\mathsf{Eff}_{\mathrm{BDTs}}$ corresponding to the considered threshold.

The background counts N_{B}, instead, are estimated from the data. A region of interest (RoI) in the invariant distribution of the candidates is defined as the $\pm 3\sigma$ interval around the hypertriton mass – both mass and σ come from MC simulations. The data with invariant mass in the RoI are excluded from the analysis to prevent possible bias. Then the remaining data, the data in the sidebands that are only background, are passed to the BDTs and selected according to Th. The selected data are fitted with a 2nd-degree polynomial. The fit function allows extrapolating the number of expected background counts N_{B} in the RoI. Finally, S is computed, and the procedure is repeated for the next Th value. After estimating the S for each Th value, the threshold that maximises $S \times \mathsf{Eff}_{\mathrm{BDTs}}$ is chosen as $\mathrm{Th}_{\mathrm{best}}$.

Figure 5.13 shows an example of this computation referred to the $2 < ct \leq 4\,\mathrm{cm}$ ct-bin. The right figure presents the estimate of S. The signal counts (orange points) are referred to as pseudo-data, while the blue points represent the real hypertriton candidates outside the RoI, selected with threshold $\mathrm{Th}_{\mathrm{best}}$ and fitted with the 2nd-degree polynomial (red line). The red shaded area represents the background extrapolated in the RoI (N_{B}), and the orange area corresponds to the estimated number of hypertritons (N_{S}). The plot on the left, instead, shows $S \times \mathsf{Eff}_{\mathrm{BDTs}}$ as a function of the 1000 Th values in which it is computed, with the related uncertainty. In Table 5.9 the $\mathrm{Th}_{\mathrm{best}}$ values found with this method are reported for each ct-bin. Those values are used to reject all the hypertriton candidates with lower scores in the related bin.

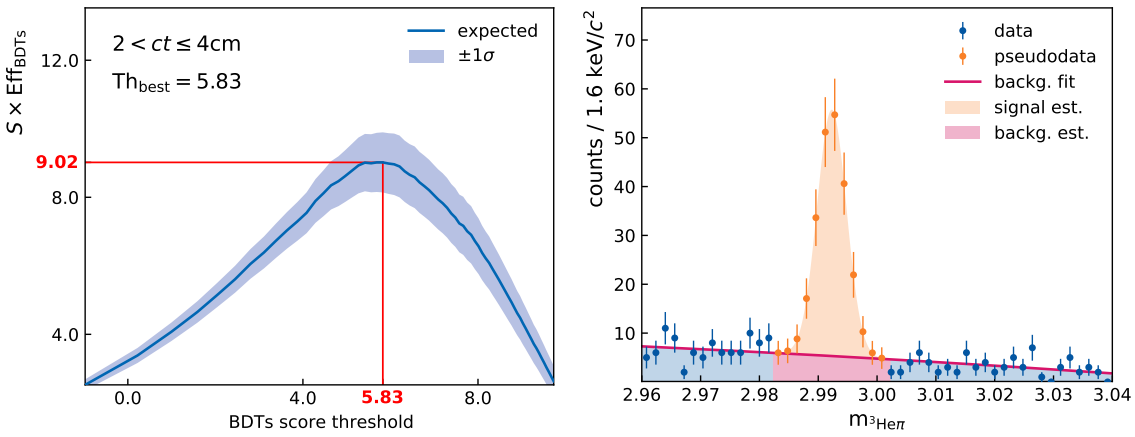

(a) **(b)**

Figure 5.13: Both the figures refer to the BDTs selection optimisation procedure in the $2 < ct \leq 4\,\text{cm}$ ct-bin. (a) expected $S \times \text{Eff}_{\text{BDTs}}$ as a function of the Th, the $\pm 1\sigma$ uncertainty on the estimation derives from the uncertainty on the expected number of ${}^{3}_{\Lambda}\text{H}$. (b) the invariant mass distribution of the data in the sidebands (blue points) – used to extrapolate the background in the signal region – is represented together with the pseudo-data used as an estimate of the signal (orange points), properly reshaped. The plot is related to the Th_{best} value obtained for this ct-bin.

Bin number	Th_{best}
1	5.43
2	5.83
3	5.61
4	5.45
5	5.74
6	5.47
7	5.21
8	5.02
9	5.56

Table 5.9: Th_{best} obtained for each model.

Chapter 6

Measurement of the Hypertriton Lifetime and B_Λ

6.1 Signal Extraction

After estimating the $\mathrm{Th}_{\mathrm{best}}$ values by using the method presented in the previous section (Section 5.6.3), the ${}^{3}_{\Lambda}\mathrm{H}$ candidates are split into bins according to their ct (see Table 5.6 for the definitions of the bins) and passed to the corresponding BDTs. The BDTs assign the score to each candidate. If the score is below the $\mathrm{Th}_{\mathrm{best}}$, the candidate is rejected. Finally, the invariant mass distribution of the selected candidates ($m_{{}^{3}\mathrm{He}\pi}$) is built for each ct-bin.

The invariant mass distributions are then fitted to extract the number of observed hypertritons and the mass value. The fit is done using the `RooFit` package [133], a library designed to build complex fit models in the `ROOT` environment. `RooFit` allows using many different classes of functions to build p.d.f.s and to combine them to build composite models that are arbitrary linear combinations of individual p.d.f.s. The composite model used to fit the invariant mass distributions is:

$$M(x) = f \cdot S(x) + (1 - f) \cdot B(x) \tag{6.1}$$

where $M(x)$ is the fit model, $S(x)$ is the p.d.f. of the signal component, $B(x)$ is the p.d.f. of the background component and f is the fraction of the events that belongs to the signal. The normalization of the model is automatically kept into account by `RooFit`. The signal p.d.f. $S(x)$ is derived from the MC data. The MC hypertritons are split according to the ct and selected by the BDTs with the same procedure adopted for the real data. Then, in each ct-bin, the invariant mass distribution of the selected MC hypertritons is used to build $S(x)$ with an adaptive KDE implemented in `RooFit` [134]. For the background model $B(x)$ a first degree polynomial is used.

The choice of the KDE for $S(x)$ is due to the necessity to faithfully model the signal component of the data in order to obtain the mass value with extremely high precision.

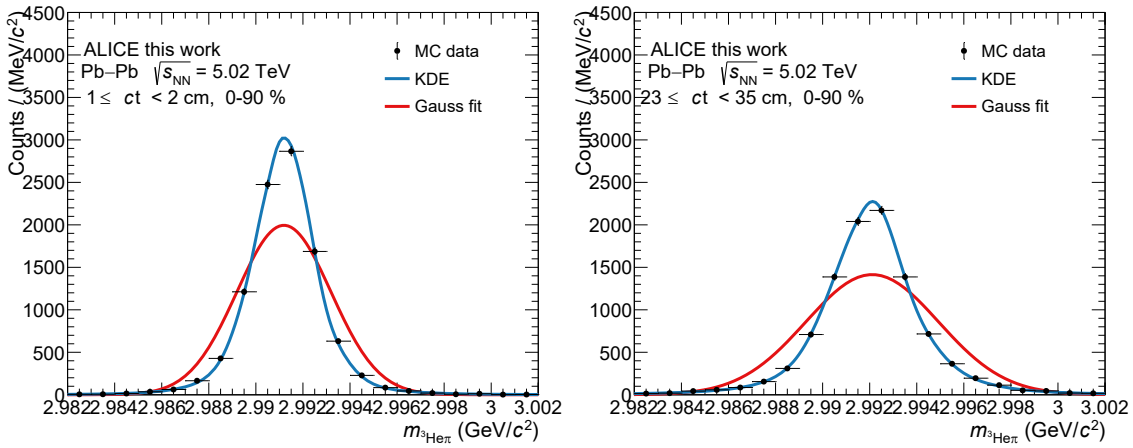

(a) **(b)**

Figure 6.1: The invariant mass distribution of the MC hypertritons after the reconstruction is compared with the p.d.f. obtained with the KDE and a gaussian p.d.f. fitted to the distribution for the (a) $1 \leq ct < 2$ cm and (b) $23 \leq ct < 35$ cm ct-bins. The gaussian is clearly not suitable for the description of the invariant mass distributions.

The study of the MC data shows that, after the reconstruction process, the invariant mass distribution of the selected ${}^3_\Lambda$H does not have a Gaussian shape (Figure 6.1). Hence a data-driven p.d.f. based on the MC data provides a more reliable model for the signal. Finally, an unbinned maximum likelihood fit is performed for each ct-bin as presented in Figures 6.2 and 6.3. The figures also report the value of the ${}^3_\Lambda$H mass ($m_{{}^3_\Lambda\mathrm{H}}$) and the number of observed ${}^3_\Lambda$H ($\mathrm{N_{obs}}$) for each fit. The following paragraphs provide more details about the procedure adopted to estimate $m_{{}^3_\Lambda\mathrm{H}}$ and $\mathrm{N_{obs}}$ from the invariant mass fit.

${}^3_\Lambda$H mass value The only parameter estimated in the fit of a non-parametric p.d.f. to a given data set is, in general, the normalisation. In fact a non-parametric p.d.f. can not *slide* with respect to the independent variable. `RooFit` provides a tool to allow such a p.d.f. to slide along the independent variable to adjust the peak position to the data correctly. This is done by adding a fit parameter Δm defined as follow:

$$\Delta m = m_{\mathrm{MCrec}} - m_{\mathrm{fit}}, \tag{6.2}$$

where m_{MCrec} is the value of the mass corresponding to the peak in the data used to build the KDE – the reconstructed and ML-selected ${}^3_\Lambda$H in this case, hence the name – and m_{fit} is the mass value corresponding to the peak of the fitted data. Basically `RooFit` simultaneously fits the MC data to build $S(x)$ finding m_{MCrec} and the real data with $S(x)$ finding m_{fit}. Therefore the parameter estimated in the simultaneous fit is Δm.

In the Monte Carlo data, the hypertritons are generated with a mass value of $m_{\text{MCgen.}} = 2.991\,31\ \text{GeV}/c^2$. After the reconstruction, the $m_{^3\text{He}\pi}$ distribution of the ML-selected hypertritons shows a gaussian-like shape with the peak at m_{MCrec}, where the value of m_{MCrec} depends on the ct-bin. Therefore, a systematic error equal to $m_{\text{MCgen}} - m_{\text{MCrec}}$ is expected – referred as *reconstruction shift* in this thesis. The measured hypertriton mass $m_{^3_\Lambda\text{H}}$ is derived from the fitted parameter Δm by using a formula that takes into account the correction for the reconstruction shift and it is reported in the following:

$$\begin{aligned} m_{^3_\Lambda\text{H}} &= m_{\text{MCgen}} - \Delta m = m_{\text{MCgen}} - (m_{\text{MCrec}} - m_{\text{fit}}) \\ &= m_{\text{fit}} + (m_{\text{MCgen}} - m_{\text{MCrec}}). \end{aligned} \tag{6.3}$$

number of observed $^3_\Lambda$H The number of observed $^3_\Lambda$H (N_{obs}) derives from the invariant mass fit by multiplying the parameter f of $M(x)$ for the number of selected $^3_\Lambda$H candidates.

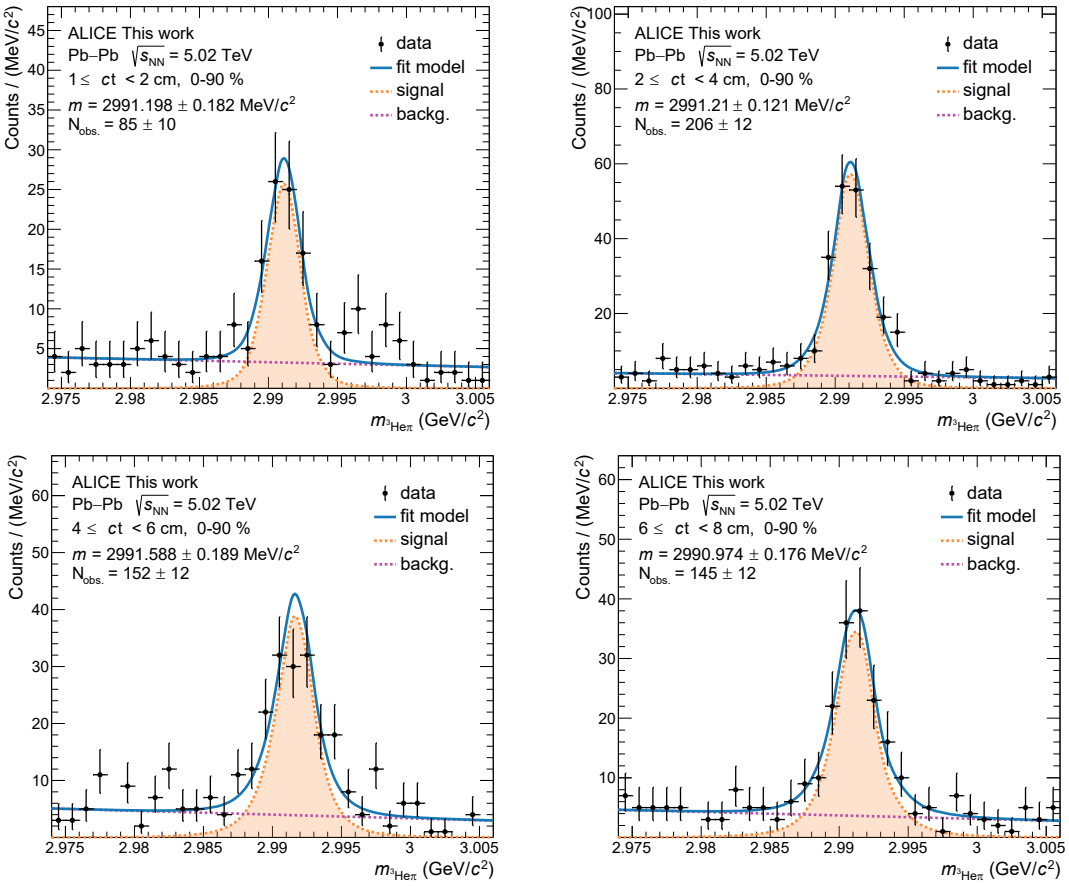

Figure 6.2: Invariant mass distribution of the $^3_\Lambda$H and $^{\overline{3}}_{\overline{\Lambda}}\overline{\text{H}}$ candidates fitted with the composite model (blue line) used to extract the number of observed hypertritons and the mass value. The figures refers to the first 4 ct-bins.

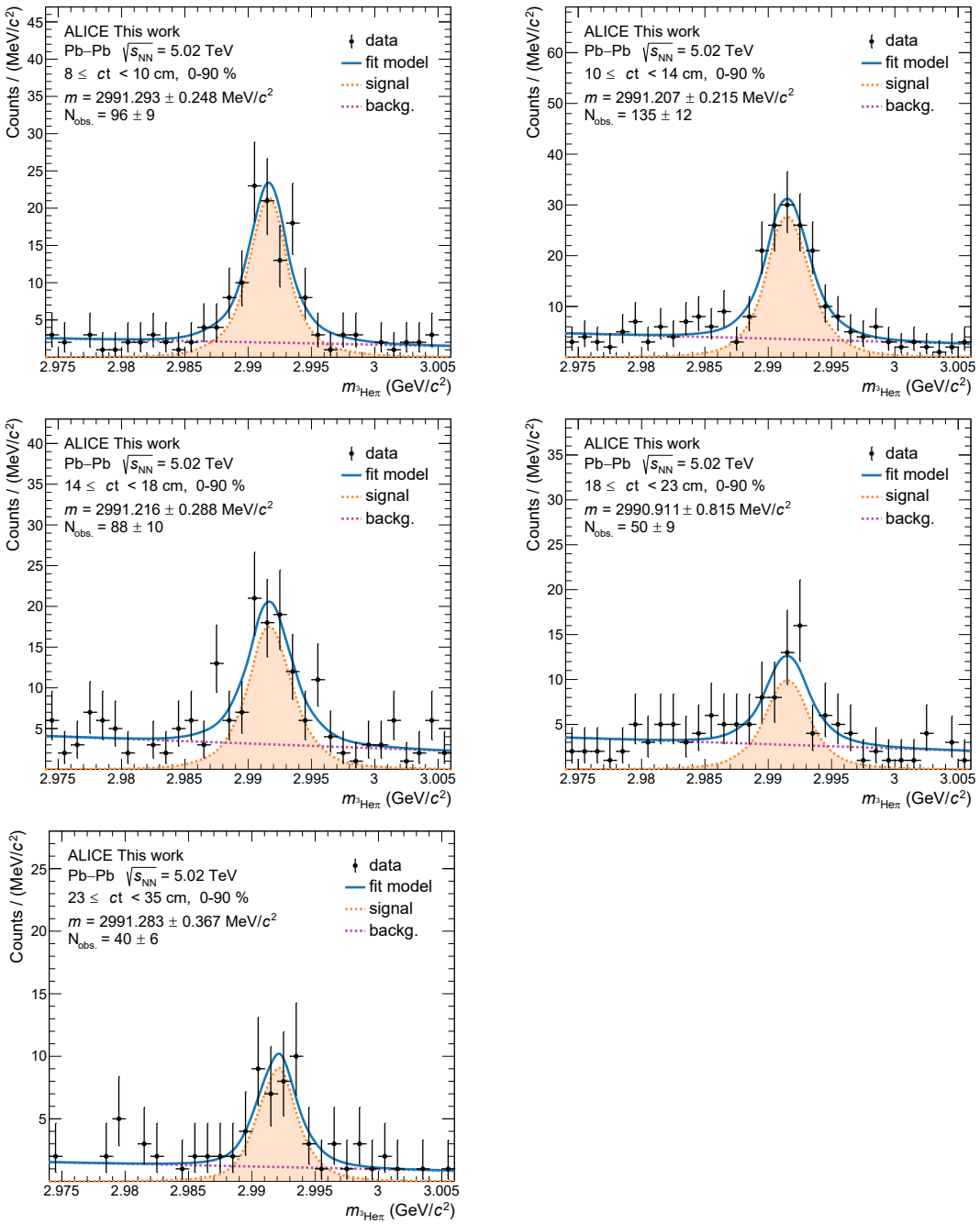

Figure 6.3: Invariant mass distribution of the ${}^{3}_{\Lambda}\mathrm{H}$ and ${}^{\overline{3}}_{\overline{\Lambda}}\overline{\mathrm{H}}$ candidates fitted with the composite model (blue line) used to extract the number of observed hypertritons and the mass value. The figures refers to the last 5 ct-bins.

6.2 Lifetime Measurement

The method used to measure the ${}^{3}_{\Lambda}\mathrm{H}$ and ${}^{3}_{\Lambda}\overline{\mathrm{H}}$ lifetime is the so-called $\mathrm{d}N/\mathrm{d}ct$ *spectrum method*. The method relies on the exponential fit of the number of ${}^{3}_{\Lambda}\mathrm{H}$ and ${}^{3}_{\Lambda}\overline{\mathrm{H}}$ 2-body decays over ct. The number of the 2-body decays as a function of the ct ($\mathrm{d}N/\mathrm{d}ct$) derives from the number of *observed* decays ($\mathrm{N}_{\mathrm{obs}}$) in the different ct-bins. Those numbers are then corrected with appropriate correction factors, considering the absorption in the detectors material, the pre-selection efficiency and the BDTs efficiency. Finally, the exponential fit of the $\mathrm{d}N/\mathrm{d}ct$ distributions provides the mean lifetime parameter $\tau({}^{3}_{\Lambda}\mathrm{H})$. The $\mathrm{d}N/\mathrm{d}ct$ spectrum is the method used by the ALICE Collaboration for previous hypertriton lifetime measurements [98, 100].

While the corrections for the pre-selection and the BDTs efficiencies are trivial, the absorption correction needs a detailed discussion. The following section provides insights into the calculation of the absorption correction.

6.2.1 Absorption Correction

The absorption correction (C_{abs}) is evaluated by simulating the passage of the ${}^{3}_{\Lambda}\mathrm{H}$ through the detector with GEANT4. In GEANT4 the transport of both ${}^{3}_{\Lambda}\mathrm{H}$ and ${}^{3}_{\Lambda}\overline{\mathrm{H}}$ is not distinguishable from that of the triton, underestimating the hypernuclei cross-section in the detector material. Therefore, the ${}^{3}\overline{\mathrm{He}}$ is used as a proxy for the ${}^{3}_{\Lambda}\mathrm{H}$ to study the absorption probability in the detectors.

According to [135] the ${}^{3}_{\Lambda}\mathrm{H}$ inelastic cross-section in the detector material is expected to be ≈ 1.5 times that of the ${}^{3}\overline{\mathrm{He}}$ ($\sigma_{\mathrm{inel.}\,{}^{3}\overline{\mathrm{He}}}$). Thus, dedicated Monte Carlo data with injected ${}^{3}\overline{\mathrm{He}}$ are used to estimate the absorption correction.

The ${}^{3}\overline{\mathrm{He}}$ p_{T} distribution has been reshaped with a sampling method – as was done for the MC hypertritons (Section 5.5.1) – to reproduce the measured distribution [121] and the passage of the ${}^{3}\overline{\mathrm{He}}$ has been simulated in GEANT4 with an inelastic cross-section increased by a factor 1.5 with respect to the nominal value. Each ${}^{3}\overline{\mathrm{He}}$ is assigned with a decay length (l) extracted from an exponential distribution with parameter $L_{{}^{3}_{\Lambda}\mathrm{H}} = 7.25\,\mathrm{cm}$. $L_{{}^{3}_{\Lambda}\mathrm{H}}$ represents the hypertriton mean decay length measured by ALICE in 2019 [100]. After travelling a distance l the ${}^{3}\overline{\mathrm{He}}$ is considered decayed. Thereby the ${}^{3}\overline{\mathrm{He}}$ mimics the hypertriton decay. Then, if the ${}^{3}\overline{\mathrm{He}}$ has any inelastic interactions with the material before getting to l it is considered absorbed. The fraction of absorbed ${}^{3}\overline{\mathrm{He}}$ defines the absorption probability $P(\mathrm{abs}) = \mathrm{N}_{\mathrm{abs}}/\mathrm{N}_{\mathrm{tot}}$, where $\mathrm{N}_{\mathrm{abs}}$ is the number of absorbed ${}^{3}\overline{\mathrm{He}}$ and $\mathrm{N}_{\mathrm{tot}}$ is the number of total ${}^{3}\overline{\mathrm{He}}$. The absorption correction C_{abs} is finally defined as $C_{\mathrm{abs}} = 1/(1 - P(\mathrm{abs}))$. Figure 6.4 shows $1 - P(\mathrm{abs})$ estimated in the ct-bins used in this analysis.

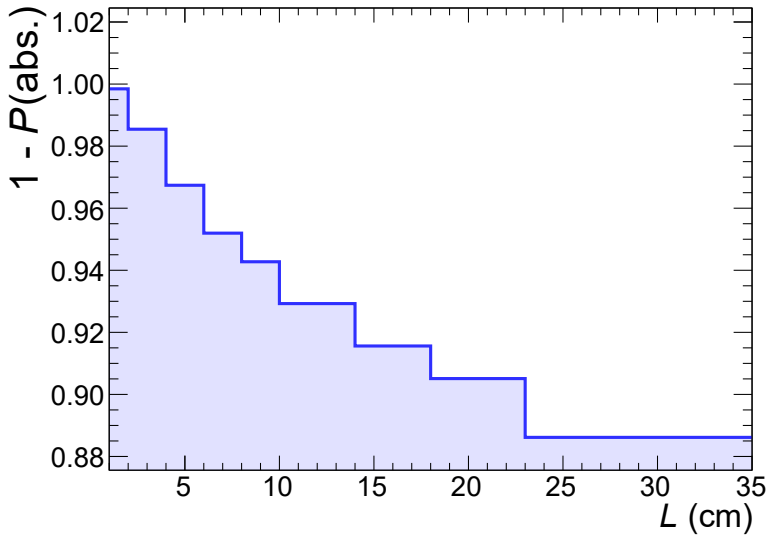

Figure 6.4: The inverse of the absorption correction C_{abs} as a function of ct in the 9 ct-bins used to build the $\mathrm{d}N/\mathrm{d}ct$ spectrum in this analysis.

6.2.2 $\mathrm{d}N/\mathrm{d}ct$ Spectrum

The $\mathrm{d}N/\mathrm{d}ct$ spectrum is obtained from $\mathrm{N}_{\text{obs}}(ct)$, the number of observed 2-body decays in a defined ct interval. In this analysis it is defined through the following formula:

$$\mathrm{d}N/\mathrm{d}ct = \mathrm{N}_{\text{obs}}(ct) \cdot C_{\text{eff.}} \cdot C_{\text{BDTs}} \cdot C_{\text{abs}} \cdot \frac{1}{\Delta ct} \tag{6.4}$$

where $C_{\text{eff.}} = 1/\mathrm{Eff}_{\text{p.s.}}$ and $C_{\text{BDTs}} = 1/\mathrm{Eff}_{\text{BDTs}}$ are the pre-selection and the BDTs efficiency respectively, C^{i}_{abs} follows the definition provided in the previous section and $\frac{1}{\Delta ct}$ is the width of the ct interval. The obtained $\mathrm{d}N/\mathrm{d}ct$ spectrum is fitted with an exponential function

$$N(ct) = N_0 \cdot e^{-\frac{ct}{c\tau}} \tag{6.5}$$

where N_0 is the normalisation of the parameter and τ is the mean ${}^{3}_{\Lambda}\mathrm{H}$ lifetime. The result of the fit is shown in Figure 6.5 where the blue dots represent the $\mathrm{d}N/\mathrm{d}ct$ distribution and the red line the fit function.

6.2.3 Systematic Uncertainties

The systematic uncertainties originate from the ${}^{3}_{\Lambda}\mathrm{H}$ selection, the signal extraction and the input cross-section used to estimate the ${}^{3}_{\Lambda}\mathrm{H}$ absorption in the detector. The different contributions are considered uncorrelated, and the total uncertainty derives from the quadratic sum of the individual contributions. A detailed description of each contribution to the total systematic uncertainty is reported in the following.

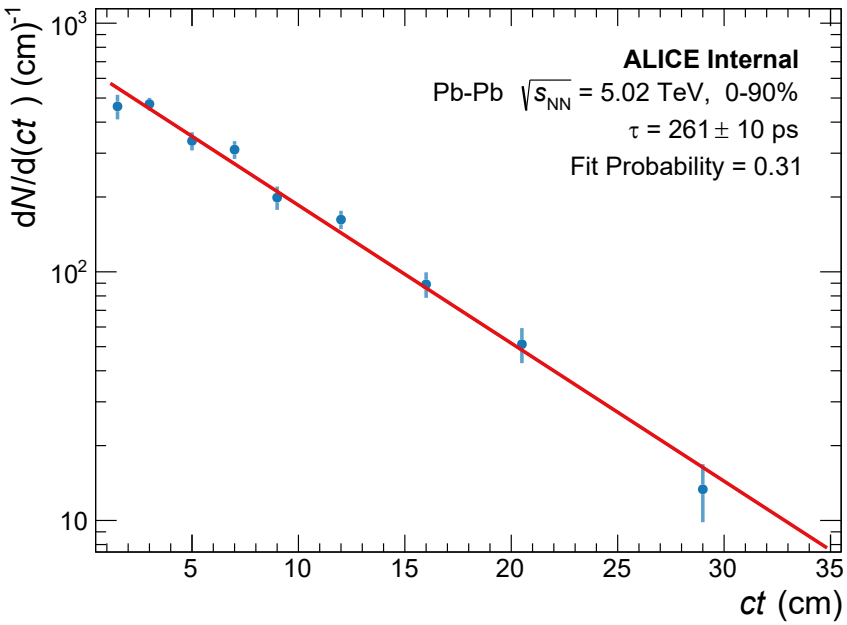

Figure 6.5: Corrected number of the hypertritons 2-body decays (blue points) fitted to extract the mean lifetime parameter with an exponential function (red line). The error bars represent the statistical uncertainties on the number of hypertritons dominated by the uncertainty on N_{obs}. The reported uncertainty on the mean lifetime is the statistical uncertainty obtained from the fit.

$^{3}_{\Lambda}$H selection and signal extraction

The impact of the BDTs selection and the signal extraction in determining the $^{3}_{\Lambda}$H lifetime is assessed with a multi-trial approach, allowing to estimate the related systematic uncertainty.

For each ct-bin 21 possible thresholds on the BDTs score and 3 possible fit models for the signal extraction are considered. The 21 thresholds corresponds to a span of $\pm 10\,\%$ for the efficiency range around the Th_{best} value with $1\,\%$ steps. This range ensures a good signal extraction for all the thresholds. The 3 fit models, instead, differs for the p.d.f. used for the background component $B(x)$. In addition to the first-degree polynomial, a second-degree polynomial and an exponential function are used. Those options for $B(x)$ ensure a fair background description in the signal region.

Considering 21 possible BDTs selections and 3 fit models, there are 63 possible signal extraction configurations for each ct-bin. It is possible to obtain a lifetime measurement by choosing a signal extraction configuration in each bin and then following the procedure described in Section 6.2.2 to compute the lifetime starting from N_{obs}. Therefore, having 9 ct-bins and 63 configurations in each bin, there are 63^9 possible and

independent lifetime measurements. The variation of the lifetime measurement with the different signal extraction configurations provides an estimate of the systematic uncertainties related to the candidates' selection and the signal extraction. The huge number of available combinations – $63^9 \approx 1.6 \times 10^{16}$ – makes the evaluation of all the possible measurements unfeasible. Therefore, 10^5 randomly sampled combinations have been considered. Figure 6.6 shows the distribution of the lifetime values obtained for the considered combinations. The standard deviation (RMS) of the distribution represents the systematic uncertainty related to the ${}^3_\Lambda\mathrm{H}$ selection and signal extraction, and it amounts to $5.3\,\mathrm{ps}$.

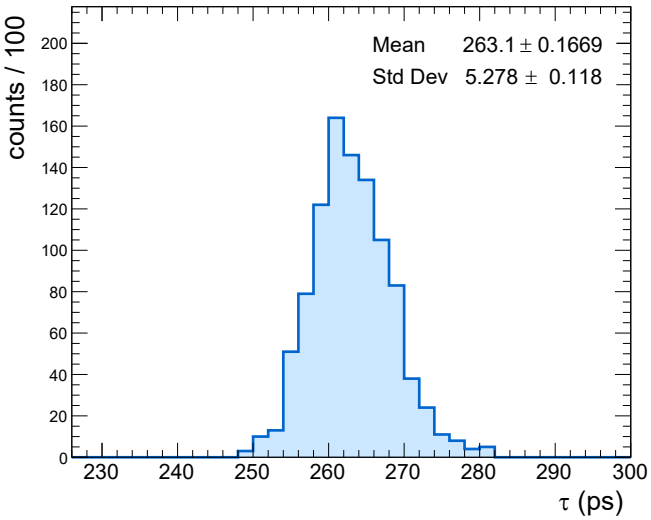

Figure 6.6: Distribution of the 10^5 lifetime values obtained by varying the ${}^3_\Lambda\mathrm{H}$ candidates selection and signal extraction configuration in each ct-bin. The variations of the configurations are randomly sampled in a $\pm 10\,\%$ range around the $\mathrm{Eff}_{\mathrm{BDTs}}$ value. The background model used for the fit of the invariant mass distribution is also randomly chosen between a first degree polynomial, a second degree polynomial and an exponential. The variations in each ct-bin are independent.

Absorption Correction

As already mentioned, the absorption correction derives from the ${}^3\overline{\mathrm{He}}$ cross-section increased by a factor 1.5, employed as a proxy for the ${}^3_\Lambda\mathrm{H}$ cross-section in the detector material. The systematic uncertainty related to this correction is estimated by computing an absorption correction with the nominal ${}^3\overline{\mathrm{He}}$ cross-section and measuring the corresponding lifetime. Then this lifetime value is compared to the one found using the increased ${}^3\overline{\mathrm{He}}$ cross-section. The absolute difference between the two measurements is

3 ps and represents the estimated systematic uncertainty associated with the absorption correction.

Table 6.1 summarises the contributions to the systematic uncertainty.

Systematic uncertainties	
Source	**Value**
Candidates selection and signal extraction	2 %
Absorption correction	1.1 %
Total	2.3 %

Table 6.1: Summary of the systematic uncertainties for the lifetime measurement. The total uncertainty is the quadratic sum of the single sources.

6.2.4 Results

The value of the ${}^{3}_{\Lambda}\mathrm{H}$ lifetime measured in this thesis is:

$$\tau({}^{3}_{\Lambda}\mathrm{H}) = 261 \pm 10\ (\mathrm{stat.}) \pm 6\ (\mathrm{syst.})\ \mathrm{ps}. \tag{6.6}$$

With a relative statistical uncertainty of $\sim 0.038\,\%$, this result increases the precision of the ALICE measurement of a factor ~ 4. Regarding the relative systematic uncertainty, the improvement with respect to the previous ALICE measurement amounts to a factor $\sim$ 3. The ML selection simplified the systematic uncertainty estimation related to the hypertriton selection. The BDTs maps the features - 11 in this case - in just one selection variable, the BDTs score. This allowed estimating the systematic uncertainty by only varying the BDTs score selection instead of varying 11 different selections independently. Furthermore, the multi-trial approach implemented for the exploration of the BDTs score space allows sampling of a considerable number of selection configurations (10^5), making the estimate robust.

The systematic uncertainty of the previous lifetime measurement, published by ALICE in 2019, was dominated by the contribution of the absorption correction estimate. The absorption correction contribution has been reduced with the improved method based on the ${}^{3}\overline{\mathrm{He}}$ cross-section. In the present analysis, with a relative value of $\sim 1.1\,\%$, it is not prevalent; indeed, it has an almost negligible contribution to the total systematic uncertainty.

The extremely small statistical and systematic uncertainties make this measurement the most precise ever achieved. Thanks to the increased number of events collected

by ALICE and the innovative analysis methods, including the ML-based selection of the hypertriton and the enhanced systematic uncertainty estimate, it was possible to achieve this outstanding result.

6.3 B_Λ Measurement

The Λ-separation energy (B_Λ) of the hypertriton is calculated by using the following formula:

$$B_\Lambda = m_{\mathrm{d}} + m_\Lambda - m_{^3_\Lambda\mathrm{H}} \tag{6.7}$$

where m_{d} is the mass of the deuteron (d), m_Λ is the mass of the Λ baryon and $m_{^3_\Lambda\mathrm{H}}$ is the mass of the $^3_\Lambda$H. Therefore the determination of the B_Λ relies on the measurement of the $^3_\Lambda$H mass.

The deuteron mass used in this analysis is that recommended by the Committee on Data of the International Science Council (CODATA) [136], while the Λ mass is taken from the PDG [4]. In Table 6.2 the values of the masses are reported. The following sections discuss and illustrate the $^3_\Lambda$H mass measurement achieved in this analysis and the related B_Λ value.

The accuracy of the invariant mass fit and the candidates' reconstruction are crucial elements to reaching a highly accurate and reliable mass measurement. Therefore, these aspects of the analysis have been cross-checked. The analysis of Monte Carlo data has shown that dedicated corrections are needed to avoid biases in the fit. Section 6.3.1 discuss the check of the fit procedure and the resulting mass correction. The possibility of a *mass shift* effect in the reconstruction of the invariant mass distribution, instead, has been checked by measuring the mass of the Λ baryon and comparing the measured mass with the PDG value [4]. The difference between the Λ mass obtained in this analysis and the PDG value serves to correct the mass shift. This part of the analysis is discussed in Section 6.3.2

Particle	**Mass** (MeV/c^2)
d	1875.612 942 57(57)
Λ	1115.683(6)

Table 6.2: Values of the mass of the deuteron and the Λ baryon used in this analysis to compute B_Λ. The value of the deuteron mass is taken from the CODATA [136] while the value of the Λ mass is taken from the PDG [4].

6.3.1 Correction for the Fit Bias

The crux of measuring the B_Λ is to have a precise and accurate measurement of the ${}^3_\Lambda$H mass. As already discussed, in each ct-bin, the fit of the invariant mass distribution provides a measurement of the ${}^3_\Lambda$H mass. In particular, in Section 6.1, it is highlighted that the actual fit parameter is not the ${}^3_\Lambda$H mass itself. It is, instead, the Δm parameter and the ${}^3_\Lambda$H mass is derived using Equation (6.3). Thus, it is crucial to check the fit procedure's accuracy and correct for any possible systematic error.

The fit of the Monte Carlo data with the model $M(x)$ provides an estimate of the accuracy of the mass measurement. It is important to remember here the definition of the fit parameter $\Delta m = m_{\text{MCrec}} - m_{\text{fit}}$, where m_{MCrec} is the mass of the MC used to build the signal p.d.f. with the KDE and m_{fit} is the mass of the fitted data. Based on this definition, if the fitted distribution is the MC itself, Δm is expected to be 0. Any deviation from 0 that is statistically significant represents a systematic error in the fit procedure – called *fit bias* in the context of this thesis. The mass measurement must consider the fit bias and correct this effect.

In Figure 6.7 the values found for the fit bias (C_{fit}) in all the ct-bins are reported. These values represent the correction to the value of the mass extracted from the invariant mass fit.

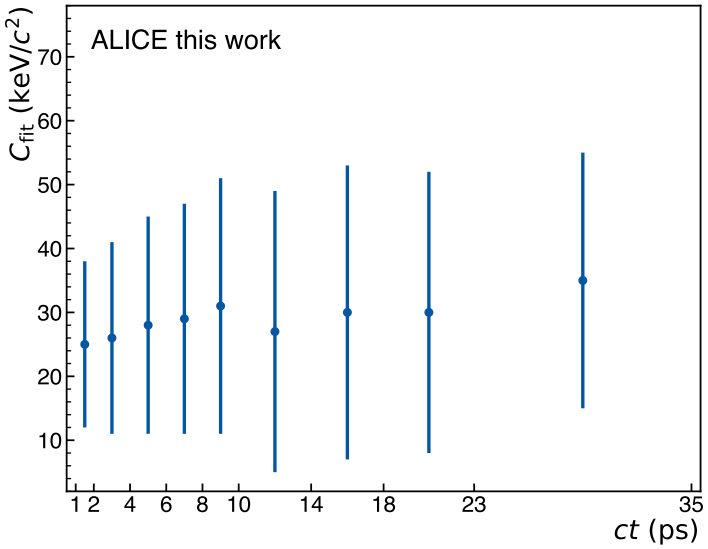

Figure 6.7: C_{fit} represent the value of the fit parameter when the fit procedure is applied to the Monte Carlo data used to build the KDE p.d.f. of the signal.

6.3.2 Correction for the Mass Shift

In this thesis, the *mass shift* effect is defined as the shift of the mass value of the measured particle with respect to the *true value*. It is due to the distortion of the invariant mass distribution induced by the experiment. The true value of the mass of any particle is unknown; however, it is possible to have an estimate of the mass shift measuring a particle whose mass is known with high precision[1] from different experiments (reference value). The comparison between the measured value and the reference value provides an estimate of the mass shift, allowing the application of a correction factor to overcome this systematic error.

The Λ baryon is the obvious choice for this test. In the assumption of loosely bound ${}^{3}_{\Lambda}\mathrm{H}$, the microscopic mechanism of the Λ decay is – almost – the same as that of the ${}^{3}_{\Lambda}\mathrm{H}$. Furthermore, the lifetimes of the Λ and the ${}^{3}_{\Lambda}\mathrm{H}$ are similar, and the same goes for the decay products, as already discussed in Section 3.1.1. Therefore, the experimental conditions for measuring the Λ mass are very close to those of the ${}^{3}_{\Lambda}\mathrm{H}$ mass, which makes this test on the Λ extremely reliable.

The study is done on a sample of Λ baryon candidates belonging to the same data set of Pb–Pb collisions at $\sqrt{s_{\mathrm{NN}}} = 5.02\,\mathrm{TeV}$ used for the ${}^{3}_{\Lambda}\mathrm{H}$ analysis. The Λ candidates are handled with the same procedure used for the ${}^{3}_{\Lambda}\mathrm{H}$ candidates. The process follows what is already discussed in Chapter 5. This section gives only a brief description, and more details are given where it is needed to highlight the differences with respect to the ${}^{3}_{\Lambda}\mathrm{H}$ analysis.

The Λ are identified reconstructing the charged mesonic 2-body decay (Equation (3.1)). The track cuts listed in Table 6.3 are applied to all the possible daughter tracks and the decay products – the protons and the pions – are then identified with the $n\sigma_{TPC}$ method described in Section 5.4.1 by requiring $n\sigma_{TPC} < 3$ for both species. The offline V^0-finder builds the Λ candidates starting from the identified daughter tracks, and the candidates with decay radius $R > 3\,\mathrm{cm}$ are rejected. Furthermore, only the candidates with $0.5 \leq p_{\mathrm{T}} < 3\,\mathrm{GeV}/c$ are considered for this analysis.

Track selections
$\lvert\eta\rvert < 0.8$
$n_{\mathrm{TPCcluster}} \geq 70$
$\chi^2/n_{\mathrm{TPCcluster}} \leq 4$
Kink topology rejected

Table 6.3: Summary of the selections applied to the analysed tracks.

[1] The uncertainty should be, in principle, negligible if compared to the expected uncertainty of the method to be tested.

The Training and Test set employs the Monte Carlo Λ for the signal, in analogy to what was done for the hypertriton. The background candidates are taken from the sidebands of the invariant mass distribution – see Section 5.5.1 and Section 5.5.2 for more details. The limits imposed to the invariant mass to define the sidebands are $m_{\mathrm{p}\pi} < 1100\,\mathrm{MeV}/c^2$ and $m_{\mathrm{p}\pi} > 1130\,\mathrm{MeV}/c^2$, considering that the expected value of the Λ mass is $1115.683\,\mathrm{MeV}/c^2$. The training features included in the Training and Test Set are listed in Table 6.4. A BDTs model is trained using the same set of hyperparameters used for the ${}^3_\Lambda\mathrm{H}$ analysis, and the BDTs score threshold is set to the value corresponding to $\mathsf{Eff}_{\mathrm{BDTs}} = 80\,\%$ that is the average value of the $\mathsf{Eff}_{\mathrm{BDTs}}$ for the hypertriton selection. Thanks to the extremely high number of selected Λ, it is possible to extract the signal as a function of the ct in more bins than those used in the ${}^3_\Lambda\mathrm{H}$ analysis. Finally, the invariant mass distribution is fitted using `RooFit`. The composite p.d.f. model used for the fit is similar to the one used for the ${}^3_\Lambda\mathrm{H}$. The only difference, in this case, is that the $S(x)$ p.d.f. is represented by a double-Gaussian Crystal Ball (DSCB) function [137, Appendix D] instead of a KDE model. The signal has been extracted in 60 ct-bins, from 5 to 35 ps.

Features variables	**Category**
$n\sigma_{\mathrm{TPC}}$ p	particle id.
$\mathrm{DCA}_{\mathrm{pv}}$ p	
$\mathrm{DCA}_{\mathrm{pv}}$ π	
$\mathrm{DCA}_{\mathrm{daug}} \leq 1\,\mathrm{cm}$	decay topology
$\mathrm{DCA}_{\text{mother-pv}}$	
$\cos(\theta_{\mathrm{pa}})$	

Table 6.4: List of the features with which the BDTs are fed.

In each ct-bin, the reconstruction shift – that is the difference between the mass of the generated MC Λ, and the mass of the reconstructed Λ: $m_{\mathrm{MCgen}} - m_{\mathrm{MCrec}}$ – is measured using the Monte Carlo data, and the Λ mass is consequently corrected. Therefore, after the correction, a value for the Λ mass experimentally measured ($m_\Lambda^{\mathrm{ALICE}}$) is obtained in each ct-bin. Finally, the difference (Δm_{lmb}) between $m_\Lambda^{\mathrm{ALICE}}$ and the PDG value of m_Λ is computed. In Figure 6.8 the values obtained for Δm_{lmb} are presented. In the plot the weighted average with the associated uncertainty $\overline{\Delta m_\Lambda} = 35.8 \pm 3.5\,\mathrm{keV}/c^2$ is also reported. It represents the estimate of the mass shift used to correct the value of the ${}^3_\Lambda\mathrm{H}$ mass in this analysis.

The correction for the mass shift is further checked with a multi-trial approach, similar to that used to estimate the systematic uncertainty for the candidates' selection

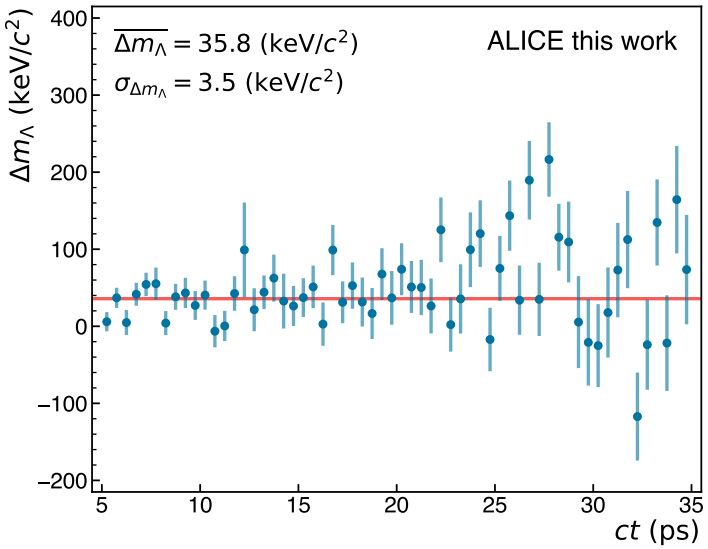

Figure 6.8: Difference between the Λ mass measured by ALICE using the same analysis techniques employed for the ${}^{3}_{\Lambda}\mathrm{H}$ in this thesis and the PDG value, as a function of the particle proper time. The weighted mean – reported in the top left of the plot and represented as a red line – is used as correction factor for the mass shift effect.

and signal extraction. For each ct-bin a set of variations of the Th corresponding to a $\pm 10\,\%$ $\mathrm{Eff}_{\mathrm{BDTs}}$ range is considered. Randomly picking a threshold among the possible 21, for each bin, one obtains a m_Λ measurement and consequently an estimate of the mass shift correction. By repeating this operation a sufficient number of times, one can estimate the mass shift correction variation for different signal selection configurations. Figure 6.9 shows the distribution of 10^4 mass shift corrections obtained following this procedure. The mean value of the distribution ($\overline{C_{\mathrm{shift}}} = 38.14 \pm 0.04\,\mathrm{keV}/c^2$, $\sigma_{C_{\mathrm{shift}}} = 3.68 \pm 0.03\,\mathrm{keV}/c^2$) is compatible within 1σ with the mass shift correction ($\overline{\Delta m_\Lambda} = 35.8 \pm 3.5\,\mathrm{keV}/c^2$). This confirms that the choice of the correction obtained using $\mathrm{Eff}_{\mathrm{BDTs}} = 80\,\%$ in all the bins is adequate.

6.3.3 ${}^{3}_{\Lambda}\mathrm{H}$ Mass Measurement

The value of ${}^{3}_{\Lambda}\mathrm{H}$ mass extracted from the invariant mass fit is corrected to consider the fit bias and the mass shift presented in the previous sections. Therefore, the corrected value of the ${}^{3}_{\Lambda}\mathrm{H}$ mass ($m^{\mathrm{cor}}_{{}^{3}_{\Lambda}\mathrm{H}}$) is:

$$m^{\mathrm{cor}}_{{}^{3}_{\Lambda}\mathrm{H}} = m_{{}^{3}_{\Lambda}\mathrm{H}} + C_{\mathrm{fit}} - C_{\mathrm{shift}} \tag{6.8}$$

where $m_{{}^{3}_{\Lambda}\mathrm{H}}$ is the mass obtained from the invariant mass fit (Equation (6.3)), C_{fit} is the correction for the fit bias and C_{shift} is the correction for the reconstruction shift – that

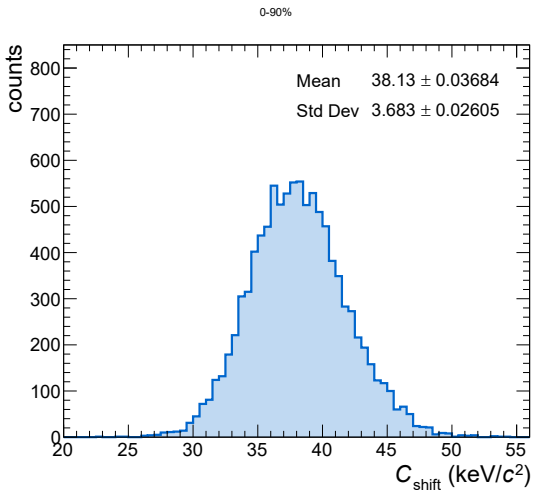

Figure 6.9: Distribution of 10^4 different mass shift corrections obtained by randomly variating the signal selection configuration for the measurement of the Λ mass.

is $C_{\text{shift}} = \overline{\Delta m_\Lambda}$. Finally, the measured value for the ${}^3_\Lambda$H mass ($m^{\text{ALICE}}_{{}^3_\Lambda\text{H}}$) is the weighted mean of the corrected masses measured in each ct-bin and it corresponds to:

$$m^{\text{ALICE}}_{{}^3_\Lambda\text{H}} = 2991.219 \pm 0.063\,\text{MeV}/c^2. \tag{6.9}$$

Figure 6.10 shows the $m^{\text{ALICE}}_{{}^3_\Lambda\text{H}}$ as a function of the ct; the red line represents the weighted mean and the orange area the statistical uncertainty related to the mean.

6.3.4 Systematic Uncertainties

The systematic uncertainty originates mainly from the candidates' selection and signal extraction as it is for the lifetime measurement presented in Section 6.2.3. A further cross-check is done to test the robustness of the analysis method by measuring the ${}^3_\Lambda$H mass on a sample of candidates selected using linear cuts instead of the BDTs. The study of the systematic uncertainty has been done directly on the B_Λ, the target of this analysis.

${}^3_\Lambda$H Selection and Signal Extraction

The estimate of the systematic uncertainty related to the ${}^3_\Lambda$H selection and signal extraction is done, basically, in the same way as that of the lifetime measurement (Section 6.2.3). For each ct-bin 21 possible thresholds on the BDTs score, corresponding to a $\pm 10\,\%$ efficiency range around the Th_{best} value, are considered. The variations on the fit model are done by changing the signal component $S(x)$ since, in the case of the mass measurement, it is more critical to evaluate the impact of the signal shape

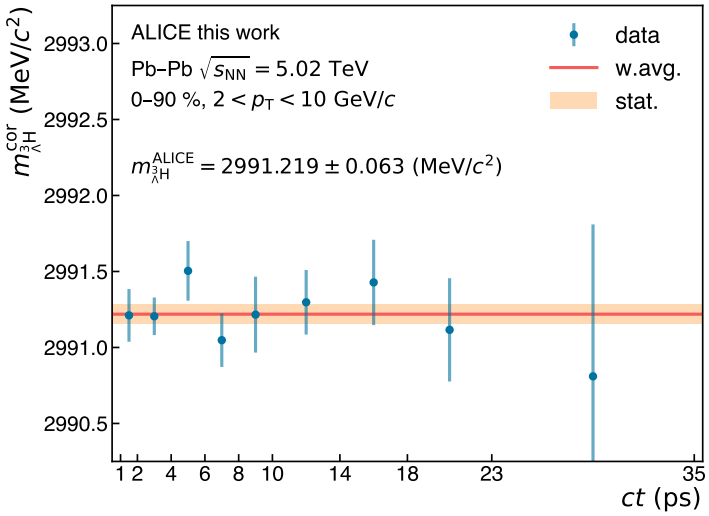

Figure 6.10: The corrected values of the hypertriton mass $m^{\text{cor}}_{^3_\Lambda\text{H}}$ (blue points) are shown as a function of the ct, together with the weighted average of the values (red line) that represent measured value of the $^3_\Lambda$H mass obtained in this work: $m^{\text{ALICE}}_{^3_\Lambda\text{H}}$. The orange area represents the statistical uncertainty on the weighted average.

on the measurement than the background shape. On the other hand, the background shape has been checked and found irrelevant in the derivation of the mass value. Two signal models are considered, the p.d.f. built using the KDE and the double-Gaussian Crystal Ball. It is possible to obtain a mass measurement – and consequently a B_Λ – by choosing a signal extraction configuration among the 42 available in each ct-bin, correcting the mass with the adequate factors and by computing the weighted average of the corrected values. However, again, the number of possible measurements is enormous. Therefore, 10^5 examples among the 42^9 possibilities are sampled, obtaining as many B_Λ measurements. The RMS of the distribution of the B_Λ values – shown in Figure 6.11 – corresponds to 27.5 keV. This value represents the estimate of the systematic uncertainty related to the $^3_\Lambda$H selection and signal extraction.

Cross-Check on the Λ Mass

The correction for the mass shift effect plays an essential role in this analysis. Since it relies on the ALICE measurement of the Λ mass (m^{ALICE}_Λ), it is essential to check this result.

The value of the Λ mass used for the mass shift correction derives from an ML-based selection of the Λ candidates, in analogy to what was done for the $^3_\Lambda$H selection. This value is cross-checked by measuring the Λ mass, selecting the candidates without the BDTs and using linear selections on the physical properties of the candidates. The set

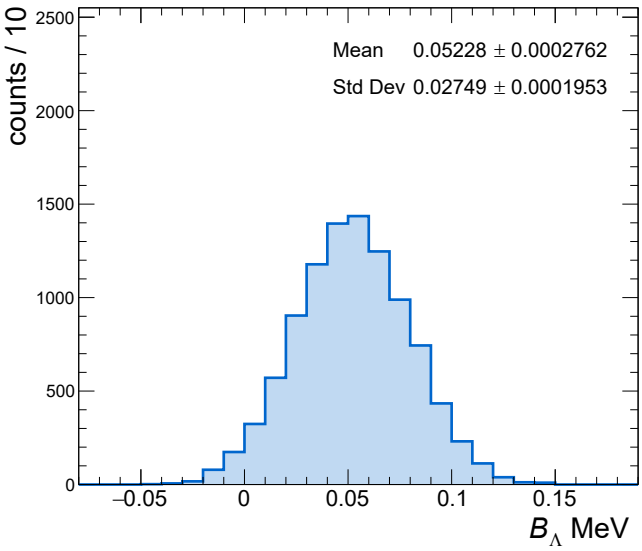

Figure 6.11: Distribution of the 10^5 B_Λ values obtained by varying the ${}^3_\Lambda$H candidates selection and signal extraction configuration in each ct-bin. The variations of the configurations are randomly sampled in a $\pm 10\,\%$ range around the $\mathrm{Eff}_{\mathrm{BDTs}}$ value. The signal model used for the fit of the invariant mass distribution is also randomly chosen between an MC based KDE of the signal and a double-Gaussian Crystal Ball. The variations in each ct-bin are independent.

of linear selections – reported in Table 6.5 – is the same used in ALICE for the measurement of the lambda lifetime. Using the linear selection, the mass of the Λ baryon is measured in different ct-bins. Figure 6.12 reports the difference between the measured mass and the PDG value, computed in each bin. The weighted mean of the differences is 50.3 ± 4.2 keV, and it represents an independent estimation of the mass shift correction factor.

The difference between the correction factor obtained with the ML selection ($C^{\mathrm{ML}}_{\mathrm{shift}}$) and the one obtained applying linear selections ($C^{\mathrm{lin}}_{\mathrm{shift}}$) is about $14\,\mathrm{keV}/c^2$. The discrepancy between the two values is significant in terms of Λ mass but well within the uncertainty on the ${}^3_\Lambda$H mass. The goal of the Λ mass measurement is to estimate the correction factor for the mass shift effect applied to the ${}^3_\Lambda$H mass. Therefore, the difference between the two methods results in uncertainty on the mass shift correction, and it is taken into account, introducing a further systematic uncertainty of $14\,\mathrm{keV}/c^2$.

Table 6.6 summarises all the contributions to the systematic uncertainty.

Features variables	**Category**
$\lvert\eta\rvert < 0.8$	track quality
$n_{\text{TPCcrossrows}} \geq 80$	
$n_{\text{TPCcluster}} \geq 80$	
$\chi^2/n_{\text{TPCcluster}} \leq 2.5$	
$n\sigma_{\text{TPC}}$ p < 3	particle id.
$n\sigma_{\text{TPC}}$ $\pi < 3$	
$0.2 < p_{\text{T}}^{\text{p}} < 10\,\text{GeV}/c$	V^0-finder
$0.2 < p_{\text{T}}^{\pi} < 2\,\text{GeV}/c$	
$\text{DCA}_{\text{daug}} < 1\,\text{cm}$	
$\text{DCA}_{\text{V0pv}} < 0.5\,\text{cm}$	
$R_{\text{pv-sv}} > 3\,\text{cm}$	
$\cos(\theta_{\text{pa}}) > 0.995$	

Table 6.5: List of the linear cuts used for the selection of the Λ candidates.

Systematic uncertainties	
Source	**Value**
Candidates selection and signal extraction	27.5 keV
C_{shift} - ML Vs. linear	14 keV
Total	31 keV

Table 6.6: Summary of the systematic uncertainties for the B_Λ measurement. The total uncertainty is the quadratic sum of the single sources.

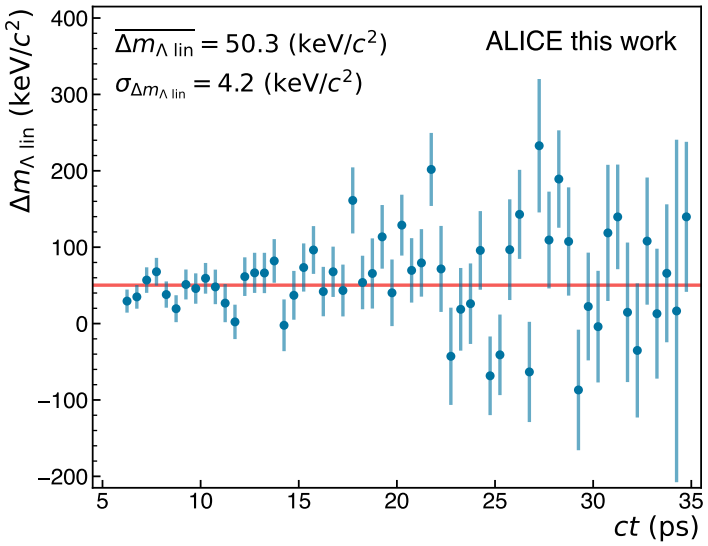

Figure 6.12: Difference between the Λ mass measured by ALICE using linear selections and the PDG value, as a function of the particle proper time. The weighted mean – reported in the top left of the plot and represented as a red line – is used to estimate the systematic uncertainty related to the correction factor for the mass shift effect.

6.3.5 Results

The final value of the ${}^{3}_{\Lambda}\mathrm{H}$ mass measured in this thesis is:

$$m_{{}^{3}_{\Lambda}\mathrm{H}} = 2991.219 \pm 0.063\ (\mathrm{stat.}) \pm 0.030\ (\mathrm{syst.})\ \mathrm{MeV}/c^2 \tag{6.10}$$

and consequently the value obtained for the Λ-separation energy is:

$$B_\Lambda = 77 \pm 63\ (\mathrm{stat.}) \pm 30\ (\mathrm{syst.})\ \mathrm{keV}. \tag{6.11}$$

The excellent precision of these measurements is the result of the innovative techniques adopted for signal extraction, the invariant mass fit, and the ALICE apparatus's tracking capabilities. The use of the ML-based selections, combined with the multi-trial approach for the selection variation, allowed the minimisation of the systematic uncertainties. Another crucial factor for the systematic uncertainty is the direct estimate of the mass shift effect obtained by measuring the Λ mass. This estimate made it possible to precisely correct the value extracted from the invariant mass fit. The correction allowed avoiding a large systematic uncertainty induced by a conservative estimate of the ALICE's bias in the reconstruction of the 2-body decay, leading the systematic uncertainty down to just 30 keV.

With a statistical uncertainty of 63 keV and a systematic uncertainty of 30 keV, this measurement outperforms the precision of the only other measurement obtained in modern digital-readout experiments [117], and it is more precise and robust than any other measurement of the hypertriton mass and B_Λ measurements.

Chapter 7

Conclusions

The focus of the research project carried on with this thesis is the study of the hypertriton features by measuring its lifetime and separation energy. In particular, the purpose was to address the hypertriton lifetime puzzle by measuring its lifetime and Λ-separation energy with the highest precision possible. In fact, these measurements are of utter importance to finally shed light on the hypertriton structure and provide new insight for a better understanding of the hyperon-nucleon interactions.

The ALICE experiment, in past years, had already proved to be highly competitive with the other leading experiments worldwide for the study of the hypertriton. Moreover, thanks to its outstanding tracking and PID performances and the increased integrated luminosity delivered by the LHC during the Run 2 data taking, a step forward in the precision of the lifetime and B_Λ measurement was expected. However, the innovative analysis techniques adopted for the hypertriton identification and the improvements in the systematic uncertainty analysis allowed to exceed the expectations.

This final chapter is devoted to discussing the findings of this research by comparing both the lifetime and the Λ-separation energy to the previous experimental results and the theoretical expectations. Ultimately, these results can be summarised by two summary plots that are reported in Figure 7.1 and Figure 7.2.

In Figure 7.1, the lifetime obtained in this thesis ($\tau(^{3}_{\Lambda}\mathrm{H})_{\mathrm{thesis}}$) is compared with the other measurements performed in recent years with digital readout experiments and with state-of-the-art theoretical calculations. As mentioned in the previous chapter, $\tau(^{3}_{\Lambda}\mathrm{H})_{\mathrm{thesis}}$ is the most precise determination of the $^{3}_{\Lambda}\mathrm{H}$ lifetime ever achieved. It is in agreement with the earlier ALICE measurements [98, 100], with a maximum discrepancy lower than 1.5σ. Excluding the STAR (2018) measurement [99] - around 3σ away - $\tau(^{3}_{\Lambda}\mathrm{H})_{\mathrm{thesis}}$ is also compatible with the previous measurements obtained by STAR [81] and HypHI [96]. However, the compatibility between the measurements is mainly due to the significant uncertainties of STAR (2010) and HypHI (2013). In addition, the value of $\tau(^{3}_{\Lambda}\mathrm{H})_{\mathrm{thesis}}$ is compatible with the lifetime of the free Λ baryon.

The value of $\tau(^{3}_{\Lambda}\mathrm{H})_{\mathrm{thesis}}$ is also in full agreement with one of the most recent prediction reported in [103]. In this work, Hildenbrand et al. computed the hypertriton

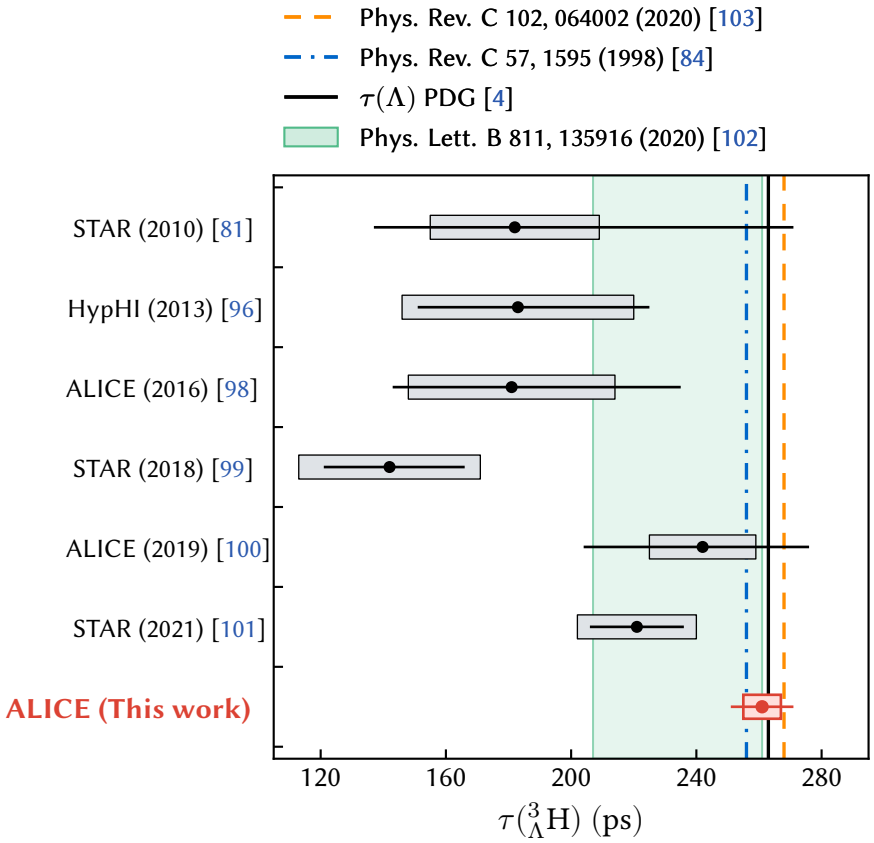

Figure 7.1: $^{3}_{\Lambda}$H lifetime value (red point) obtained in this analysis compared to published results from digital readout experiments (black points). The vertical lines and bands represent state-of-the-art theoretical calculations of the $^{3}_{\Lambda}$H lifetime.

lifetime as a function of the $\tau(^{3}_{\Lambda}\mathrm{H})$ in an effective field theory with Λ and deuteron as degrees of freedom. Assuming $B_{\Lambda} = 130\,\mathrm{keV}$, which means the hypertriton is loosely bound, they found $\tau(^{3}_{\Lambda}\mathrm{H}) \approx 268\,\mathrm{ps}$ that is extremely close to the $\tau(\Lambda)$ and in complete agreement with the outcomes of the present thesis. Kamada et al. estimated $\tau(^{3}_{\Lambda}\mathrm{H}) = 256\,\mathrm{ps}$ [84], also in good agreement with $\tau(^{3}_{\Lambda}\mathrm{H})_{\mathrm{thesis}}$. Their calculation relies on a rigorous determination of the $^{3}_{\Lambda}$H wave function as a solution of the three-body Faddeev equations and includes realistic NN and YN interactions. The predictions of Pérez-Obiol et al., obtained in a chiral effective field theory framework [102], are particularly interesting. They predict a wide range of lifetimes depending on the assumption of the B value. So, it follows that for compact hypertriton -i.e. high B_{Λ}- the predicted lifetime is much lower than the result of this thesis. Instead, the predictions are compatible with the value of $\tau(^{3}_{\Lambda}\mathrm{H})_{\mathrm{thesis}}$ expected for a loosely bound hypertriton -i.e. low B_{Λ}. Therefore, one can conclude that the hypertriton lifetime measured in this thesis

strongly supports the loosely bound nature of the hypertriton.

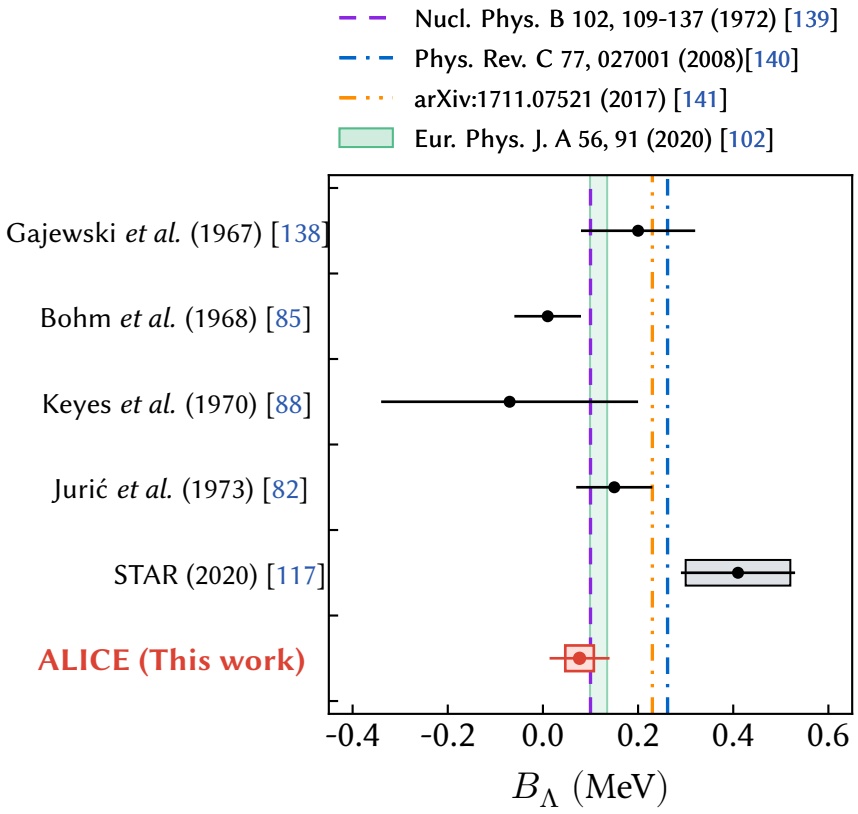

Figure 7.2: ${}^{3}_{\Lambda}\mathrm{H}$ B_Λ value (red point) obtained in this analysis com- pared to published results (black points). The vertical lines and bands represent state-of-the-art theoretical calculations of the ${}^{3}_{\Lambda}\mathrm{H}$ B_Λ.

The second crucial plot of this thesis is Figure 7.2, in which the hypertriton Λ-separation energy measured in this thesis ($B_{\Lambda\,\mathrm{thesis}}$) is compared with previous measurements and theoretical calculations. A direct comparison with the late sixties [85, 138] and early seventies measurements [82, 88] is not trivial. Those measurements performed in bubble chambers and nuclear emulsions were affected by systematic uncertainties of which an estimate is not available. However, the most accepted value of B_Λ (0.13 ± 0.05 (stat.) $\pm$ 0.04 (syst.) MeV) relies on a combined analysis of the data collected in [82] and [85] and $B_{\Lambda\,\mathrm{thesis}}$ is in full agreement with this value. The most recent measurement performed by STAR [117] instead is 1.8σ from $B_{\Lambda\,\mathrm{thesis}}$, but it should be noted that it is affected by large uncertainties. For what concerns the theoretical calculations, the predictions from SU(6) quark model for baryon-baryon interactions [140] and auxiliary field diffusion Monte Carlo [141] are disfavoured. The predictions

from SU(3) χEFT [102] and Dalitz et al. [139] - based on a simple model employing ΛN and ΛNN potentials - are in full agreement with $B_{\Lambda\ \text{thesis}}$.

It is essential to mention that the STAR measurement showed some tension with the common view of a loosely bound hypertriton, leading the community to question the hypertriton nature. However, the uncertainties of those measurements did not allow to discern among different hypothesis. In the light of the results presented in this thesis, it is possible to say that the experimental findings strongly support the hypothesis that the hypertriton is a loosely bound hypernucleus, with a B_Λ compatible with zero and a mean lifetime close to that of a free Λ baryon. Therefore, it is questionable whether it still makes sense to talk about a "hypertriton puzzle".

Appendix A

Additional figures

In this appendix, additional figures that could not be found space in the text are reported for completeness.

The comparison of the features distributions for each ct-bin of the training and test set are presented in Figures A.1, A.2, A.3, A.4, A.5, A.6, A.7, A.8 and A.9. The evolution of the probability density functions of each feature through the different ct-bins are presented in Figures A.10a, A.10b, A.10c, A.10d, A.11a, A.11b, A.11c, A.11d, A.12a, A.12b and A.12c. The signal and the background components are compared to show their different behaviour. Figures A.13, A.14 and A.15 shows the comparisons of the correlation matrix of the signal and the background component of the training and test set for each ct-bin. The distributions of the BDTs score in the training and test set are compared, and the sensitivity and the specificity of the models in the different ct-bins are presented in Figures A.16 and A.17 and **??**. Figures A.18, A.19 and A.20 are related to the BDTs selection optimization procedure. On the left the target functions of the optimization – i.e. the $S \times \mathrm{Eff}_{\mathrm{BDTs}}$ – as a function of the threshold on the BDTs score are presented for all the models. On the right, the invariant mass distributions of the data and pseudo-data – used to estimate the expected significance – obtained selecting with the optimized threshold are presented.

The comparison of the invariant mass distribution of the reconstructed MC hypertritons with the p.d.f. obtained with the KDE and a gaussian fitted to the distribution, for all the ct-bins, is presented in Figure A.21.

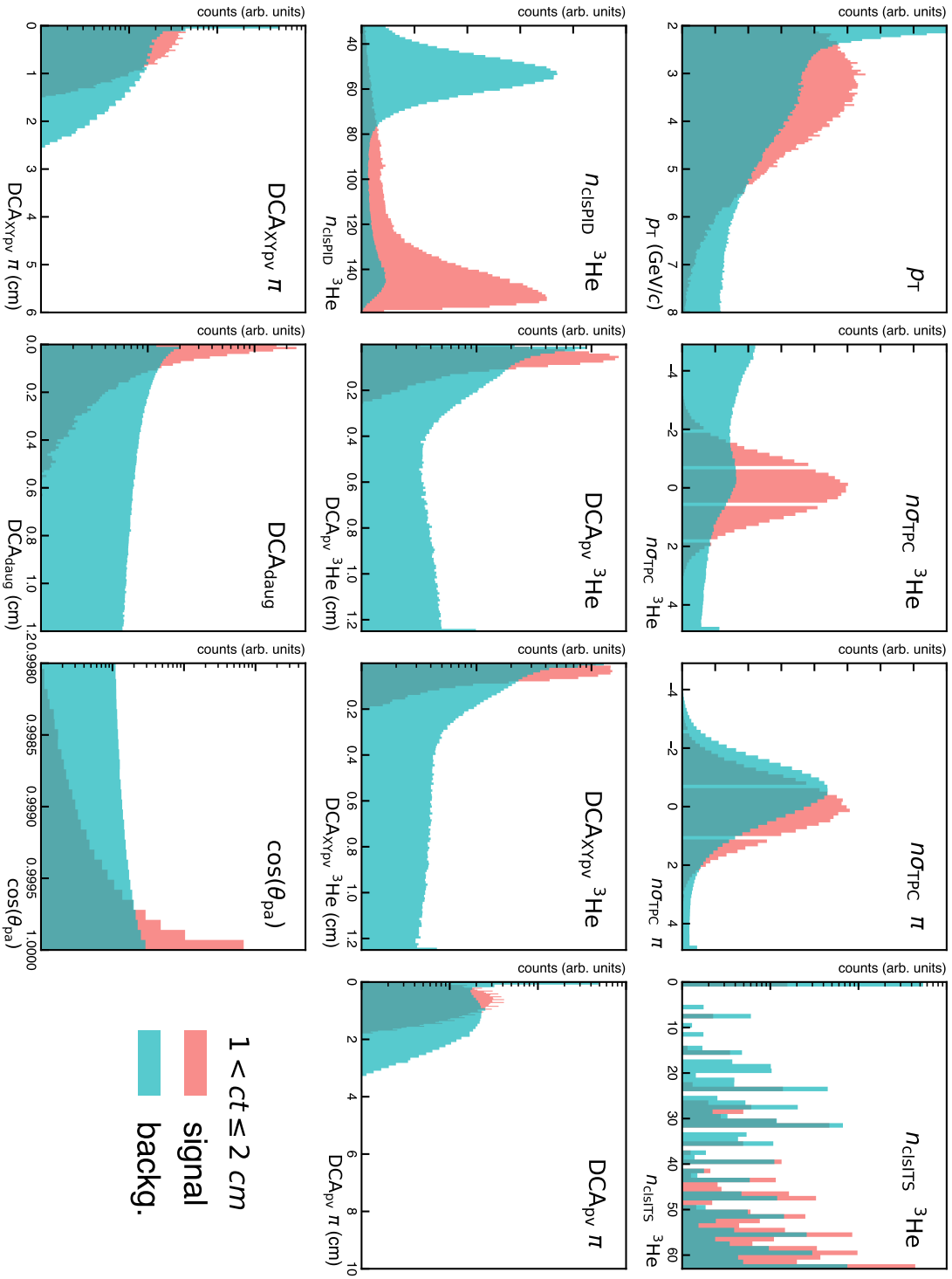

Figure A.1: Comparison between the signal component (red) and the background component (green water) of the training and test set in the $1 < ct \leq 2$ cm interval.

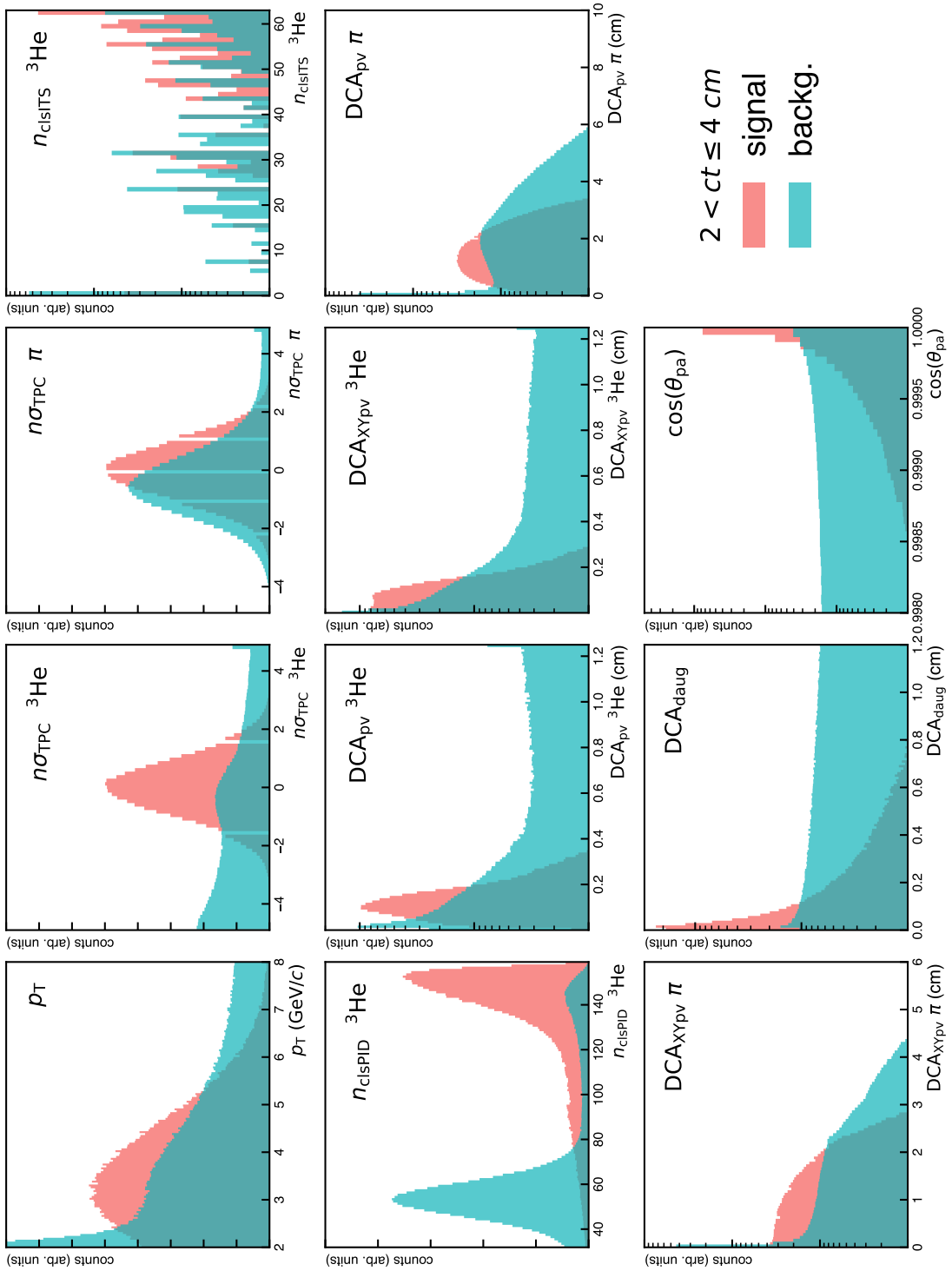

Figure A.2: Comparison between the signal component (red) and the background component (green water) of the training and test set in the $2 < ct \leq 4$ cm interval.

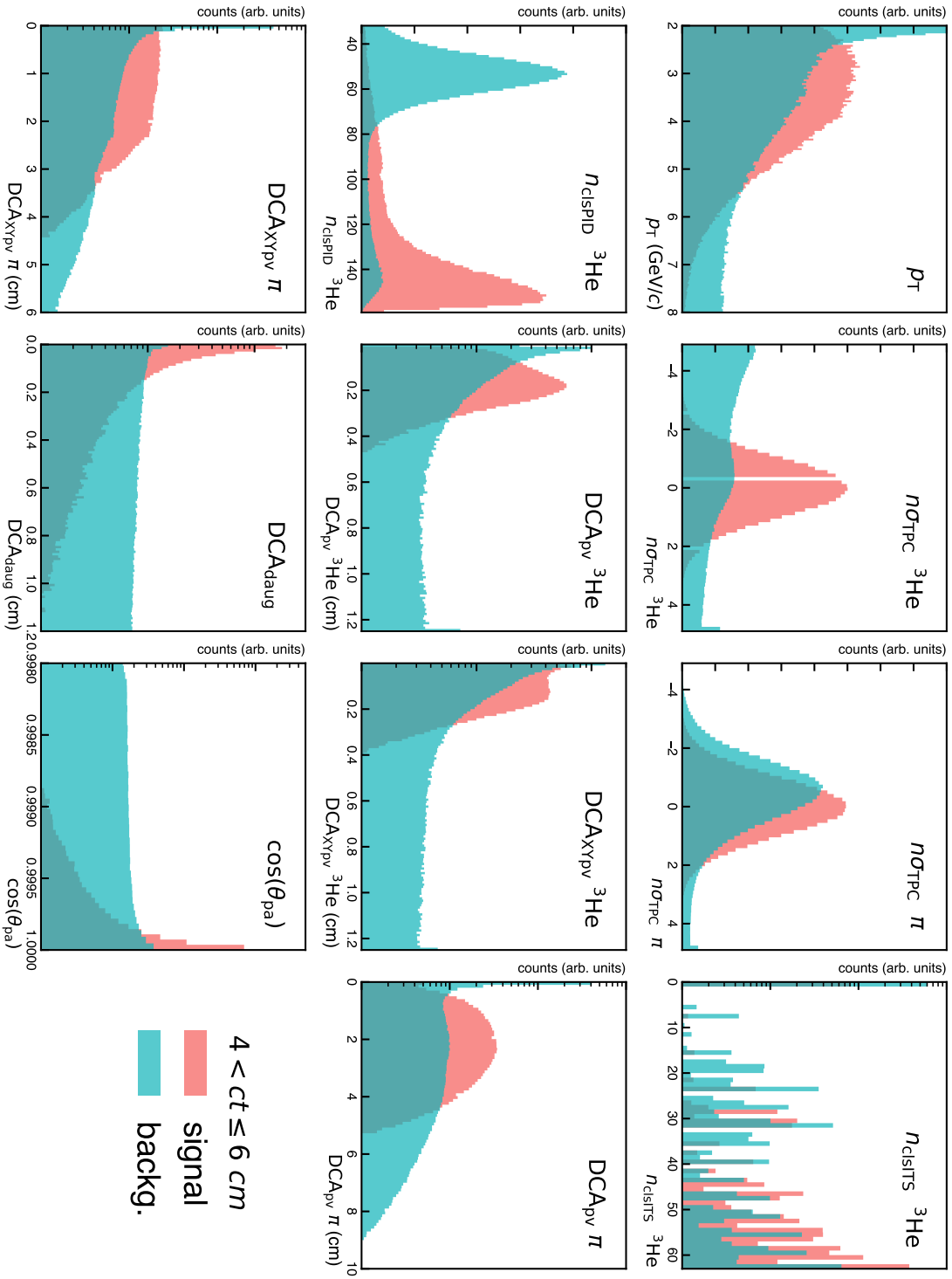

Figure A.3: Comparison between the signal component (red) and the background component (green water) of the training and test set in the $4 < ct \leq 6$ cm interval.

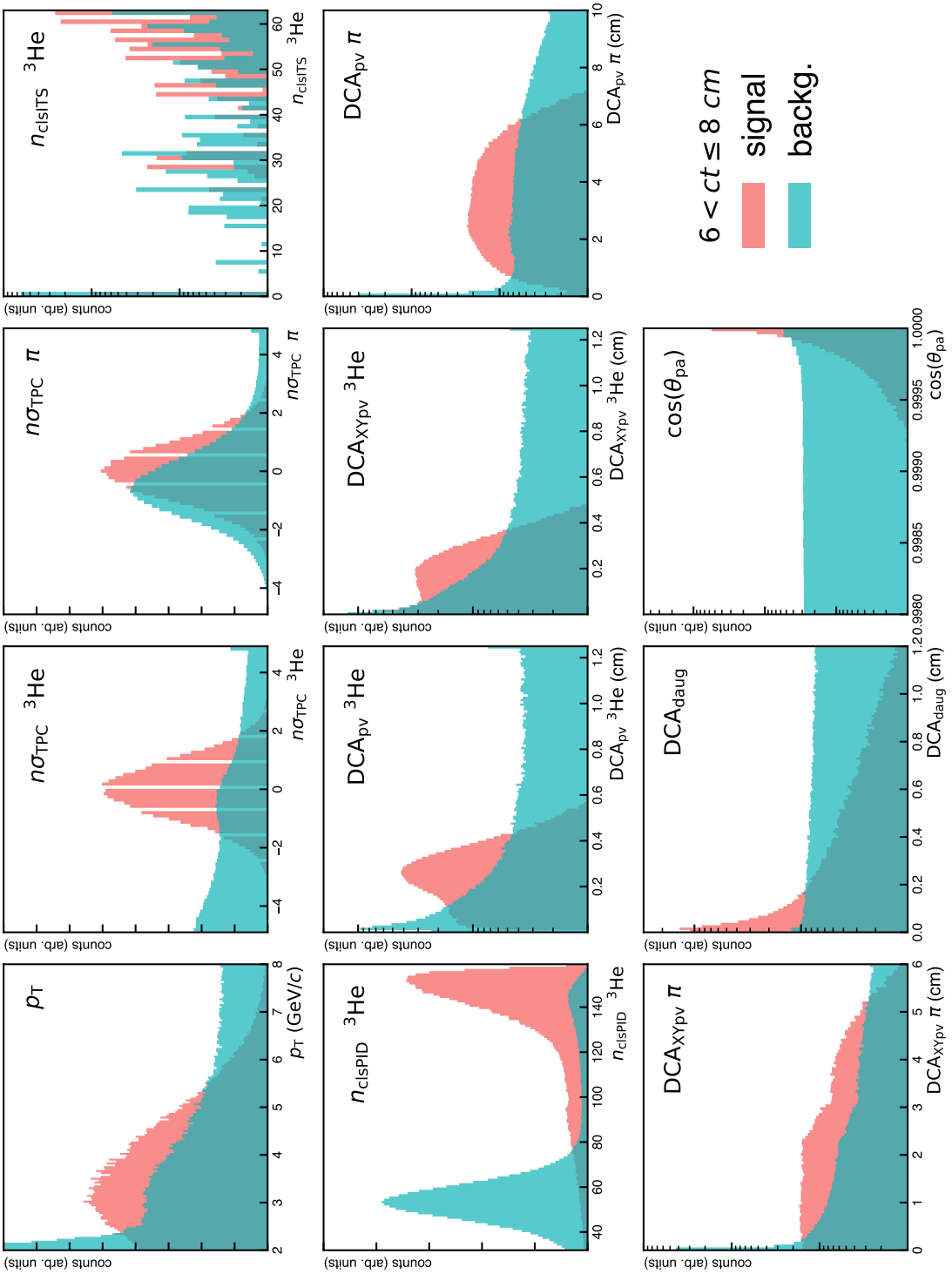

Figure A.4: Comparison between the signal component (red) and the background component (green water) of the training and test set in the $6 < ct \leq 8$ cm interval.

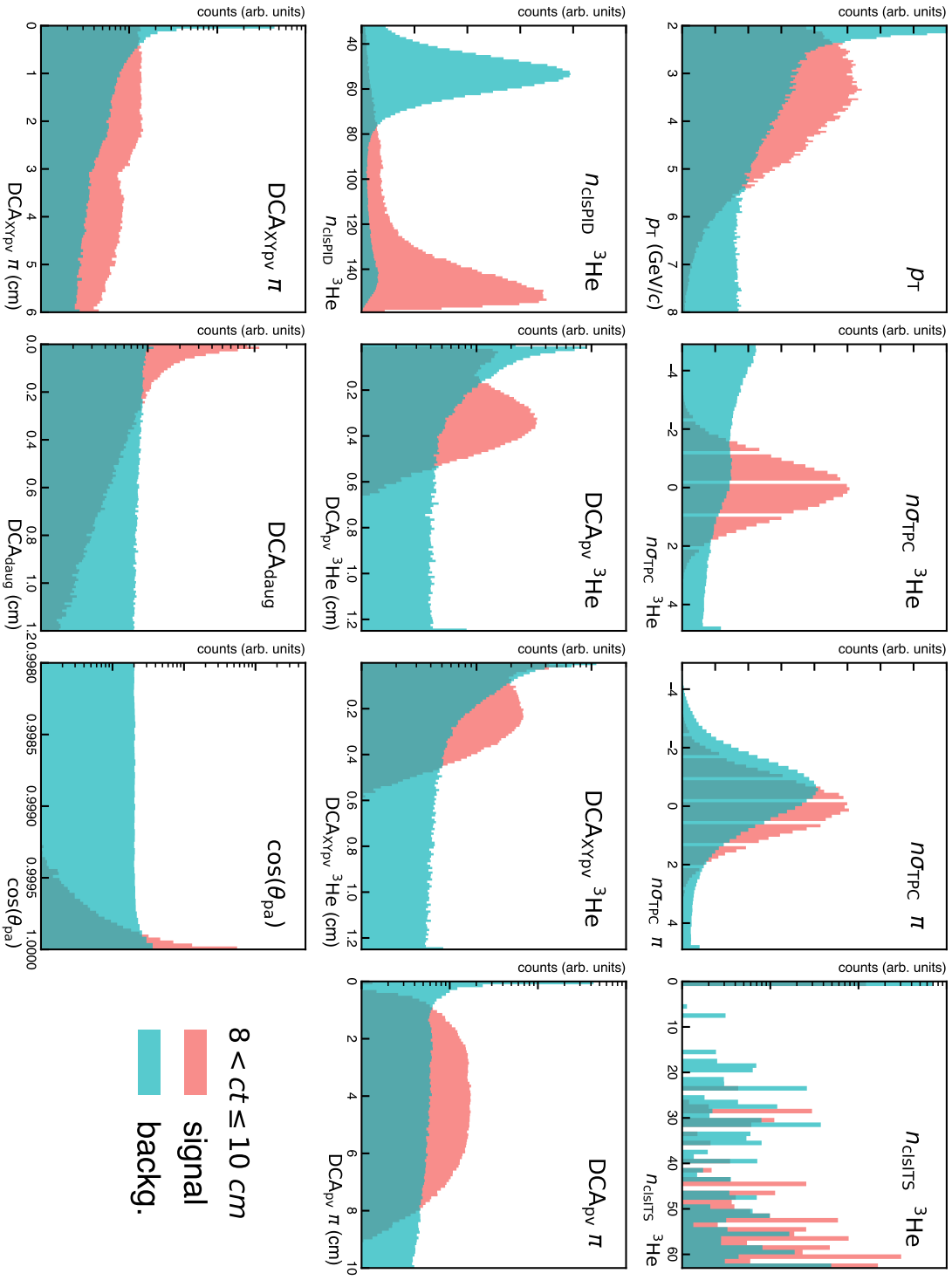

Figure A.5: Comparison between the signal component (red) and the background component (green water) of the training and test set in the $8 < ct \leq 10$ cm interval.

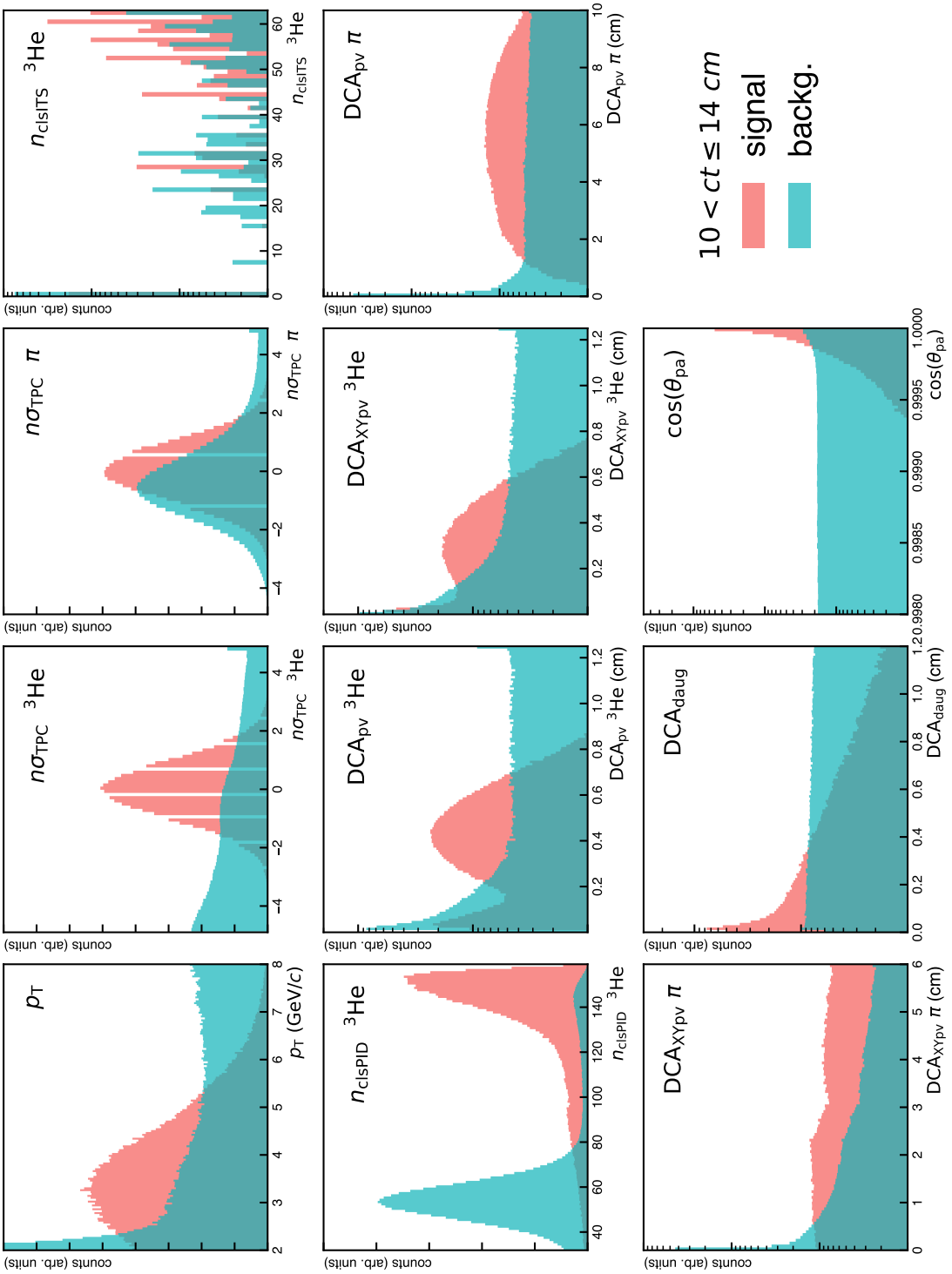

Figure A.6: Comparison between the signal component (red) and the background component (green water) of the training and test set in the $10 < ct \leq 14$ cm interval.

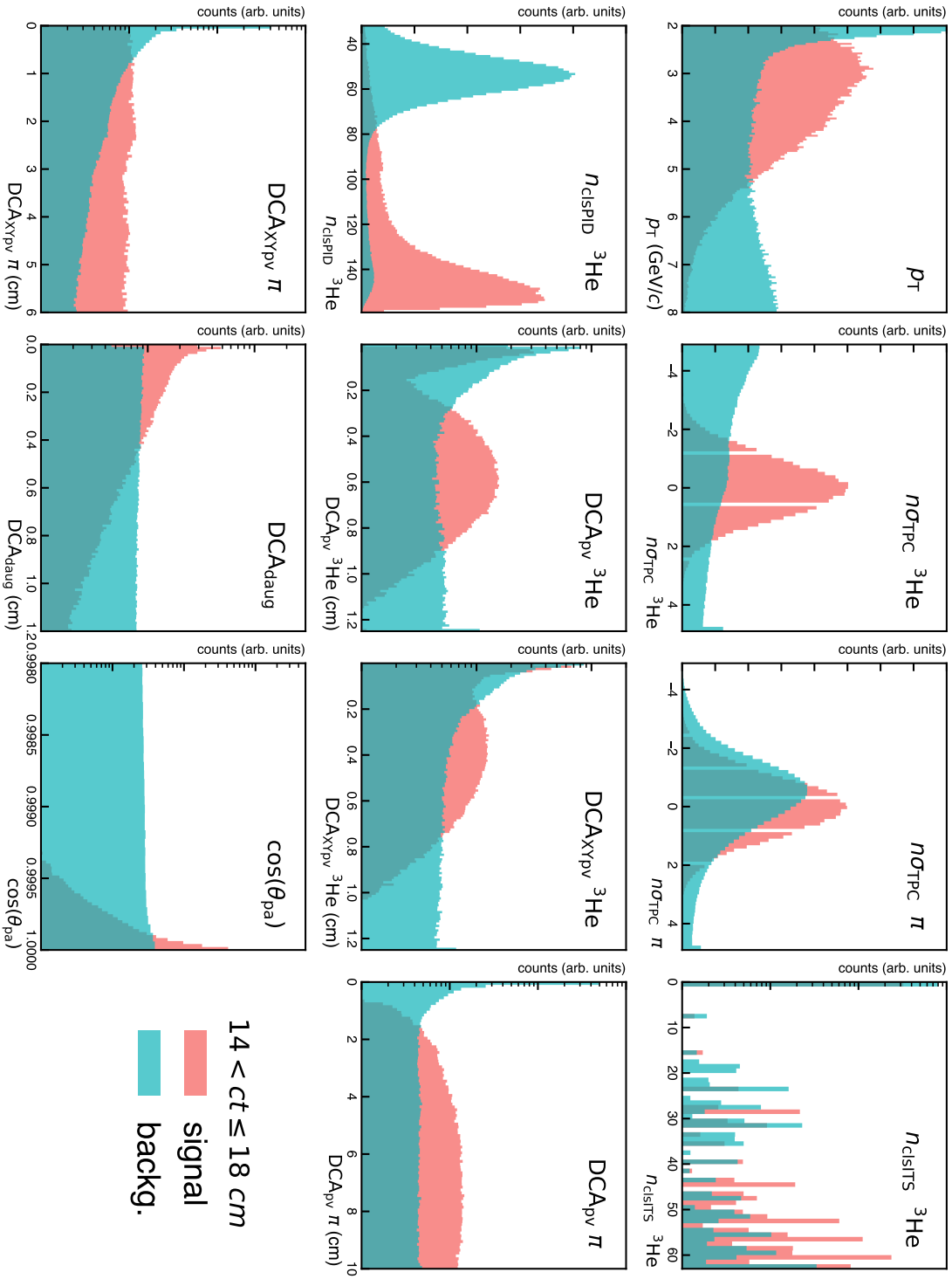

Figure A.7: Comparison between the signal component (red) and the background component (green water) of the training and test set in the $14 < ct \leq 18$ cm interval.

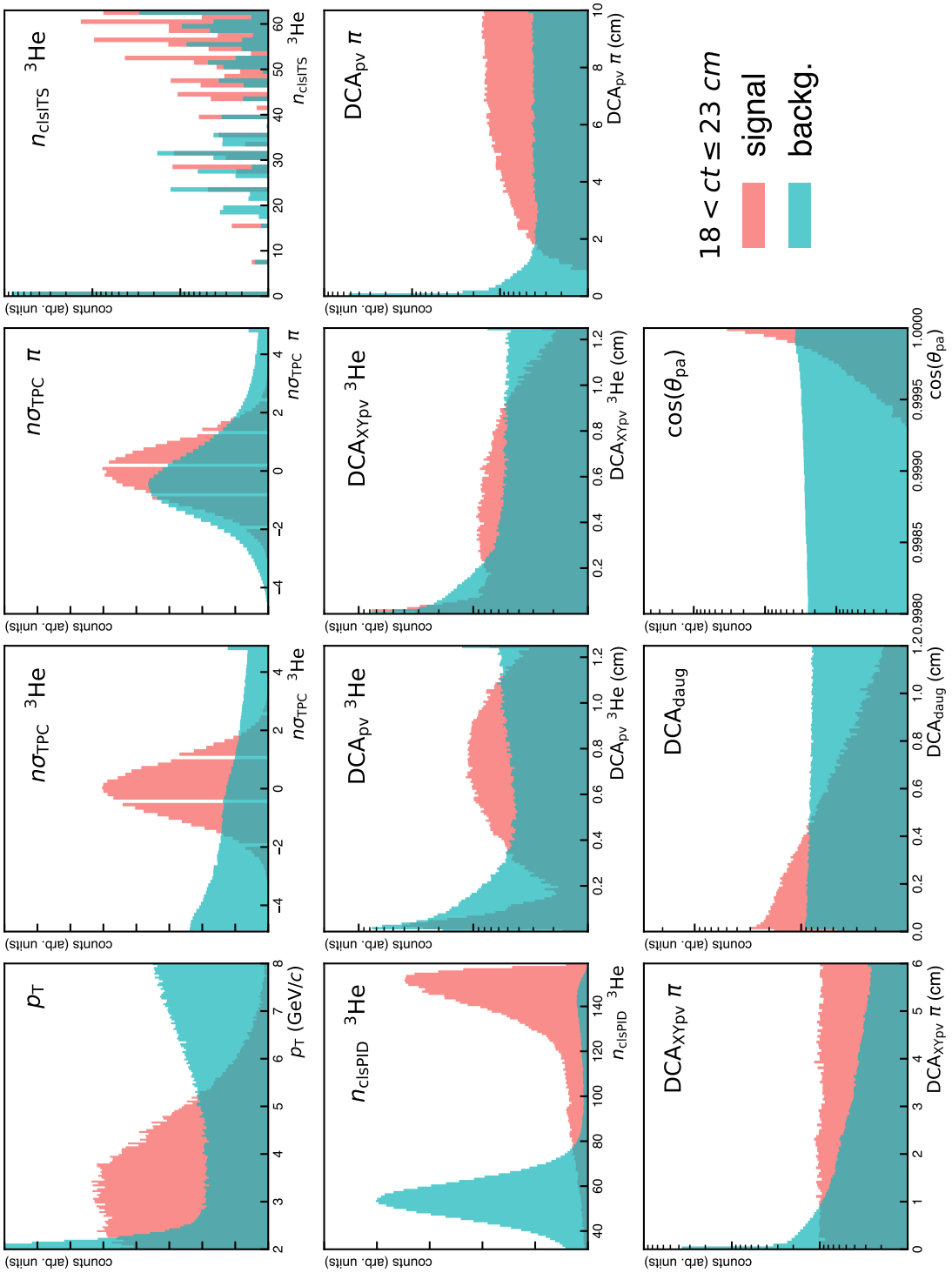

Figure A.8: Comparison between the signal component (red) and the background component (green water) of the training and test set in the $18 < ct \leq 23$ cm interval.

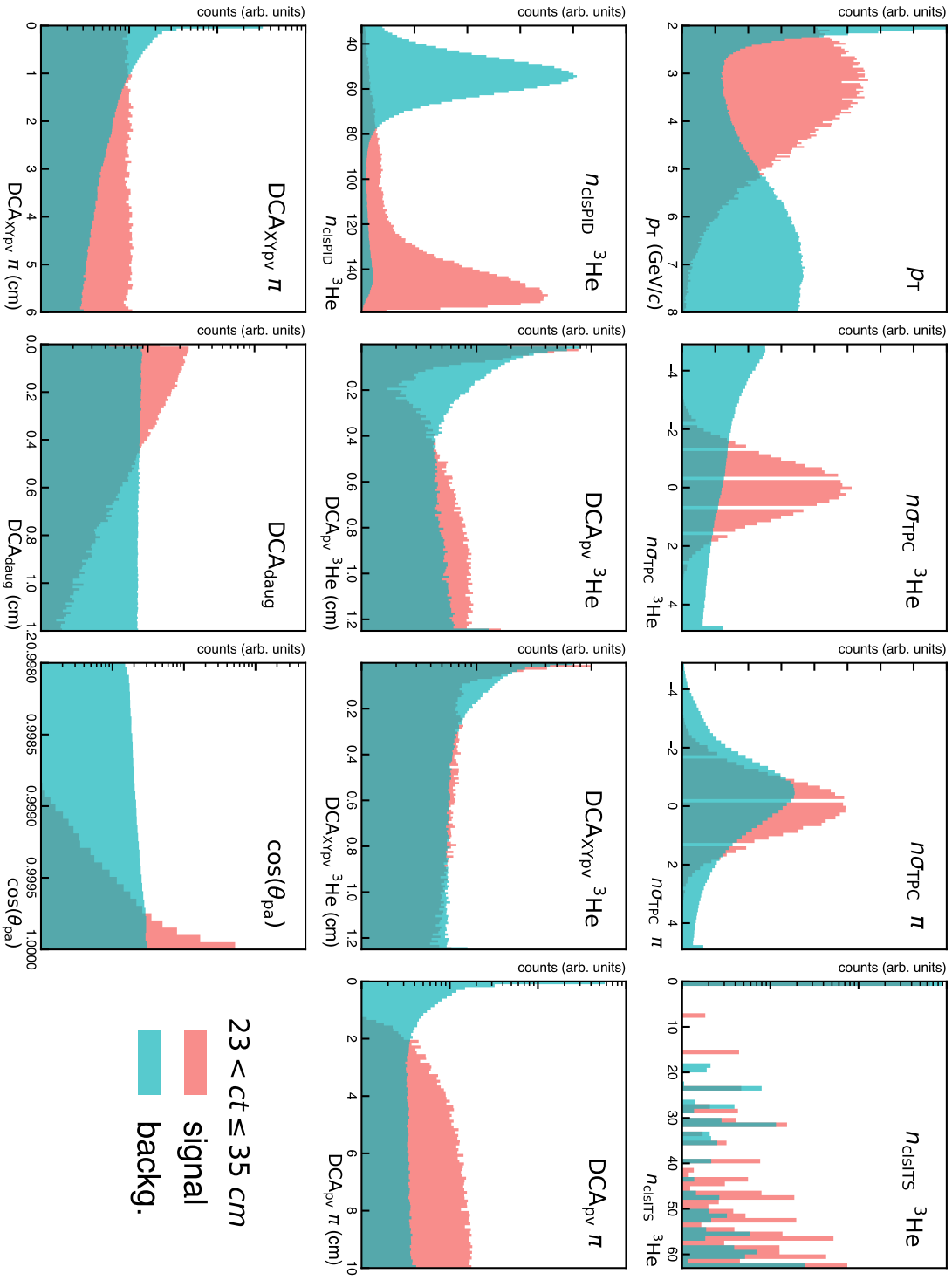

Figure A.9: Comparison between the signal component (red) and the background component (green water) of the training and test set in the $23 < ct \leq 35$ cm interval.

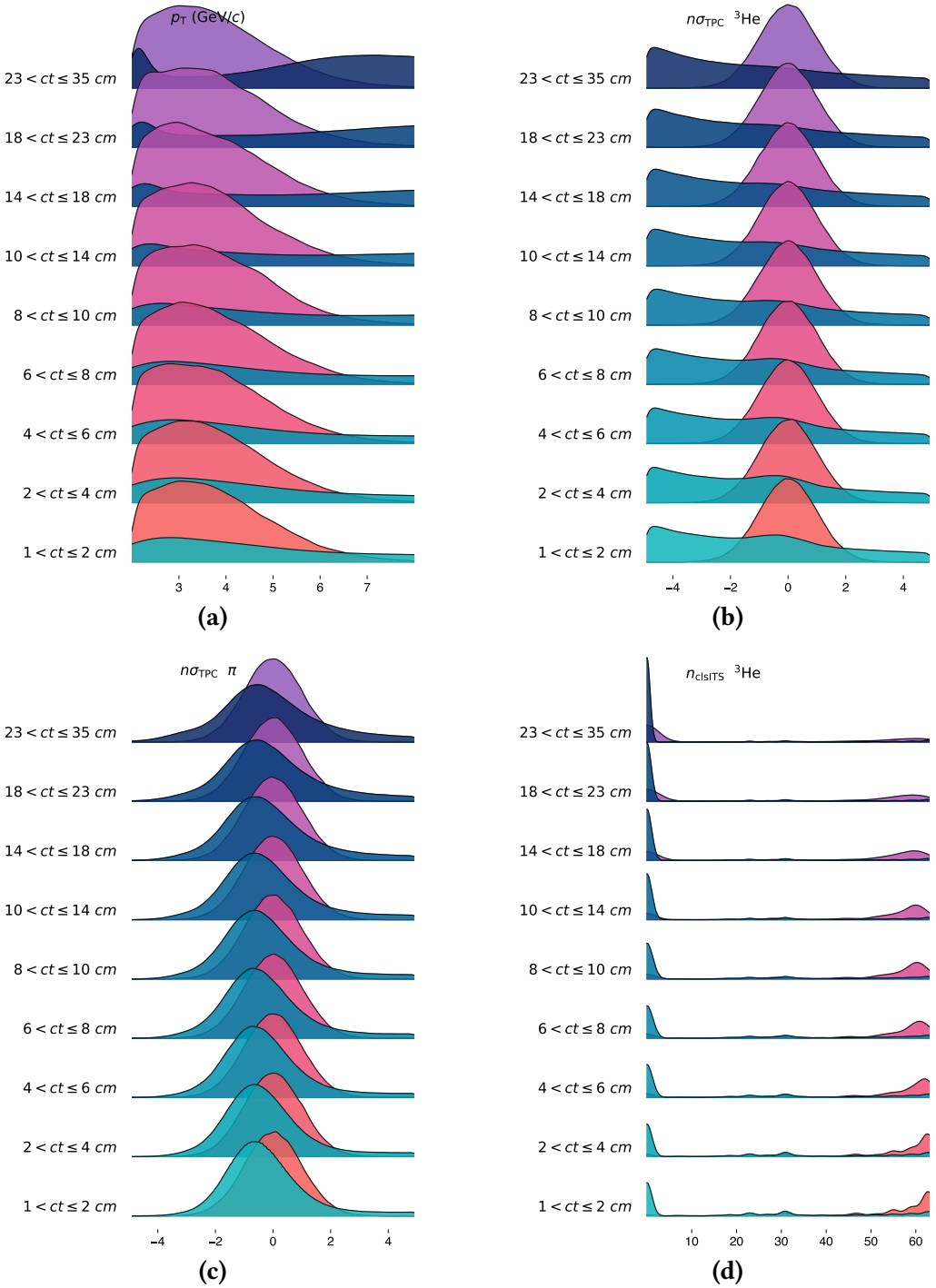

Figure A.10: Evolution of the p.d.f.s of the signal (scale of reds) and background (scale of blues) components of the TTS in the 9 ct-bins, for the p_T (a), the $n\sigma_{TPC}$ ^{3}He (b), $n\sigma_{TPC}$ π (c) and the n_{clsITS} ^{3}He features. The p.d.f.s are derived with a KDE.

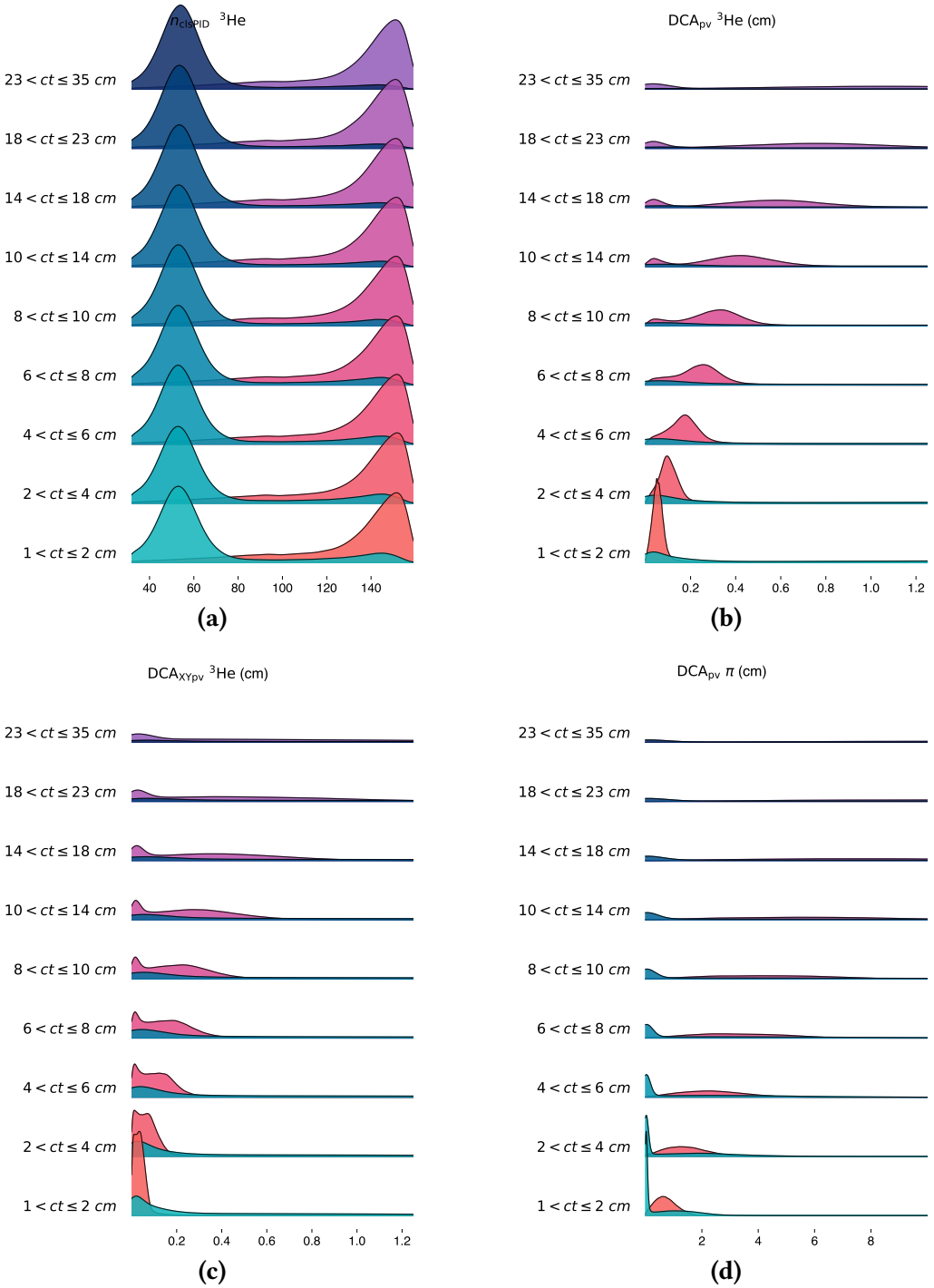

Figure A.11: Evolution of the p.d.f.s of the signal (scale of reds) and background (scale of blues) components of the TTS in the 9 ct-bins, for the n_{clsPID} ^{3}He (a), the DCA$_{\text{pv}}$ ^{3}He (b), DCA$_{\text{XYpv}}$ ^{3}He (c) and the DCA$_{\text{pv}}$ π features. The p.d.f.s are derived with a KDE.

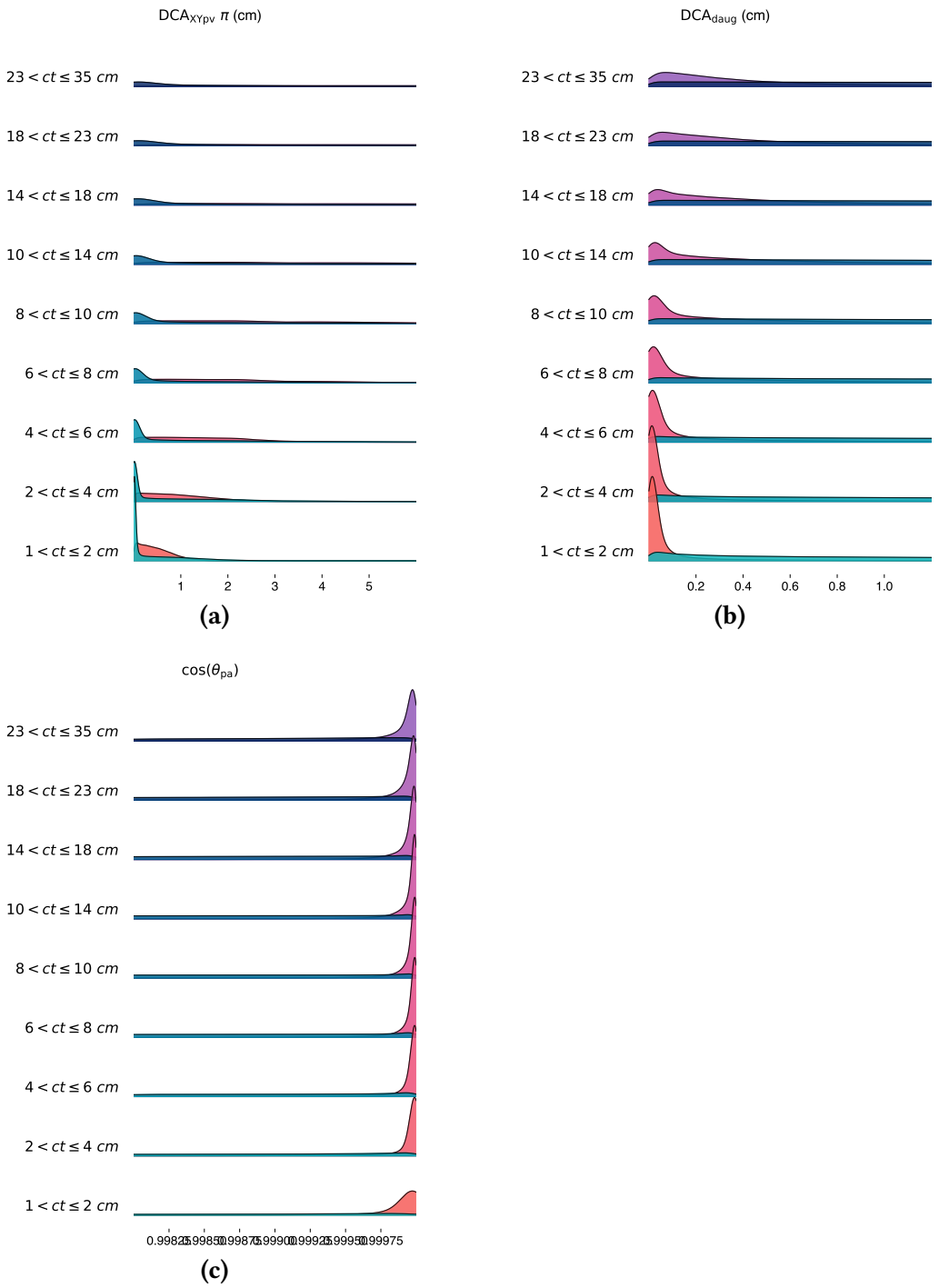

Figure A.12: Evolution of the p.d.f.s of the signal (scale of reds) and background (scale of blues) components of the TTS in the 9 ct-bins, for the DCA_{XYpv} π (a), the DCA_{daug} (b) and the $\cos(\theta_{\text{pa}})$ (c) features. The p.d.f.s are derived with a KDE.

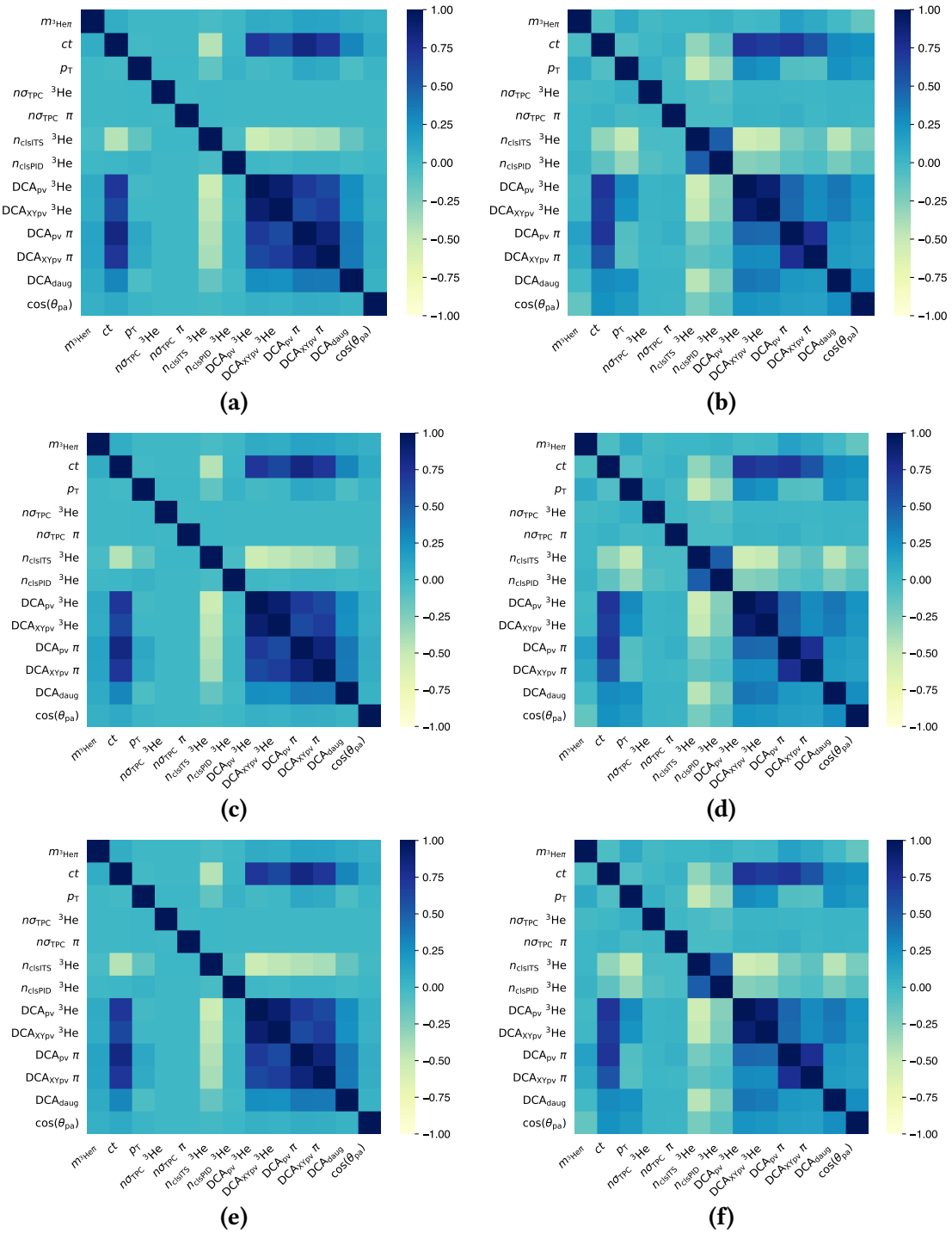

Figure A.13: Correlation matrix of the features of the signal (a, c and e) and the background (b, d and f) components of the training and test set in the ct intervals $1 < ct \leq 1\,\mathrm{cm}$ (first row), $2 < ct \leq 4\,\mathrm{cm}$ (second row) and $4 < ct \leq 6\,\mathrm{cm}$ (third row). The invariant mass and the proper time of the mother particle are also reported.

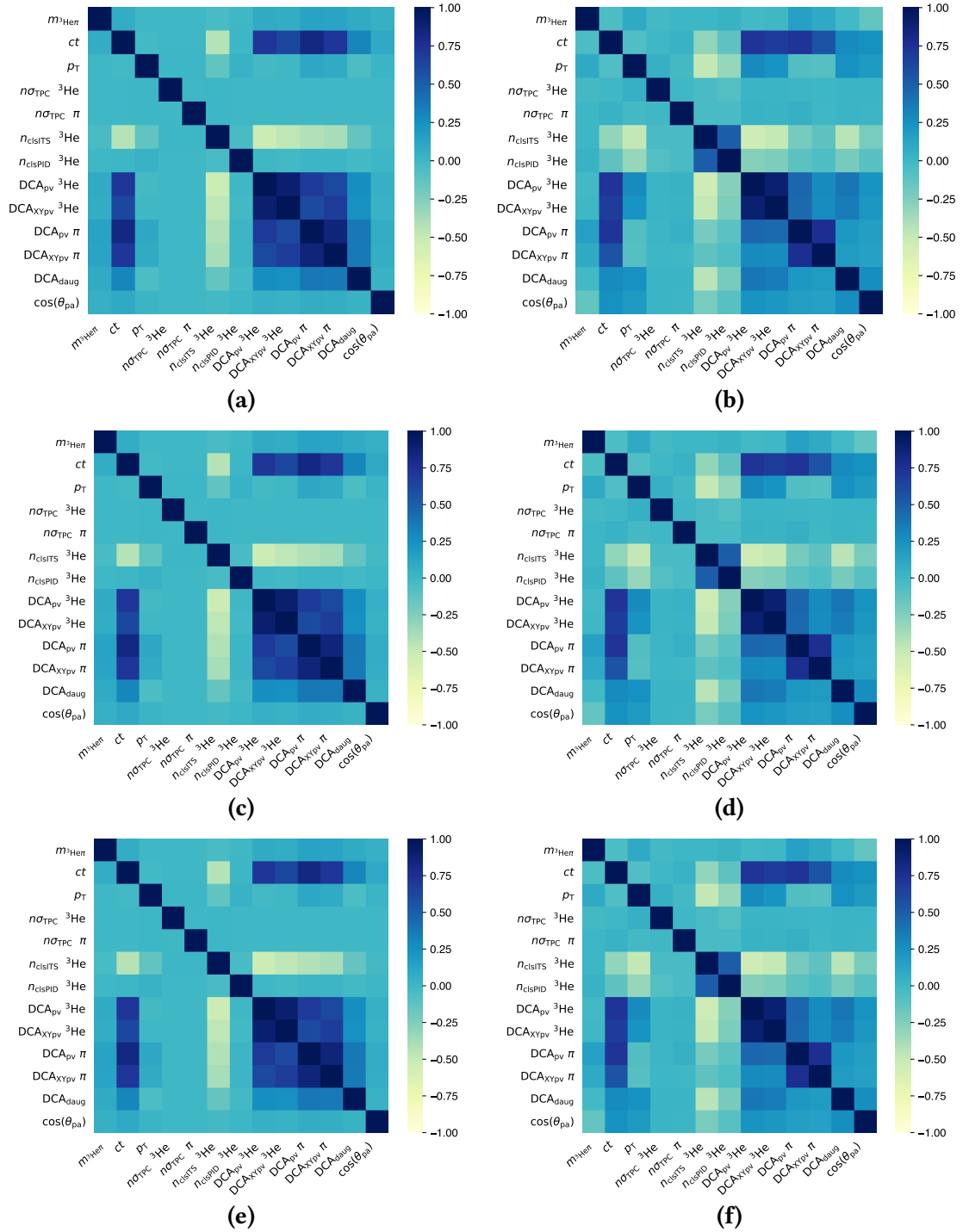

Figure A.14: Correlation matrix of the features of the signal (a, c and e) and the background (b, d and f) components of the training and test set in the ct intervals $6 < ct \leq 8\,\mathrm{cm}$ (first row), $8 < ct \leq 10\,\mathrm{cm}$ (second row) and $10 < ct \leq 14\,\mathrm{cm}$ (third row). The invariant mass and the proper time of the mother particle are also reported.

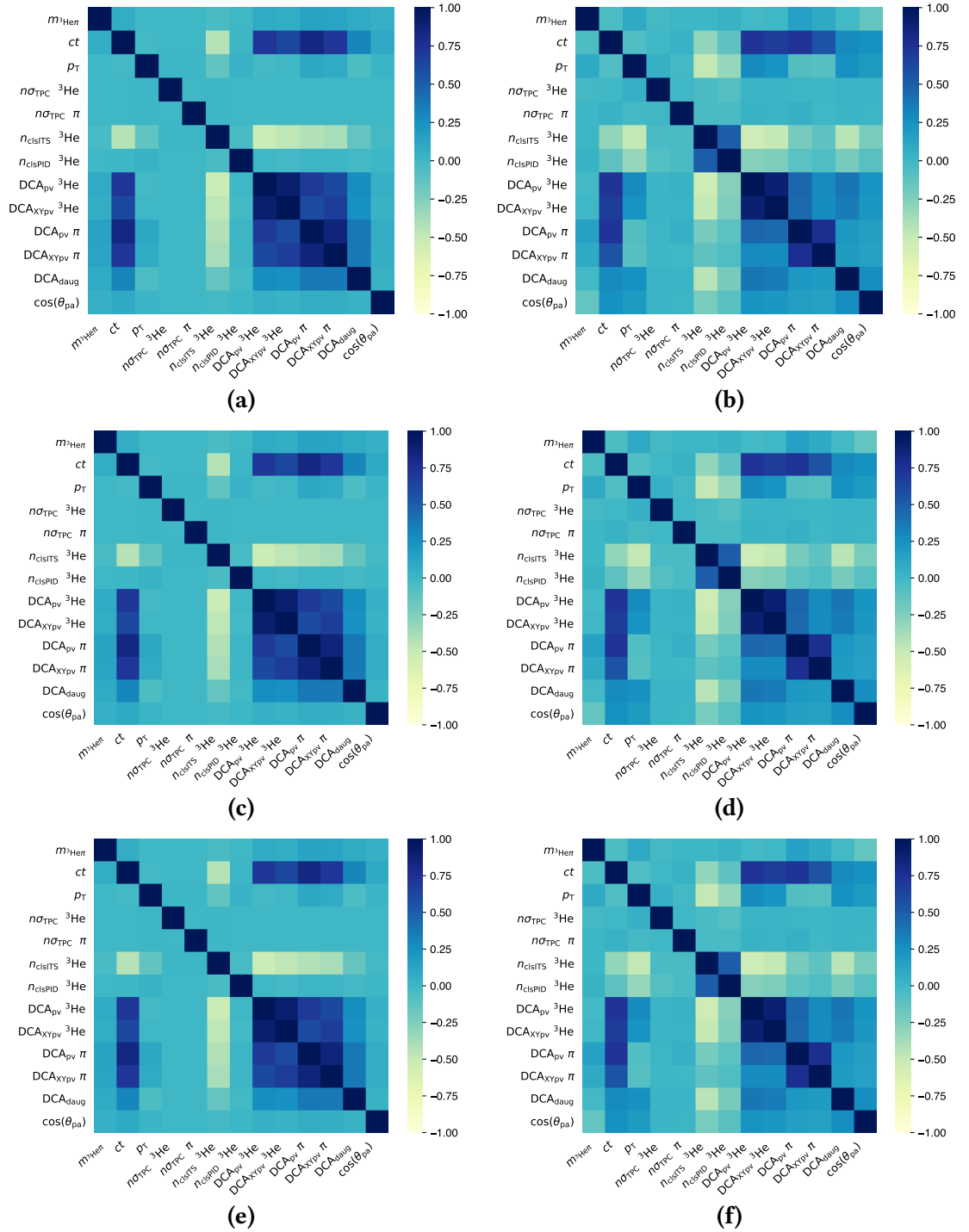

Figure A.15: Correlation matrix of the features of the signal (a, c and e) and the background (b, d and f) components of the training and test set in the ct intervals $14 < ct \leq 18$ cm (first row), $18 < ct \leq 23$ cm (second row) and $23 < ct \leq 35$ cm (third row). The invariant mass and the proper time of the mother particle are also reported.

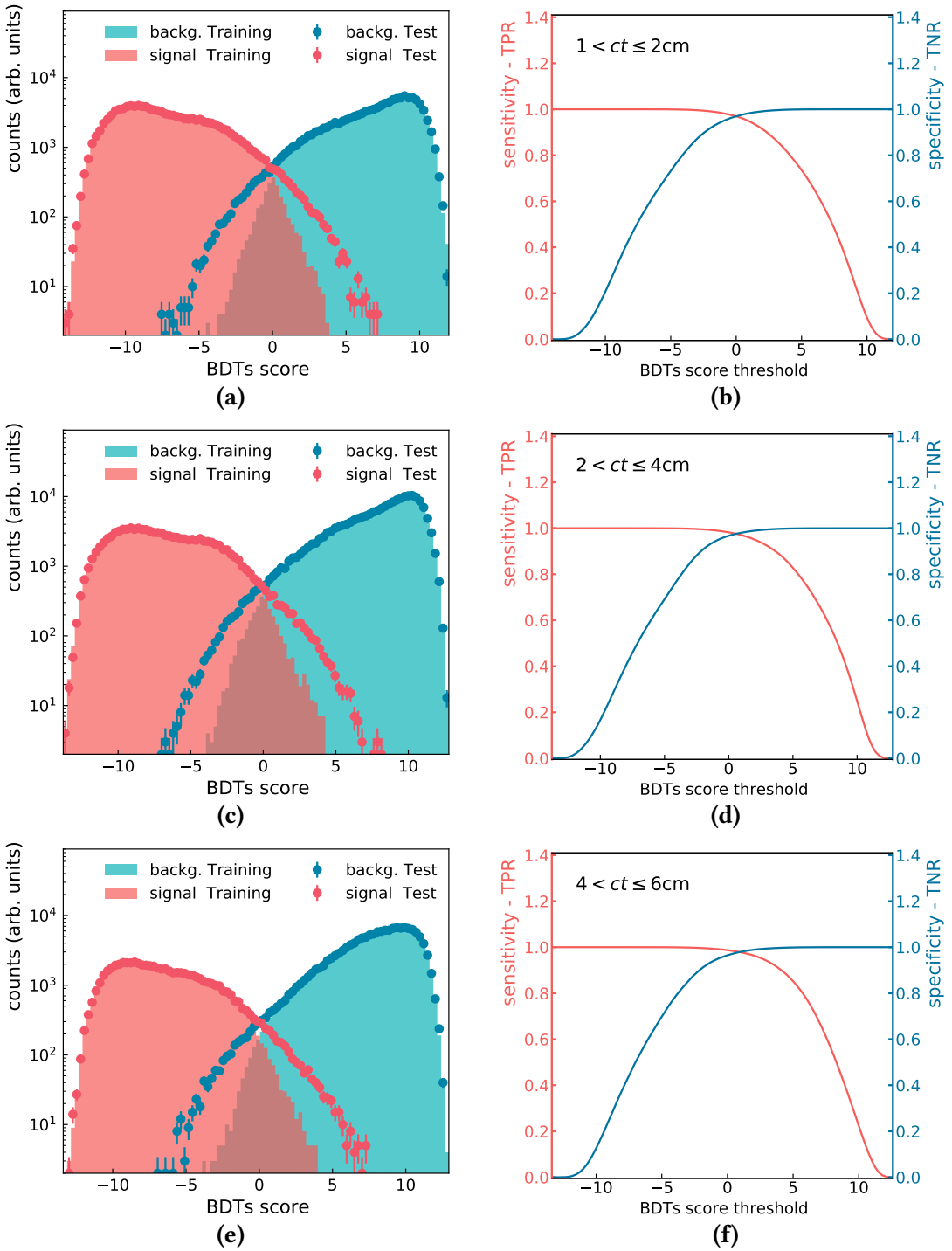

Figure A.16: (a, c and e) BDTs score distribution in the training (markers) and test (filled area) sets for the signal (red) and the background (green water). (b, d and f) TPR in red and TNR in blue of the model selection computed in the test set as a function of the threshold on the BDTs score. The plots are referred to the $1 < ct \leq 2$ cm (first row), $2 < ct \leq 4$ cm (second row) and $4 < ct \leq 6$ cm (third row) ct-bins.

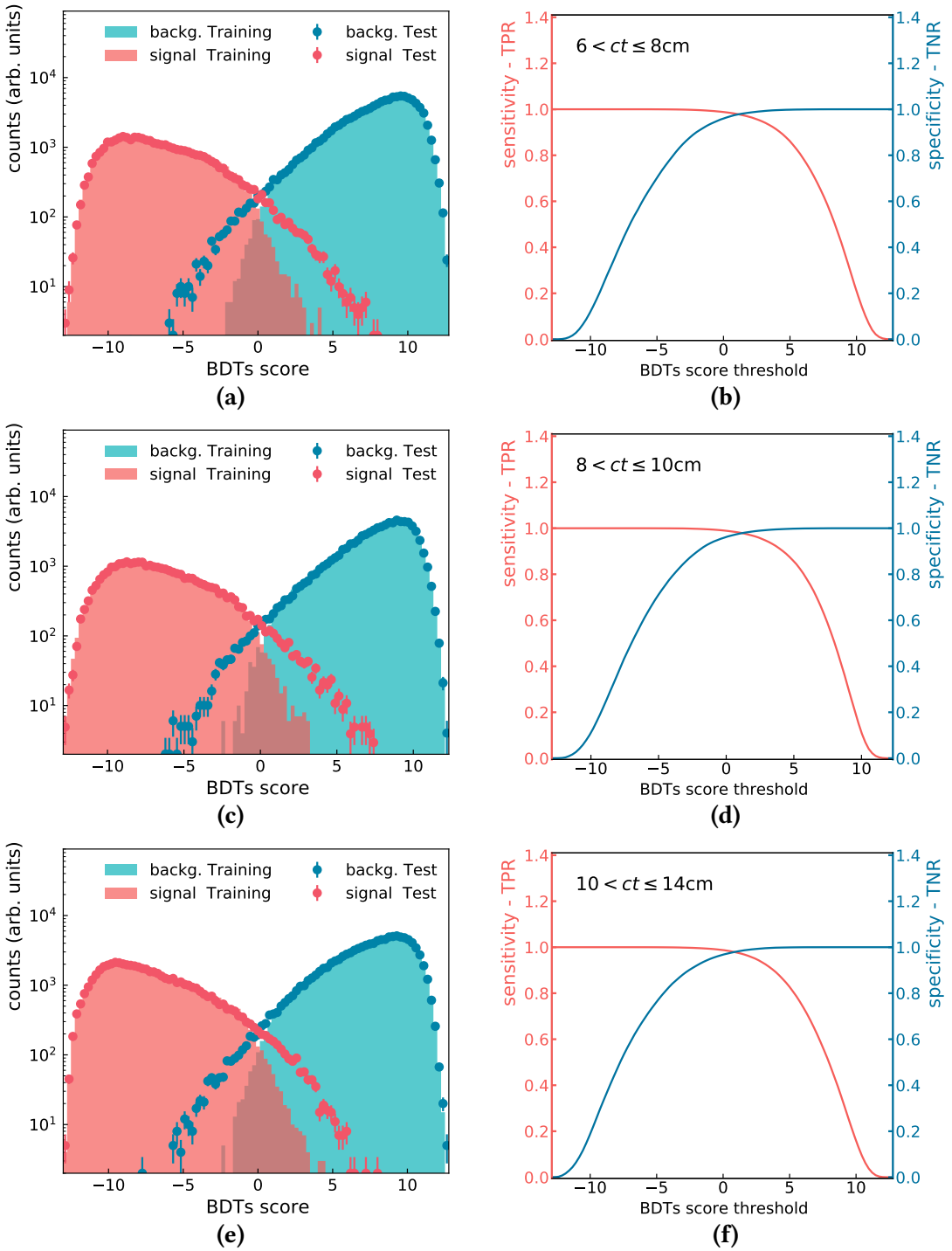

Figure A.17: (a, c and e) BDTs score distribution in the training (markers) and test (filled area) sets for the signal (red) and the background (green water). (b, d and f) TPR in red and TNR in blue of the model selection computed in the test set as a function of the threshold on the BDTs score. The plots are referred to the $6 < ct \leq 8$ cm (first row), $8 < ct \leq 10$ cm (second row) and $10 < ct \leq 14$ cm (third row) ct-bins.

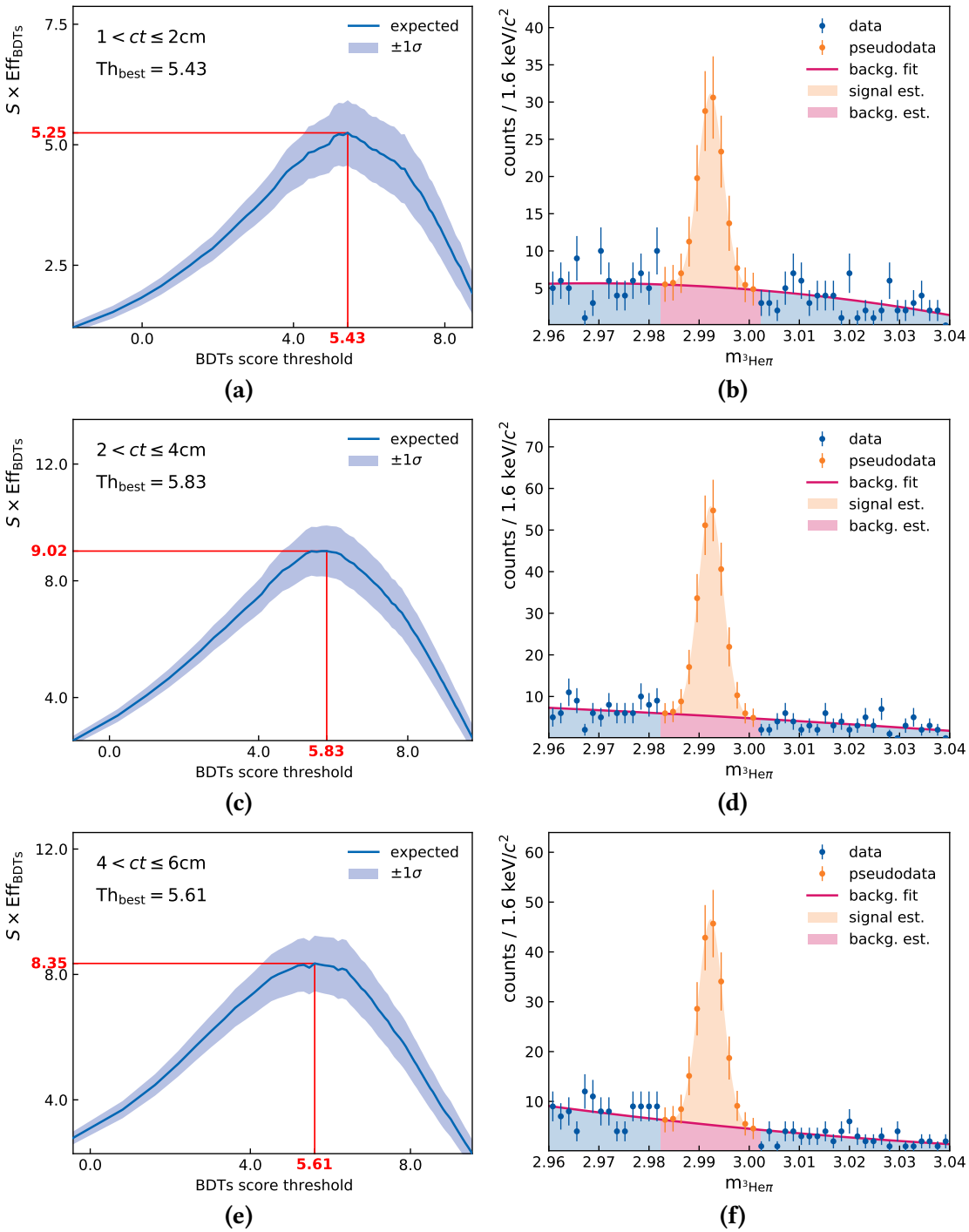

Figure A.18: Figures related to the BDTs selection optimization in the $1 < ct \leq 2$ cm (first row), $2 < ct \leq 4$ cm (second row) and $4 < ct \leq 6$ cm (third row) ct-bin. (a, c and e) expected $S \times \text{Eff}_{\text{BDTs}}$ as a function of the Th. (b, d and f) the invariant mass distribution – obtained selecting with the estimated best threshold – of the data in the sidebands is represented together with the pseudo-data used as an estimate of the signal.

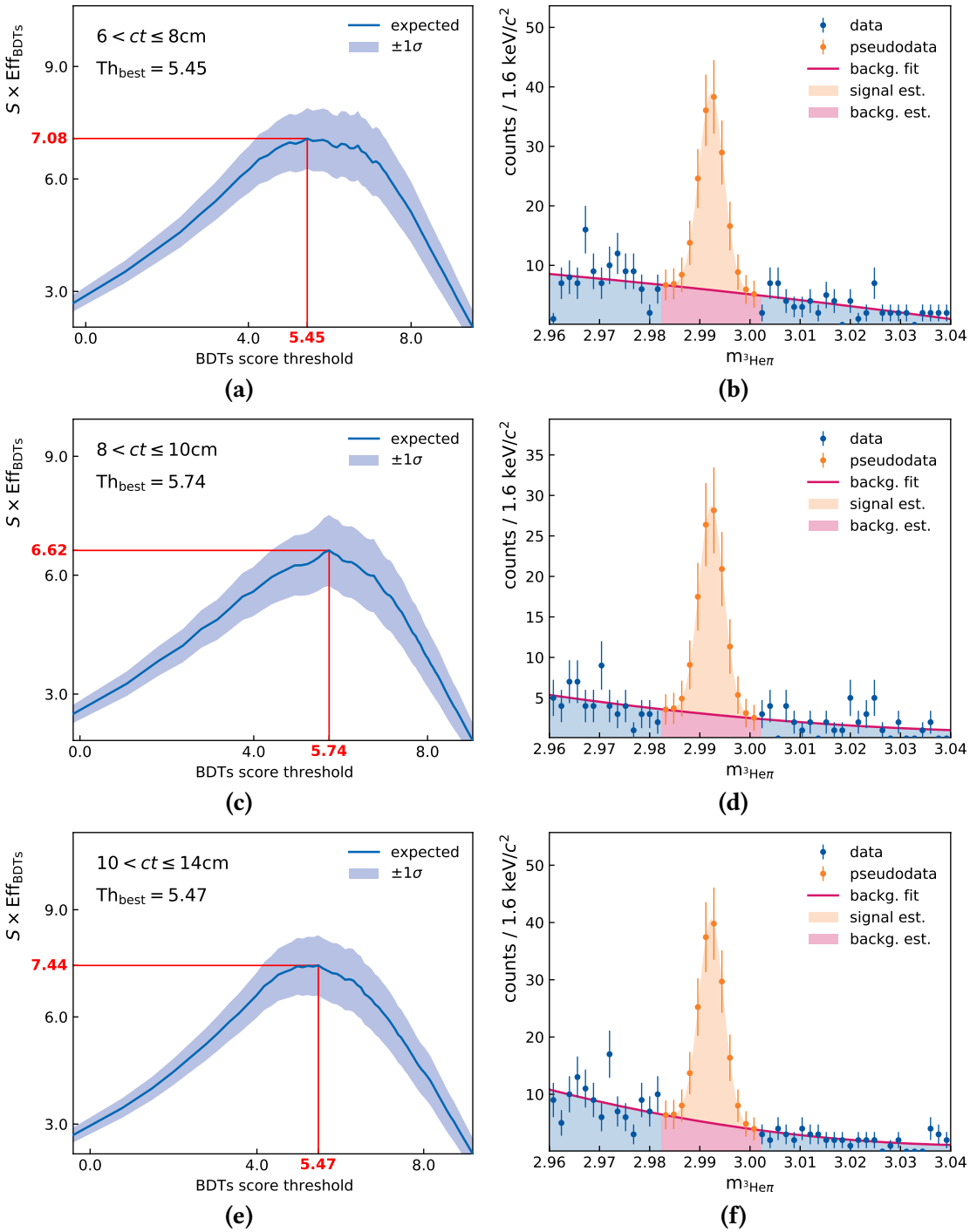

Figure A.19: Figures related to the BDTs selection optimization in the $6 < ct \leq 8$ cm (first row), $8 < ct \leq 10$ cm (second row) and $10 < ct \leq 14$ cm (third row) ct-bin. (a, c and e) expected $S \times \text{Eff}_{\text{BDTs}}$ as a function of the Th. (b, d and f) the invariant mass distribution – obtained selecting with the estimated best threshold – of the data in the sidebands is represented together with the pseudo-data used as an estimate of the signal.

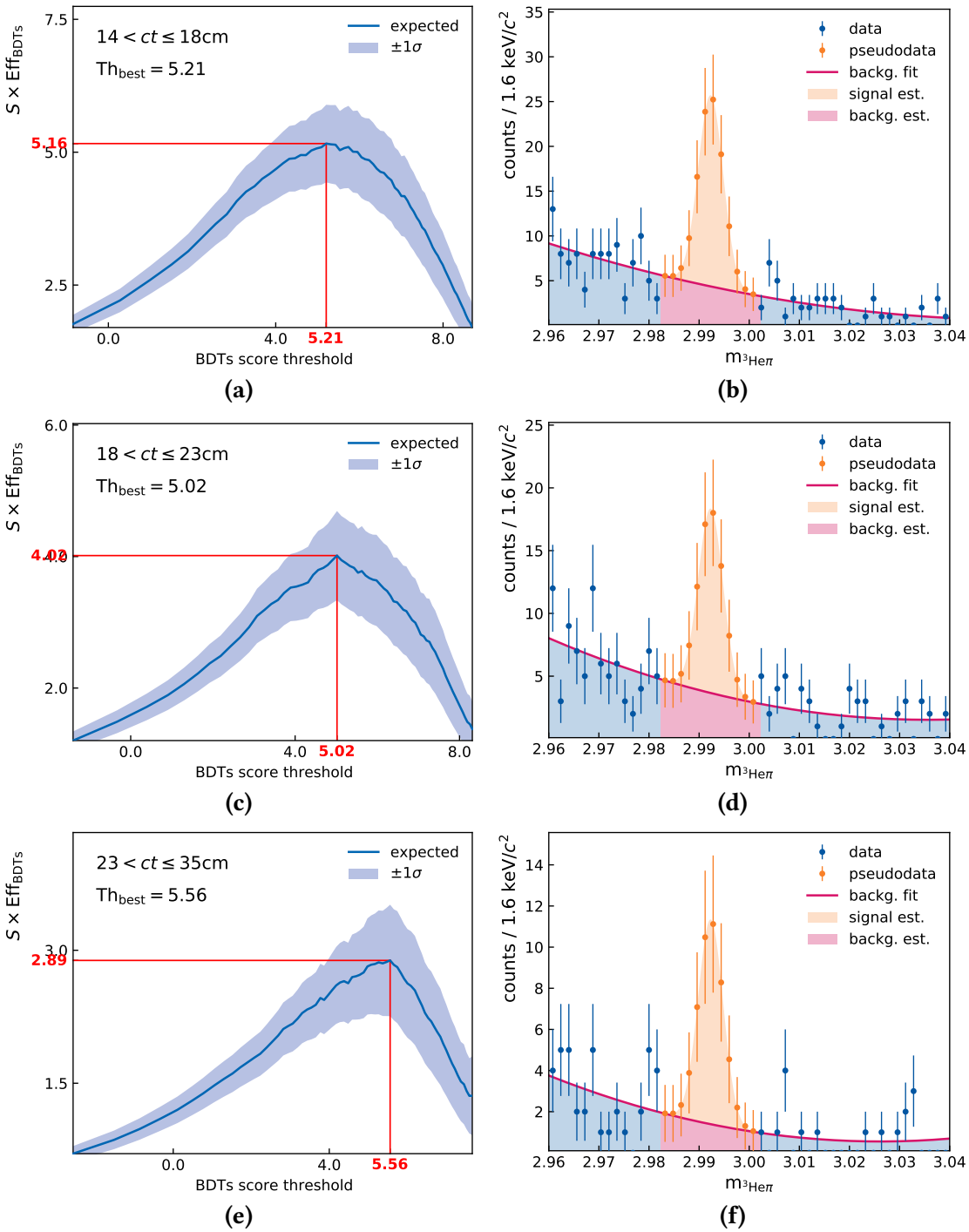

Figure A.20: Figures related to the BDTs selection optimization in the $14 < ct \leq 18$ cm (first row), $18 < ct \leq 23$ cm (second row) and $23 < ct \leq 35$ cm (third row) ct-bin. (a, c and e) expected $S \times \text{Eff}_{\text{BDTs}}$ as a function of the Th. (b, d and f) the invariant mass distribution – obtained selecting with the estimated best threshold – of the data in the sidebands is represented together with the pseudo-data used as an estimate of the signal.

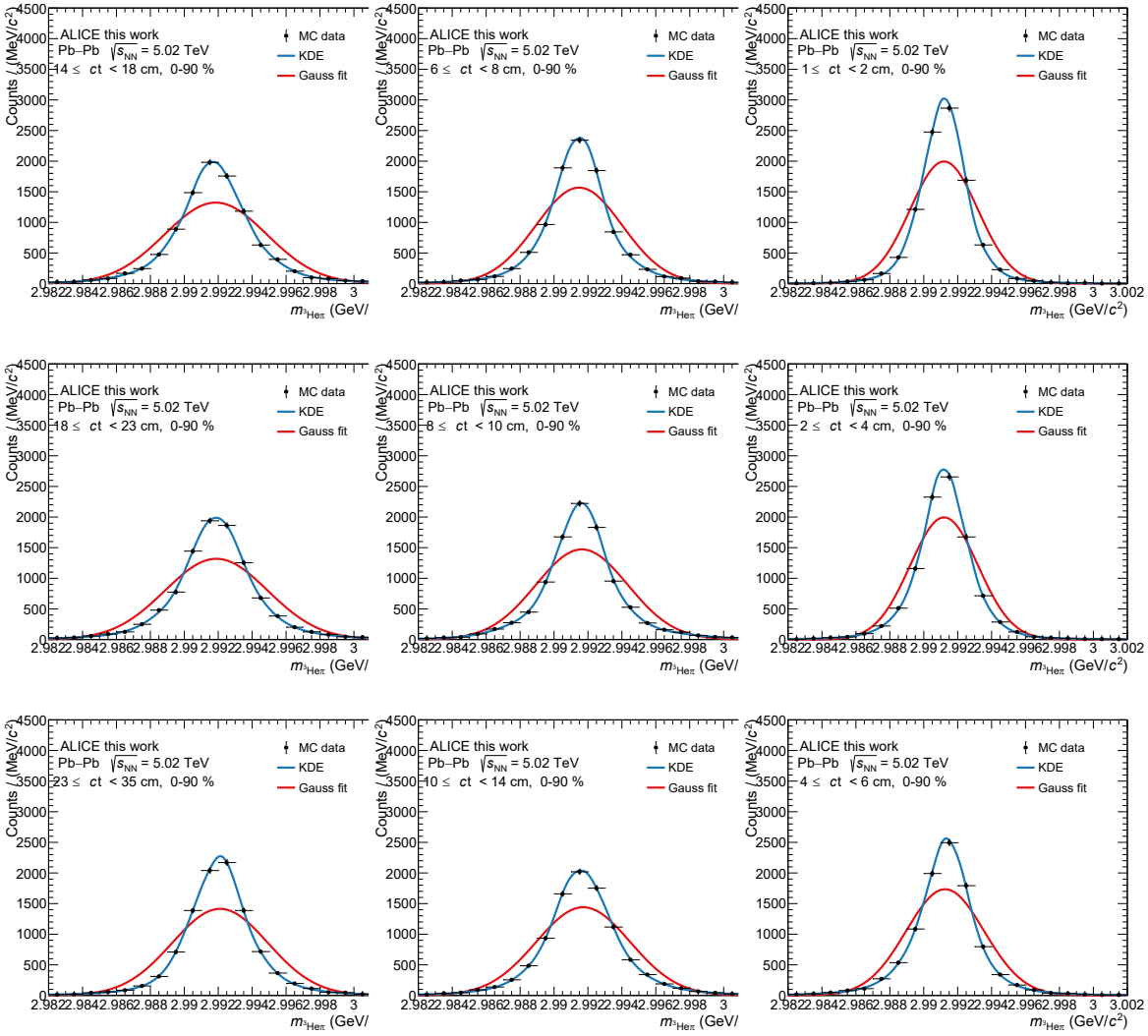

Figure A.21: The invariant mass distribution of the MC hypertritons after the reconstruction is compared with the p.d.f. obtained with the KDE and a gaussian p.d.f. fitted to the distribution for all the *ct*-bins. The gaussian is clearly not suitable for the description of the invariant mass distributions.

Bibliography

[1] J. P. Ostriker et al., "Cosmic concordance," 10.48550/arXiv.astro-ph/9505066 (1995) (cit. on p. 1).

[2] P. A. R. Ade et al. (Planck Collaboration), "Planck 2015 results - XIII. Cosmological parameters," A&A **594**, A13 (2016) (cit. on p. 1).

[3] N. Aghanim et al. (Planck Collaboration), "Planck 2018 results - VI. Cosmological parameters," A&A **641**, A6 (2020) (cit. on p. 1).

[4] P. Zyla et al. (Particle Data Group), "Review of Particle Physics," PTEP **2020**, 083C01 (2020) (cit. on pp. 1, 3–4, 57, 59, 85, 114, 126).

[5] M. E. Peskin et al., *An introduction to quantum field theory* (Westview, Boulder, CO, 1995) (cit. on p. 1).

[6] H. Fritzsch et al., "Advantages of the Color Octet Gluon Picture," Phys. Lett. B **47**, 365–368 (1973) (cit. on p. 1).

[7] J. C. Ward, "On the Renormalization of Quantum Electrodynamics," Proc. Phys. Soc. London, Sect. A **64**, 54–56 (1951) (cit. on p. 2).

[8] H. D. Politzer, "Reliable Perturbative Results for Strong Interactions?" Phys. Rev. Lett. **30**, 1346–1349 (1973) (cit. on p. 3).

[9] D. J. Gross et al., "Ultraviolet Behavior of Non-Abelian Gauge Theories," Phys. Rev. Lett. **30**, 1343–1346 (1973) (cit. on p. 3).

[10] K. G. Wilson, "Confinement of quarks," Phys. Rev. D **10**, 2445–2459 (1974) (cit. on p. 4).

[11] S. Dürr et al., "Ab Initio Determination of Light Hadron Masses," Science **322**, 1224–1227 (2008) (cit. on p. 4).

[12] H. Bohr et al., "Hadron Production from a Boiling Quark Soup," Nucl. Phys. B **128**, 275–293 (1977) (cit. on p. 5).

[13] M. G. Alford et al., "Color superconductivity in dense quark matter," Rev. Mod. Phys. **80**, 1455–1515 (2008) (cit. on p. 5).

[14] M. Alford, "Color-Superconductins Quark Matter," Annu. Rev. Nucl. Part. Sci **51**, 131–160 (2001) (cit. on p. 5).

[15] T. Tanimoto et al., "Massive neutron stars with a color superconducting quark matter core," Phys. Rev. C **101**, 055204 (2020) (cit. on p. 5).

[16] M. G. Orsaria et al., "Phase transitions in neutron stars and their links to gravitational waves," J. Phys. G: Nucl. Part. Phys. **46**, 073002 (2019) (cit. on p. 6).

[17] M. Harrison et al., "The RHIC Accelerator," Annu. Rev. Nucl. Part. Sci. **52**, 425–469 (2002) (cit. on p. 7).

[18] M. L. Miller et al., "Glauber Modeling in High-Energy Nuclear Collisions," Annu. Rev. Nucl. Part. Sci. **57**, 205–243 (2007) (cit. on pp. 7–8).

[19] C. Gale et al., "Hydrodynamic Modeling of Heavy–Ion Collision," Int. J. Mod. Phys. A **28**, 1340011 (2013) (cit. on p. 11).

[20] U. W. Heinz et al., "Evidence for a new state of matter: An Assessment of the results from the CERN lead beam program," 10.48550/arXiv.nucl-th/0002042 (2000) (cit. on p. 13).

[21] S. Acharya et al. (ALICE Collaboration), "Production of charged pions, kaons, and (anti–)protons in Pb–Pb and inelastic pp collisions at $\sqrt{s_{\mathrm{NN}}}$ = 5.02 TeV," Phys. Rev. C **101**, 044907 (2020) (cit. on p. 15).

[22] B. I. Abelev et al. (STAR Collaboration), "Systematic measurements of identified particle spectra in pp, d + Au, and Au + Au collisions at the STAR detector," Phys. Rev. C **79**, 034909 (2009) (cit. on pp. 14–15).

[23] S. S. Adler et al. (PHENIX Collabboration), "Identified charged particle spectra and yields in Au+Au collisions at S(NN)**1/2 = 200-GeV," Phys. Rev. C **69**, 034909 (2004) (cit. on pp. 14–15).

[24] B. Abelev et al. (ALICE Collaboration), "Pion, Kaon, and Proton Production in Central Pb–Pb Collisions at $\sqrt{s_{\mathrm{NN}}}$=2.76 TeV," Phys. Rev. Lett. **109**, 252301 (2012) (cit. on pp. 14–15, 17).

[25] P. Bozek, "Flow and interferometry in 3+1 dimensional viscous hydrodynamics," Phys. Rev. C **85**, 034901 (2012) (cit. on p. 14).

[26] Y. A. Karpenko et al., "Femtoscopic scales in central A+A collisions at RHIC and LHC energies in hydrokinetic model," J. Phys. G **38**, edited by Y. Schutz et al., 124059 (2011) (cit. on p. 14).

[27] E. Schnedermann et al., "Thermal phenomenology of hadrons from 200A GeV S+S collisions," Phys. Rev. C **48**, 2462–2475 (1993) (cit. on pp. 15, 91).

[28] L. Adamczyk et al. (STAR Collaboration), "Beam-Energy Dependence of Charge Separation along the Magnetic Field in Au + Au Collisions at RHIC," Phys. Rev. Lett. **113**, 052302 (2014) (cit. on p. 16).

[29] J. Adam et al. (ALICE Collaboration), "Anisotropic flow of charged particles in Pb-Pb collisions at $\sqrt{s_{\mathrm{NN}}}$ = 5.02 TeV," Phys. Rev. Lett. **116**, 132302 (2016) (cit. on p. 17).

[30] N. Armesto, "Nuclear shadowing," J. Phys. G: Nucl. Part. Phys. **32**, R367–R393 (2006) (cit. on p. 18).

[31] J. W. Cronin et al., "Production of hadrons at large transverse momentum at 200, 300, and 400 GeV," Phys. Rev. D **11**, 3105–3123 (1975) (cit. on p. 18).

[32] V. Khachatryan et al. (CMS Collaboration), "Charged-particle nuclear modification factors in PbPb and pPb collisions at $\sqrt{s_{\mathrm{NN}}} = 5.02\,\mathrm{TeV}$," J. High Energy Phys. **04**, 039 (2017) (cit. on pp. 18–19).

[33] S. Acharya et al. (ALICE Collaboration), "Measurement of D^0, D^+, D^{*+} and D_s^+ production in Pb-Pb collisions at $\sqrt{s_{\mathrm{NN}}} = 5.02$ TeV," J. High Energy Phys. **10**, 174 (2018) (cit. on pp. 19–20).

[34] A. M. Sirunyan et al. (CMS Collaboration), "In–medium modification of dijets in PbPb collisions at $\sqrt{s_{\mathrm{NN}}} = 5.02\,\mathrm{TeV}$," J. High Energy Phys. **05**, 116 (2021) (cit. on p. 20).

[35] S. Acharya et al., "Centrality and transverse momentum dependence of inclusive J/Ψ production at midrapidity in Pb–Pb collisions at $\sqrt{s_{\mathrm{NN}}} = 5.02\,\mathrm{TeV}$," Phys. Lett. B **805**, 135434 (2020) (cit. on pp. 21–22).

[36] X. Du et al., "Sequential regeneration of charmonia in heavy-ion collisions," Nucl. Phys. A **943**, 147–158 (2015) (cit. on pp. 21–22).

[37] A. Andronic et al., "Transverse momentum distributions of charmonium states with the statistical hadronization model," Phys. Lett. B **797**, 134836 (2019) (cit. on pp. 21–22).

[38] A. Sirunyan et al. (CMS Collaboration), "Measurement of nuclear modification factors of $\Upsilon(1S)$, $\Upsilon(2S)$, and $\Upsilon(3S)$ mesons in PbPb collisions at $\sqrt{s_{\mathrm{NN}}} = 5.02\,\mathrm{TeV}$," Phys. Lett. B **790**, 270–293 (2019) (cit. on pp. 22–23).

[39] A. M. Sirunyan et al. (CMS Collaboration), "Constraints on the Initial State of Pb-Pb Collisions via Measurements of Z-Boson Yields and Azimuthal Anisotropy at $\sqrt{s_{NN}} = 5.02$ TeV," Phys. Rev. Lett. **127**, 102002 (2021) (cit. on p. 23).

[40] C. Loizides et al., "Absence of jet quenching in peripheral nucleus–nucleus collisions," Phys. Lett. B **773**, 408–411 (2017) (cit. on p. 24).

[41] J. Adam et al. (ALICE Collaboration), "Direct photon production in Pb–Pb collisions at $\sqrt{s_{\mathrm{NN}}} = 2.76\,\mathrm{TeV}$," Phys. Lett. B **754**, 235–248 (2016) (cit. on pp. 24–25).

[42] C. Lefèvre, "The CERN accelerator complex. Complexe des accélérateurs du CERN," 2008 (cit. on p. 28).

[43] S. van der Meer, *Calibration of the effective beam height in the ISR*, tech. rep. (CERN, Geneva, 1968) (cit. on p. 29).

[44] "LHC Machine," J. Instrum. **3**, edited by L. Evans et al., S08001 (2008) (cit. on p. 29).

[45] M. L. Mangano, "Introduction to the theory of LHC collisions," Les Houches Lect. Notes **97**, edited by L. Baulieu et al., 107–139 (2015) (cit. on p. 29).

[46] F. Carminati et al. (ALICE Collabboration), "ALICE: Physics Performance Report, Volume I," J. Phys. G: Nucl. Part. Phys. **30**, 1517–1763 (2004) (cit. on pp. 30–31).

[47] B. Alessandro et al. (ALICE Collaboration), "ALICE: Physics Performance Report, Volume II," J. Phys. G: Nucl. Part. Phys. **32**, 1295–2040 (2006) (cit. on pp. 30–31).

[48] K. Aamodt et al. (ALICE Collaboration), "The ALICE experiment at the CERN LHC," J. Instrum. **3**, S08002–S08002 (2008) (cit. on pp. 31, 36, 42, 45).

[49] B. B. Abelev et al. (ALICE Collaboration), "Performance of the ALICE Experiment at the CERN LHC," Int. J. Mod. Phys. A **29**, 1430044 (2014) (cit. on pp. 32–33, 41, 45–46).

[50] B. Adeva et al. (L3 Collaboration), "The Construction of the L3 Experiment," Nucl. Instrum. Meth. A **289**, 35–102 (1990) (cit. on p. 32).

[51] F. Carena et al. (ALICE Collaboration), "The ALICE data acquisition system," Nucl. Instrum. Meth. A **741**, 130–162 (2014) (cit. on p. 39).

[52] M. Krzewicki et al., "The ALICE High Level Trigger: status and plans," **664**, 082023 (2015) (cit. on p. 39).

[53] R. Brun et al., "Geant3," https://inspirehep.net/files/822595acd3e6c8936bd720fe (1987) (cit. on pp. 40, 79).

[54] S. Agostinelli et al., "Geant4—a simulation toolkit," Nucl. Instrum. Methods Phys. Res., Sect. A **506**, 250–303 (2003) (cit. on pp. 40, 80).

[55] J. Allison et al., "Geant4 developments and applications," IEEE Trans. Nucl. Sci. **53**, 270–278 (2006) (cit. on pp. 40, 80).

[56] J. Allison et al., "Recent developments in GEANT4," Nucl. Instrum. Methods Phys. Res., Sect. A **835**, 186–225 (2016) (cit. on pp. 40, 80).

[57] CERN, *Official CERN FLUKA Website*, https://fluka.cern/ (visited on 02/05/2022) (cit. on p. 40).

[58] G. Battistoni et al., "Overview of the FLUKA code," Annals Nucl. Energy **82**, 10–18 (2015) (cit. on p. 40).

[59] C. Ahdida et al., "New Capabilities of the FLUKA Multi-Purpose Code," Front. Phys. **9**, 10.3389/fphy.2021.788253 (2022) (cit. on p. 40).

[60] R. Fruhwirth, "Application of Kalman filtering to track and vertex fitting," Nucl. Instrum. Meth. A **262**, 444–450 (1987) (cit. on p. 42).

[61] G. Agakichiev et al., "A new robust fitting algorithm for vertex reconstruction in the CERES experiment," Nucl. Instrum. Methods Phys. Res., Sect. A **394**, 225–231 (1997) (cit. on p. 45).

[62] R. Brun et al., "ROOT: An object oriented data analysis framework," Nucl. Instrum. Meth. A **389**, edited by M. Werlen et al., 81–86 (1997) (cit. on p. 47).

[63] L. Rolandi et al., *Particle Detection with Drift Chambers* (2008) (cit. on p. 49).

[64] M. Danysz et al., "Delayed disintegration of a heavy nuclear fragment: I," Lond. Edinb. Dubl. Phil. Mag. **44**, 348–350 (1953) (cit. on p. 53).

[65] D. Davis, "50 years of hypernuclear physics: I. The early experiments," Nucl. Phys. A **754**, 3–13 (2005) (cit. on pp. 53, 58).

[66] T. R. Saito et al., "New directions in hypernuclear physics," Nat. Rev. Phys. **3**, 803–813 (2021) (cit. on pp. 54–55, 60).

[67] F. Weber, "Strangeness in neutron stars," J. Phys. G: Nucl. Part. Phys. **27**, 465–474 (2001) (cit. on p. 54).

[68] F. Weber et al., "Strangeness in Neutron Stars," Int. J. Mod. Phys. D **16**, 231–245 (2007) (cit. on p. 54).

[69] P. B. Demorest et al., "A two-solar-mass neutron star measured using Shapiro delay," Nature **467**, 1081–1083 (2010) (cit. on p. 54).

[70] J. Antoniadis et al., "A Massive Pulsar in a Compact Relativistic Binary," Science **340**, 1233232 (2013) (cit. on p. 54).

[71] E. D. Barr et al., "A massive millisecond pulsar in an eccentric binary," Mon. Not. R. Astron. Soc. **465**, 1711–1719 (2016) (cit. on p. 54).

[72] Y. Yamamoto et al., "Hyperon mixing and universal many-body repulsion in neutron stars," Phys. Rev. C **90**, 045805 (2014) (cit. on p. 54).

[73] H. Ekawa et al., "Observation of a Be double-Lambda hypernucleus in the J-PARC E07 experiment," Prog. Theor. Exp. Phys. **2019**, 10.1093/ptep/pty149 (2019) (cit. on p. 55).

[74] S. H. Hayakawa et al. (J-PARC E07 Collaboration), "Observation of Coulomb-Assisted Nuclear Bound State of $^{-}--^{14}$N System," Phys. Rev. Lett. **126**, 062501 (2021) (cit. on p. 55).

[75] K. Nakazawa et al., "Experimental Study of Double-Λ Hypernuclei with Nuclear Emulsion," Prog. Theor. Phys. Suppl. **185**, 335–343 (2010) (cit. on p. 55).

[76] H. Takahashi et al., "Observation of a ${}^{6}_{\Lambda\Lambda}$He double hypernucleus," Phys. Rev. Lett. **87**, 2125021–2125025 (2001) (cit. on p. 55).

[77] E. Botta et al., "Status and perspectives of experimental studies on hypernuclear weak decays," Riv. del Nuovo Cim. **9**, 387–448 (2015) (cit. on p. 56).

[78] E. Bauer et al., "Role of ground-state correlations in hypernuclear nonmesonic weak decay," Phys. Rev. C **81**, 064315 (2010) (cit. on p. 56).

[79] K. Itonaga et al., "Hypernuclear Weak Decays," Prog. Theor. Phys. Suppl. **185**, 252–298 (2010) (cit. on p. 56).

[80] A. Bonetti et al., "On the possible ejection of a meson-active triton from a nuclear disintegration," Il Nuovo Cimento (1943-1954) **11**, 210–212 (1954) (cit. on p. 56).

[81] B. I. Abelev et al. (STAR Collaboration), "Observation of an Antimatter Hypernucleus," Science **328**, 58–62 (2010) (cit. on pp. 57, 59, 61, 125–126).

[82] M. Jurič et al., "A new determination of the binding-energy values of the light hypernuclei ($A \leq 15$)," Nucl. Phys. B **52**, 1–30 (1973) (cit. on pp. 57–58, 60, 127).

[83] B. Povh et al., "Nuclear Stability," in *Particles and Nuclei: An Introduction to the Physical Concepts* (Springer Berlin Heidelberg, 2015), pp. 25–40 (cit. on p. 57).

[84] H. Kamada et al., "π-mesonic decay of the hypertriton," Phys. Rev. C **57**, 1595–1603 (1998) (cit. on pp. 58, 126).

[85] G. Bohm et al., "A determination of the binding-energy values of light hypernuclei," Nucl. Phys. B **4**, 511–526 (1968) (cit. on pp. 58, 60, 127).

[86] E. Harth et al., "Hyperfragment studies in the helium bubble chamber," in (1964) (cit. on pp. 58–59, 61).

[87] G. Keyes et al., "New Measurement of the ${}_{\Lambda}H^{3}$ Lifetime," Phys. Rev. Lett. **20**, 819–821 (1968) (cit. on pp. 58–59, 61).

[88] G. Keyes et al., "Properties of ${}_{\Lambda}H^{3}$," Phys. Rev. D **1**, 66–77 (1970) (cit. on pp. 58–59, 61, 127).

[89] G. Keyes et al., "A measurement of the lifetime of the ${}_{\Lambda}H^{3}$ hypernucleus," Phys. Lett. B **67**, 269–283 (1973) (cit. on pp. 58–59, 61).

[90] R. J. Prem et al., "Lifetimes of Hypernuclei, ${}_{\Lambda}H^{3}$, ${}_{\Lambda}H^{4}$, ${}_{\Lambda}H^{5}$," Phys. Rev. **136**, B1803–B1806 (1964) (cit. on pp. 58–59, 61).

[91] Y. W. Kang et al., "Lifetimes of Light Hyperfragments," Phys. Rev. **139**, B401–B406 (1965) (cit. on pp. 58–59, 61).

[92] R. E. Phillips et al., "Lifetime of ${}_{\Lambda}H^{3}$," Phys. Rev. Lett. **20**, 1383–1386 (1968) (cit. on pp. 58–59, 61).

[93] R. E. Phillips et al., "Lifetimes of Light Hyperfragments. II," Phys. Rev. **180**, 1307–1318 (1969) (cit. on pp. 58–59, 61).

[94] G. Bohm et al., "On the lifetime of the ${}_{\Lambda}H^{3}$ hypernucleus," Nucl. Phys. B **16**, 46–52 (1970) (cit. on pp. 58–59, 61).

[95] S. Avramenko et al., "A study of the production and lifetime of the lightest relativistic hypernuclei," Nucl. Phys. A **547**, 95–100 (1992) (cit. on pp. 59, 61).

[96] *Beam Energy Scan on Hypertriton Production and Lifetime Measurement at RHIC STAR*, Vol. 904-905 (2013), pp. 551c–554c (cit. on pp. 59, 61, 125–126).

[97] C. Rappold et al., "Hypernuclear spectroscopy of products from 6Li projectiles on a carbon target at 2A GeV," Nucl. Phys. A **913**, 170–184 (2013) (cit. on pp. 59, 61).

[98] J. Adam et al. (ALICE Collaboration), "$^{3}_{\Lambda}$H And $^{\overline{3}}_{\overline{\Lambda}}\overline{\mathrm{H}}$ production in pb–pb collisions at $\sqrt{s_{\mathrm{NN}}} = 2.76$ TeV," Phys. Lett. B **754**, 360–372 (2016) (cit. on pp. 59–61, 103, 109, 125–126).

[99] L. Adamczyk et al. (STAR Collaboration), "Measurement of the ^{3}H lifetime in Au+Au collisions at the BNL Relativistic Heavy Ion Collider," Phys. Rev. C **97**, 054909 (2018) (cit. on pp. 59, 61, 125–126).

[100] S. Acharya et al. (ALICE Collaboration), "$^{3}_{\Lambda}$H And $^{\overline{3}}_{\overline{\Lambda}}\overline{\mathrm{H}}$ lifetime measurement in pb–pb collisions at $\sqrt{s_{\mathrm{NN}}} = 5.02$ TeV via two-body decay," Phys. Lett. B **797**, 134905 (2019) (cit. on pp. 59–61, 109, 125–126).

[101] M. Abdallah et al. (STAR Collaboration), "Measurements of $^{3}_{\Lambda}$H and $^{4}_{\Lambda}$H Lifetimes and Yields in Au+Au Collisions in the High Baryon Density Region," 10.48550/arXiv.2110.09513 (2021) (cit. on pp. 59, 61, 126).

[102] A. Pérez-Obiol et al., "Revisiting the hypertriton lifetime puzzle," Phys. Lett. B **811**, 135916 (2020) (cit. on pp. 60, 126–128).

[103] F. Hildenbrand et al., "Lifetime of the hypertriton," Phys. Rev. C **102**, 064002 (2020) (cit. on pp. 60, 125–126).

[104] V. N. Vapnik et al., "On the Uniform Convergence of Relative Frequencies of Events to Their Probabilities," Theory of Probability & Its Applications **16**, 264–280 (1971) (cit. on p. 67).

[105] V. Vapnik, *The Nature of Statistical Learning Theory* (Springer, 2014) (cit. on p. 67).

[106] J. Tromp et al., "Combinatorics of Go," in Computers and Games, edited by H. J. van den Herik et al. (2007), pp. 84–99 (cit. on p. 68).

[107] S. Steinerberger, "On the number of positions in chess without promotion," Int. J. Game Theory **44**, 761–767 (2015) (cit. on p. 68).

[108] B. R. Kiran et al., "Deep Reinforcement Learning for Autonomous Driving: A Survey," 10.48550/ARXIV.2002.00444 (2020) (cit. on p. 68).

[109] K. Shao et al., "A Survey of Deep Reinforcement Learning in Video Games," arXiv e-prints, 10.48550/arXiv.1912.10944 (2019) (cit. on p. 68).

[110] D. Silver et al., "Mastering the game of Go without human knowledge," Nature **550**, 354–359 (2017) (cit. on p. 68).

[111] S. B. Kotsiantis, "Decision trees: a recent overview," Artif. Intell. Rev. **39**, 261–283 (2013) (cit. on p. 71).

[112] R. E. Schapire, "The Boosting Approach to Machine Learning: An Overview," in *Nonlinear estimation and classification*, edited by D. D. Denison et al. (Springer New York, 2003), pp. 149–171 (cit. on p. 72).

[113] M. Stone, "Cross-Validatory Choice and Assessment of Statistical Predictions," Journal of the Royal Statistical Society: Series B (Methodological) **36**, 111–133 (1974) (cit. on p. 74).

[114] J. Snoek et al., "Practical Bayesian Optimization of Machine Learning Algorithms," arXiv e-prints, 10.48550/arXiv.1206.2944 (2012) (cit. on p. 75).

[115] N. Quadrianto et al., "Gaussian Process," in *Encyclopedia of machine learning*, edited by C. Sammut et al. (Springer US, Boston, MA, 2010), pp. 428–439 (cit. on p. 75).

[116] J. Schwinger, "The Theory of Quantized Fields. I," Phys. Rev. **82**, 914–927 (1951) (cit. on p. 78).

[117] J. Adam et al. (STAR Collaboration), "Measurement of the mass difference and the binding energy of the hypertriton and antihypertriton," Nat. Phys. **16**, 409–412 (2020) (cit. on pp. 78, 123, 127).

[118] J. Jowett et al., "The 2018 heavy-ion run of the LHC," WEYYPLM2. 4 p (2019) (cit. on p. 78).

[119] X. N. Wang et al., "hijing: A Monte Carlo model for multiple jet production in pp, pA, and AA collisions," Phys. Rev. D **44**, 3501–3516 (1991) (cit. on p. 79).

[120] E. Bartsch, "Recent results on light (anti-)nuclei production with ALICE at the LHC," J. Phys. Conf. Ser. **1602**, 012022 (2020) (cit. on p. 85).

[121] S. Acharya et al. (ALICE Collaboration), "First measurement of the absorption of $^{3}\overline{\mathrm{He}}$ nuclei in matter and impact on their propagation in the galaxy," 10.48550/arXiv.2202.01549 (2022) (cit. on pp. 91, 109).

[122] C. P. Robert et al., *Random Variable Generation* (Springer New York, New York, NY, 2004), pp. 35–77 (cit. on p. 91).

[123] J. Adams et al., "ρ^0 Production and possible modification in Au + Au and $p+p$ collisions at $\sqrt{s_{NN}} = 200$ GeV," Phys. Rev. Lett. **92**, 092301 (2004) (cit. on p. 91).

[124] M. Gazdzicki et al., "Background subtraction from the dilepton spectra in nuclear collisions," 10.48550/arXiv.hep-ph/0003319 (2000) (cit. on p. 91).

[125] M. C. Abreu et al. (NA38 and NA50 Collaborations), "Dimuon and charm production in nucleus-nucleus collisions at the CERN-SPS," Eur. Phys. J. C **14**, 443–455 (2000) (cit. on p. 91).

[126] A. Adare et al. (PHENIX Collaboration), "Detailed measurement of the e^+e^- pair continuum in $p + p$ and Au + Au collisions at $\sqrt{s_{NN}} = 200$ GeV and implications for direct photon production," Phys. Rev. C **81**, 034911 (2010) (cit. on p. 91).

[127] D. Drijard et al., "Study of event mixing and its application to the extraction of resonance signals," Nucl. Instrum. Methods Phys. Res. **225**, 367–377 (1984) (cit. on p. 92).

[GPL] *GNU General Public License*, version 3, Free Software Foundation, June 29, 2007 (cit. on p. 98).

[128] *Python Package Index - PyPI*, https://pypi.org/ (visited on 02/15/2022) (cit. on p. 98).

[129] T. Chen et al., "XGBoost: A Scalable Tree Boosting System," in Proceedings of the 22nd acm sigkdd international conference on knowledge discovery and data mining, KDD '16 (2016), pp. 785–794 (cit. on p. 99).

[130] T. X. Contributors, *XGBoost - ML Challenge Winning Solutions (incomplete list)*, (1999) https://github.com/dmlc/xgboost/blob/master/demo/README.md (visited on 02/14/2022) (cit. on p. 99).

[131] F. Nogueira, *Bayesian Optimization: Open source constrained global optimization tool for Python*, 2014 (cit. on p. 99).

[132] Wikipedia, *Early stopping — Wikipedia, L'enciclopedia libera*, 2022 (cit. on p. 102).

[133] W. Verkerke et al., "The RooFit toolkit for data modeling," eConf **C0303241**, edited by L. Lyons et al., MOLT007 (2003) (cit. on p. 105).

[134] K. S. Cranmer, "Kernel estimation in high-energy physics," Comput. Phys. Commun. **136**, 198–207 (2001) (cit. on p. 105).

[135] "Interaction of hypertritons with nuclei at high energies," Nucl. Phys. A **632**, 624–632 (1998) (cit. on p. 109).

[136] E. Tiesinga et al., "CODATA recommended values of the fundamental physical constants: 2018," Rev. Mod. Phys. **93**, 025010 (2021) (cit. on p. 114).

[137] M. J. Oreglia, "A Study of the Reaction $\psi' \to \gamma\gamma\psi$," PhD thesis (Standford University, 1980) (cit. on p. 117).

[138] W. Gajewski et al., "A compilation of binding energy values of light hypernuclei," Nucl. Phys. B **1**, 105–113 (1967) (cit. on p. 127).

[139] R. Dalitz et al., "Phenomenological study of s-shell hypernuclei with ΛN and ΛNN potentials," Nucl. Phys. B **47**, 109–137 (1972) (cit. on pp. 127–128).

[140] Y. Fujiwara et al., "Addendum to triton and hypertriton binding energies calculated from SU_6 quark-model baryon-baryon interactions," Phys. Rev. C **77**, 027001 (2008) (cit. on p. 127).

[141] D. Lonardoni et al., "Medium-mass hypernuclei and the nucleon-isospin dependence of the three-body hyperon-nucleon-nucleon force," 10.48550/arXiv.1711.07521 (2017) (cit. on p. 127).

This Ph.D. thesis has been typeset by means of the TEX-system facilities. The typesetting engine was LuaLATEX. The document class was `toptesi`, by Claudio Beccari, with option `tipotesi=scudo`. This class is available in every up-to-date and complete TEX-system installation.